



University
of Glasgow

DIRECTED ENERGY DEPOSITION FLOW
CONTROL FOR HIGH SPEED INTAKE
APPLICATIONS

ANDREW RUSSELL

Submitted in fulfilment of the requirements for the
Degree of Doctor of Philosophy

Aerospace Sciences Research Division
School of Engineering
College of Science and Engineering
University of Glasgow

November 2019

© 2019

EXECUTIVE SUMMARY

One of the key enabling technologies for high speed airframes is the propulsion system. Some of the important factors in any widely used propulsion system are reliability and efficiency. Both of these performance indicators are areas that can still be improved for a popular high speed propulsion system, the Ramjet/Scramjet. Regarding the propulsion system efficiency, one component that has a significant impact is the intake. Specifically the intake efficiency, often quantified by the total pressure loss, can significantly influence the overall system performance. Now considering the reliability of the system, a phenomenon known as unstart can present issues for a Ramjet/Scramjet during its operation. This phenomenon refers to the ejection of the shock structure, known as a shock train, from within the internal duct in the ramjet/Scramjet called the isolator. This results in a bow shock upstream of the propulsion system intake leading to significant drag increases and thrust decreases due to reductions in intake mass flow.

This work aims to propose methods that can tackle both of the issues highlighted above. The goal is to use energy deposition based flow control methods to improve the system performance. To achieve this, the first step was the improvement of the available wind tunnel facilities. Through the careful examination and numerical simulations of the existing wind tunnel design, key issues are identified and solved methodically. This included the re-design of the nozzle; both the subsonic and supersonic sections of the nozzle are carefully designed. The diffuser is also re-designed to ensure it is suitable for the desired test section Mach number. Finally, the location of the wind tunnel relative to the vacuum tank is examined and changes are made in order to reduce the conductance present within the system to a level at which the desired mass flow rate could be achieved, and the wind tunnel can operate at the desired flow conditions.

It has previously been shown that the inclusion of a cavity within the isolator can improve the unstart margin. However the introduction of a cavity will result in an increase in the drag of the overall propulsion system. Therefore the aim of this work, with regard to improving the unstart performance of the propulsion system, is to examine how energy deposition flow control can be used to control a supersonic cavity flow. This research will examine the use of nanosecond, high voltage dielectric barrier

discharge (ns-DBD) plasma actuators to control the cavity flow. However before this, the interaction of the cavity with the baseline internal duct flow was examined. This was in order to classify the scale of cavity that could be included in a duct before the influence on the flow was too large for the duct to start. Through Schlieren imaging, it is shown that increasing cavity scale led to an increase in the cavity shear layer which, in turn, became a limiting factor in the ability of the supersonic duct flow to start successfully. It is suggested that increasing cavity length is the dimension with the largest impact on the starting of the duct flow. This work allowed the cavity being examined for flow control applications to be appropriately scaled so as to still allow the supersonic duct flow to start correctly.

The second topic that is necessary before the cavity flow control can be examined is the characterisation of the ns-DBD actuators. The key goal of this section of research is to identify the combination of actuators parameters that resulted in the strongest flow control influence, measured in this case by the generated pressure wave strength. This characterisation process is conducted through the image processing of the captured Schlieren images during the actuator operation. It is found that the only parameters investigated with significant impact on the actuator control authority are electrode length and dielectric thickness. Shorter electrodes and thinner dielectric barriers are found to be the most successful, for the same electrical input signal used and the same dielectric material. Whilst characterising the actuators for control authority, the electrical efficiency of the actuators is also investigated using electrical measurements, quantitative Schlieren and infrared thermography. The quantitative Schlieren and electrical measurements were found to give accurate results, however they did not present any clear conclusions regarding how the geometric parameters investigated influenced the electrical efficiency. The infrared thermography was unsuccessful due to the small temperature variations being measured and the relatively large uncertainty of the equipment used.

Following the characterisation of the ns-DBD plasma actuators, they were applied as flow control to the supersonic cavity flow. Laser vibrometry, Schlieren and oil flow are used to investigate the impact that these actuators have on the baseline supersonic cavity flow. It is found that the actuators available are not able to provide any measureable flow control authority on the baseline cavity flow.

The other performance indicator highlighted above is the efficiency of the intake. This study focuses on the improvement of intake total pressure recovery through the use of laser energy deposition flow control. The aim of the flow control is to mitigate the separation observed on the external compression ramp and, as a result, mitigate the negative impact of the buzz instability, commonly observed in supersonic intakes. It is shown that the use of laser energy deposition can provide an improvement in total pressure recovery and does reduce the impact of these buzz instability modes. It is also illustrated how, for a particular set of example conditions, this could improve the overall fuel consumption of a given Ramjet propulsion system.

CONTENTS

EXECUTIVE SUMMARY	i
LIST OF FIGURES	xiii
LIST OF TABLES	xiv
ACKNOWLEDGEMENTS	xv
AUTHOR'S DECLARATION	xvi
NOMENCLATURE & ABBREVIATIONS	xvii
1 INTRODUCTION	1
1.1 RAMJET PROPULSION FUNDAMENTALS	1
1.1.1 INTAKES	2
1.1.2 ISOLATORS	3
1.2 ACTIVE FLOW CONTROL	4
1.3 MOTIVATION FOR RESEARCH	5
1.4 RESEARCH OBJECTIVES	5
1.5 THESIS OVERVIEW	6
1.6 RELATED PUBLICATIONS	6
2 EXPERIMENTAL AND NUMERICAL METHODS	8
2.1 MEASUREMENT TECHNIQUES	8
2.1.1 SCHLIEREN IMAGING	8
2.1.2 SURFACE OIL FLOW VISUALISATION	10
2.1.3 PRESSURE TRANSDUCERS	12
2.1.4 NANOSECOND HIGH VOLTAGE MEASUREMENTS	14
2.1.5 INFRARED THERMOGRAPHY	17
2.1.6 LASER DOPPLER VIBROMETRY (LDV)	20
2.2 COMPUTATIONAL FLUID DYNAMICS (CFD) METHODOLOGY	21
2.2.1 FUNDAMENTALS OF CFD	21
2.2.2 TURBULENCE MODELLING	23
2.2.3 NUMERICAL SOLUTION	24

2.2.4	MESH GRID	24
2.2.5	TIME DOMAIN	26
3	EXPERIMENTAL FACILITIES AND METHODOLOGIES	27
3.1	THE SUPERSONIC INDRAFT FACILITY	27
3.1.1	FUNDAMENTALS OF INTERMITTENT SUPERSONIC WIND TUNNELS	27
3.1.2	HIGH SPEED TUNNEL REDESIGN	28
3.1.3	WIND TUNNEL OVERHAUL BREAKDOWN	43
3.2	FINALISED WIND TUNNEL CHARACTERISATION	57
3.2.1	CFD SIMULATION	57
3.2.2	PRESSURE MEASUREMENTS	60
3.2.3	SCHLIEREN IMAGING	62
3.3	CONCLUSIONS	64
4	EFFECT OF CAVITY GEOMETRY ON SUPERSONIC DUCT FLOW	67
4.1	SUPERSONIC CAVITY FLOW CHARACTERISTICS	67
4.1.1	CAVITY FLOW CLASSIFICATION	67
4.1.2	OPEN CAVITY RESONANCE MODES	68
4.1.3	PREVIOUS STUDIES ON CAVITY FLOW CONTROL	70
4.1.4	INTERACTION BETWEEN SHOCK TRAIN AND CAVITY	71
4.2	INITIAL CAVITY WIND TUNNEL MODEL	74
4.2.1	DESIGN REQUIREMENTS	74
4.2.2	END RESULT OF DESIGN PROCESS FOR BASELINE CAVITY	76
4.2.3	CAVITY MODEL VARIATIONS	77
4.3	SCHLIEREN VISUALISATION	80
4.4	CONCLUSIONS	85
5	CHARACTERISATION OF DIELECTRIC BARRIER DISCHARGE PLASMA ACTUATORS	88
5.1	DIELECTRIC BARRIER DISCHARGE (DBD) PLASMA ACTUATORS	89
5.1.1	NANOSECOND DIELECTRIC BARRIER DISCHARGE (NS-DBD) PLASMA ACTUATORS	90
5.2	QUANTITATIVE SCHLIEREN EXPERIMENTAL TECHNIQUE	94
5.2.1	CALIBRATED SCHLIEREN	94
5.3	MANUFACTURING AND DESIGN OF ACTUATORS	98
5.3.1	PHOTOLITHOGRAPHY	98
5.3.2	APPLICATION OF PHOTOLITHOGRAPHY TO DBD ACTUATORS	98
5.4	ACTUATOR PARAMETERS TO BE INVESTIGATED	99
5.5	CHARACTERISATION OF NS-DBD ACTUATORS	100
5.5.1	TEST CONDITIONS	100
5.5.2	QUALITATIVE SCHLIEREN IMAGING	100
5.5.3	ELECTRICAL MEASUREMENTS	105

5.5.4	INFRARED THERMOGRAPHY	112
5.5.5	CALIBRATED SCHLIEREN	118
5.6	CONCLUSIONS	128
5.6.1	FINALISED ACTUATOR DESIGN	129
6	SUPERSONIC CAVITY FLOW CONTROL	131
6.1	SUPERSONIC CAVITY CONTROL	131
6.1.1	APPLICATION OF SUPERSONIC CAVITY FLOW CONTROL	132
6.1.2	CAVITY MODEL	133
6.1.3	EXPERIMENTAL MEASUREMENTS RECORDED	134
6.2	VIBROMETER EVALUATION	135
6.3	OIL FLOW VISUALISATION	140
6.4	SCHLIEREN IMAGING	143
6.4.1	HIGH FREQUENCY SCHLIEREN IMAGING	143
6.4.2	TIME AVERAGED SCHLIEREN	145
6.5	VIBROMETER MEASUREMENTS	146
6.6	CONCLUSIONS	146
7	LASER ENERGY DEPOSITION FOR THE SUPPRESSION OF SEPARATION ON AN AXISYMMETRIC CONE INTAKE	151
7.1	SUPERSONIC INTAKES AND THE APPLICATION OF FLOW CONTROL	151
7.2	LASER ENERGY DEPOSITION FOR FLOW CONTROL	154
7.3	WIND TUNNEL FACILITY	156
7.3.1	INTAKE MODEL	157
7.4	RESULTS POST-PROCESSING	158
7.4.1	CONVENTIONAL SCHLIEREN PHOTOGRAPHY	158
7.4.2	PRESSURE MEASUREMENTS	160
7.5	RESULTS	161
7.5.1	FREQUENCY DOMAIN ANALYSIS	162
7.5.2	SCHLIEREN IMAGING ANALYSIS	174
7.5.3	PRESSURE RECOVERY COMPARISON AND RESULTANT IMPACT ON THEORETICAL THRUST	180
7.6	CONCLUSIONS	183
8	CONCLUSIONS AND FUTURE WORK	186
8.1	CONCLUSIONS	186
8.1.1	SUPERSONIC WIND TUNNEL DESIGN	186
8.1.2	NS-DBD ACTUATOR CHARACTERISATION	187
8.1.3	NS-DBD PLASMA ACTUATORS FOR SUPERSONIC CAVITY FLOW CONTROL	188
8.1.4	APPLICATION OF LASER ENERGY DEPOSITION TO IMPROVE RAMJET INTAKE PERFORMANCE	189

8.2	FUTURE WORK	189
8.2.1	NS-DBD ACTUATOR CHARACTERISATION	190
8.2.2	NS-DBD CAVITY FLOW CONTROL	190
8.2.3	LASER ENERGY DEPOSITION TO IMPROVE RAMJET INTAKE PERFORMANCE	190
	BIBLIOGRAPHY	200

LIST OF FIGURES

1.1	Example of a dual mode Ramjet/Scramjet during operation.	2
1.2	Illustration of a basic cavity geometry.	3
2.1	Diagram of the Schlieren setup at the University of Glasgow	11
2.2	Diagram of the oil flow visualisation setup on the supersonic indraft facility at the University of Glasgow	13
2.3	Diagram of the current shunt and how it is mounted to the high voltage system.	16
2.4	Schematic of a typical microbolometer “pixel”	19
2.5	Schematic of the working principle of a Heterodyne Laser Doppler Vibrometer	22
3.1	Schematic showing the dimensions of the final wind tunnel design	27
3.2	Basic schematic of a laval nozzle	29
3.3	Graphical representation of the Mach-Area relationship defined by equation 3.2	30
3.4	Interaction of a characteristic with a wall	32
3.5	Illustration of the characteristics that begin at the nozzle throat and travel downstream.	32
3.6	Diagram of nozzle contour generated through the method of characteristics.	39
3.7	Relationship between normal shock Mach number and the stagnation pressure loss across it[1]	39
3.8	Wind tunnel geometry that illustrates an oblique shock diffuser.	40
3.9	Illustration of typical oblique shock diffuser efficiency[1]	41
3.10	Figure illustrating the final diffuser design.	42
3.11	Total and static pressure measurement location used during the wind tunnel design process.	43
3.12	Total and static pressure measurements for the initial setup of the wind tunnel (each line in the plot is a separate run of the supersonic wind tunnel).	44

3.13	Isentropic Mach number calculated from total and static pressure measurements for the initial setup of the wind tunnel (each line in the plot is a separate run of the supersonic wind tunnel).	45
3.14	Average Schlieren Image of Tunnel Running with Initial Setup	45
3.15	Total pressure ratio for the wind tunnel run with the valve replaced	45
3.16	Mach number for the wind tunnel run with the valve replaced	46
3.17	Average Schlieren Image of Tunnel Run with the Replacement Valve.	46
3.18	Test section total pressure (each line represents a tunnel test)	47
3.19	Total pressure ratio between test section and atmospheric pressure (each line represents a tunnel test)	48
3.20	Normal Shock Mach number from total pressure ratio between test section and atmospheric pressure (each line represents a tunnel test)	48
3.21	An example of an instantaneous Schlieren image taken of the diverging portion of the supersonic nozzle	49
3.22	Location of the normal shock in the nozzle in pixels. For reference, the left hand edge of figure 3.21 is 0 pixels and the right hand edge is 1024.	49
3.23	Instantaneous Schlieren image of the tunnel start up shock train as it travels downstream in the wind tunnel	54
3.24	Static pressure profile recorded 34.6mm downstream of the beginning of the wind tunnel test section	55
3.25	Mach number profile calculated from Bernoulli's principle from static and total pressure measurements	55
3.26	Error in the comparison of measured pressure and actual pressure when numerically solving the compressible Bernoulli equation.	55
3.27	Schematic showing the dimensions of the final wind tunnel design	56
3.28	Basic schematic displaying the vacuum system and the connection to the wind tunnel	56
3.29	Evolution of the Centreline Mach number profile extracted from CFD simulations as the mesh density was altered	57
3.30	Static pressure recorded at the static pressure port in the diffuser.	58
3.31	Static pressure extracted from CFD at the same location as the pressure measurement recorded within the diffuser.	59
3.32	CFD Mach contour of the final wind tunnel design.	59
3.33	Diagram of static pressure ports located on the test section floor	60
3.34	Static pressure profile along the tunnel floor centreline and off centre at $\frac{1}{4}$ tunnel width compared to static pressure extracted from CFD at the corresponding location (only centreline as CFD is 2D)	61
3.35	Pseudo-Continuous (measurement with 1mm resolution) static pressure profile on tunnel floor extracted from CFD	62
3.36	Approximation of the boundary layer thickness extracted from Schlieren imaging compared to Theoretical and CFD values.	64

3.37	Illustration of the node points representing the boundary layer thickness extracted from the Schlieren images.	65
4.1	Diagram of the expected flow field in (a) open and (b) closed cavity flow fields	68
4.2	Illustration of the various levels of flow control classification	72
4.3	Hermann's swallowing function	73
4.4	Cross-sectional view of baseline cavity model located in wind tunnel (top) and orthographic projection of wind tunnel with cavity model installed (bottom)	78
4.5	Graphical representation of the cavity geometries tested	78
4.6	Graphical representation of the cavity geometries tested	79
4.7	3D model view of cavity installed in the wind tunnel with the modular block included for the case with the cavity geometry set to 162mm in length, 20.25mm in depth and $\frac{L}{D} = 8$	79
4.8	Series of Schlieren images at various stages in the indraft supersonic wind tunnel start up process (81mm long, 13.5mm deep cavity)	82
4.9	Series of Schlieren images at various stages in the indraft supersonic wind tunnel start up process (40.5mm long, 27mm deep cavity)	83
4.10	Series of Schlieren images showing the starting shock obstructed by the cavity shear layer/ shock-induced separation (121.5mm long and 20.25mm deep)	84
4.11	Illustration of unsteady start up shock location for unstarted wind tunnel/intake	85
4.12	Visualisation of cavity classification where blue indicates a cavity that allows the intake to start and red indicates a cavity that unstarts the intake. The only points that are test data are the black circles overlaid on the colour plot. Points on the edge of red/blue indicate cavities where both an unstarted and a started intake were observed in different tests. This is simply a result of the unsteadiness of this interaction.	87
5.1	General diagram of a DBD plasma actuator	91
5.2	Schlieren imaging across a plasma actuator illustrating that each plasma filament creates a pressure wave[2]	92
5.3	Comparison of range and sensitivity for a knife-edge cutoff and a graded filter cutoff[3]. The recorded Schlieren images show the image intensity across a knife edge in image (a) and the graded filter in image (b). Image (c) plots the variation in pixel intensity across the lens for each of images (a) and (b).	95
5.4	Schlieren image showing the variation in intensity across the calibration lens and the calibration fit between intensity and refraction angle generated from the image[4]	96
5.5	An example of a DBD actuator created using photolithography.	99

5.6	Intensity profile of phase averaged Schlieren images, one for each phase averaged frame in which the pressure wave is present	101
5.7	Combined Schlieren image showing pressure wave propagation away from DBD surface	102
5.8	Variation in pressure wave strength with varying high voltage electrode width.	103
5.9	Variation in pressure wave strength with varying ground width.	104
5.10	Variation in pressure wave strength with varying electrode gap.	104
5.11	Variation in pressure wave strength with varying dielectric thickness.	104
5.12	Variation in pressure wave strength with varying electrode length.	105
5.13	Calibrated voltage pulse output from nanopulse generator (purely resistive load)	107
5.14	Comparison of calibrated voltage signals (ns-DBD load)	107
5.15	Close up comparison of calibrated voltage signals (ns-DBD)	107
5.16	Example of calibrated voltage signal across an ns-DBD actuator and a exponentially decaying sine wave fit superimposed	108
5.17	Example of voltage pulse area considered for trapezoidal integration in order to calculate pulse energy	109
5.18	Variation in electrical energy consumed per pulse with varying high voltage electrode width	110
5.19	Variation in electrical energy consumed per pulse with varying ground electrode width	110
5.20	Variation in electrical energy consumed per pulse with varying electrode separation	110
5.21	Variation in electrical energy consumed per pulse with varying dielectric thickness	111
5.22	Variation in electrical energy consumed per pulse with varying electrode length	111
5.23	Temperature profile along the length of the plasma discharge	114
5.24	Temperature profile at two different points: the edge of the high voltage electrode and the reverse side of the actuator	114
5.25	Variation in thermal energy lost over the course of the discharge with varying high voltage electrode width	114
5.26	Variation in thermal energy lost over the course of the discharge with varying ground electrode width	115
5.27	Variation in thermal energy lost over the course of the discharge with varying electrode separation	115
5.28	Variation in thermal energy lost over the course of the discharge with varying dielectric thickness	115
5.29	Variation in thermal energy lost over the course of the discharge with varying electrode length	116

-
- 5.30 Schlieren image and extracted temperature profiles illustrating the check carried out to ensure the calibrated Schlieren was set up and operated accurately 120
- 5.31 Set of images that show the evolution of the temperature profile above the DBD plasma actuator with 0.4mm dielectric thickness at (a) 10ms (b) 20ms (c) 30ms (d) 40ms (e) 70ms and (f) 100ms from the beginning of the plasma discharge. 122
- 5.32 Set of images that show the evolution of the temperature profile above the DBD plasma actuator with 0.8mm dielectric thickness at (a) 10ms (b) 20ms (c) 30ms (d) 40ms (e) 70ms and (f) 100ms from the beginning of the plasma discharge. 123
- 5.33 Set of images that show the evolution of the temperature profile above the DBD plasma actuator with 1.6mm dielectric thickness at (a) 10ms (b) 20ms (c) 30ms (d) 40ms (e) 70ms and (f) 100ms from the beginning of the plasma discharge. 124
- 5.34 Temperature profile 1mm above an ns-DBD plasma actuator with 0.4mm dielectric thickness at $x = 0, 1, 2, 3, 4$ and 5mm downstream of the high voltage electrode. 126
- 5.35 Temperature profile 1mm above an ns-DBD plasma actuator with 0.8mm dielectric thickness at $x = 0, 1, 2, 3, 4$ and 5mm downstream of the high voltage electrode. 126
- 5.36 Temperature profile 1mm above an ns-DBD plasma actuator with 1.6mm dielectric thickness at $x = 0, 1, 2, 3, 4$ and 5mm downstream of the high voltage electrode. 126
- 5.37 Temperature profile 1mm above the actuator surface at 1, 10 and 50ms for actuators with 0.4mm, 0.8mm and 1.6mm dielectric thickness. 127
- 5.38 Cumulative energy added across the imaging area for each of the dielectric thicknesses tested (as a function of time) 128
- 6.1 Frequency domain analysis of unsteady pressures at the centre of the cavity floor, extracted from CFD simulations. 137
- 6.2 Frequency domain analysis of vibration measurements recorded at the centre of the cavity floor. 138
- 6.3 PSD of the laser vibrometer data recorded during a bump test conducted on the wind tunnel structure. 138
- 6.4 Frequency domain analysis of pressure measurements recorded at the centre of the cavity floor. 139
- 6.5 Side by side comparison of cavity resonant frequencies observed using different techniques. 139
- 6.6 Side by side comparison of cavity resonant frequencies observed using different techniques. 141
- 6.7 Oil flow visualisation of the cavity floor at various stages in the wind tunnel starting process, including the final steady state flow field. 142

6.8	Comparison of the separation point predicted from the 2D CFD simulations and the separation location extracted from the oil flow visualisation. The red region on both the oil flow image and the CFD static pressure plot shows the separation location as suggested by the oil flow.	143
6.9	The steady state oil flow visualisation for each of the flow control forcing frequencies examined.	144
6.10	Visualisation of the frequency domain extracted from Schlieren imaging of the region above the ns-DBD plasma actuator electrodes.	145
6.11	Time averaged Schlieren imaging across the entire cavity flow field for each of the forcing frequencies examined.	147
6.12	PSD of the vibration measurements captured from the centre of the cavity floor for each of the various forcing frequencies tested.	148
7.1	Illustration of the three supersonic intake modes of operation	153
7.2	Illustration of the compressible, viscous flow field observed for an intake operating in the subcritical regime.	153
7.3	Illustration of relevant dimensions highlighted on model schematic.	158
7.4	Schematic of Intake model	159
7.5	Illustration of regions along which the PSD was calculated where the red line is the segment parallel to the compression cone (1mm from the surface) and the green line is the segment along the centre line of the isolator.	160
7.6	Schlieren image indicating the key features observed in the baseline flow field.	162
7.7	Time series of Schlieren images that illustrate the various stages in the interaction between the supersonic intake flowfield and the laser generated, thermal bubble.	163
7.8	Power spectral density (PSD) of total pressure fluctuations within the intake with no laser energy deposition.	164
7.9	Power spectral density (PSD) of total pressure fluctuations within the intake with laser energy deposition pulsed at 1kHz.	165
7.10	Power spectral density (PSD) of total pressure fluctuations within the intake with laser energy deposition pulsed at 10kHz.	165
7.11	Power spectral density (PSD) of total pressure fluctuations within the intake with laser energy deposition pulsed at 30kHz.	165
7.12	Power spectral density (PSD) of total pressure fluctuations within the intake with laser energy deposition pulsed at 50kHz.	166
7.13	Power spectral density (PSD) of total pressure fluctuations within the intake with laser energy deposition pulsed at 60kHz.	166
7.14	Power spectral density (PSD) of Schlieren imaging intensity along the centreline of the intake isolator.	169
7.15	Schlieren image of the baseline flow with the flow feature highlighted that is thought to be responsible for the oscillations observed within the isolator.	170

7.16	Power spectral density (PSD) of Schlieren imaging intensity 1mm above the external compression ramp.	171
7.17	Diagram illustrating key geometric parameters that are used in the Taylor-Maccoll equation.	172
7.18	An illustration of the measured cone shock angle overlaid on a Schlieren image.	172
7.19	Schlieren image with the profile highlighted that was used for the calculation of the intake resonant frequency modes.	174
7.20	PSD for each of the test cases in the location shown in figure 7.19.	175
7.21	PSD intensity at the identified intake resonant frequency across the entire Schlieren image for each excitation frequency.	176
7.22	Post-processed Schlieren images showing the observed deviation from the mean image intensity for the baseline case and the 1kHz laser pulse frequency case.	178
7.23	Post-processed Schlieren images showing the observed deviation from the mean image intensity for the 10kHz and 30kHz laser pulse frequency cases.	179
7.24	Variation in non-dimensional separation location (σ) with time.	180
7.25	RMS average non-dimensional separation location (σ).	181
7.26	Percentage change in pressure recovery, relative to the baseline case, due to pulsed laser energy deposition.	181
7.27	Percentage reduction in fuel mass flow rate required to achieve a choked flow at the exit of the hypothetical ramjet combustor.	183

LIST OF TABLES

3.1	Conductance of the various pipework configurations used for the wind tunnel	52
3.2	Absolute percentage difference between coincident mesh densities at various points on the wind tunnel centreline	58
3.3	Test Section Boundary Layer Growth Rate Comparison	63
4.1	Predicted Rossiter Modes for Cavities of Various Lengths	76
5.1	Summary of geometric actuator parameters varied	100
5.2	Effect of electrode separation on actuator efficiency	117
5.3	Effect of ground electrode width on actuator efficiency	117
5.4	Effect of high voltage electrode width on actuator efficiency	117
5.5	Effect of electrode length on actuator efficiency	118
5.6	Effect of dielectric thickness on actuator efficiency	118
5.7	Summary of the electrical energy consumed, the thermal energy added to the surrounding air and the associated efficiency of energy conversion for ns-DBD plasma actuators of varying dielectric thickness.	128
6.1	Rossiter resonant frequencies calculated from the Heller modified Rossiter equation.	136
7.1	Mach number variation downstream of the conical shock and downstream of the normal shock.	173
7.2	Resonant frequencies within the isolator, predicted from equation 7.4, for the two different isolator Mach numbers calculated (see table 7.1).	173

ACKNOWLEDGEMENTS

I wish to express my sincere appreciation to my supervisors, Professor Kostas Kontis and Dr. Hossein Zare-Behtash. Their continuous support and technical guidance this project would not have been possible. I would also like to thank Professor Sasoh and the researchers at Nagoya University in Japan for their generosity in hosting me and their support with the work I carried out during my time there.

I would also like to thank Shaun Skinner, Andrew Cusick, Angus Brown, David Pickles and Jonathan Mcgolgan for their support over the years with their helpful discussions but mostly thanks for the completely unrelated conversations that made the whole experience more enjoyable.

Thanks to my family, particularly my Mum and Dad, for their neverending support and encouragement, not just during my years working towards my PhD but for the years leading up to this point. Without this, I would never have achieved what I have.

Finally, a special thanks goes to my girlfriend, Jane. You have put up with more moaning, late nights and PhD related breakdowns than anyone else over the past few years and have been a rock throughout. Without your support with listening to me ramble, making more dinners than I can count and just generally being there when I needed you I would never have made it this far.

All of this work would not have been possible without the funding contributions from the EPSRC (PhD grant) and the University of Glasgow (mobility scholarship). Without their support, this project could not have reached its goal.

AUTHOR'S DECLARATION

"I declare that, except where explicit reference is made to the contribution of others, that this dissertation is the result of my own work and has not been submitted for any other degree at the University of Glasgow or any other institution."

Printed Name: Andrew Russell

Date: 05/04/2020

NOMENCLATURE & ABBREVIATIONS

UNITS

All units of measurement throughout this thesis conform to the *Système Internationale*, with deviations from this rule noted where appropriate.

SYMBOLS

The following symbols are used throughout this thesis. Where a symbol is used only briefly, it is defined at the appropriate point in the text.

LATIN

A	Area
a	Speed of sound / Rossiter phase delay
C	Conductance
C_p	Specific heat capacity
d	Penetration depth
e	Electron charge
E	Energy
f	Frequency/focal length
\mathbf{I}	Identity tensor
I	Current
k	Gladstone-Dale constant
k_c	Vortex convection velocity ratio
K	Characteristic constant (Method of Characteristics)
Kn	Knudsen number

L	Impedance/Length
L/D	Cavity length to depth ratio
M	Mach number
m	Mass/Mode number
n	Refractive index
n_+	Positive ion density
P	Pressure
Pr	Prandtl number
q_{pV}	Throughput
Q	Heat flux
\mathbf{R}	Reynolds stress tensor
r	Lens radius
R	Ideal gas constant
Re	Reynolds number
\mathbf{S}	mean strain rate tensor
St	Strouhal number
t	Time
T	Temperature
U	Velocity
V	Voltage
X	Characteristic length
y^+	Dimensionless wall distance
GREEK	
α	Thermal diffusivity
δ	Displacement thickness
$\Delta\phi$	Voltage drop
ϵ	Emissivity
η	Efficiency

γ	Heat capacity ratio
κ	Turbulent kinetic energy
λ	Wavelength
μ	Dynamic viscosity / Mach angle
ν	Prandtl-Meyer function / Thermal velocity
ϕ	Transport variable
ρ	Air density / thermal reflectivity
σ	Root mean square error / Boltzmann Constant
ω	Specific dissipation rate
Ω	Electrical Resistance
θ	Flow deflection angle/boundary layer thickness
τ	Time constant / thermal transmissivity

SUBSCRIPTS

+/-	left/right running characteristic
∞	Freestream
τ	Turbulent eddy
D	Diffuser
e	Exit condition
exp	Experimental result
fit	Calibration fit result
$init$	Initial condition
max	Maximum
o	stagnation condition
t	Condition at the throat
s	source

SUPERSCRIPTS

*	Sonic condition
---	-----------------

ABBREVIATIONS

CAD	Computer aided design
CFD	Computational fluid dynamics
CFL	Courant-Friedrichs-Levy
DBD	Dielectric barrier discharge
DC	Direct current
EMF	Electromotive force
EMI	Electromagnetic interference
FFT	Fast fourier transform
fps	Frames per second
FR	Flame retardant
IR	Infrared
LAFPA	Localised arc filament plasma actuator
LDV	Laser doppler vibrometry
LED	Light emitting diode
LIG	Liquid in gas
PCB	Printed circuit board
<i>PR</i>	Pressure recovery
PSD	Power spectral density
ROIC	Read out integrated circuit
SLR	Single-lens reflex
TSP	Temperature sensitive paint
UV	Ultraviolet

CHAPTER 1

INTRODUCTION

1.1 RAMJET PROPULSION FUNDAMENTALS

A ramjet is a type of airbreathing engine that, conceptually, is very simple. It uses the ram compression of air against its geometry to compress and decelerate the incoming air. Fuel is then added and burned in the combustion chamber and the air is expanded and accelerated to high speeds through the jet nozzle. It is a simple concept, however in practice there are many challenges to its operation.

Early Ramjet concepts date back to the early 1900's[5], however the first patent for a practical Ramjet application was not until 1926 when Carter patented a Ramjet device for applications to artillery shells. It wasn't until the late 1940's that an aircraft first flew powered solely by a Ramjet, the french Leduc 0.10. As Ramjets cannot provide static thrust, due to the necessary ram compression, the aircraft was launched in mid-air from a mothership. The first truly successful Ramjet powered aircraft was the Nord 1500 Griffon II. This experimental aircraft featured a dual turbojet-Ramjet propulsion system allowing the aircraft to take-off under turbojet power and then use the ramjet once travelling at fast enough speeds. An in-depth history of Ramjet propulsion is presented by Fry[5] if more information is desired.

The modes of operation, and the associated challenges, of a ramjet type propulsion system are heavily dependant on the freestream Mach number at which it is flying. Between Mach 3 and Mach 5, a Ramjet provides the largest specific impulse of any hydrogen fueled engine.[6] In this regime, a typical ramjet will decelerate the freestream flow to subsonic Mach numbers at the entrance to the combustor through a combination of external and internal compression. The internal compression takes place within the component known as the isolator. This is simply a duct within which the internal shock system is isolated from the combustor entrance. Ensuring the pre-combustion shock structure is isolated from the combustor has been shown to improve the overall performance of the system.[7] The drawbacks to the inclusion of

an isolator include increased weight and drag of the system as a whole.

At higher flight Mach numbers, the possible heat addition is limited such that the pressure rise in the combustor is not sufficient to support the internal shock system. As such the entirety of the internal flow is supersonic and the ramjet becomes a Scramjet. Figure 1.1 presents an example of flow through a conceptual ramjet design. In Scramjet operating mode, the isolator no longer appears to serve a significant purpose. However, if too much heat is added within the isolator the combustor can become thermally choked and tend to unstart the engine. This set of circumstances is the reason that an isolator is important, even in a Scramjet mode of operation. A correctly sized isolator can ensure that in these conditions, the shock structure generated due to the thermal choking is contained within the engine and does not exit the intake.

1.1.1 INTAKES

As mentioned above, Ramjets compress the incoming flow through ram compression of the air due to the physical geometry of the intake. The aim of the intake here is to provide a large compression ratio while limiting the total pressure losses. There are however competing requirements such as the ability to start the intake which, if too large a compression ratio is required will lead to the necessity of complex intake designs such as variable geometry and boundary layer bleed to start the intake.

Intake geometries can be split into three separate types: external, internal and mixed compression. Internal compression intakes compress the flow solely through shock waves that are contained within the engine itself. This can result in comparatively short intake designs, however this has the drawback of usually requiring some sort of aid to start the engine such as variable geometry, mass flow bleed etc. External compression geometries, as suggested by the name, compress the flow by shock waves external to the engine itself. These have the benefit of being simpler to start due to overboard spillage (see chapter 7 for more information on this), leading to a larger range of possible operating speeds but with the drawback that they are, generally

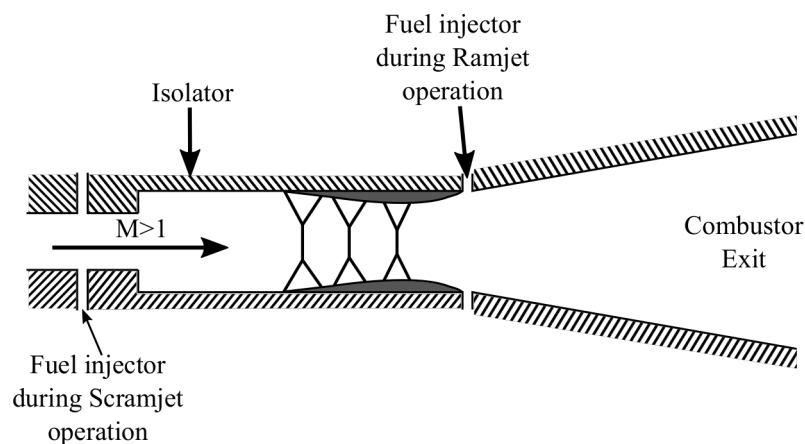


FIGURE 1.1: Example of a dual mode Ramjet/Scramjet during operation.

speaking, larger and thus heavier than a solely internal compression intake. Another very important benefit of external compression is its inherent stability i.e. the engine cannot unstart. Unstart refers to the process where the internal shock system is expelled from the engine and forms an external shock wave. However, as the flight Mach number increases, the losses associated with a solely external compression system begin to increase and the efficiency of the intake reduces. Therefore at higher Mach numbers, intakes often use a mixture of both external and internal compression, and these are known as mixed compression intakes.

One topic within supersonic intake research in general that attracts significant interest is instabilities that arise within the intake. The interaction between the compressible flow features i.e. shock waves and the intake boundary layer can result in a variety of instabilities (see chapter 7). These instabilities are generally a result of operation of the intake at off-design conditions and result in decreases in efficiency relative to the ideal operating conditions. These instabilities could lead to structural fatigue and thrust loss. They are therefore an important area of study not only to understand the phenomenon, but also to attempt to mitigate the effect of such instabilities.

1.1.2 ISOLATORS

The importance of the isolator to both Ramjet and Scramjet operating modes is highlighted above. For Scramjet operation in particular, a key design feature is the length of the isolator. During normal Scramjet operation, the length of the isolator is largely unimportant. However during an unstart event the isolator must be long enough to adequately contain the internal shock structure. The aim is to minimise the length of the isolator, to reduce drag and weight, while still being able to contain the shock structure during unstart. There are novel means by which this unstart margin is achieved, not necessarily solely through the length of the isolator. It has been shown that unstart due to an increase in back pressure can be delayed by the addition of a cavity to the isolator. [8] A cavity in this case refers to a rectangular cutout removed from the floor of the isolator duct (see figure 1.2 for a visualisation) However, the addition of the cavity will result in an increase in the drag of the isolator, mitigating the advantage gained by reducing the isolator length. One possibility that requires further exploration is the reduction of this drag increase due to the cavity.

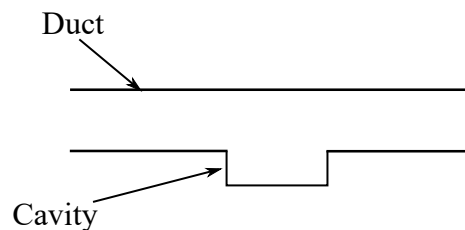


FIGURE 1.2: Illustration of a basic cavity geometry.

1.2 ACTIVE FLOW CONTROL

Flow control is a term that is used to describe techniques that aim to influence an existing flow field. The idea was first suggested by Prandtl[9]. The field can be further split into two distinct categories: active and passive flow control. Passive flow control refers to a means of control which does not have the means to modulate its influence and cannot be turned on or off. There are many examples of passive flow control applied to supersonic flow such as bumps[10], vane type vortex generators[11] and micro vortex generators[12] to name a few. Under specific circumstances some passive flow control techniques have proven to be effective, however there are a number of drawbacks to passive flow control. The two most significant are that the flow control cannot be turned off when no longer required and that it cannot be modified for different flight conditions. Both of the points outlined tend to result in unwanted drag increases at off-design conditions that can detract from the overall performance improvement provided by the flow control in the first place.

The second category mentioned was active flow control. The significant difference between passive and active flow control is that active flow control can be modulated in amplitude and it can be turned on and off. This difference generally means that, depending on the specific method of flow control and the application, both of the significant drawbacks to passive flow control are avoided entirely with active flow control. There are a plethora of examples of active flow control applied to supersonic flows such as the suppression of shock-induced separation using boundary layer bleed[13] or the use of synthetic jets to influence a separation shock wave[14].

One subset of active flow control techniques that has shown promise in recent years are energy deposition techniques. There are a number of techniques that this term encompasses including high voltage discharge methods, laser energy deposition methods and microwave discharge methods. There are a certain benefits that these types of active flow control methods have in comparison to other well known techniques. One benefit is that they have zero net mass flux i.e. there is no impact on the net mass flow rate due to energy deposition methods, unlike boundary layer bleed methods for example. This can be important for applications to engine intakes as a drop in mass flow rate is undesirable. They also, for the most part, have no complex moving parts in comparison to techniques such as flaps or, again, boundary layer bleed. This is important in real world applications as less moving, mechanical parts leads to generally less maintenance and less opportunity for failures. Another benefit that is specific to laser energy deposition (and to a lesser extent microwave discharge) is the ability of the flow control to act from a distance. This is particularly useful for areas where mounting equipment necessary for other techniques can be difficult, such as the tip of an intake compression ramp for example.

1.3 MOTIVATION FOR RESEARCH

Since the first research into supersonic aerodynamics/fluid dynamics, there has been consistent levels of interest. However in recent years there has been an increase in development and future research for both civilian[15] and military applications[16][17]. One of the key enabling technologies that still requires significant research are efficient propulsion systems. As highlighted by the increasing interest in the development of the Sabre engine by Reaction Engines, ramjets/scramjets are a promising technology to meet the future requirements of supersonic travel. However, as highlighted above, there are still obstacles to overcome. This research will focus on improving the overall performance of ramjets/scramjets through the application of energy deposition methods of active flow control. The first topic of interest will focus on improving the operability/reducing the weight of scramjets. Previous work has shown that cavities located within the isolator can delay unstart[8] thus improving the unstart margin of a scramjet. However the cavity introduces undesired drag to the system; the reduction of this drag will be the focus here. The objectives will be to first examine the baseline flow field and how this changes with the addition of a cavity. This research, along with the majority of this work, is carried out using the Mach 1.8 indraft supersonic wind tunnel facility. Particular interest will be paid during the start up of the facility regarding the interaction of the cavity with the wind tunnel start up shock train. Following this, high voltage plasma discharge will be used to try and influence the naturally occurring resonance within the cavity flow field. The second topic will focus on the external compression ramp of a supersonic intake. The objective here will be to use laser energy deposition to influence the instabilities that occur under certain operating conditions. The impact on intake performance will be examined and the overall impact on a hypothetical engine's performance will be demonstrated. This second section of work which focuses on laser energy deposition was carried out at the Nagoya University in Japan using an indraft supersonic (Mach 1.92) wind tunnel. Therefore throughout the text there will be some references to the wind tunnel setup etc. at Nagoya University as opposed to the University of Glasgow where the rest of the research was conducted.

1.4 RESEARCH OBJECTIVES

The overall objectives for this research can be described as:

1. Characterise ns-DBD plasma actuators both in terms of flow control authority and thermal efficiency.
2. Investigate the fundamental thermal behaviour of DBD plasma actuators.
3. Investigate the flow field resulting from the interaction of a confined duct (isolator) and a cavity.
4. Implement ns-DBD plasma actuators as a means of supersonic cavity flow

control.

5. Implement pulsed laser energy deposition as a means to influence the instabilities which occur in an external supersonic intake flow. Measure the impact on the intake efficiency and overall propulsion system performance as a result of this flow control.
6. During the above objectives, characterise and implement the use of innovative experimental methods as appropriate such as quantitative Schlieren, IR imaging and laser vibrometry.

1.5 THESIS OVERVIEW

Following the introduction above, the remainder of this thesis is split into chapters as follows:

- Chapter 2 provides a detail account of the various experimental and numerical methods used throughout this work.
- Chapter 3 details the redesign and characterisation of the wind tunnel facilities used for this research.
- Chapter 5 describes the characterisation of the ns-DBD actuators, highlighting the impact of various geometric parameters. It also includes analysis of the fundamental thermal behaviour of ns-DBD plasma actuators.
- Chapter 4 presents the largely qualitative analysis of the flow field resulting from the introduction of a cavity to a confined, supersonic duct flow.
- Chapter 6 details the attempts made to use ns-DBD plasma actuators to control supersonic cavity flows. The primary focus is how the ns-DBD plasma actuators can be used to influence the naturally occurring resonance within these cavity flows.
- Chapter 7 presents the application of laser energy deposition as a flow control method for external supersonic intakes. The aim of the flow control is to mitigate the impact of instability modes present within the intake and to quantify the potential impact on the overall propulsion system performance.

1.6 RELATED PUBLICATIONS

Russell, A., Zare-Behtash, H. and Kontis, K. (2016). Joule Heating Flow Control Methods for high-speed flows. *Journal of Electrostatics*, 80, 34-68.

Takahiro, U., Russell, A., Zare-Behtash, H. and Kontis, K. (2018). Temporal variation of the spatial density distribution above a nanosecond pulsed dielectric barrier discharge plasma actuator in quiescent air. *Physics of Fluids*, 30(11).

Wojewodka, M., White, C., Ukai, T., Russell, A. and Kontis, K. (2019). Pressure dependency on a nanosecond pulsed dielectric barrier discharge plasma actuator. *Physics of Plasmas*, 26(6).

Russell, A., Myokan, M., Bottini, H., Sasoh, A., Zare-Behtash, H. and Kontis, K. (2019). Application of Laser Energy Deposition to Improve Performance for High Speed Intakes. *Propulsion and Power*.

Russell, A., Zare-Behtash, H. and Kontis, K. (TBC) Application of Laser Doppler Vibrometry for Measuring Resonant Frequencies driven by Fluid Pressure Fluctuations. *Journal of Measurement*. (Submitted for Publication)

Russell, A., Zare-Behtash, H. and Kontis, K. (TBC) Impact of a Cavity Geometry on the Starting Characteristics of a Rectangular Duct. (Work in progress)

CHAPTER 2

EXPERIMENTAL AND NUMERICAL METHODS

It is important to explain and discuss the techniques, both experimental and numerical, which have been used to examine the topic under investigation. This section will first examine the range of experimental techniques used including Schlieren, surface oil flow visualisation, infrared thermography, and pressure measurements. Afterwards, the computational fluid dynamics (CFD) methodology will be explained; this will focus on the decisions made with regards to the numerical modelling rather than the solver itself, StarCCM+, as it is a well-known commercial solver.

2.1 MEASUREMENT TECHNIQUES

2.1.1 SCHLIEREN IMAGING

Schlieren is a widely used technique for visualising density gradients in fluid flows. Investigation of the fundamental laws of physics that form the backbone of Schlieren imaging can be traced back to the 1600's when Robert Hooke observed the refraction of light as it travels through a fluid of varying density[18]. However the inventor of the Schlieren technique as it is known today is widely regarded to be a German physicist, August Toepler[19]. His German origin is the reason for the name of the technique. The english translation of Schlieren means "streaks", refering to the patterns observed in refracted light, a result of density changes in the fluid. Schlieren is a completely unintrusive technique, this along with being able to achieve a global measurement rather than just a point measurement makes it incredibly useful for examining flows with large density gradients. The main restriction with Schlieren however is that in its simplest and most used format it is entirely qualitative. However, as will be discussed later in this work, careful calibration of the setup can provide useful quantitative data if done correctly.

FUNDAMENTAL PRINCIPLES

The basic principle that allows Schlieren to be used to visualise density gradients is that the refractive index of a gas is affected by the density of said gas. Equation 2.1 illustrates the mathematical relationship between refractive index and the density of a gas:

$$n - 1 = k\rho \quad (2.1)$$

Equation 2.1 is known as the Gladstone-Dale relationship where n is the refractive index of the fluid, ρ is the density of the fluid and k is the Gladstone-Dale constant which changes depending on the fluid in question. It illustrates how, as density changes within a fluid, so does the refractive index. Therefore if a beam of collimated light is shone through a fluid, changes in density will result in a change in refractive index, distorting the collimated beam of light. These distortions manifest themselves in dark and bright areas in the captured image. These changes in light intensity highlight the areas of changing density. This type of imaging describes shadowgraphy, first documented in research in 1780[20] and is a very simple technique that uses the same fundamental principle. In order to capture a Schlieren image the collimated light must be focused by an optical element after the area of interest. Then a knife edge can be placed at the focal point to block a portion of the light. This increases the sensitivity of the system when compared to shadowgraphy. The sensitivity of a Schlieren system has been shown to be equivalent to $S = \frac{f_2}{h}$ [21]. where S is the system sensitivity, f_2 is the focal length of the second mirror and h is the proportion of the light passing the cutoff device, most often a knife edge. Therefore, for a fixed system i.e. a fixed focal length for the second mirror in a 2 mirror z-type system (see next section) the only way to modify the sensitivity is to modify the proportion of the light blocked by the knife edge. Clearly, as the proportion of the light that is allowed past the knife edge is reduced the sensitivity increases. The trade-off for this is that as more light is blocked by the knife edge, a more powerful light source is required to ensure sufficient illumination of the image.

EQUIPMENT SETUP

This research uses fundamentally the same setup as Toepler used in his experiments, the so-called Z-type Schlieren system that is still widely used today. Figure 2.1 provides a diagram that visualises the setup as used with the University of Glasgow wind tunnel. A Z-type Schlieren system has 7 main components: a light source, two focusing lenses, a slit, two concave parabolic mirrors, a knife edge, and a camera. The slit is placed at the focal distances of both the initial focusing lens and the first parabolic mirror. To ensure an even light intensity across the image the knife edge must be positioned precisely at the focal distance of the second parabolic mirror. The

attraction of a Z-type Schlieren system is that it minimises the physical space required for the system. However, for the work carried out at the University of Glasgow, another addition was made to the system to allow the system to be used in the space available. Flat mirrors were used to steer the beam of collimated light across the wind tunnel test section. This was necessary as the focal length of the parabolic mirrors was 6ft and there was not sufficient physical space in the vicinity of the wind tunnels to allow operation of the Schlieren system without the flexibility allowed by the use of the extra mirrors. The setup at Nagoya University was the same except that no flat mirrors were required. The setup at University of Glasgow used a Xenon arc lamp from Newport Photonics, two 20cm diameter flat mirrors, two 8 inch diameter parabolic mirrors, a horizontal knife edge and a Photron SA-1 high speed camera. At Nagoya University a pulsed diode laser of 640nm wavelength and 10ns pulse duration was used as the light source with two, 300mm diameter parabolic mirrors, a horizontal knife edge a high-speed Phantom camera were used.

LIMITATIONS

There are limitations of Schlieren that must be highlighted. The first is the quality of images that could be recorded of the wind tunnel test section at University of Glasgow. Due to restrictions in budget, high quality optical glass that was strong enough to be used on the side of the wind tunnel (such as the BK7 optical glass used in Nagoya) was unavailable. As such, standard tempered glass was used to ensure the tunnel remained structurally sound. Due to the process by which tempered glass is manufactured, there is significant variation in density and thus refractive index across it [22]. As such there are significant non-uniformities across the glass that could not be avoided. These do not prevent useful information from being extracted from the Schlieren images but they do lower the optical quality of the images.

Another limitation of the Schlieren set was the repeatability of the sensitivity. As mentioned in the description above, the sensitivity of a Schlieren setup is controlled fundamentally by the fraction of light blocked by the knife edge. Due to the flexibility of the setup at the University of Glasgow it was not always possible to position the knife edge in such a manner as to block the same fraction of light every time the system was setup/moved. This is not a significant issue, however for some of the measurements explained in later sections it does add a degree of uncertainty that is difficult to quantify, even if it is thought to be insignificant.

2.1.2 SURFACE OIL FLOW VISUALISATION

Another simple, yet enlightening, qualitative flow visualisation technique is surface oil flow visualisation. The principle of oil flow is very simple, a fluorescent oil mixture is deposited in the region of interest in the wind tunnel before the tunnel is switched on. Images/video can then be recorded of the oil flow during the running of the tunnel to visualise the streamlines of the flowfield. For subsonic applications where the flow is

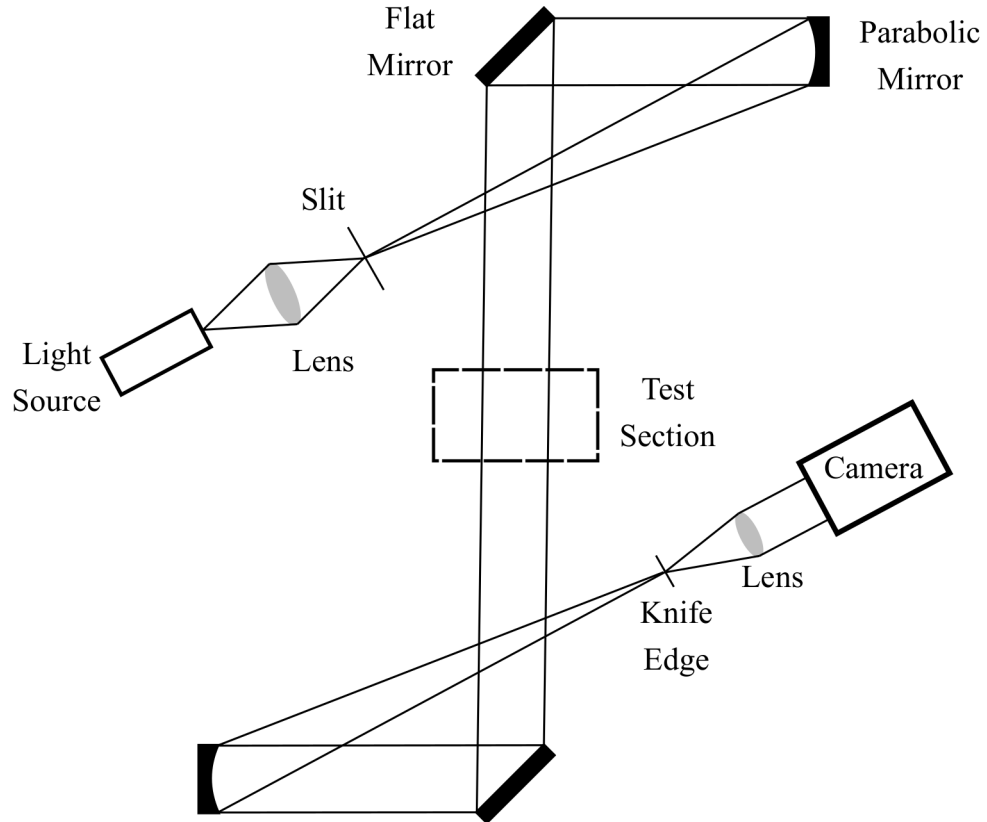


FIGURE 2.1: Diagram of the Schlieren setup at the University of Glasgow

steady, images are often recorded after the wind tunnel has been run. However for supersonic applications this is not feasible as the normal shock/shock train structure that passes down the tunnel at the end of the run will affect the details of the oil flow visualisation. Therefore for supersonic applications, such as this research, the images must be recorded live as the tunnel is running, even for steady phenomenon. Oil flow is particularly useful for visualising separation points in the flow as oil tends to gather at the separation locations.

OIL FLOW FORMULA

The key component in the recipe for oil used for surface oil flow visualisation is the viscosity of the mixture. If the viscosity is too low then the oil flow will travel too quickly and no useful images will be available. If the viscosity is too high then the oil flow will barely move, obstruct the flow, and the result will be the same. It is also important to recognise that the viscosity needed for the oil flow is linked to the expected velocity in the flow field. For this work a recipe from a previous study[23] was used. It was proven to provide useful results in the region of Mach 1.3 to 1.9 and as such, is appropriate for this work. The oil was mixed in glass vials and the quantities measured using a HRB-e 203 digital electronic scale. The mixture used was 10g fluorescent powder, 12g paraffin oil, 2.4g of silicon oil, and 10 of drops oleic acid. The last two components control the viscosity of the formula, therefore the quantities are key.

LIMITATIONS

The first drawback of oil flow is that it can only provide information on the model surface, and the second is that it is entirely qualitative. The last limitation however is not immediately obvious at first glance and did impose a somewhat significant limitation on the results recorded. This limitation is the frame rate achievable by the system used. The choice for the equipment available had to be made between frame rate and image resolution. As a result the frame rate was limited to 30fps. For the application this technique was used for (explained in the relevant section), the frame rate was deemed less important than the resolution as the information desired could be achieved from the average images. Therefore, although restricting, this issue did not result in any significant issue for the research carried out.

TUNNEL SETUP

Other than the oil flow, the two main components necessary for oil flow visualisation are the camera and a light source. In order to maintain the quality of the images it is important that the camera is kept as close to perpendicular to the surface being visualised as possible. It is also important to have uniform illumination across the area of interest in order to achieve consistent visualisation across the region of interest. For this study the camera used was a Canon EOS 600D SLR camera. An SLR camera was used instead of a high-speed camera so that a higher resolution was achieved. It is also the case that for the oil flow visualisation carried out, only the steady state flow field was of interest so high speed imaging was unnecessary. The illumination was provided by an ISSI continuous LED lamp operating at 460nm. Figure 2.2 illustrates how the equipment was setup around the wind tunnel for surface oil flow visualisation.

2.1.3 PRESSURE TRANSDUCERS

UNIVERSITY OF GLASGOW FACILITY

For pressure measurements conducted at the University of Glasgow, Kulite pressure transducers were used for static pressure measurements. The transducers had to be calibrated before they were used for experiments. This was done by applying a known pressure to each transducer using a Druck DPI 610 precision portable pressure calibrator. The pressure was incremented in approximately 0.1bar increments and at each increment the output voltage of the transducer was measured via an in-house Labview program. This process was repeated for both increasing and decreasing pressure in order to attempt to quantify the hysteresis expected due to the mechanical construction of the transducer. The measured hysteresis is explained later in the errors section for this work.

The mounting location for pressure transducers is very important when response time of the transducer is important i.e. high frequency measurements. Both the diameter of the pressure tapping and the length of tubing connecting the tapping to

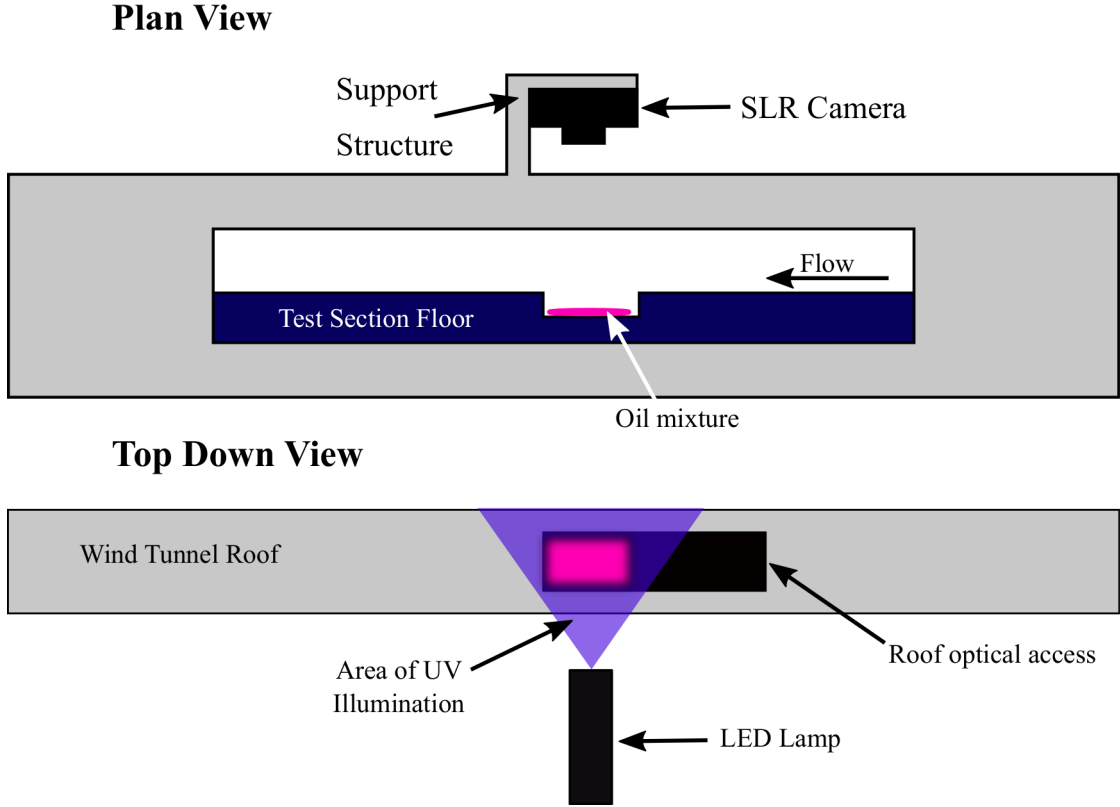


FIGURE 2.2: Diagram of the oil flow visualisation setup on the supersonic indraft facility at the University of Glasgow

the surface of the transducer are important when trying to resolve high frequency components of pressure measurements. Bajsic et al.[24] conducted an insightful study on the effect that tubing length and tapping diameter can have on the settling time for pressure measurements. It was shown that for the tapping/tubing diameter, the optimal value is in the region of 1mm in diameter, but that the true optimal value will vary depending on the tubing length. Therefore, due to restrictions on available internal diameters, tappings and tubing with 1mm internal diameter were used. When considering tubing length, they showed that even for tubing only 100mm in length, the settling time for a 1% dynamic error was approximately 36ms. Equation 2.2 illustrates how this can be related to the time constant of the system and then to the cutoff frequency:

$$t_{1\%} = -\tau \cdot \ln(0.01)$$

$$f = \frac{1}{2\pi\tau} \quad (2.2)$$

where $\tau_{1\%}$ is the settling time for a 1% dynamic error and f is the cutoff frequency. So for a $t_{1\%} = 0.036s$, this results in a cutoff frequency $f = 20.36Hz$. This is much too low for the expected resonant cavity frequencies (discussed in a later section). Therefore for any measurement requiring a fast response time, the transducers must

be surface mounted to avoid any tubing. For measurements that were not dependent on fast response times the transducers were connected via rubber tubing to pressure taps on the model surface. This was necessary since space was limited around the wind tunnel and so where surface mounted transducers were unnecessary, they were avoided.

NAGOYA UNIVERSITY FACILITY

For the work carried out at Nagoya University, both static and total pressure measurements were recorded. A fast time response was important for some of the total pressure measurements recorded, therefore a flush mounted piezoelectric transducer was used. The piezoelectric transducer used was a H112A21 manufactured by PCB Inc. and has a response time of $1\mu s$. For the measurements of total and static pressure where time response was unimportant a static pitot probe and centreline total pressure probe was used with a TOKYO AIRCRAFT Digital Pressure Gauge DG-920N.

LIMITATIONS AND ERRORS

Regarding the limitations of this technique, there are two important issues. The first is that the measurement is a point measurement and therefore the information available is limited to a certain number of discrete locations. While not a significant issue for this study, it is a limitation of the technique. The other significant issue is that the transducers, and the equipment that is used to record the signals from the transducers, are very sensitive to electromagnetic interference. This can be seen from observations of the baseline tunnel measurements and explains the small signal spike seen as the tunnel starts in later pressure plots (an example is seen in section 3.2 in figure 3.30). However for the later work where ns-DBD plasma actuators are in operation, there is significant electromagnetic interference generated; such that the National Instruments DAQ system consistently crashed (most likely due to the susceptibility of the USB connection to electromagnetic interference). There was no solution found for this, the impact of which is discussed in a later section.

Regarding the errors associated with these measurements, there are a number of sources: hysteresis, non-linearity of the response, and repeatability errors are the main sources. These are accounted for as a single error source provided in the data sheet for the Kulites, at a quoted maximum of $\pm 0.5\%$ of the full scale output, equivalent to 5mV or 3.1Pa.

For the system in Nagoya the same sources of error are present. The datasheet for the system quotes the total error as $\pm 0.1\%$ of the full scale output ± 1 digit. This equates to an uncertainty of $\pm 0.21kPa$.

2.1.4 NANOSECOND HIGH VOLTAGE MEASUREMENTS

One of the components of the plasma actuator characterisation, discussed in more depth later, is the measurement of the voltage supplied to the actuator. Measuring

high voltage or signals with fast pulse edges (nanosecond in length) in isolation is not difficult to do accurately with off the shelf technology. However when these two features are combined in one signal, recording measurements is no longer a simple task. The main difficulty with the measurement is that, with fast pulse edges, it is important to minimise the inductive reactance to avoid signal overshoot and unwanted dynamic responses to a step input. It was determined that a suitable method for measuring the voltage was to use the back-current shunt technique.[25] This method uses a shunt resistor with a very small resistance value (usually a few hundred $m\Omega$ at most) that is connected across the shielding on the coaxial cable that supplies the high voltage signals to the DBD plasma actuator. Figure 2.3 illustrates the current shunt connections across the coaxial cable. From transmission line theory, the voltage level in the core of the cable can be related to the current being drawn from the supply (the same value everywhere i.e. the core and the shielding) by equation 2.3:

$$V_{supply} = L_{characteristic} \cdot I \quad (2.3)$$

where V_{supply} is the supply voltage, I is the current through the transmission line and $L_{characteristic}$ is the characteristic impedance of the transmission line. The characteristic impedance is a known value for the transmission line and in this case is 75Ω . Using a low resistance current shunt converts this current into a voltage at a level that can be read directly from an oscilloscope. The end result is a voltage that can be transformed into the voltage level through the core of the transmission line by equation 2.4:

$$V_{supply} = V_{shunt} \cdot \frac{L_{characteristic}}{R_{shunt}} \quad (2.4)$$

where V_{shunt} is the voltage measured across the current shunt and R_{shunt} is the known current shunt resistance. The fundamental principle is simple, however constructing a current shunt that can accurately capture high voltage nanosecond pulses is complicated.

CURRENT SHUNT DESIGN

The design of the current shunt proved to be quite challenging. It was found that the output signal was very sensitive to even the smallest amount of stray inductance in the design. Inductance is the property of an electrical component that causes an electromotive force (EMF), commonly referred to as a voltage, in a circuit as a result of a change in current. This EMF will always act in a direction to oppose the change in current. For this application, the edges of the voltage pulses to be measured are very fast (approximately 4ns). This results in a very fast rate of change of current over the pulse on both the rising and falling edge. Any stray inductance has the impact of

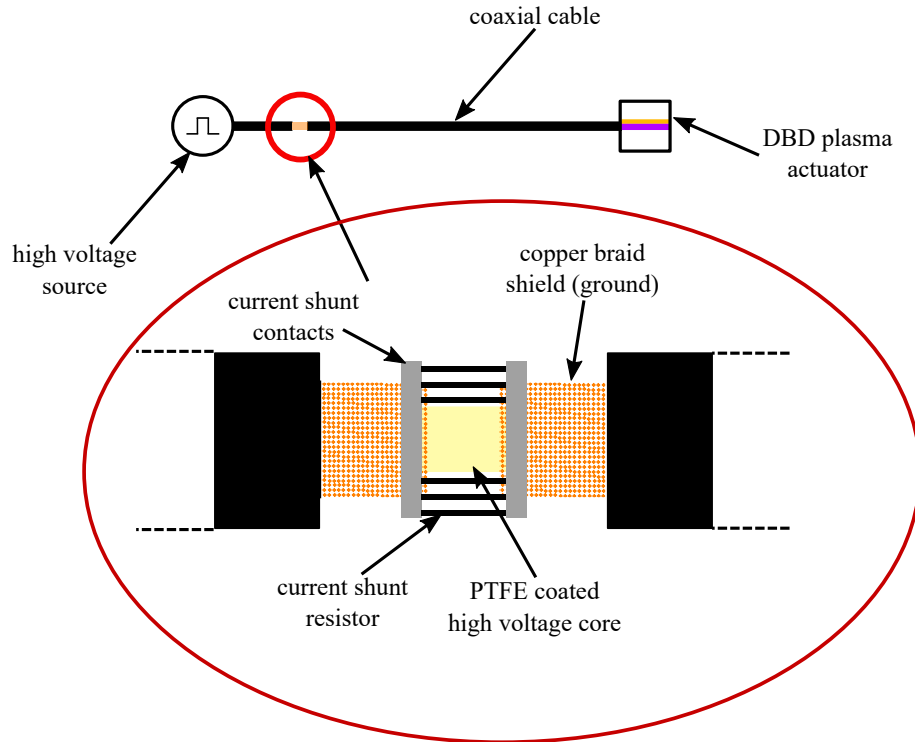


FIGURE 2.3: Diagram of the current shunt and how it is mounted to the high voltage system.

causing an oscillating signal in the measured voltage. It was found that eliminating this “ringing” in the signal was incredibly challenging due to the multiple sources of stray inductance in the circuit. A number of design choices were made in order to minimise the inductance as much as possible:

- Eliminate any wiring between the coaxial cable carrying the high voltage pulses and the current shunt (wires are a significant source of stray inductance);
- Minimise the length of wire that connects the DBD actuator to the coaxial cable for the same reason as above (although likely to be less significant);
- Use of multiple resistors in parallel, as opposed to one larger resistor, to minimise stray inductance;
- Use larger area terminals at each end of the current shunt to further minimise inductance.

The end result was a set of resistors connected in parallel that fit directly on to the ground of the coaxial cable with no wiring between the ground of the cable and the shunt. This was made up of twenty 4.7Ω resistors connected in parallel to give a total shunt resistance of $235\text{m}\Omega$. With a coaxial cable that had a characteristic impedance of 75Ω , the voltage measured across the shunt using an oscilloscope was factored up by 319.15 to give the actual voltage through the centre of the coaxial cable.

LIMITATIONS

There are a couple of issues that could not be resolved with regards to the application of this measurement technique. This first is the accuracy of the current shunt calibration. Ideally the shunt would be calibrated using a pulse generator that produces a known voltage pulse, however such a device was not available for use. Therefore the theoretical value had to be used as presented in equation 2.4 ($\frac{L_{characteristic}}{R_{shunt}}$). This has been shown in a previous study[26] to be a very good approximation of the true value and so this was not considered a significant issue.

The second issue was not a limitation of the current shunt itself, but of the electrical properties of the rest of the system. The impedance of the cable was found to not match that of the generator and this created unwanted reflections within the measurement. This particular limitation and the effect of this on the results will be discussed in chapter 5.

2.1.5 INFRARED THERMOGRAPHY

There are a variety of techniques that have been developed to measure temperatures over the years. The most common techniques used are liquid in gas (LIG) thermometers, thermocouples, thermistors, temperature sensitive paint (TSP) and optical/total radiation thermography. However for this research there a number of factors that rule out most of these options. A significant issue with the environment being examined is the presence of high voltage electricity at the measurement location. This implies that thermocouples cannot be used, as a thermocouple is formed of two different electrical conductors, both of which would conduct the high voltage electricity (10kV+) and damage the sensor. Thermistors are also unusable for the same reason. TSP sensors (i.e. cameras used to record the images) will not be at risk themselves from high voltage electricity. However it was not known how the paint would react to high voltage electricity, therefore it was deemed sensible to avoid TSP for this application in favour of a more risk free solution. LIG thermometers, while simple to use, are relatively inaccurate due to their analogue nature. They are also not ideal for surface measurement as they are dependant on the temperature of the medium they are immersed in. This leaves the only viable measurement technique to be thermography.

CALCULATING TEMPERATURE FROM EMITTED RADIATION

Thermography is the measurement and interpretation of radiation emitted from all bodies according to the black body radiation laws[27][28]. The energy radiated from bodies that we now call infrared radiation was first discovered by English physicist William Herschel in 1800 and subsequently studied by a number of physicists.[29] From the work of these physicists, Plancks law (see equation 2.5) was developed that allowed the quantification of the energy flux per wavelength emitted by a black body in a vacuum, per unit area:

$$E_{b\lambda}(\lambda, T) = \frac{C_1}{\lambda^5 \left(e^{\frac{C_2}{\lambda T}} - 1 \right)} \quad (2.5)$$

where C_1 and C_2 are constants, T is the body temperature and λ is the emission wavelength. This was then taken further to allow the calculation of total energy flux (energy across all wavelengths) by integrating Plank's law over the spectrum of wavelengths. This equation is known as the Stefan-Boltzmann law:

$$E_b = \int_0^{\infty} E_{b\lambda}(\lambda, T) d\lambda = \sigma T^4 \quad (2.6)$$

where σ is the Stefan-Boltzmann constant. If the closed form of the fractional emissive power function is introduced (equation 2.7[30]) and it is noted that detectors used in infrared cameras are usually limited to a specific range of wavelengths, then E_b can be evaluated as equation 2.8:

$$f(\lambda T) = \frac{15}{\pi^4} \sum_{n=1}^{\infty} \left(\frac{e^{-n\zeta}}{n} \left(\zeta^3 + \frac{3\zeta^2}{n} + \frac{6\zeta}{n^2} + \frac{6}{n^3} \right) \right) \quad (2.7)$$

$$E_{b,\lambda_1-\lambda_2}(T) = \sigma T^4 (f(\lambda_2 T) - f(\lambda_1 T)) \quad (2.8)$$

where ζ is a function of wavelength. The above equations hold perfectly true for a black body, however for real objects that do not absorb all electromagnetic radiation, the fraction of energy emitted must be considered. A real object can react in three ways to incoming radiation: reflection, absorption or transmission. If energy conservation is considered then equation 2.9 is created:

$$\alpha_r + \rho_r + \tau_r = 1 \quad (2.9)$$

where α_r is the object absorptivity, ρ_r is the object reflectivity and τ_r is the object transmissivity. For a black body, $\alpha_r = 1$ which means that both τ_r and ρ_r are 0. When total energy radiated is considered, a real object generally radiates less energy than a black body. A parameter known as emissivity, ϵ_t , is generally used to relate the energy emitted by a real body to that of a black body at the same temperature:

$$\epsilon_t(T) = \frac{E(T)}{E_b(T)} \quad (2.10)$$

This parameter allows the radiation measured by a detector to be related to the radiation that would be measured from a black body at the same temperature and thus, through the equations described above, the temperature of the real object can be calculated.

DEVICE FOR MEASURING RADIATED ENERGY

For this work a device that uses a microbolometer detector was used. This is a form of thermal detector first introduced by Langley in 1881[31]. Bolometers are a general set of detectors that measure radiation by using a detector that has a temperature dependant resistance.[29] These have the advantage compared to other sensors of being uncooled and not having a necessary cool down time between each recording. Microbolometer-based devices typically have an array of pixels mounted on a single read out integrated circuit (ROIC). Each pixel is in the form of a “table” with the sensor material forming the “table top”. The sensor material will either be vanadium oxide or amorphous silicon. The material for the “legs” of the table must be chosen carefully as they must conduct electricity in order for the change in resistance of the sensor to be measured, however they must be thermally insulative so as to isolate the sensor itself. A reflective mirror is often placed between the sensor material and the ROIC to enhance the level of radiation absoroptioin by the sensor itself. Figure 2.4 illustrates this physical structure of the sensor.

For this work the FLIR A655sc infrared camera was used. It uses an uncooled microbolometer with a spectral detection range of 7.5-14 μ m. It is capable of recording images at up to 200Hz with an accuracy of $\pm 2^\circ$ C.

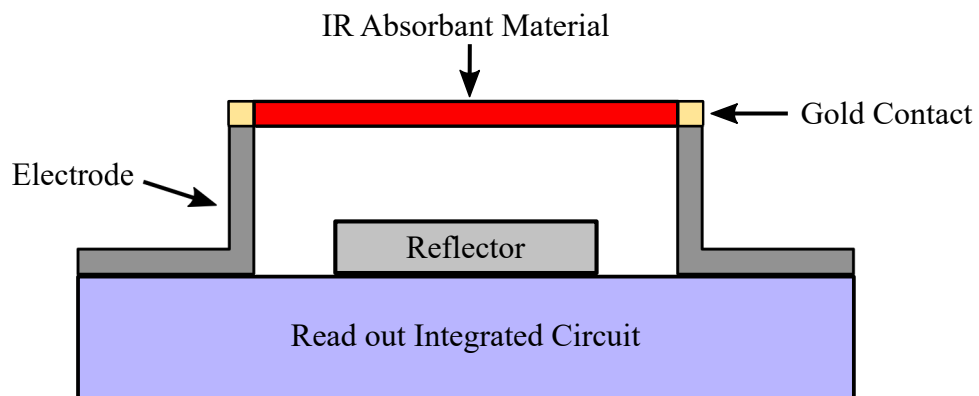


FIGURE 2.4: Schematic of a typical microbolometer “pixel”

LIMITATIONS AND ERRORS

There are a number of limitations and error sources that must be taken into account when examining the data from the IR camera. There were two main limitations imposed as a result of the hardware used: the accuracy of the temperatures recorded, and the length of time over which data could be accurately recorded. Results presented later in chapter 5 will highlight that in some cases the measured temperature changes can be very small. In some cases this resulted in measured temperature changes that were within the uncertainty limitation of the camera. However it is not clear whether this uncertainty will be an issue when examining a temperature difference that occurs during a single measurement. This issue is discussed in more detail in chapter 5.

The length of time over which data could be recorded was a limiting factor as a result of an undesired phenomenon produced by the DBD plasma actuator/ nano-second pulse voltage generator. NS-DBD plasma actuators and nanosecond pulse voltage generators generate significant electromagnetic interference. This particular IR camera has a motorised lens control that is used to adjust the lens focus from the software. This is useful but also means that the lens focus is affected by the plasma actuators as the electromagnetic interference resulted in a current generated in the motor causing the focal position to change. This resulted in the IR camera losing focus as the DBD actuator was operated. The end result was that the camera was limited to operating for approximately 0.15s before the focus was too poor to record accurate data. This judgement was made based on examination of images recorded for a longer period of time and only saving images up to a point in time where the camera was still focused on the surface of the plasma actuator.

2.1.6 LASER DOPPLER VIBROMETRY (LDV)

Laser vibrometry is the process of using laser light to detect the vibrations present in the target object. The technique is possible due to the Doppler effect where the observed frequency of a signal is dependant on the velocity of the object. As the object moves towards the measurement location, the observed frequency increases and vice-versa as the object moves away.

There are two types of LDV devices: homodyne and heterodyne. In this case the equipment used is a heterodyne vibrometer, a schematic of which is shown in figure 2.5. The laser beam is split into two separate beams: a reference beam and the test beam. The reference beam is passed through a Bragg cell which effectively adds a large frequency shift to the reference beam. This shift is necessary in order for the direction of the vibration to be measured by the system. The test beam passes along a separate path and onto the measurement target. The velocity of the target results in a shift in the frequency of the laser beam reflected back to the measurement device. The test beam and the reference beam are then recombined and reach the detector. Throughout this process the frequency and phase of the two beams have changed however their polarisation state as they reach the detector is the same. Therefore they interfere with

each other to form a frequency modulated signal. A frequency modulated signal is one in which there are two signals: a carrier frequency and a modulating frequency. The modulating frequency is the data of interest in this case. The frequency of the laser light itself is too high (4.74×10^{14} Hz for the PDV-100) for the detector to measure, however the beat frequency can be detected. Due to the superposition of the two beams, the modulating signal is the Bragg cell frequency plus the doppler shift. It is this frequency which is detected by the vibrometer and the difference between the measured modulation frequency and the known Bragg cell frequency is the doppler shift due to the measured surface velocity. The velocity of the target vibration can be calculated through rearranging equation 2.11[32]:

$$f_T = 2V_s(t)\lambda \quad (2.11)$$

where f_T is the target frequency, V_s is the target vibration velocity, λ is the laser wavelength and θ is the angle that the laser makes with the reflection surface.

For this work the Polytec PDV-100 single axis laser vibrometer was used. This device is capable of measuring vibration frequencies up to 22kHz and can measure vibrational velocities as low as $0.02\mu\text{m/s}$. The vibrational velocities measured can then be transformed into the frequency domain in order to gather information regarding the vibration modes of the target and their relative amplitudes.

LIMITATIONS

For the purpose that this technique was used, there are minimal limitations of the system. The only limitation is that the system only allowed for a single point measurement and as such multiple tests had to be run with the device targetted at different components. This could have been achieved in one test with a multi point vibrometer. This was however a insignificant limitation as it simply extended the number of tests required and did not limit the available data.

2.2 COMPUTATIONAL FLUID DYNAMICS (CFD) METHODOLOGY

2.2.1 FUNDAMENTALS OF CFD

The term CFD in this case refers to the solution of the set of partial differential equations that govern flow physics, the Navier-Stokes equations. These equations can be derived directly from the conservation principles for mass, momentum and energy

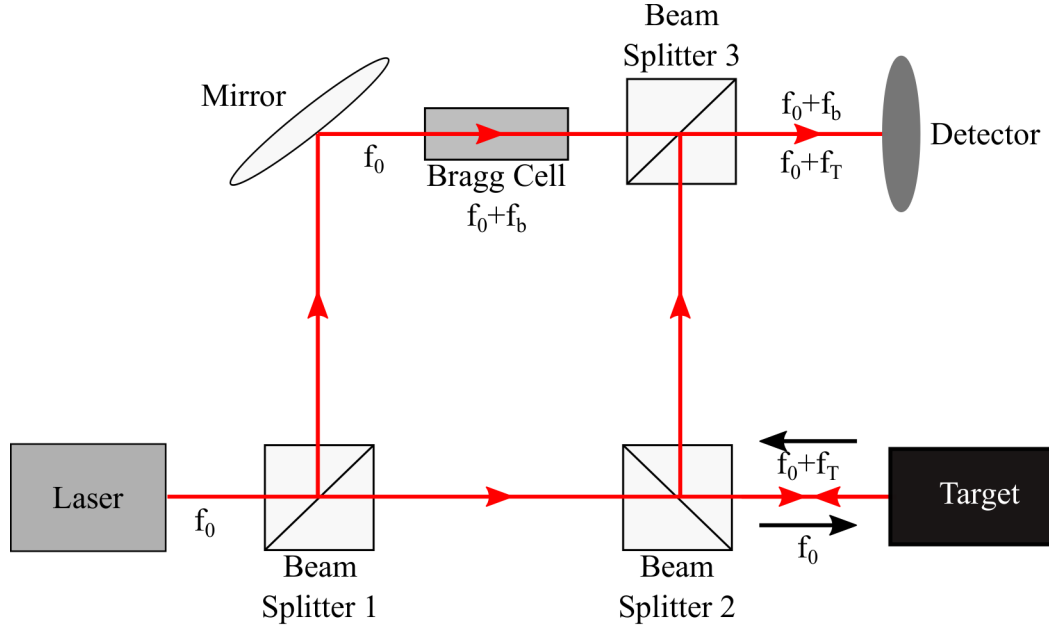


FIGURE 2.5: Schematic of the working principle of a Heterodyne Laser Doppler Vibrometer

and are shown in the set of equations below (equation 2.12).

$$\begin{aligned} \frac{\partial \rho}{\partial t} + \nabla \cdot (\rho \mathbf{v}) &= 0 \\ \frac{\partial(\rho \mathbf{v})}{\partial t} + \nabla \cdot (\rho \mathbf{v} \otimes \mathbf{v}) &= -\nabla \cdot (p \mathbf{I}) + \nabla \cdot \mathbf{T} + \mathbf{f}_b \\ \frac{\partial(\rho E)}{\partial t} + \nabla \cdot (\rho E \mathbf{v}) &= \mathbf{f}_b \cdot \mathbf{v} + \nabla \cdot (\mathbf{v} \cdot \boldsymbol{\sigma}) \nabla \cdot \mathbf{q} + S_E \end{aligned} \quad (2.12)$$

The Navier-Stokes equations are very computationally expensive to solve directly, so a commonly used approach is to use the so-called Reynolds-Averaged Navier-Stokes equations and is acknowledged as the most efficient means of solving aerospace related fluid dynamic systems[33]. These equations are obtained through a time averaging process which decomposes the instantaneous transport variable into a mean and a fluctuating component.

$$\phi = \bar{\phi} + \phi' \quad (2.13)$$

Equation 2.13 presents this decomposition where ϕ is the transport variable, $\bar{\phi}$ is the mean component and ϕ' is the fluctuating component. The end result of this process when applied to the instantaneous Navier Stokes equations is that the instantaneous properties are replaced with averaged components and a new term appears in the momentum equations, the Reynolds stress tensor. This tensor is formed of the products of the fluctuating velocity components and introduces a problem into CFD known as the closure problem, due to there being more unknowns than equations to solve. To close the system of governing equations, models have been created that allow this

tensor to be represented in terms of the mean components. These models are known as turbulence models.

2.2.2 TURBULENCE MODELLING

As mentioned above, using turbulence models is the most computationally efficient means of numerically solving the Navier Stokes equations. However there are different models that can be used, each has positives and negatives associated with it and each has certain problem types that it can be used to solve effectively. For this work, as the CFD results are not the primary focus, it was decided against analysing the impact on the numerical results of using different turbulence models. Instead, the outcomes of research carried out previously on a similar problem were used to select the turbulence model. Gnani et al.[34] observed that for an internal duct flow with an adverse pressure gradient, the Wilcox $\kappa - \omega$ turbulence model provided results that correlated well with experimental results. This correlates well with the information presented in the user documentation for STAR-CCM+ (the commercial CFD software used for this work)[35] where it is reported that a significant advantage of the $\kappa - \omega$ model over the popular $\kappa - \epsilon$ model (another two equation eddy viscosity turbulence model) is improved performance for boundary layers under an adverse pressure gradient. As such, this model was used for the CFD work carried out for this research.

WILCOX $\kappa - \omega$ TURBULENCE MODEL

The Wilcox $\kappa - \omega$ turbulence model is a two equation eddy viscosity model. Eddy viscosity models were first proposed by Boussinesq in 1877[36] and are based on turbulence consisting of the constant forming and dissipation of small eddies, within which the Reynolds stresses are proportional to mean velocity gradients. This led to the Boussinesq approximation shown in equation 2.14:

$$\mathbf{R} = 2\mu_t \mathbf{S} - \frac{2}{3}(\mu_t \nabla \cdot \bar{\mathbf{v}}) \mathbf{I} \quad (2.14)$$

where \mathbf{S} is the mean strain rate tensor, μ_t is the turbulent eddy viscosity, $\bar{\mathbf{v}}$ is the mean velocity vector and \mathbf{I} is the identity tensor. The manner in which the turbulent eddy viscosity is calculated is what defines each different turbulence model.

The Wilcox $\kappa - \omega$ model is a two equation model that solves transport equations for the turbulent kinetic energy, κ , and the specific dissipation rate, ω , which is the dissipation rate per unit turbulent kinetic energy. The turbulent eddy viscosity is calculated using equation 2.15:

$$\mu_t = \rho \kappa T \quad (2.15)$$

where ρ is density, κ is the turbulent kinetic energy and T is the turbulent time scale.

For the variant of the $\kappa - \omega$ model used here (the standard variation) equation 2.16 is used to calculate the turbulent time scale.

$$T = \frac{\alpha^*}{\omega} \quad (2.16)$$

ω and κ are obtained from the transport equations 2.17:

$$\begin{aligned} \frac{\partial}{\partial t}(\rho\kappa) + \nabla \cdot (\rho\kappa\bar{v}) &= \nabla \cdot [(\mu + \sigma_\kappa\mu_t)\nabla\kappa] + P_\kappa - \rho\beta^* f_{\beta^*}(\omega\kappa - \omega_0\kappa_0) + S_\kappa \\ \frac{\partial}{\partial t}(\rho\omega) + \nabla \cdot (\rho\omega\bar{v}) &= \nabla \cdot [(\mu + \sigma_\omega\mu_t)\nabla\omega] + P_\omega - \rho\beta f_\beta(\omega^2 - \omega_0^2) + S_\omega \end{aligned} \quad (2.17)$$

where σ represents a model coefficient, P are production terms, S is a source term and f is a modification factor.

2.2.3 NUMERICAL SOLUTION

STAR-CCM+ uses a finite volume discretisation approach. To solve the mathematical model, the conservation equations are discretised in space and time to create a system of algebraic equations. All of these can be represented by a generic transport equation and in integral form it becomes equation 2.18:

$$\frac{d}{dt} \int_V \rho\phi dV + \int_A \rho\mathbf{v}\phi \cdot d\mathbf{a} = \int_A \Gamma\nabla\phi d\mathbf{a} + \int_V S_\phi dV \quad (2.18)$$

the four intergral terms from left to right represent the transient term, the convective flux, the diffusive flux and the source term. For each transport property these fluxes are solved in the same manner, however the numerical manner in which each of these intergrals is solved varies. The details are not covered here as the numerical results are not the main area of interest for this research, however details can be found if desired in the STAR-CCM+ user manual[35].

2.2.4 MESH GRID

Typically, mesh grids can be categorised into two types: structured and unstructured. Structured grids are highly regular and elements are typically quadrilateral (in 2D). Unstructured grids are less regular and are more often used when the domain has irregular geometric properties that are not easily discretised by a structured grid. Typically triangular elements are used for unstructured grids.

Due to the method by which STAR-CCM+ generates a 2D grid, it was found that an unstructured polygonal grid had to be used. The reasoning being that the software allows a 2D structured simulation to be solved, however the mesh generation must be done in 3D and then converted to 2D. However there is a direct 2D mesher available, but it does not have the ability to create structured mesh. The reason why this limited

the options available was one of computational power. The PC available to generate the mesh could not cope with the large RAM requirements imposed by the 3D meshing. Therefore a polygonal mesh was used for this work in STAR-CCM+. The mesh created is initially one made of triangular elements (as is common for unstructured meshing) and is then automatically converted to a polygonal mesh by the software.

One key parameter used to define the mesh grid is the dimensionless wall distance, y^+ . This parameter is used as an indicator of how the interaction with the solid wall should be treated by the simulation and is calculated through equation 2.19. Boundary layer resolution is important for most fluid flow simulations but none more so than the internal duct flows being studied. In these types of flows the boundary layer growth is not only key to the flow properties near the walls but also to the flow conditions and the flow structures present in the core flow of the duct. It is important that the value of y^+ is well understood as its value is used to determine how to solve the mathematical model at the wall; how accurately the model is solved at the wall will have a large impact on the accuracy of the entire solution.

$$\begin{aligned} y^+ &= \frac{yu_\tau}{\nu} \\ u_\tau &= \sqrt{\frac{\tau_w}{\rho}} \end{aligned} \quad (2.19)$$

In order to understand the importance of the non-dimensional wall distance it is first important to understand the composition of the boundary layer. The boundary layer can be split into three sublayers: the viscous sublayer, the buffer layer, and the log-law layer. The extent of each sublayer can be defined to be within a certain y^+ range. The viscous sublayer is a laminar region very close to the no-slip boundary and is dominated by viscous effects. Here $y^+ < 5$ and $y^+ = u^+$ where u^+ is the non-dimensional velocity. The log-law layer is the outermost section of the inner boundary layer that is dominated by a mixture of viscous and turbulent effects. In this region the non-dimensional velocity can be estimated by the so-called ‘‘law of the wall’’ shown in equation 2.20:

$$u^+ = \frac{1}{k} \ln y^+ + C^+ \quad (2.20)$$

This region is contained within $30 < y^+ < 500$. The final region of the inner boundary layer is the buffer region. This region is contained within $5 < y^+ < 30$ and acts as a transition between the two previously discussed layers. The non-dimensional velocity profile is not well defined mathematically in this region and as such it is common practice to avoid having the cell centre of a CFD mesh within this region i.e. $5 < y^+ < 30$.

Now, having explained the fundamental relationship between the non-dimensional wall distance and the flow properties, the importance of the mesh y^+ value in relation

to the solution methodology can be explained. There are three methods available with regards to wall treatment in STAR-CCM+: low- y^+ treatment, high- y^+ treatment and all- y^+ treatment. For low- y^+ treatment there is no modelling used for the boundary profile, instead the transport equations are solved directly. The issue with this is that the cell refinement near the wall has to be incredibly fine, the first cell must have a y^+ value of approximately 1. Particularly with high Reynolds number flows such as the supersonic flows being examined in this research, the physical wall distance (y) must be incredibly small for a y^+ near 1. This means that the cell refinement near the wall must have a very high resolution, resulting in unreasonably large computational cost for the simulation. The high- y^+ wall treatment on the other hand does not resolve either the viscous sublayer or the buffer layer but instead assumes that the cell closest to the wall lies in the outermost region of the inner boundary layer where the log-law rule is applicable. For this treatment the y^+ of the wall cell centre should be greater than 30. The advantage of this wall treatment is in computational cost, the refinement needed at the wall boundary is significantly lower than with the low y^+ treatment (specifically for high Re flows). The last treatment, all- y^+ , is actually the most useful as the software chooses which of the above treatments to use depending on the cell y^+ . It can also resolve values in the buffer layer of the inner boundary layer, however as mentioned previously it is still recommended to avoid cells with $5 < y^+ < 30$.

For this research the all- y^+ treatment was deemed most useful as the STAR-CCM+ documentation[35] states that this should be used whenever possible. For the $\kappa - \omega$ turbulence model used, the wall treatment defines a turbulent production and specific dissipation rate for use in the wall cells. The detailed description of these can be found in the STAR-CCM+ documentation but they are dependant on wall distance, flow velocity, Reynolds number turbulent kinetic energy and fluid density.

2.2.5 TIME DOMAIN

CFD modelling can be used for both steady and unsteady flow fields. For this work the modelling of the baseline wind tunnel facility was done using the steady solver within STAR-CCM+ as the section of the flow field of interest is generally a steady flow. However for the modelling of the cavity flow field use of the unsteady solver was necessary due to the inherently unsteady nature of this type of flow. The additional details considered for the unsteady modelling is discussed within chapter 6 where the unsteady CFD is implemented.

CHAPTER 3

EXPERIMENTAL FACILITIES AND METHODOLOGIES

Following on from the previous chapter, in which both the experimental and numerical techniques used throughout this work were explained, this chapter will focus on the wind tunnel that was used for the majority of the work. The re-design work carried out on the facility to enable the wind tunnel to run successfully is the main focus here. The design decisions regarding this are discussed in detail and are presented alongside the results (numerical and experimental). Figure 3.1 provides an outline of the geometry resulting from the wind tunnel design process. Finally, the resulting supersonic indraft facility is characterised using the experimental methods available, namely Schlieren and pressure measurements. These results are also compared to CFD results of the final facility design.

3.1 THE SUPERSONIC INDRAFT FACILITY

3.1.1 FUNDAMENTALS OF INTERMITTENT SUPERSONIC WIND TUNNELS

Intermittent supersonic wind tunnels all have fundamentally the same components, irrespective of the flow regime being investigated. These are the nozzle, test section, diffuser and a means of creating a pressure difference across the system. The nozzle and diffuser will be discussed in the proceeding sections. The test section will vary

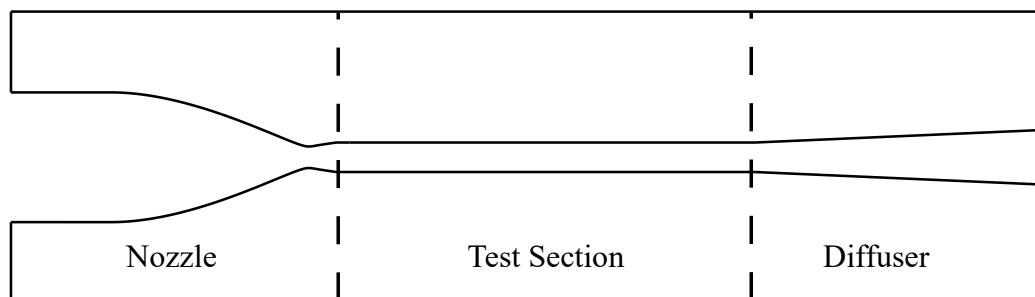


FIGURE 3.1: Schematic showing the dimensions of the final wind tunnel design

depending on the application that the facility is designed for. In this case the topic of interest is isolators in a supersonic propulsion system. As a result, the facility is designed such that the test section is also the wind tunnel model i.e. an isolator.

There are two distinctly methods of creating the pressure difference necessary to run an intermittent supersonic wind tunnel. One is to create a reservoir of high pressure air upstream of the nozzle that is forced through the nozzle to a reservoir downstream of the wind tunnel, this results in what is known as a blowdown wind tunnel. The other method is to create a low pressure reservoir downstream of the diffuser that draws atmospheric air in through the nozzle when the operating valve is opened. This is known as an indraft wind tunnel and is what is used in this case. The downstream reservoir is a 35m³ tank. To evacuate the tank a BUSCH DS 8161 vacuum pump is used. This pump is rated to an ultimate pressure of 3×10^{-3} mbar, however due to a variety of factors: use of mild steel (rather than stainless steel) for the vacuum pipework will result in corrosion and micro-pores, leaks in various valves and the limited aperture of the connection from the pump to the reservoir, the system was limited to an operating ultimate pressure of approximately 20mbar. The tunnel is operated via the actuation of a Humphrey 410-70 solenoid valve controlled via a custom built control unit. This control unit allows the user to set the opening time of the valve via an analogue dial. This dial interfaces with the circuitry to control how long the command voltage is supplied to the solenoid in order to open the valve.

3.1.2 HIGH SPEED TUNNEL REDESIGN

As mentioned at the beginning of the chapter, there were some issues with how the facility was converted from a transonic to a supersonic facility. These problems are focused on the nozzle and the diffuser. There was also an issue discovered with regard to the physical location of the tunnel, specifically the length of pipework between the facility and the vacuum tank, and the diameter of this pipework. Each of these areas will now be discussed in detail examining what the issues were, and how they have been addressed. The order that they are discussed in is not necessarily the order in which modifications were carried out, but instead the order in which they appear, spatially, in the facility i.e. nozzle, diffuser and finally the connections between the diffuser and the vacuum reservoir.

NOZZLE

The nozzle is the component in any supersonic wind tunnel that accelerates the fluid flow from subsonic to supersonic velocities. In this section, first the fundamentals of nozzle design are discussed and then these fundamentals are combined with empirical design rules from previous experimental studies.

The fundamental analysis of nozzles stems from the explanations provided in Modern Compressible Flow [1]. An important assumption to remember throughout this analysis is that it is assumed the flow through the nozzle is isentropic. Nozzle design

at its simplest can be reduced down to the relationship between Mach number and area. If a simple Laval shaped nozzle is considered, figure 3.2, the flow at the throat is set to sonic speed and this condition is denoted by an *. Therefore the area at the throat is known as A^* , the flow speed is u^* and the density is ρ^* . At any other point in the nozzle these quantities are simply denoted as A , u and ρ . If the continuity equation is written between these two positions then equation 3.1

$$\rho^* u^* A^* = \rho u A \quad (3.1)$$

Equation 3.1 can be manipulated[1], remembering the equations for stagnation density ratio and the energy equation, to give equation 3.2:

$$\left(\frac{A}{A^*}\right)^2 = \frac{1}{M^2} \left[\frac{2}{\gamma+1} \left(1 + \frac{\gamma-1}{2} M^2\right) \right]^{\frac{\gamma+1}{\gamma-1}} \quad (3.2)$$

Equation 3.2 is known as the Area-Mach number relation and illustrates an important result. It is clear that if this equation were to be rearranged for M that it would be dependant on the ratio $\frac{A}{A^*}$. Figure 3.3 shows graphically the result of this relationship.

This equation is the driving factor that determines the area ratio between the nozzle throat and the test section. In this case the test section dimensions are already known and as such, this relationship will dictate the area of the nozzle throat. The test section cross-sectional area is 0.00549m^2 and the desired test section Mach number is 2. Tabulated data is widely available that provides the area ratio $\frac{A}{A^*}$ required to achieve a desired Mach number. From this data, the required area ratio for this facility is $\frac{A}{A^*} = 1.687$. This leads to a nozzle throat area of 0.00325m^2 .

The other important feature in the design of a supersonic nozzle is the contour. If the desired flow is to be uniform and shock free then the contour must be carefully designed to cancel shock reflections generated in the nozzle expansion. One commonly

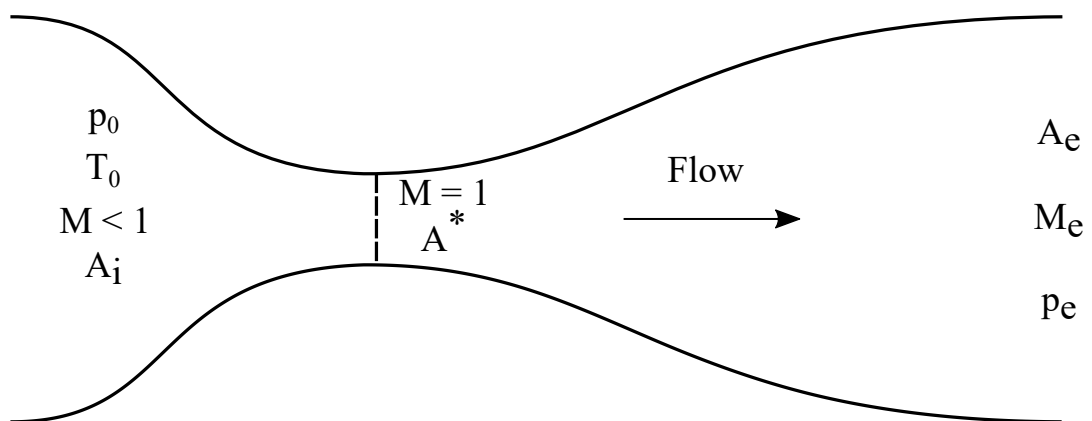


FIGURE 3.2: Basic schematic of a laval nozzle

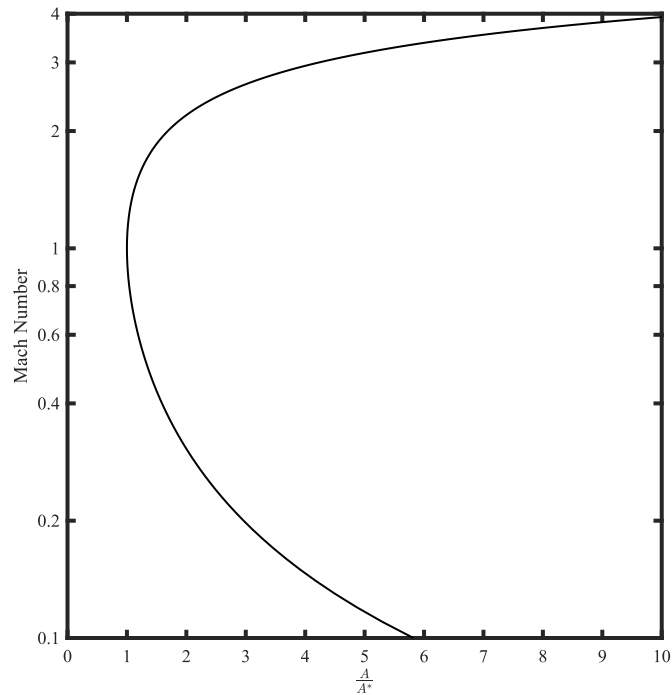


FIGURE 3.3: Graphical representation of the Mach-Area relationship defined by equation 3.2

used method for nozzle design is the method of characteristics. This method revolves around Mach lines (known as characteristics for this work) and solving the governing equations in terms of stream function and velocity potential. However it is limited to inviscid, irrotational flow. It was first developed by Hadamard[38] and is particularly convenient as the variation of supersonic flow only occurs across these characteristics. The method can be broken down into three fundamental steps. Step 1: Find the characteristic lines where flow variables are continuous but the flow derivatives are unknown. Step 2: Manipulate the conservation equations such that they only hold along the characteristics. These are known as the compatibility equations. Step 3: Solve the compatibility equations along the characteristics; beginning from the given initial conditions until the entire flow field is mapped out.

This process has been examined extensively in literature[1] and so the entire derivation will not be discussed. However it is important to convey some key results before its application to supersonic nozzle design is discussed.

One key result of the method of characteristics are equations 3.3 and 3.4. These can be shown to be true for the left running and right running characteristic respectively through a combination of mass and momentum conservation, matrix algebra, vector algebra and Prandtl-Meyer theory.

$$\theta - \nu = K_+ \quad (3.3)$$

$$\theta + \nu = K_- \quad (3.4)$$

K_+ and K_- are constants on the left and right running characteristic lines respectively, ν is the Prandtl-Meyer function and θ is the flow deflection angle. The next important step to understand is the interaction between characteristics and solid walls. This is important as the characteristics will interact with the solid nozzle contour. Figure 3.4 illustrates the features of this interaction. From the diagram, C_{-1} intersects the wall so it can be assumed that $K_{-2} = K_{-1}$ i.e.:

$$K_{-1} = \theta_1 + \nu_1 = \theta_2 + \nu_2 = K_{-2} \quad (3.5)$$

At the wall $\theta_2 = \theta_{w2}$ due to the standard flow tangency condition at a wall i.e.:

$$\nu_2 = K_{-1} - \theta_{w2} \quad (3.6)$$

This value of ν_2 can be used to calculate M_2 and thus μ_2 . From this newly calculated data at the wall C_{-1} can be redrawn with an average angle as equation 3.7:

$$\frac{(\theta_1 + \theta_2)}{2} - \frac{\mu_1 + \mu_2}{2} \quad (3.7)$$

This newly drawn characteristic, $C_{(1-2)}$, will now intersect the wall at a new point 2. This now becomes an iterative process, repeating the steps above until $\Delta\theta_{w2}$ is within an acceptable tolerance. As the characteristics are Mach lines, as proven mathematically earlier in this section, they change the flow direction by an infinitesimal amount which, in supersonic flow, will accelerate or decelerate the flow. A left running wave, C_- , will result in an increase of θ while a right running wave, C_+ , will decrease angle θ .

Now if this is applied to a supersonic nozzle, it can be assumed that the Mach wave at the throat is normal to the flow ($\mu = 90^\circ$). This is likely to not be completely accurate as the sonic line is likely to be at least slightly curved due to the contraction in the subsonic section however it is a reasonable estimate to make. At the corner of the throat an expansion fan will turn the flow away from the centreline on both top and bottom surfaces. The flow that encountered the C_- wave first will then immediately encounter the C_+ wave and return to axial flow (for a symmetric nozzle) and similarly for the flow that encountered the C_+ wave first. This expansion fan is made up of a number of characteristics; when an analysis is carried out, the number of characteristics defined is important as it will impact the accuracy of the study. After the flow first turns at the throat, here $\theta_w = \theta_{wMax}$, the nozzle contour is continuously turned back towards the axial direction. This, if designed correctly, has the effect of "cancelling" the characteristics by turning them to be parallel to the wall. The result is a clean, wave free nozzle exit flow.

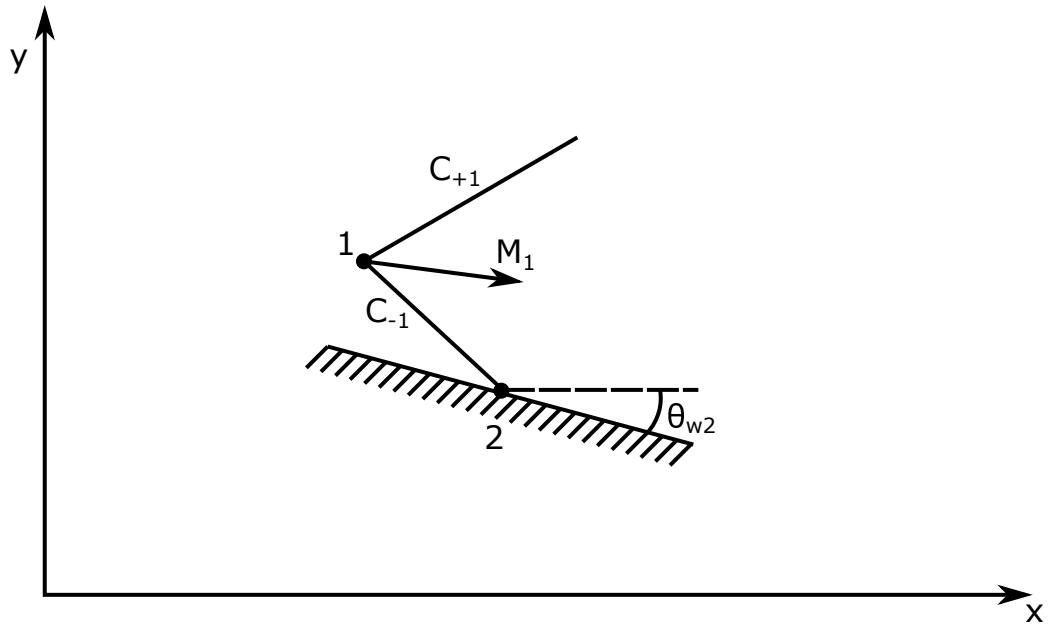


FIGURE 3.4: Interaction of a characteristic with a wall

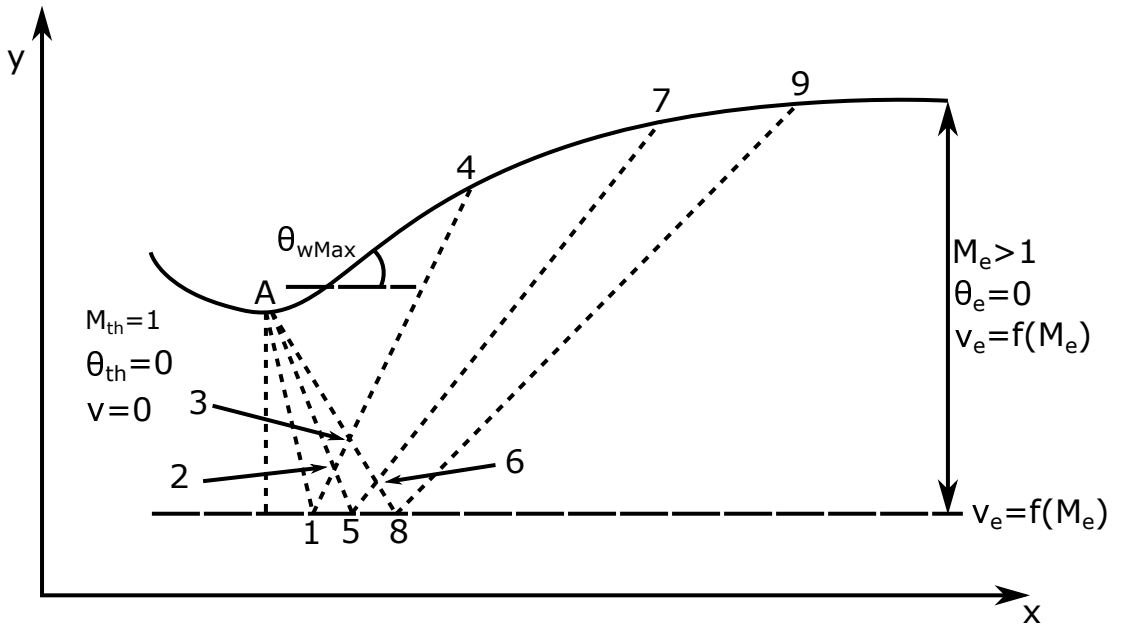


FIGURE 3.5: Illustration of the characteristics that begin at the nozzle throat and travel downstream.

Figure 3.5 provides a visualisation of the method of characteristics applied to a wind tunnel nozzle. The centreline of the nozzle can be treated as a solidwall to make use of the symmetry condition. The exit conditions, M_e and v_e , are already known as these are the desired design conditions for the nozzle. γ and R are assumed to be constant throughout, this is not the case in reality due to expansion of the fluid but it is a reasonable assumption due to the limited change that actually occurs. Beginning at the nodes where information is known, if node 8 is considered in figure 3.5 the flow angle at this point must be zero as it is on the centreline i.e. $\theta_8 = 0$. The C_- characteristic that travels from node A to node 8 has the same value of K_- at each node. Therefore:

$$\theta_8 + v_8 = \theta_A + \mu_A \quad (3.8)$$

In this case, node 8 is the final node on the symmetry plane and as such has the same flow condition as the exit i.e. $v_e = v_8$. The Prandtl-Meyer function at A is also known as $v_{th} = 0$ as, by design, $v(M = 1) = 0$. From this and knowing that $\theta_A = \theta_{wMax}$ then the following can be written:

$$\theta_A = \theta_{wMax} = v(M_A) - v(1) = v(M_A) \quad (3.9)$$

$$\begin{aligned} \theta_8 + v_8 = v_e = \theta_A + \mu_A = 2\theta_{wMax} \\ \theta_{wMax} = \frac{v_e}{2} \end{aligned} \quad (3.10)$$

Now consider the first characteristic the flow encounters after the throat, that between node A and node 1. A starting value is required for θ_1 , this should be 0 as node 1 is on the centreline but it cannot be in order to achieve a solution for this problem as a non-zero value is required to start the calculation. As above, the Prandtl-Meyer function at $M=1$ is 0; as such the following is true:

$$\begin{aligned} v_1 = \theta_{init} \\ K_{-1} = \theta_1 + v_1 = 2\theta_{init} \\ K_{+1} = \theta_1 - v_1 = 0 \end{aligned} \quad (3.11)$$

From this value of v_1 , M_1 can be calculated which in turn will provide μ_1 . $C_{-(A-1)}$ can then be graphed using the same average angle rule as described previously. For the second characteristic, in this case it is the characteristic running between node A and node 5, the flow turning angle is incremented by $\Delta\theta$ (a value set by the user). From this, equation 3.11 and the definition of the Prandtl-Meyer function the following is

shown:

$$\begin{aligned}\theta_A &= \theta_{init} + \Delta\theta \\ \theta_A - \theta_{init} &= \nu_A - \nu_1 \\ \nu_A &= \theta_A\end{aligned}\tag{3.12}$$

From this the corresponding equation for K_{-2} is:

$$K_{-2} = \theta_2 + \nu_2 = 2(\theta_{init} + \Delta\theta)\tag{3.13}$$

Equation 3.13 has two unknowns, another equation is necessary in order to solve it. This comes from realising that node 2 has a common C_+ characteristic with node 1:

$$K_{+2} = \theta_2 - \nu_2 = K_{+1} = 0\tag{3.14}$$

If equations 3.13 and 3.14 are solved simultaneously then:

$$\theta_2 = \nu_2 = \theta_{init} + \Delta\theta\tag{3.15}$$

ν_2 allows the calculation of M_2 and then μ_2 . This allows the graphing of C_{-1} and C_{-2} . Using similar logic from the previous node for characteristic C_{-3} gives:

$$\begin{aligned}\nu_3 &= \theta_3 = \theta_{init} + 2\Delta\theta \\ K_{-3} &= \theta_3 + \nu_3 = 2(\theta_{init} + 2\Delta\theta) \\ K_{+3} &= \theta_3 - \nu_3 = K_{+1} = 0\end{aligned}\tag{3.16}$$

In this example there are only 3 characteristics so the flow turning angle at node 3 is equal to the maximum flow turning angle:

$$\begin{aligned}\theta_3 = \theta_{wMax} = \nu_3 &= \theta_{init} + 2\Delta\theta = \frac{\nu_e}{2} \\ K_{-3} &= \nu_e\end{aligned}\tag{3.17}$$

Further to this, note that the flow properties at nodes 3 and 4 are equal:

$$\begin{aligned}\theta_4 &= \theta_3 = \theta_{wMAX} \\ \nu_4 &= \nu_3 = \theta_{wMAX}\end{aligned}\tag{3.18}$$

The wall angle between two nodes on the wall is calculated as the average flow angle at the two nodes in question. For nodes A and 4 in this example the angle is θ_{wMAX} . Moving on to node 5; it lies on the centreline meaning that the flow angle is 0, $\theta_5 = 0$.

It is also on the same negative characteristic as node 2 i.e. $K_{-5} = K_{-2}$. These two results can be combined to give the following:

$$\begin{aligned} v_5 &= v_e - 2\Delta\theta \\ K_{+5} &= \theta_5 - v_5 = 2\Delta\theta - v_e \end{aligned} \quad (3.19)$$

Now consider node 6 which lies at the intersection of C_{-3} and C_{+5} . From the derivation earlier in the section the following can be shown:

$$\begin{aligned} \theta_6 &= \frac{K_{-3} + K_{+5}}{2} = \Delta\theta \\ v_6 &= \frac{K_{-3} - K_{+5}}{2} = v_e - \Delta\theta \end{aligned} \quad (3.20)$$

Also, flow properties at nodes 6 and 7 are identical, i.e.:

$$\begin{aligned} \theta_7 &= \theta_6 = \Delta\theta \\ v_7 &= v_6 = v_e - \Delta\theta \end{aligned} \quad (3.21)$$

As before, the wall angle between two nodes is the average of the flow angle at each of them:

$$\theta_{w(4-7)} = \frac{\theta_4 + \theta_7}{2} = \frac{\theta_{wMAX} + \Delta\theta}{2} \quad (3.22)$$

Node 8 is on the x-axis and it is the last node, therefore the following is true:

$$\begin{aligned} \theta_8 &= 0 \\ v_8 &= v_e \\ K_{-8} &= v_e \\ K_{+8} &= -v_e \end{aligned} \quad (3.23)$$

For the wall angle between nodes 7 and 9, the last part of the straightening section, the angle is defined as follows:

$$\theta_{w(7-9)} = \frac{\theta_7 + \theta_9}{2} = \frac{\Delta\theta}{2} \quad (3.24)$$

Equation 3.24 is a generic result that will always hold for the final node on the straightening section due to the 0° flow angle downstream of this point for a properly designed nozzle. That is the final step in the process of using method of characteristics to design a supersonic nozzle. There will be a discrepancy between the achieved area ratio and the desired area ratio from data tables. This is due to the initial θ angle used to begin the calculation and the finite number of characteristics used to define the

nozzle shape. Using a very small value of θ_{init} and a large number of characteristics is key to minimising the error in the final solution.

One issue with using the method of characteristics to design a supersonic nozzle is that it does not account for any viscous effects in the nozzle. Studies have been conducted to investigate the impact that the boundary layer has on the nozzle design Mach number. A previous study[39] suggested that in high Reynolds number flows the method of characteristics can be used to accurately design the shape of the nozzle contour as in these flows the boundary layer is thin relative to the height of the test section. Liepmann[40] suggested that an assumption of a thin boundary layer (as well as negligible heat transfer through the contour walls) was acceptable up to a Mach number of 3 which would suggest it was an appropriate assumption for this research. In order to examine this assumption in more detail, the boundary layer thickness can be calculated based on previous research.

The method used is proposed by Stratford et al.[45] where an examination of a number of different methods including Tucker[41] and Rogers et al.[42] was conducted. Within the study it was shown that for Reynolds number in the region of 1×10^6 , equation 3.25 could be used to calculate boundary layer displacement thickness, δ^* :

$$\theta = 0.046(1 + 0.8M^2)^{0.44} X Re_x^{-\frac{1}{5}} \quad (3.25)$$

Using this method the boundary layer displacement thickness value, δ^* , was found to be 0.19mm. The key point here is that the displacement thickness of the boundary layer is less than 0.4% of the test section height. This value is an estimate of the boundary layer from theory and is not expected to be very accurate when compared to boundary layer measurements. However, even if the value is marginally different from the actual value, the boundary layer thickness will remain insignificant compared to the test section height. This would suggest that the assumption of a thin boundary layer is an acceptable one and that it can be assumed that there is no need to complicate the nozzle design from the method of characteristics by applying viscous corrections. As such, the supersonic section of the nozzle contour was calculated directly using the method of characteristics described above.

One area of nozzle design that is not often considered in any detail is the converging, subsonic section. This is an important area when designing a new nozzle as the geometry here can have a noticeable impact on the flow quality in the supersonic outlet flow. An ideal subsonic contraction contour should meet a number of requirements:

- The half height at the throat must match the requirement for choked flow (as discussed in detail in the previous section).
- The contour should decrease monotonically from the inlet to the throat.
- The gradient of the contour should be 0 at the tunnel inlet.

- At the throat, the gradient of the function should be zero while the rate of change of the gradient should not equal zero.

These requirements necessitate a solution that would be infinite in length. Ho and Emanuel [46] suggested a contour that follows an error function as shown in equation 3.26:

$$f(x) = a + b \cdot \text{erf}[\eta(z)] \quad (3.26)$$

$$a = 1, b = \frac{y_i - 1}{\text{erf}[\eta(-1)]}, z = \frac{x}{L_c}, \eta(z) = \frac{z^{m+1}}{1 + (-1)^m(m+1)z^{m+2}}$$

The contour is only dependant on 3 independent variables: y_i , m and L_c . y_i is the inlet half height normalised by the half height of the nozzle throat and so is a measure of the degree of the overall nozzle contraction. m is the order of flatness of the wall at the nozzle throat. Finally, L_c is the length of the contraction section normalised by the half height of the nozzle throat. The value for L_c was chosen to be 10. This is based on the research of Ho and Emanuel[46] where the effect on centreline and wall Mach number was examined for $1 \leq L_c \leq 5$. It was found that for low values of L_c the Mach number at the wall was higher than 1, indicating a curved sonic line. It was also found that the gradient of Mach number near the exit increased as L_c decreased. It was found in this study that a value of 5 or more was sufficient to avoid this behaviour. However as there was little restriction on the physical length of the intake at this facility it was decided to make the intake non-dimensional contraction length twice that value to avoid the possibility that the cutoff between unacceptable and acceptable distortion could depend on the facility. The other two variables, y_i and m , have less of an impact on the Mach number gradient along the centreline and the Mach number at the wall than L_c , however it is still important to consider. For the order of flatness at the nozzle throat, the study shows that a larger value has the result of moving the steep part of the Mach number gradient upstream and away from the throat which is preferable for uniform flow at the throat. For this reason a value of $m=4$ was chosen for this nozzle. As the effect of y_i on the flow uniformity at the throat was marginal, the main concern for this design was that it was preferable, given the surroundings and for safety reasons, that the Mach number to the intake was as low as possible. As a result of this it was decided to use a larger value i.e. $y_i = 6$ in order to minimise the Mach number. However when the contour for the contraction and the contour derived from the method of characteristics were combined a problem was discovered. The combination of these two contours would result in a throat region that did not have a smooth change of gradient but instead had an abrupt change in nozzle contour gradient. It was decided that this was unacceptable and so a compromise had to be made. Modifying the supersonic section of the nozzle was not possible as the contour was carefully designed to be wave free in the test section. This meant that the subsonic contraction section had to be changed. The basic principles from the study by Ho and Emanuel[46] were preserved however the error function near the supersonic throat

was manually “blended” to give a smooth transition across the throat and into the supersonic section of the nozzle. The end result for the nozzle contour is shown in figure 3.6.

DIFFUSER

The diffuser is a key component in a supersonic wind tunnel as it is the section of the tunnel where the flow is decelerated, in ideal scenarios to subsonic speeds, before it enters the downstream reservoir. Fundamentally, a diffuser is not required for a supersonic wind tunnel to run, however it will greatly reduce the pressure ratio required for the facility to operate correctly. As an example, the facility in question in this research is designed for $M = 2$ flow. For this Mach number and a nozzle that exhausts directly into air the required stagnation pressure ratio is equal to 7.824. The next logical step is to include a straight duct at the exit of the nozzle, i.e. a test section, that exhausts into the atmosphere. The difference is that the pressure required is a combination of the pressure ratio across a normal shock at the facility design Mach number and the isentropic pressure ratio at the same Mach number, i.e.:

$$\frac{p_o}{p_\infty} = \frac{p_o}{p_1} \frac{p_1}{p_2} \quad (3.27)$$

Therefore for a Mach 2 facility this would result in a pressure ratio $\frac{p_o}{p_\infty} = 1.739$. This is a vast improvement on the previous value required, however with the addition of a properly designed diffuser this may be reduced even further. If a simple diverging duct is added downstream then this can slow the subsonic flow behind the normal shock to almost zero before it exhausts to atmosphere. This means that the stagnation and total pressures are equal at this point. Also, if the expansion through the diffuser is considered to be isentropic, then the stagnation pressure here is equal to the stagnation pressure behind the normal shock located at the entrance to the diffuser. If this arrangement was used then the pressure ratio equation would become:

$$\frac{p_o}{p_\infty} = \frac{p_o}{p_1} \frac{p_1}{p_2} \frac{p_2}{p_o} \quad (3.28)$$

$\frac{p_2}{p_o}$ is calculated based on isentropic expansion from the Mach number downstream of the normal shock. The Mach number behind the normal shock can be calculated based on the test section Mach number, as this will be the Mach number upstream of the shock. For this facility, this results in a value of $\frac{p_2}{p_o} = 1.25$ which leads to a new value of $\frac{p_o}{p_\infty} = 1.3912$. This is an improvement on the pressure ratio required for the facility to function. There is yet another improvement that can be made to improve the efficiency of the facility. It is well known that total pressure loss will be less significant across a series of oblique shocks followed by a terminating normal shock than by a single normal shock. This is a result of the highly non-linear and unproportional relationship between upstream Mach number and total pressure loss

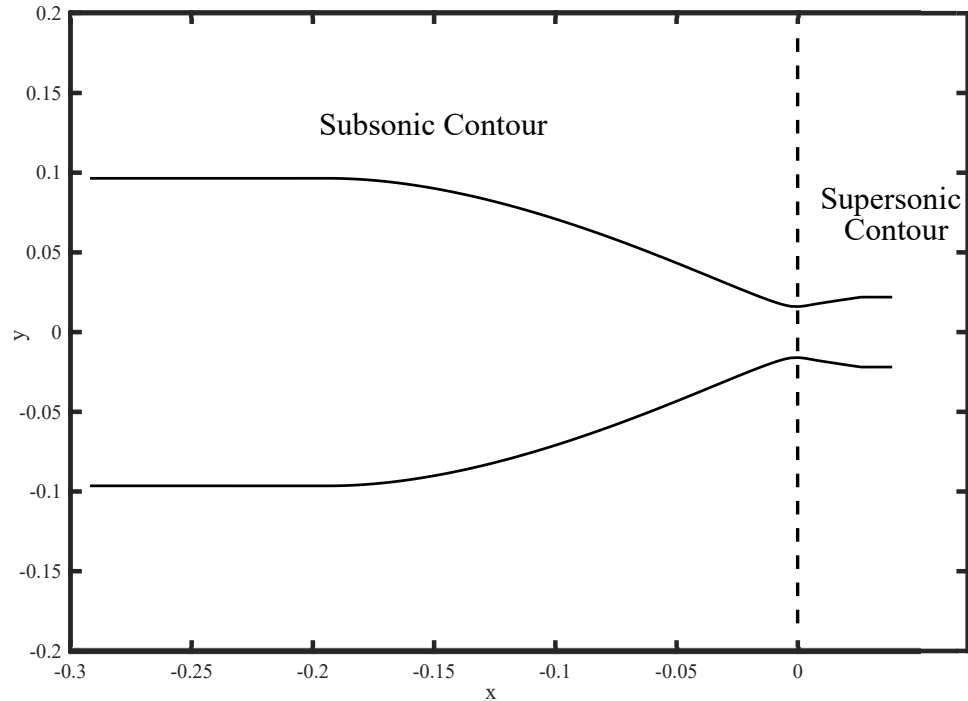


FIGURE 3.6: Diagram of nozzle contour generated through the method of characteristics.

across a normal shock wave. i.e. the increased flow turning angle caused by multiple shocks is more than counteracted by the effective decrease observed in stagnation pressure loss across a normal shock at a lower Mach number. Figure 3.7 illustrates this non-linearity between normal shock Mach number and the pressure loss across it. Therefore it is possible to create a so-called oblique shock diffuser which uses multiple oblique shocks followed by a terminating normal shock to decelerate the flow.

A generic supersonic wind tunnel geometry is shown in figure 3.8 with an oblique shock diffuser where the station numbers correspond to the series of equations above that explain the required pressure ratios. The oblique shock diffuser shown consists

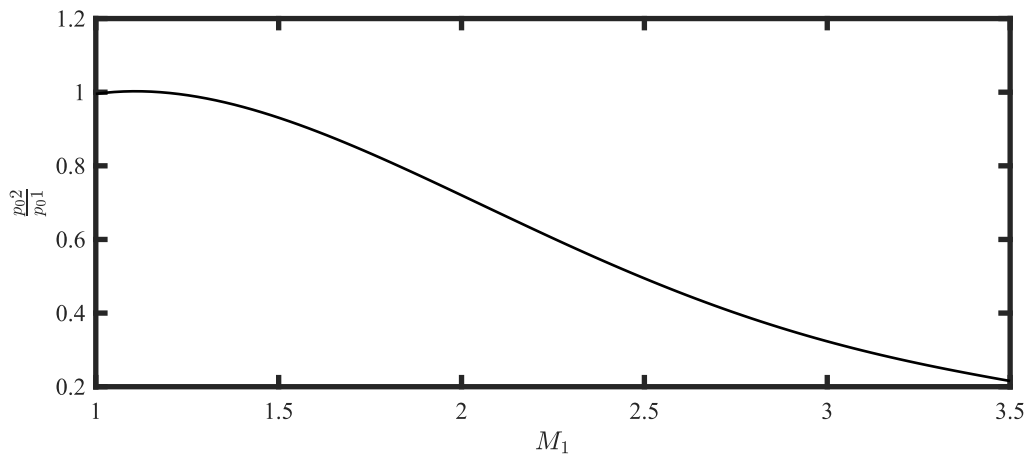


FIGURE 3.7: Relationship between normal shock Mach number and the stagnation pressure loss across it[1]

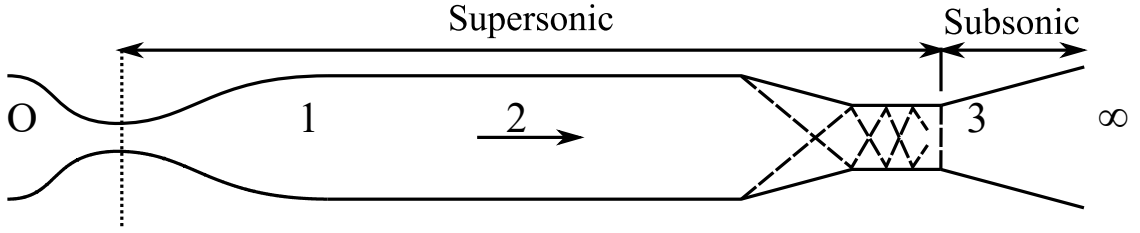


FIGURE 3.8: Wind tunnel geometry that illustrates an oblique shock diffuser.

of a compression corner on the upper and lower surface in order to initiate the series of oblique shocks, this is followed by a throat in which, ideally, the Mach number reaches 1 and finally the subsonic diffuser in which the subsonic flow decelerates and the pressure tends towards atmospheric pressure. The throat of the diffuser is a key concern of the design, this is known in the wind tunnel as the second throat (the nozzle throat is known as the first). Due to the increase in entropy between the two throats $A_{t2} > A_{t1}$, the entropy increase is due to the total pressure loss across shock waves. This can be proved mathematically by applying the continuity equation between the two locations:

$$\rho_1^* A_{t1} a_1^* = \rho_2^* A_{t2} a_2^* \quad (3.29)$$

If the equation of state for a perfect gas is substituted into equation 3.29 along with the isentropic total pressure ratio relationship at sonic speed (assumed here that both throats are at exactly Mach = 1) then the following is found:

$$\frac{A_{t2}}{A_{t1}} = \frac{p_{o1}}{p_{o2}} \quad (3.30)$$

Therefore, as p_{o2} will always be less than p_{o1} , A_{t2} always must be larger than A_{t1} . So the smallest value is given by equation 3.30, any smaller than this value and the second throat will not be able to support the mass flow rate required and will become choked, preventing the tunnel from running correctly. A larger throat will allow the tunnel to function as designed as there is no issue with supporting the required mass flow rate. However the larger the throat is made, the lower the efficiency of the tunnel becomes. There are many ways in which efficiency here has been quantified in literature, equation 3.31 is used for this study:

$$\eta_D = \frac{\left(\frac{p_{o2}}{p_o}\right)_{actual}}{\left(\frac{p_{o2}}{p_{o1}}\right)_{normalshockatM_e}} \quad (3.31)$$

Figure 3.9 illustrates equation 3.31 graphically. This illustrates the area required for peak efficiency and also that if the area is reduced beyond this the efficiency falls rapidly (as a result of the wind tunnel choking). The major problem with

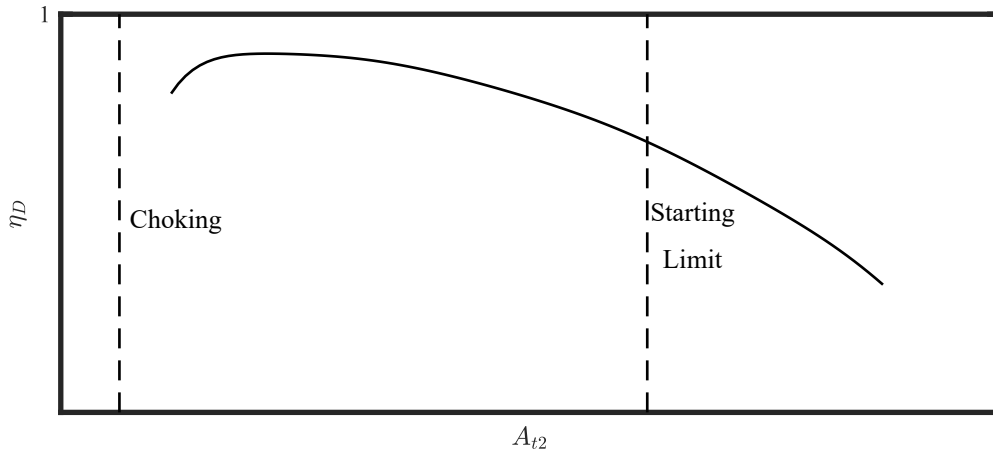


FIGURE 3.9: Illustration of typical oblique shock diffuser efficiency[1]

diffuser design that has not been mentioned is the starting problem. Supersonic wind tunnel startup is a very complex flow problem and is a phenomenon that is not well documented. Fundamentally, as the first throat chokes, a normal shock (in inviscid flow, as that is what these design calculations are based on) passes downstream through the wind tunnel. This includes the diffuser and so, at startup, the diffuser must be capable of supporting the mass flow rate behind a normal shock at the test section Mach number. Therefore this gives a new area ratio required that can be calculated from equation 3.30 using the total pressure ratio across a normal shock at the test section Mach number. It is clear that this new area ratio required for the tunnel startup is larger than the ideal case, this results in a less efficient facility. The only solution to this is the use of a variable geometry diffuser. Through the use of some sort of mechanical system, the second throat area can be modified during the run so that it is large enough to overcome the startup problem but can then be made smaller to a more ideal value for the rest of the tunnel run. Unfortunately this was not possible for the facility used in this study, as such the second throat would have to be sized so that it would be large enough not only for the ideal case but also for startup. Therefore the minimum area required for the diffuser throat was $\frac{A_{t2}}{A_{t1}} = \frac{p_{o1}}{p_{o2}} = \frac{1}{0.7209} = 1.387$. From the first throat area calculated in section 3.1.2 this results in the second throat area equal to 0.00451m^2 . However the issue with this calculation is that it does not account for viscous effects. An estimate for the boundary layer can be made using the equations derived for flat plate boundary layers. The parameter of interest here is the displacement thickness since this is a measure of the distance that the inviscid, potential flow is displaced outwards due to the velocity decrease in the boundary layer. Using the equation defined by Stratford et al.[45] (equation 3.25) to calculate δ^* , the displacement thickness can be subtracted from the dimensions of the facility to give an “effective flow area” of the wind tunnel test section that includes an estimate for the effects of viscosity. At the downstream end of the test section, this results in a “virtual” cross-sectional area of approximately 0.0046m^2 . It is clear that the effect of viscosity has led to a virtual test section area that is only marginally larger

than the area required at the second throat for tunnel startup. With this in mind it was decided that a second throat would give almost no benefit in this case as the contraction would be off the order of 3mm. So because of this and to give a margin of safety to ensure the tunnel ran, it was decided that a simple normal shock diffuser would suffice for this facility. From the literature, to avoid separation it is best that the diffuser angle is kept below 6° [47]. With this in mind it was decided that the diffuser would be designed with divergence angle of 5° . This results in a diffuser that transitions from the test section cross-sectional area of 0.00549m^2 to the valve internal cross-sectional area of 0.00811m^2 over a distance of 0.528m. This final design is illustrated in figure 3.10.

CONTROL VALVE

A component of the facility that was not initially considered when trying to diagnose root causes of the tunnels dysfunctionality was the control valve. However after inspection of the dimensions of the valve it was found that it was not suitable for the facility. Recalling the previous explanation of the importance of the dimensions of the second throat in a diffuser, the same fundamental flow physics can be applied to the valve. The theory shows that the required ratio of cross-sectional area of the first and second throat at tunnel start up is equal to the stagnation pressure ratio across a normal shock at the test section Mach number, i.e.:

$$\left(\frac{A_{t2}}{A_{t1}}\right)_{M=2.0} = \left(\frac{p_{o1}}{p_{o2}}\right)_{M=2.0} = 1.39 \quad (3.32)$$

The ball valve originally installed on the wind tunnel had a value of $\frac{A_{t2}}{A_{t1}} = 1.40$. This seems marginally sufficient when compared to the value given in equation 3.32, however these calculations have no correction for viscous effects. When the flow reaches the downstream valve the boundary layer will not be insignificant and will cause the effective area ratio between the nozzle throat and the valve to be much smaller. Therefore the valve was replaced with a solenoid controlled gate valve in order to solve the issue. The new valve has an area ratio of $\frac{A_{t2}}{A_{t1}} = 2.49$ which is a significant improvement compared to the original.

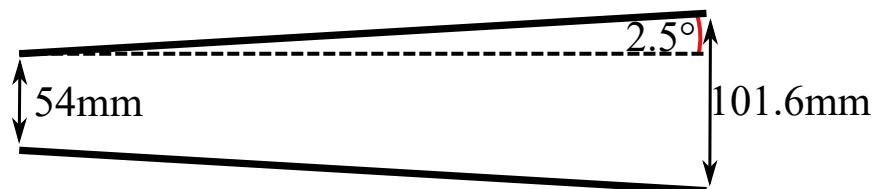


FIGURE 3.10: Figure illustrating the final diffuser design.

3.1.3 WIND TUNNEL OVERHAUL BREAKDOWN

As described above, many changes were made to the wind tunnel to solve issues with it. The following segments will explain the results achieved at each stage. Design decisions were made on the basis of results shown by the wind tunnel and the engineering analysis of the results available at each stage in the process. The only exceptions to this are the supersonic diffuser and the nozzle. The diffuser change was made before the tunnel was run as it was obvious from simple inspection that the diffuser was incorrectly designed. The nozzle was changed initially as it was deemed prudent to run the tunnel in a consistent manner throughout and due to the original nozzle being similar in design, any changes to the tunnel flow were thought to be too small to be measured with the instrumentation available.

The locations of the static and total pressure measurements used throughout this section are shown in figure 3.11.

UPDATED DIFFUSER AND NOZZLE TUNNEL CONFIGURATION

The first configuration of the tunnel tested was with the updated diffuser installed. The design of the diffuser was discussed in section 3.1.2. To conduct a first investigation of the tunnel behaviour total and static pressure measurements were taken, along with Schlieren images. Total pressure was recorded using a pitot probe located on the tunnel centreline, in both the vertical and horizontal directions. The tip of the pitot probe was 115mm downstream of the start of the test section. The static pressure was measured at a pressure port on the lower surface of the wind tunnel on the tunnel centreline and at the same horizontal position as the pitot probe. Figure 3.12 shows both the static and total pressure profiles obtained from running the total in this setup. It is clear that the drop in both the static and total pressures are too low for the tunnel to have reached supersonic speeds. This is suggested if the pressures are converted, assuming isentropic flow and using Bernoulli's equation, to Mach number as shown

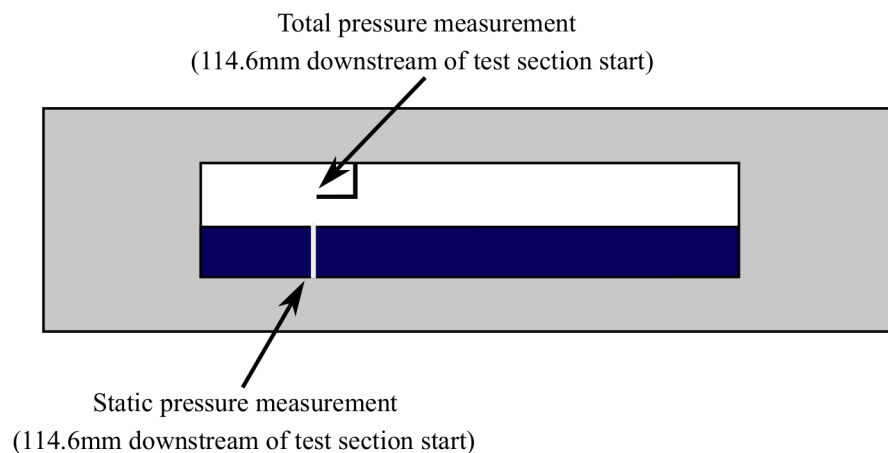


FIGURE 3.11: Total and static pressure measurement location used during the wind tunnel design process.

in figure 3.13. Finally, as expected, the average Schlieren image shown in figure 3.14 shows that there are clearly no shock waves around the pitot probe. These would be clearly visible in the Schlieren images even though the quality is not good.

TUNNEL CONFIGURATION WITH VALVE REPLACEMENT

The first change made to the tunnel was the replacement of the control valve. The reason for this was described previously in section 3.1.2. The pressure measurements taken after this alteration showed a significant change to the wind tunnel operation. Figure 3.15 shows the total pressure ratio achieved with the control valve replacement. This total pressure ratio is the ratio between total pressure measured by the pitot probe in the centre of the tunnel and total pressure upstream of the nozzle, because this is an indraft wind tunnel this is atmospheric pressure.

There is a big difference when compared to the almost constant total pressure seen with the original valve setup. The total pressure can be converted to a Mach number using normal shock relations. Equation 3.33 can be solved for the total pressure ratio across a normal shock at a given Mach number.

$$\frac{p_{02}}{p_{01}} = \left(\frac{\frac{\gamma+1}{2} M_1^2}{1 + \frac{\gamma-1}{2} M_1^2} \right)^{\frac{\gamma}{\gamma-1}} \left(\frac{1}{\frac{2\gamma}{\gamma+1} M_1^2 - \frac{\gamma-1}{\gamma+1}} \right)^{\frac{1}{\gamma-1}} \quad (3.33)$$

However it can be solved numerically in reverse i.e. for a given total pressure ratio it can be solved for the normal shock Mach number. There are lookup tables that provide the Mach number for a total pressure ratio based on this solution. As a result, the total pressure ratios shown in figure 3.15 can be converted into Mach number as shown in figure 3.16.

This suggests that the tunnel is operating at a Mach number very close to the design Mach number of the tunnel and is, at very least, supersonic. However figure 3.17 shows

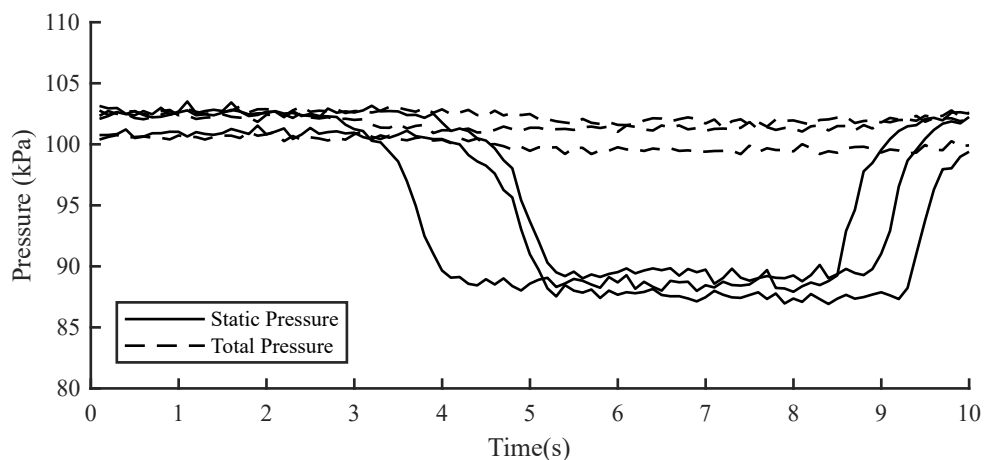


FIGURE 3.12: Total and static pressure measurements for the initial setup of the wind tunnel (each line in the plot is a separate run of the supersonic wind tunnel).

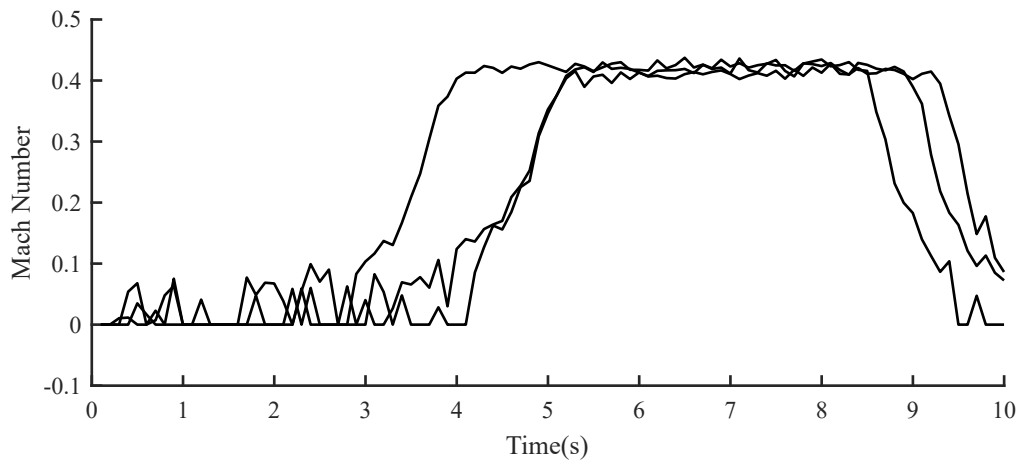


FIGURE 3.13: Isentropic Mach number calculated from total and static pressure measurements for the initial setup of the wind tunnel (each line in the plot is a separate run of the supersonic wind tunnel).

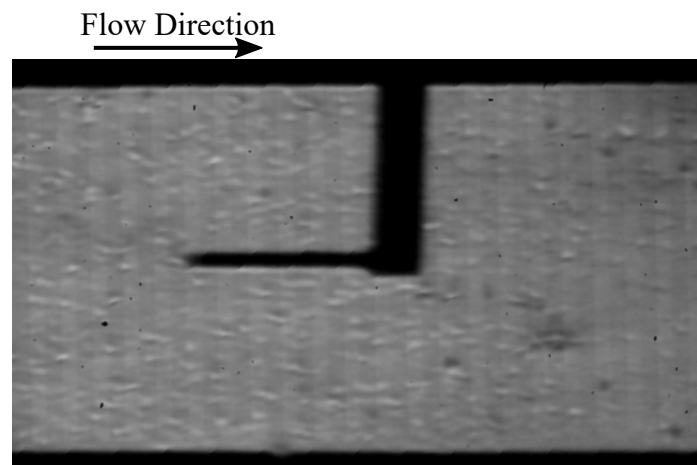


FIGURE 3.14: Average Schlieren Image of Tunnel Running with Initial Setup

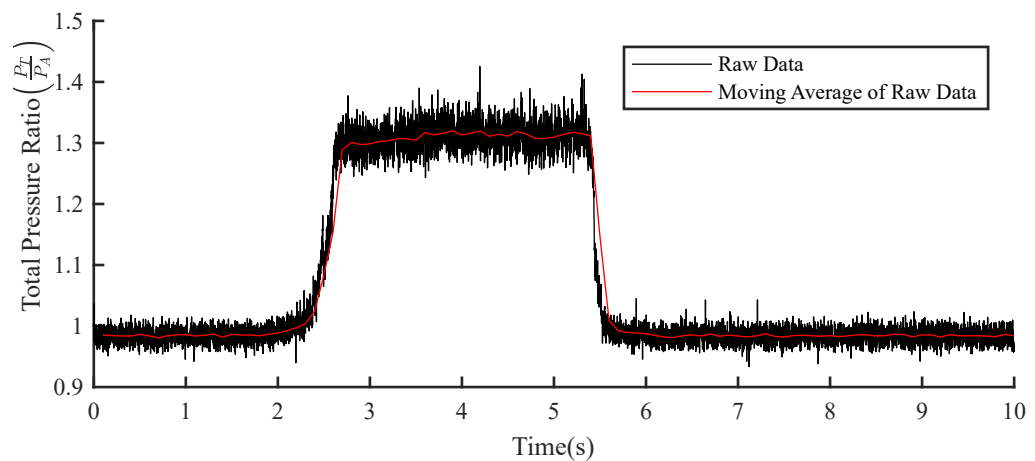


FIGURE 3.15: Total pressure ratio for the wind tunnel run with the valve replaced

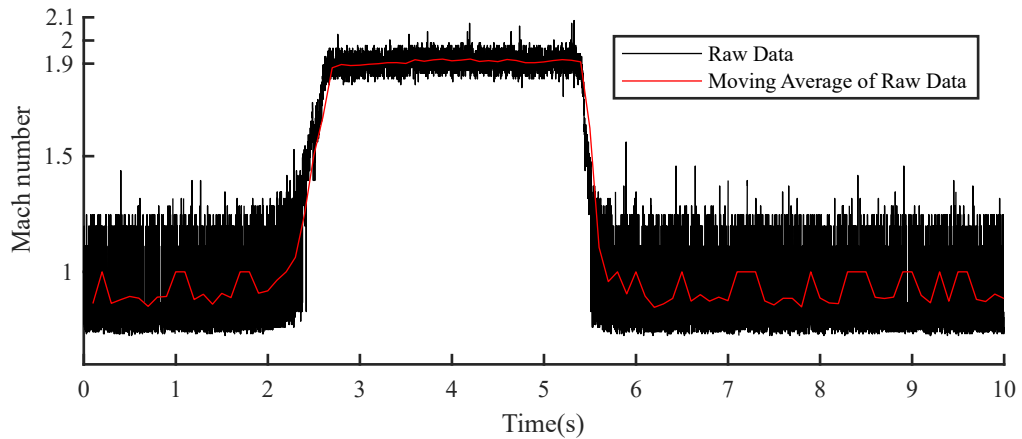


FIGURE 3.16: Mach number for the wind tunnel run with the valve replaced

that there are clearly no shock waves in the test section as would be expected.

This suggests that there is a normal shock upstream of the test section, likely near the exit of the nozzle. The possible reasons for this are discussed in the following section.

SHORTER TEST SECTION TUNNEL CONFIGURATION

The results presented in section 3.1.3 indicate that the nozzle appears to choke properly. However for some, at this point unknown, reason the tunnel was still prevented from starting. One possibility was that the boundary layer growth along the test section was significant enough that the change in “virtual” flow area was enough to prevent the normal shock from passing downstream. As it is known that a normal shock wave is not stable in a converging duct[48][49], this would explain why the pressure measurements suggest that there is a normal shock present in the flow but that it is “stuck” in the diverging portion of the nozzle. The reason being that the only region of the tunnel that is not converging is this part of the nozzle. The test section has a constant area, however boundary layer growth will result in a “virtually” contracting test section.

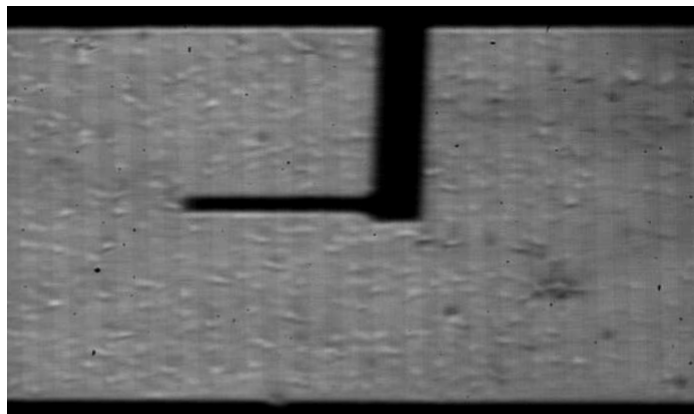


FIGURE 3.17: Average Schlieren Image of Tunnel Run with the Replacement Valve.

Based on the above hypothesis it was decided to shorten the length of the tunnel in order to restrict the maximum boundary layer thickness. Figures 3.18, 3.19 and 3.20 show the total pressure, total pressure ratio and normal shock Mach number respectively measured after this modification was made to the wind tunnel. Each line on these plots represents a different run of the tunnel. This suggests, as was the case with the previous wind tunnel iteration, that the tunnel has started properly based on the Mach number calculation. However the Schlieren imaging recorded suggests this is not the case. Due to the test section redesign, it was possible to record Schlieren images of the nozzle area. As figure 3.21 shows, the tunnel is running with a normal shock located in the diverging area of the nozzle. Figure 3.22 shows the movement of the normal shock with time. The reason for the movement from right to left during the period presented is due to the reduction in pressure ratio across the nozzle as the wind tunnel is running.

This is a very similar result to that obtained from the previous iteration of the tunnel. The only difference is the magnitude of the total pressure ratio was smaller with the shorter test section. However the assumption here is that, fundamentally, both tunnel configurations are suffering from the same issue. With the additional information provided by the Schlieren imaging, the issue was thought to be the pressure ratio across the nozzle, and as such across the entire wind tunnel, was too low. This is based on explanations given in Anderson's Modern Compressible Flow textbook[1] regarding the operation of converging-diverging nozzles at different pressure ratios. The case observed in the Schlieren imaging, a normal shock in the diverging section of the nozzle, matches the situation where the pressure ratio is enough to choke the nozzle but not enough for the nozzle to fully start. The predicted value for the pressure ratio required for the tunnel to start is $\left(\frac{p_{o1}}{p_{o2}}\right)_{M=2.0} = 1.39$, calculated in section 3.1.2. Static measurements of the vacuum level were in the region of 50mbar, based on the pirani gauges used. This equates to a pressure ratio across the wind tunnel of approximately 20. The only possibility that remained was there was some dynamic effect when the tunnel was operated that increased the pressure "seen" by

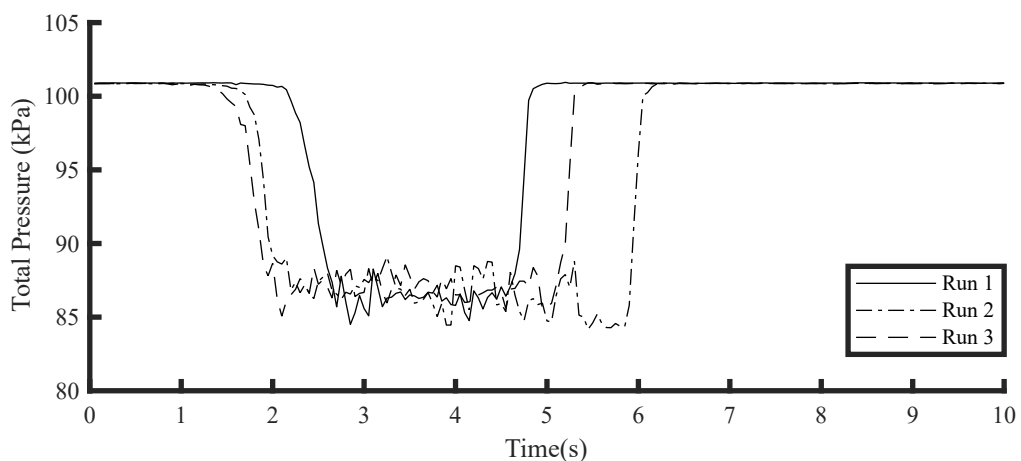


FIGURE 3.18: Test section total pressure (each line represents a tunnel test)

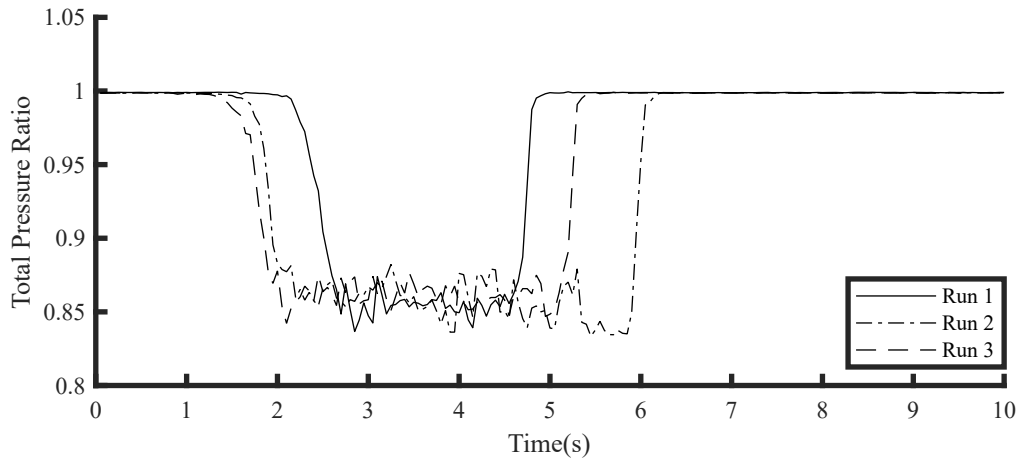


FIGURE 3.19: Total pressure ratio between test section and atmospheric pressure (each line represents a tunnel test)

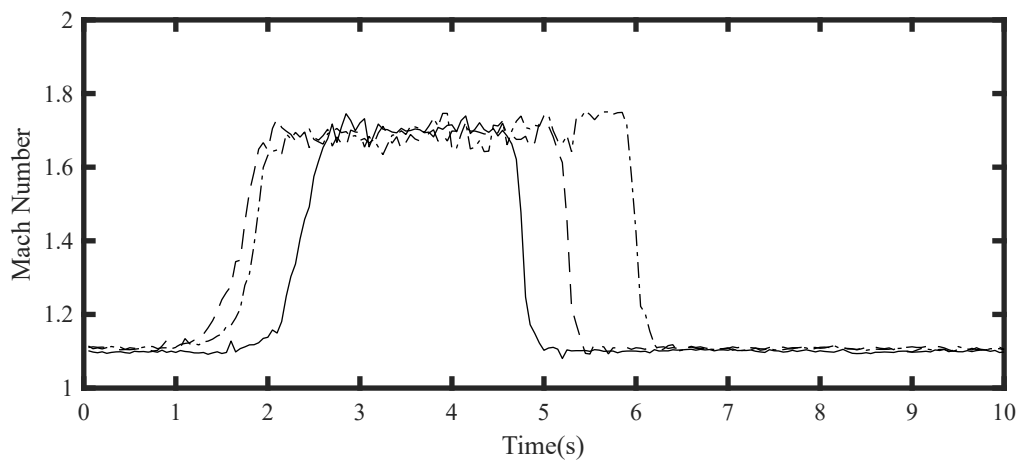


FIGURE 3.20: Normal Shock Mach number from total pressure ratio between test section and atmospheric pressure (each line represents a tunnel test)

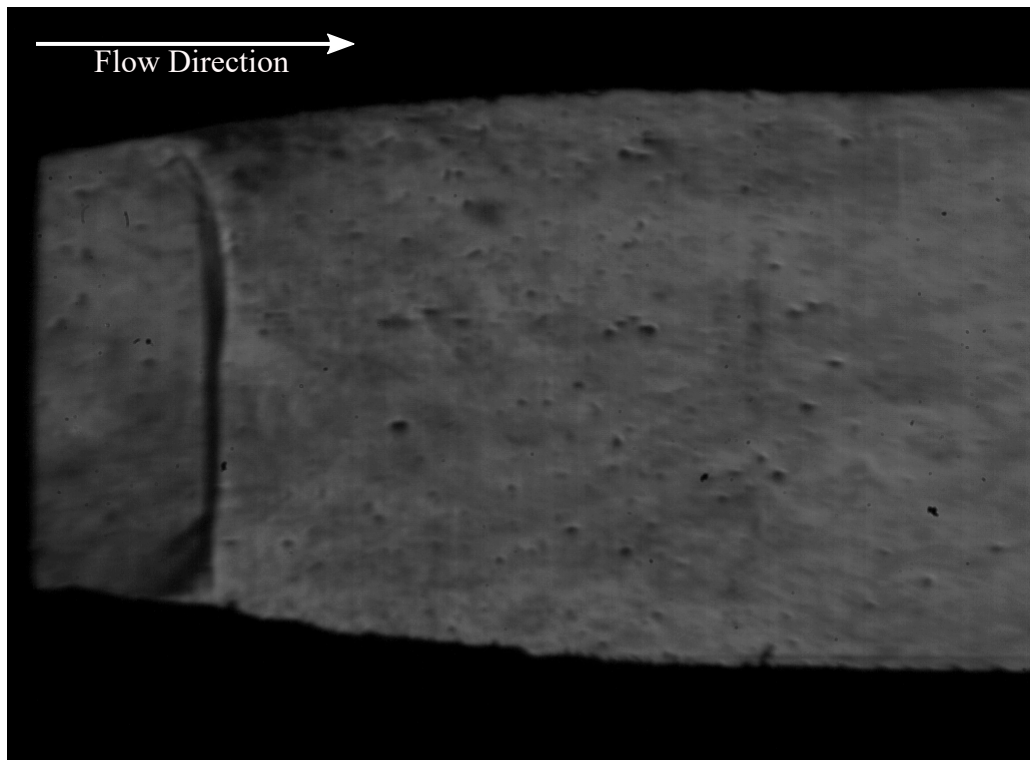


FIGURE 3.21: An example of an instantaneous Schlieren image taken of the diverging portion of the supersonic nozzle

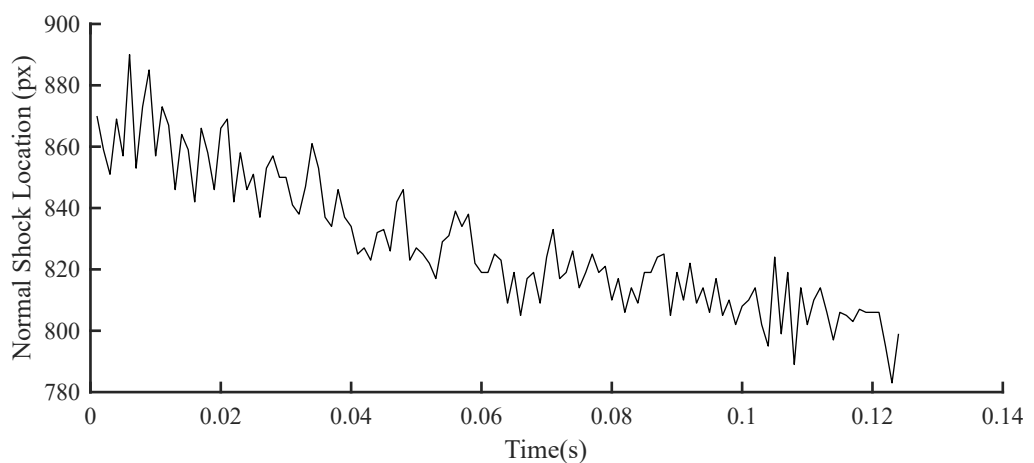


FIGURE 3.22: Location of the normal shock in the nozzle in pixels. For reference, the left hand edge of figure 3.21 is 0 pixels and the right hand edge is 1024.

the wind tunnel. The only cause of this could be conductance; this is a term often used in vacuum technology applications as a measure of the flow resistance resulting from the viscous interaction between the pipe walls and the fluid entering/exiting the vacuum system.

CONNECTING PIPEWORK IMPROVEMENT TUNNEL CONFIGURATION

The reason why the pipework connecting the wind tunnel to the vacuum tank is important is because of conductance. For this research, the importance here is determining if the pipework originally in place provides sufficient capacity for the volume flow rate required by the wind tunnel. What should be made clear is that the calculations to support this design decision were only done after the modified pipework layout had been tested. This was necessary as some of the data needed could only be recorded after the tunnel was running as expected. However the change was made without the data to prove it with confidence due to the combination of prior experience (wind tunnel use in Nagoya see chapter 7) and process of elimination, as there was nothing left of the tunnel design itself that could be preventing the tunnel from running.

Conductance can be fundamentally defined by equation 3.34:

$$C = \frac{q_{pV}}{\Delta p} \quad (3.34)$$

where C is the conductance, q_{pV} is the throughput [$Pa.m^3s^{-1}$] which is a measure of the energy flow per unit time and Δp is the pressure differential across the pipe in question. This suggests that the conductance can be considered as a measure of the volumetric flow rate through the system at the given pressure conditions. The pressure differential, Δp , is known from measurements of the vacuum pressure and ambient pressure however the conductance still needs to be calculated. Halwidl[50] provides two useful equations to calculate the conductance of a pipe in continuum flow. First it must be confirmed that the supersonic intake facility (including the vacuum system) is operating in the continuum regime. The system can be assumed to be operating in the continuum regime if the Knudsen number is less than 0.01. From Haldwidl[50], the equation for the Knudsen number is shown in equation 3.35:

$$Kn = \frac{\lambda}{D} = \frac{\mu \pi \bar{v}}{4pD} \quad (3.35)$$

where λ refers to the mean free gas path, μ is the dynamic viscosity of the gas, \bar{v} is the thermal velocity of the gas, p is the gas total pressure and D is the characteristic dimension (in this case the diameter of the pipework). If the ISA total pressure, total temperature, dynamic viscosity and an average molar mass of air of 29g/mol are used then the value of the Knudsen number is $Kn = 2.13 \times 10^{-7}$. This shows that the system is operating within the continuum regime. The next step is to determine

which of the two equations for conductance is suitable for this case. There is one conductance equation for laminar flow and one for turbulent. The Reynolds number can be estimated using equation 3.36:

$$Re = \frac{\rho v D}{\mu} \quad (3.36)$$

where ρ is air density, v is the air velocity and D is the vacuum pipe diameter. Here velocity will be estimated as the sonic velocity, this is because if the pressure ratio $\frac{p_2}{p_1} < 0.53$ then the vacuum system will choke. This provides an estimate of Reynolds number as $Re \approx 6.9 \times 10^6$ which is well above the limit of laminar flow. As a result, the equation that is used to calculate the conductance of the pipework is shown in equation 3.37[50]:

$$C_{turb} = 1.015 \cdot D^{\frac{19}{17}} \cdot \left(\frac{\bar{v}^6}{\mu}\right)^{\frac{1}{7}} \cdot \left(\frac{p_1 + p_2}{L}\right)^{\frac{4}{7}} \cdot (p_1 - p_2)^{-\frac{3}{7}} \quad (3.37)$$

where L is the length of the pipe, p_1 is the upstream pressure and p_2 is the downstream pressure. From equation 3.37 it can be shown that the units of conductance are [$m^3 s^{-1}$]. Another important rule to consider when calculating conductance is how the conductance of individual segments can be combined to establish the conductance of the entire system. A simple and effective way to do this is to treat segments of pipe in the same way that resistors in electronic circuits are treated but with the definitions switched. i.e. for pipe segments connected in series equation 3.38 can be used to calculate the total conductance, while for pipe segments connected in parallel equation 3.39 can be used.

$$C_{Total} = \frac{1}{C_1} + \frac{1}{C_2} + \dots + \frac{1}{C_n} \quad (3.38)$$

$$C_{Total} = C_1 + C_2 + \dots + C_n \quad (3.39)$$

With the three equations above (equations 3.37, 3.38 and 3.39) it is possible to calculate the conductance of the entire facility. One important point to note is that bends in the pipework can affect the conductance of the system. It has been shown[51] that a right angled bend in the pipework can be approximated in the calculation for conductance by adding a virtual length to the pipe equal to one diameter. There are two parameters still required, thermal velocity and dynamic viscosity vary with gas temperature. Equations 3.40 and 3.41 show the equations for these parameters and how they are dependant on temperature.

$$v_{th} = \sqrt{\frac{k_B T}{m}} \quad (3.40)$$

$$\mu = \mu_{ref} \left(\frac{T}{T_{ref}} \right)^{\frac{3}{2}} \frac{T_{ref} + S}{T + S} \quad (3.41)$$

where v_{th} is the thermal velocity, k_B is the Boltzmann constant, T is the gas temperature, m is the particle mass, S is the Sutherland temperature, μ is the dynamic viscosity, and the subscript $_{ref}$ refers to the reference condition used for the Sutherland law. The temperature used is that of the flow as it enters the vacuum facility downstream of the diffuser. Fundamentally, temperature varies with gas velocity in the supersonic wind tunnel. From initial CFD studies (details are available in section 3.2) the Mach number at the exit of the diffuser is unsteady, however it has been shown that the Mach number can reach 1.1 at the diffuser exit. With this in mind it was decided to use the highest value of Mach number that is feasible. The CFD also provides the temperature at this condition, 242.4k. Using this temperature to calculate the thermal velocity and dynamic viscosity, the conductance for each configuration can be calculated using equation 3.37. Three configurations in total were tested. The first configuration was the setup of the tunnel before this work had begun and consisted of an 8.8m long, 0.3m diameter pipe (with 2 right angled bends) followed by a 3.12m long, 0.1m diameter pipe (with 2 right angled bends). The second configuration consisted of an 8.8m long, 0.3m diameter pipe (with 2 right angled bends) and a 2m long, 0.1m diameter pipe (with no right angled bends). The third, and final, configuration consisted of a 9m long, 0.3m diameter pipe (with no right angled bends) and a 0.2m long, 0.1m diameter pipe (with no right angled bends). Table 3.1 summarises the conductance values calculated for each of these pipework configurations using the system of equations described above.

An interesting point to note is that these results do not provide concrete evidence as to why this change allowed the tunnel to start correctly (see section 3.1.3 for the results showing this). As previously mentioned, conductance could be used as a measure of the possible volumetric flow rate through the pipework. If it is assumed that the Mach number in the tunnel is 2 as it leaves the nozzle, then the maximum possible volumetric flow rate is equal to $2.78\text{m}^3\text{s}^{-1}$. However what is likely to be more relevant is the expected volumetric flow rate at the entrance to the vacuum pipework downstream of the diffuser. Based on the temperature and Mach number predictions from the CFD at the exit point, the expected volumetric flow rate here is $2.70\text{m}^3\text{s}^{-1}$. Now if this

Pipe Configuration	Conductance (m^3s^{-1})
First	3.490
Second	4.534
Final	13.119

TABLE 3.1: Conductance of the various pipework configurations used for the wind tunnel

value is compared to the values presented in table 3.1, it is clear that, based on the theory used, the pipework should be able to support such a volumetric flow rate. The conclusion that was arrived at was that the equations used to calculate conductance are not precise but provide estimations of conductance, as calculating conductance in viscous flows (as opposed to molecular flows more often of interest when referring to conductance) is not straightforward. However, what the results do show is that the expected volumetric flow rate required for the tunnel to run as designed is relatively close to the conductance of the first two configurations. The third configuration provides an almost 4 fold increase to the predicted conductance. Therefore it is clear that there was a significant improvement to the system conductance with the final setup used and this analysis, even if the exact value calculated was not accurate, illustrates why this new setup may allow the tunnel to start successfully.

CONDUCTANCE IMPROVEMENT (FINAL SETUP)

With the above change made to the way in which the wind tunnel was connected to the vacuum tank, the tunnel was run again. The pitot probe was removed from the test section to remove any blockage (this was done for all of the previous configurations too however there was no difference to the results presented). Figure 3.23 shows part of the shock train that passes down the supersonic facility at start up.

Along with the Schlieren image (figure 3.23) that clearly shows the wind tunnel starts as expected, there was also a static pressure profile recorded at a pressure port on the tunnel floor 34.6mm downstream of the start of the test section and the wind tunnel Mach number derived from it. The pressure profile is shown in figure 3.24 and is displayed as a moving average. The data was recorded at 100kHz however there is significant interference generated from the vacuum pump so it was decided to use a moving average in order to filter out the high frequency noise.

From this pressure profile it was possible to calculate the Mach number of the facility. If it was assumed that the nozzle was operating isentropically, Bernoulli's principle can be used to calculate the Mach number. Bernoulli's principle in compressible flow is given by equation 3.42 if it is assumed that the flow is adiabatic and the term due to gravitational acceleration is negligible, both reasonable assumptions here:

$$\frac{v^2}{2} + \left(\frac{\gamma}{\gamma-1}\right)\frac{p}{\rho} = \left(\frac{\gamma}{\gamma-1}\right)\frac{p_0}{\rho_0} \quad (3.42)$$

The static pressure in the wind tunnel is known and the atmospheric pressure and temperature are measured, allowing calculation of atmospheric density. Therefore this equation can be rearranged to give equation 3.43 and solved by numerical iteration based on isentropic flow. Isentropic flow tables are used to provide values for density, temperature and thus velocity in the Mach number range expected (1.7-2.3), these values are used to iterate equation 3.43 until the required pressure is achieved within



FIGURE 3.23: Instantaneous Schlieren image of the tunnel start up shock train as it travels downstream in the wind tunnel

a suitable tolerance.

$$p = \left(\frac{p_0}{\rho_0} - \frac{v_2}{2} \left[\frac{\gamma - 1}{\gamma} \right] \right) \rho \quad (3.43)$$

The static pressure was measured using a Kulite on the wind tunnel floor, atmospheric pressure was measured outside of the wind tunnel using a mercury barometer and atmospheric temperature was measured using a mercury thermometer. The result of this is a Mach number profile shown in figure 3.25. The Mach number was iterated to an accuracy of 0.0001 in order to reduce the error between the calculated static pressure and the actual static pressure. Figure 3.26 illustrates the error in Pa between the calculated pressure and the actual measured pressure. Before the tunnel is started the error is large, this is a result of only iterating between Mach 1.7 and 2.3. The error when the tunnel is running has a maximum value of 1.41Pa and a mean value of 0.67Pa. This is less than 0.01% error in the calculation which is deemed accurate enough for this research.

FINAL WIND TUNNEL FACILITY SCHEMATIC

Following the various sections above; presented below is a schematic showing a diagram of the dimensions of the final wind tunnel itself in figure 3.27 and the layout of the facility as part of the overall infrastructure in figure 3.28.

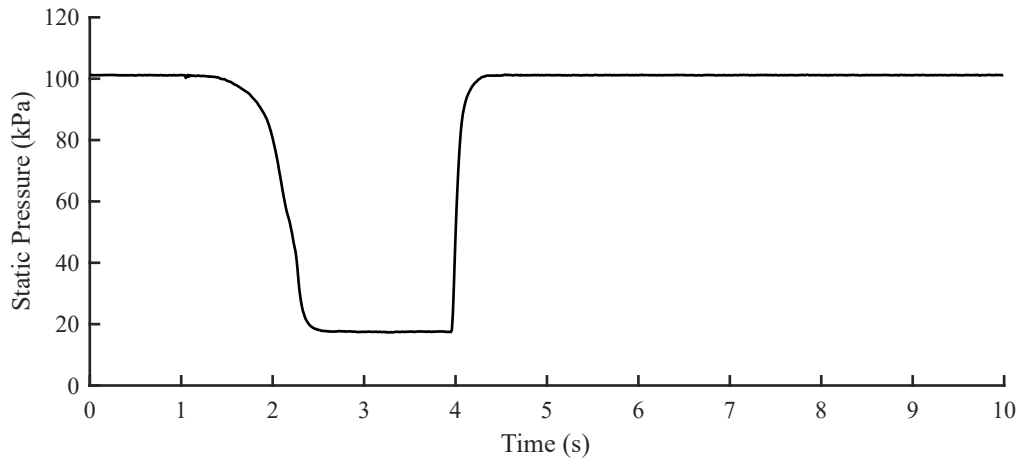


FIGURE 3.24: Static pressure profile recorded 34.6mm downstream of the beginning of the wind tunnel test section

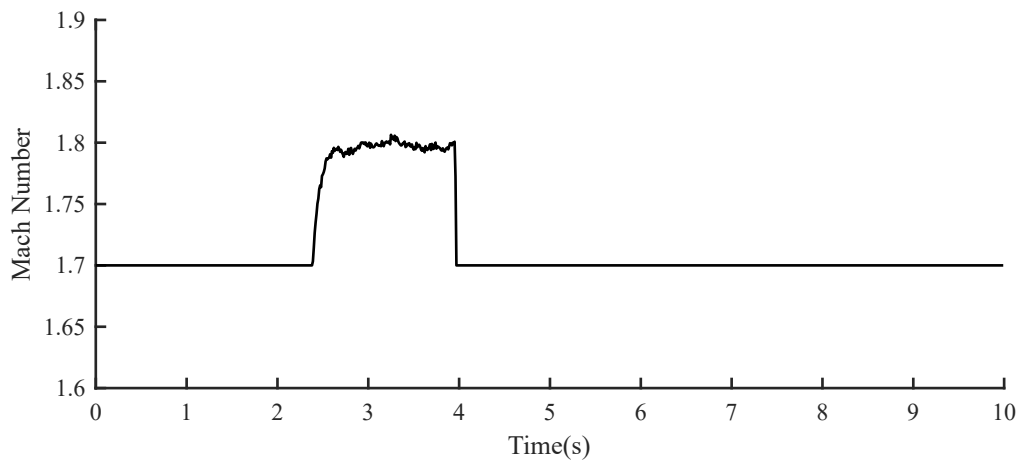


FIGURE 3.25: Mach number profile calculated from Bernoulli's principle from static and total pressure measurements

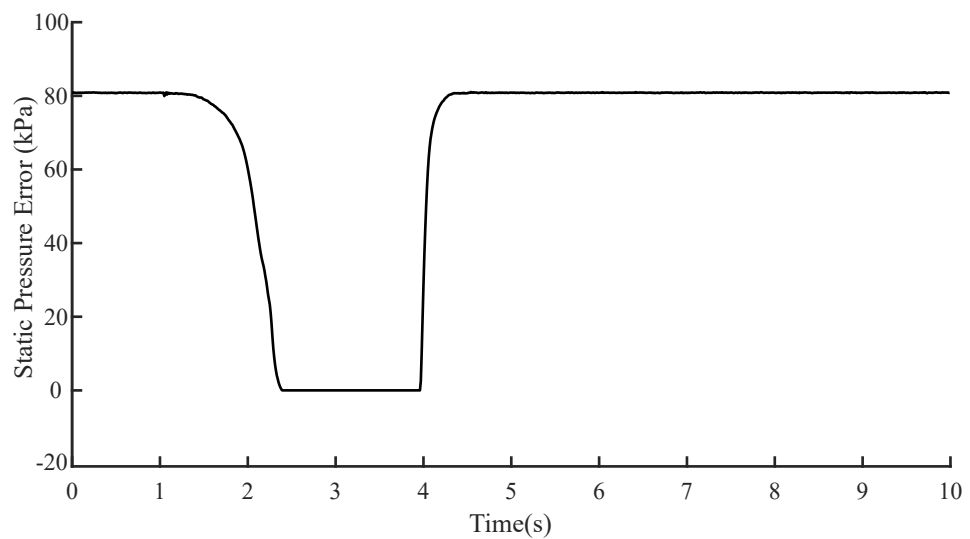


FIGURE 3.26: Error in the comparison of measured pressure and actual pressure when numerically solving the compressible Bernoulli equation.

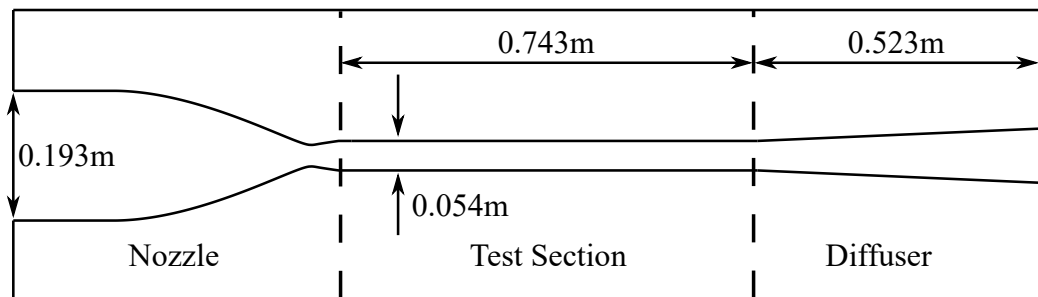


FIGURE 3.27: Schematic showing the dimensions of the final wind tunnel design

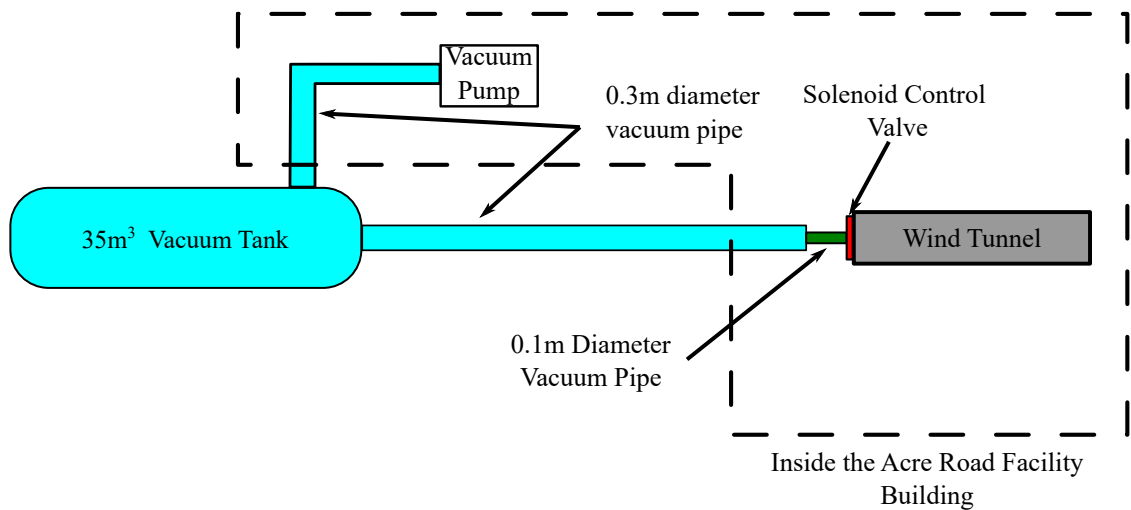


FIGURE 3.28: Basic schematic displaying the vacuum system and the connection to the wind tunnel

3.2 FINALISED WIND TUNNEL CHARACTERISATION

Now that the wind tunnel and the associated vacuum pipework had been suitably redesigned to provide a functioning indraft supersonic wind tunnel, the facility had to be characterised. The characterisation was done using static pressure measurements and Schlieren imaging. Following the recording of the pressure data, a more accurate and refined CFD simulation was created (compared to the results of the approximate simulation presented in section 3.1.2).

3.2.1 CFD SIMULATION

The general setup of the numerical simulation created is described in section 2.2. The first step necessary was to carry out a mesh convergence study. A simulation is mesh independent when a change in the cell density no longer alters the results being monitored, within a certain tolerance. Figure 3.29 presents the evolution of the centreline Mach number profile as the mesh density was iterated. It is clear that the Mach number profile for the simulations with the two largest mesh densities have collapsed onto one another and there is no significant variation between them. This along with the percentage difference between the two most refined meshes, see table 3.2, being below 1% for a range of discrete locations along the tunnel centreline indicate that the final two mesh densities can be considered mesh converged in this case.

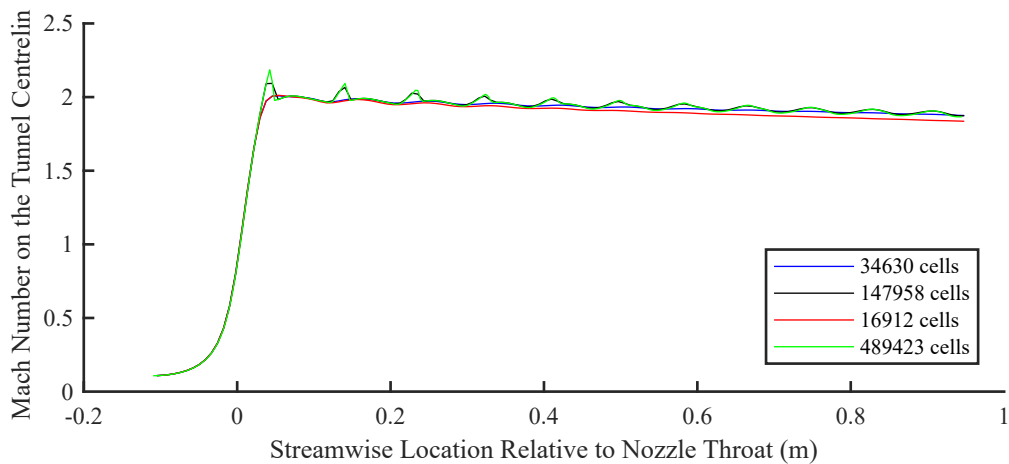


FIGURE 3.29: Evolution of the Centreline Mach number profile extracted from CFD simulations as the mesh density was altered

Mesh Density (Number of Cells)	Centreline Location Relative to the Start of the Test Section (m)			
	0.1	0.2	0.3	0.4
16912	N/A			
34630	0.31	0.59	0.72	0.91
147958	0.15	0.25	0.05	1.67
489423	0.07	0.15	0.31	0.52

TABLE 3.2: Absolute percentage difference between coincident mesh densities at various points on the wind tunnel centreline

To create an accurate numerical model of the wind tunnel, experimental pressure data was used. The simulation was improved by tuning the boundary condition at the diffuser outlet until the static pressure measured at a tapping in the diffuser could be matched. This pressure tap was located 0.938m downstream of the start of the test section and was 0.018m below the tunnel centreline (on the wind tunnel side wall). This places the port 0.195m downstream of the entry of the diffuser. Figure 3.30 presents the static pressure recorded at this port.

During the running of the tunnel the average static pressure is recorded as 36kPa. It is this value that is targeted during the boundary condition tuning. Figure 3.31 illustrates the pressure profile from the bottom to the top of the diffuser at the spanwise location of the pressure port with the outlet boundary static pressure defined as 40kPa.

This illustrates that at the location in question the pressure achieved is 35.3kPa. Due to the amount of time taken to run the CFD simulations this was deemed to be accurate enough (1.9% difference) for this work as the numerical simulations are not the primary research interest. With this boundary condition applied, the simulation result is shown in figure 3.32.

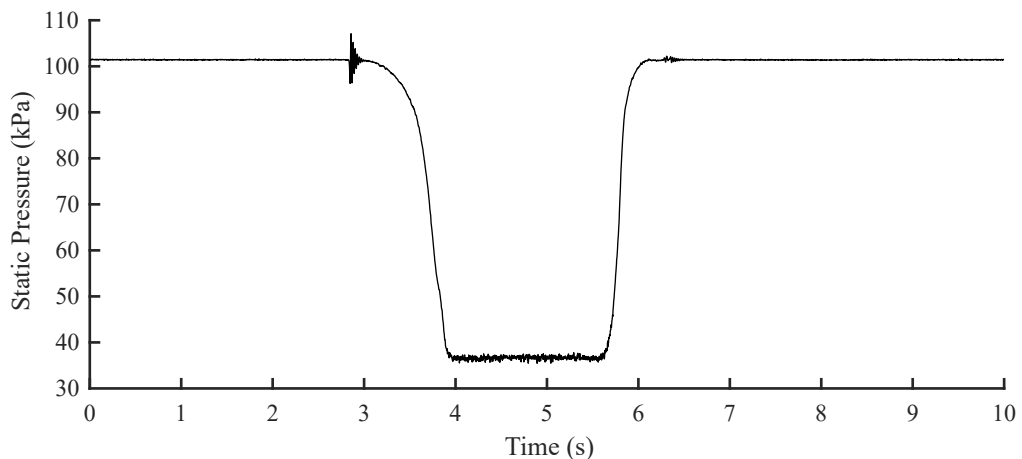


FIGURE 3.30: Static pressure recorded at the static pressure port in the diffuser.

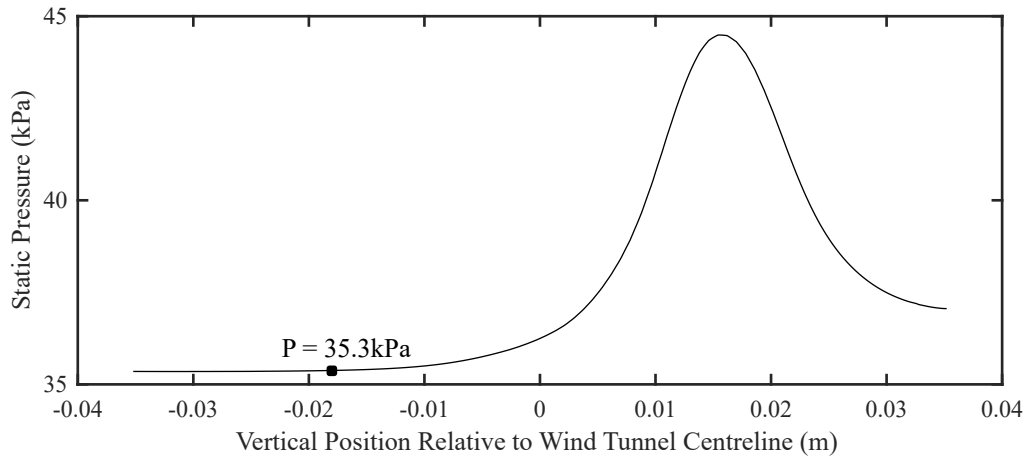


FIGURE 3.31: Static pressure extracted from CFD at the same location as the pressure measurement recorded within the diffuser.

This seems to be an accurate representation of the features present in the facility. With a realistic vacuum pressure it would be expected that there would be some form of shock structure at the entrance to the diffuser. The non-axisymmetric structure observed in the diffuser is a result of the flow field here being unsteady. Therefore this steady simulation is essentially a snapshot of the real flow. The steady modelling was deemed acceptable in this case as although the diffuser exhibits an unsteady flow field, the region of interest, the test section, is a steady flow. Two sets of data are of particular interest for comparison to the experimental results presented in the following sections. The static pressure observed from the numerical simulation can be compared to the static pressure measurements recorded in the wind tunnel (see section 3.2.2). The other measurement of interest was the boundary layer thickness, this can be extracted from the CFD at regular intervals by determining where in the boundary layer the velocity reaches 99% of the freestream value. This boundary layer measurement can then be compared to measurements of the boundary layer extracted from the Schlieren images (see section 3.2.3).

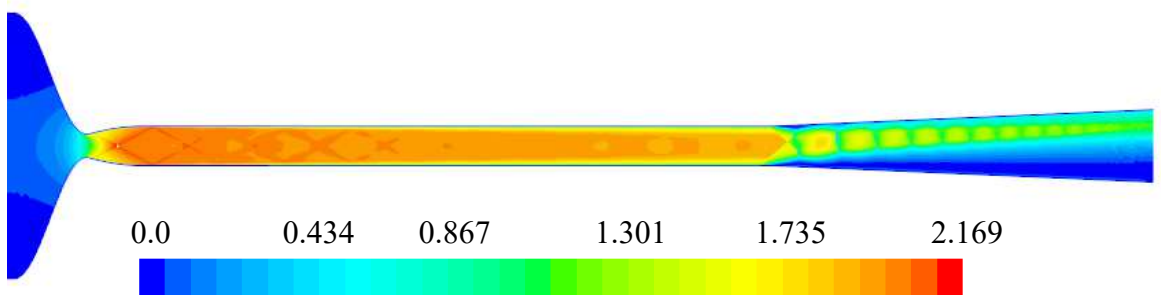


FIGURE 3.32: CFD Mach contour of the final wind tunnel design.

3.2.2 PRESSURE MEASUREMENTS

Pressure measurements were recorded using Kulite pressure transducers connected to pressure taps in the tunnel floor via rubber tubing. The reasoning behind how pressure measurements were taken is described in more detail in section 2.1.3. Ideally, total pressure measurements would have been recorded as this would have provided somewhat of a velocity profile in the vertical direction for the wind tunnel. However this was not possible as the tunnel proved very sensitive to any blockage added. If the pitot probe was situated inside the wind tunnel then it would not start successfully. As a result no total pressure measurements could be recorded.

Once the pressures were recorded, a moving average was taken of the data reducing the effective sample rate from 10kHz, at which the data was recorded, to 1kHz. This was done due to the significant high frequency noise present in the pressure signals. This was shown through investigation to originate from the vacuum pump being used. This was not an issue for this section of the work as the frequency response of the pressure signal was unimportant.

In order to measure the pressure profile a number of static ports were available along the floor of the test section. There are two sets of pressure ports: one set along the centreline of the wind tunnel and the other set offset by $\frac{1}{4}$ of the tunnel width. There are 8 ports in each set and the streamwise location of the ports are consistent between sets. This was done to measure how symmetric the flowfield is in the spanwise direction. The first pressure port was 34.6mm downstream of the beginning of the test section and the remaining ports are a further 80mm downstream of the previous port. For reference, the ports are numbered with 1 being the furthest upstream and 8 being the furthest downstream. The offset set of pressure ports are designated by the letter "a" i.e. pressure port "1a". Figure 3.33 illustrates the setup of pressure ports.

Figure 3.34 presents a comparison of the centreline pressure measurements, the off-centre pressure measurements and pressures extracted at the corresponding locations from the CFD simulation. The significant difference between the off-centre and centreline pressures at 114.6mm is thought to be due to a shock wave as a result of

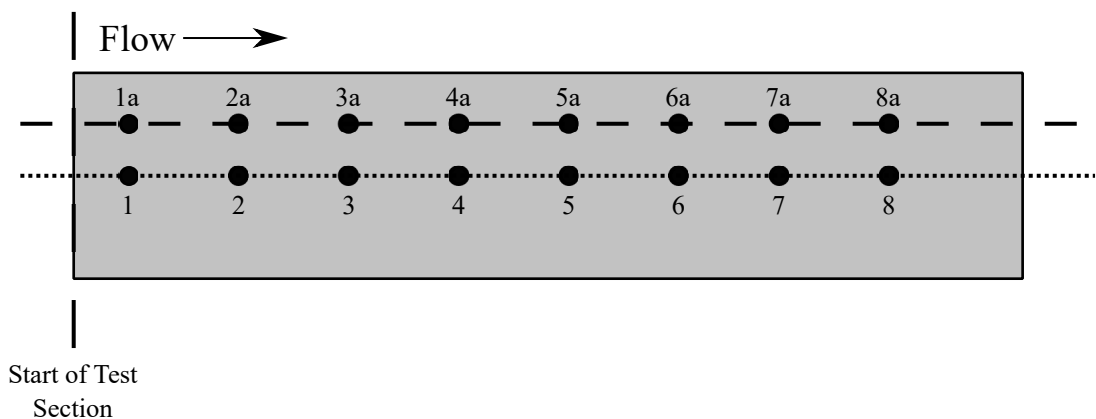


FIGURE 3.33: Diagram of static pressure ports located on the test section floor

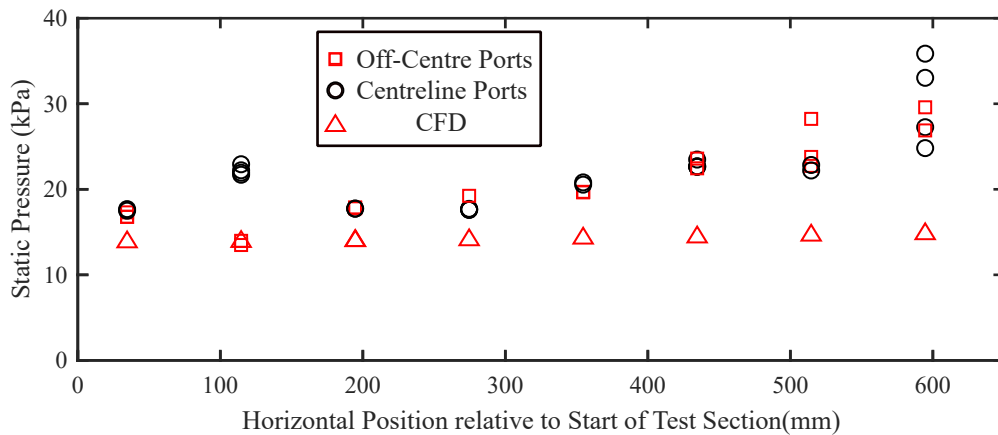


FIGURE 3.34: Static pressure profile along the tunnel floor centreline and off centre at $\frac{1}{4}$ tunnel width compared to static pressure extracted from CFD at the corresponding location (only centreline as CFD is 2D)

a imperfection in the roof of the tunnel. The resulting shock wave impinges on the tunnel floor very close to the location of this pressure measurement. This would explain the pressure rise at the centreline directly behind the shock wave and the apparent static pressure drop as the flow would likely experience local acceleration either side of the shock structure near the centre of the tunnel. The variability in experimental pressure measurements at locations 514.6mm and 594.6mm is a result of the shock train structure. Due to the vacuum pressure not being as low as would be ideal, the shock train that would normally be in the diffuser was found to be positioned near the end of the test section. In some of the tests carried out it would travel further up the test section and interfere with the pressure measurements recorded at these two downstream locations. Finally, the most significant difference is between the CFD and the experimental measurements. The CFD pressure profile starts with a similar magnitude as the experimental values. However the further downstream the flow travels, the larger the difference becomes. It is proposed that this difference is likely due to the numerous weak shock waves present in the experimental facility that are clearly not present in the CFD. Figure 3.35 presents the entire pressure profile along the tunnel extracted from the CFD, it is clear that along the tunnel test section there is a gradual increase in static pressure until the flow meets the shock train at the entrance to the diffuser.

In an ideal tunnel with a perfectly smooth surface this is what would be expected, a gradual increase in static pressure and decrease in Mach number (see figure 3.29). This is a result of the gradual increase in flow confinement due to boundary layer growth. What this does not capture compared to the experimental measurements, is the step increases in static pressure resulting from the various sources of unmodelled shock waves. These come from surface imperfections (such as that described above) and joints in the wind tunnel structure such as where the nozzle meets the test section on the upper and lower surfaces and where the two halves of the floor of the test

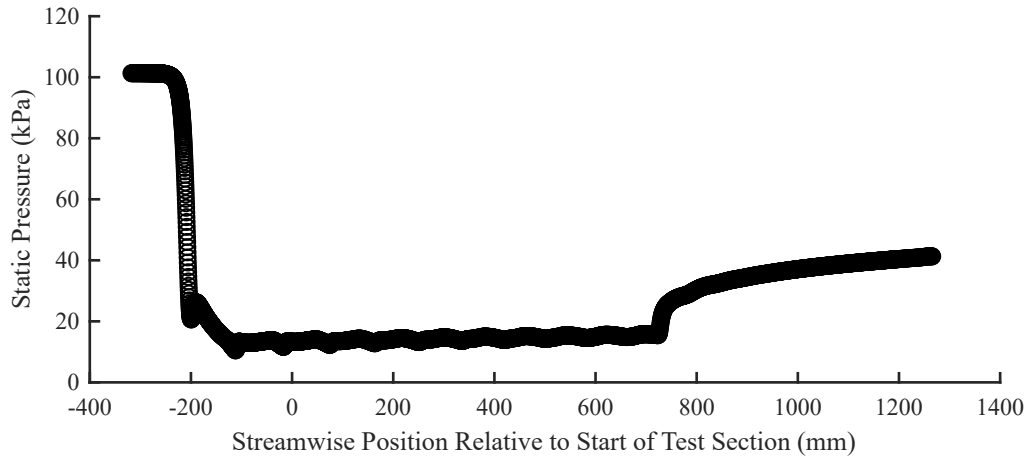


FIGURE 3.35: Pseudo-Continuous (measurement with 1mm resolution) static pressure profile on tunnel floor extracted from CFD

section meet. This also explains why even at the start of the test section, at the first measurement location, the pressures are not equal. At this point the flow has already past through a shock wave present in reality but not present in the CFD, the shock wave generated where the nozzle and test section meet on the lower surface.

The other, less important difference, occurs near the end of the test section where (as described above) the terminating shock train in the wind tunnel interferes with the pressure measurements. This does not occur in the CFD due to the ideally modelled, and steady, vacuum pressure boundary condition.

3.2.3 SCHLIEREN IMAGING

Schlieren was also used to characterise the wind tunnel. Schlieren is inherently a qualitative technique, however there are a number of ways by which it can be used to provide quantitative data. In this case the Schlieren can be calibrated dimensionally by using a known distance in the image to provide a calibration value in mm/px. Using the calibration factor it is possible to estimate the boundary layer thickness. The decision of where the edge of the boundary layer is located in the Schlieren is inherently subjective. It may have been possible to conduct this mathematically based on the intensity in the image however, due to noise in the intensity plots resulting from a combination of interference from the windows (made from toughened glass and so lacked good optical qualities) and the flow field itself, this was deemed unreliable. As such the process was done manually by selecting points in the image at the perceived boundary layer edge. Data points were recorded at 5.25mm increments, every 50 pixels as the calibration value for the Schlieren images used was 0.105mm/pix. Figure 3.36 illustrates the result of this process. The points are broken down into three groups based on the position of the Schlieren system. Due to the limited field of view of the Schlieren system, multiple sets of images had to be recorded at different positions to try and achieve a complete boundary layer profile. Three data sets were recorded at each position to produce an average image. The average image was the source

of the data points for each test in an attempt to produce a clearer outline of the boundary layer. Figure 3.37 shows one of these average images with the boundary layer thickness extracted from it superimposed (red dots) and the roof of the test section highlighted in blue for clarity. This provides an example of what was perceived to be the edge of the boundary layer when each data point was extracted. Using the individual data points extracted, as illustrated in figure 3.37, a linear best fit line was drawn for each Schlieren location. A linear best fit line was also drawn for all of the points combined. Data points were also extracted from the CFD simulations at 50mm increments from the beginning of the test section. The boundary layer thickness was taken to be the point in the boundary layer where $U = 99\%U_\infty$. These are all shown in figure 3.36 along with a line representing the theoretical value for the boundary layer. The theoretical values come from equation 3.44) which defines the theoretical boundary layer thickness[45]:

$$\delta \approx \frac{0.37x}{Re_x^{1/5}} \quad (3.44)$$

This equation is based on a flat plate turbulent boundary layer and so would not necessarily be considered accurate when used in this sort of manner. However it is interesting to note that the theoretical value, data extracted from the CFD simulation, and the values taken from the Schlieren imaging show similar boundary layer growth rates. This is with the exception of the test at position 3 from the Schlieren imaging. As this is only one test, it is assumed that this is likely an outlier to the rest of the data. The reason for this set of data demonstrating a markedly different growth rate to the others is unclear. It could be a result of a fault in the Schlieren setup for this location or user error when the data was extracted. However the latter is unlikely as similar results were obtained when the analysis of the Schlieren imaging was repeated. Table 3.3 presents the non-dimensional boundary layer growth rates for each of the different sources. The only two that vary significantly are the growth rates for all of the test areas combined and for test set 3.

However when figure 3.36 is examined, it is clear that the boundary layer thickness at the start of the test section is not consistent. Regarding the theoretical value, the

Data Source	Boundary Layer Growth Rate
Position 1	0.0255
Position 2	0.0234
Position 3	0.0366
All Positions	0.0170
Theory	0.0234
CFD	0.0259

TABLE 3.3: Test Section Boundary Layer Growth Rate Comparison

boundary layer thickness is set to zero at the start of the test section. This is not accurate but is an assumption made for the simplicity of the calculation. It is thought that the CFD measurement of the boundary layer is likely to be the most accurate. The reason being that the Schlieren will not be able to accurately show the edge of the boundary layer ($U = 0.99U_\infty$) as the density gradients at this region will be very small. Therefore, although the growth rate prediction seems reliable from Schlieren, the absolute value is not as it will underestimate the total boundary layer thickness. When propagated back to the beginning of the test section (which is out of the field of view and so could not be measured), this will result in an underprediction of the boundary layer thickness at this location. These results do suggest that all of these methods are reliable in the prediction of boundary layer growth rates for supersonic duct flows, however CFD is the only method that predicts a realistic value for absolute boundary layer thickness at any one location.

3.3 CONCLUSIONS

The aim of this chapter was to redesign the existing supersonic wind tunnel at the University of Glasgow as the original design resulted in a malfunctioning facility. The key features of the tunnel have been highlighted and redesigned where appropriate. The key changes that were found to make the biggest difference to the operation of the wind tunnel were actually found to be periphery components i.e. the control valve and the vacuum system connection.

The initial valve cross-sectional area was smaller than that of the nozzle throat and therefore the nozzle throat would not choke under the original configuration. Changing the control valve to one with a larger cross-sectional area resulted in the nozzle choking correctly. The second important modification was to the pipework connecting the wind tunnel to the vacuum system. The result was a substantial increase in the calculated conductance for the pipework and ultimately this change allowed the wind tunnel to run to the desired conditions. The outcome for this that future design work

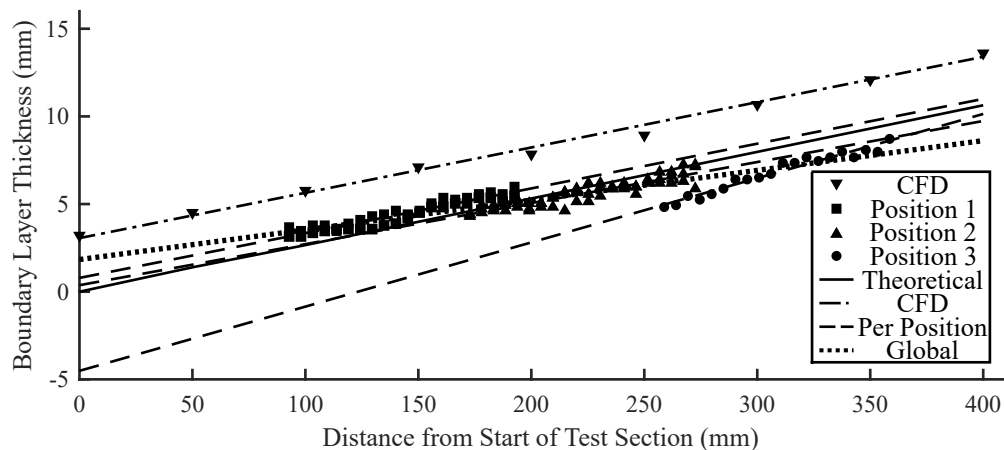


FIGURE 3.36: Approximation of the boundary layer thickness extracted from Schlieren imaging compared to Theoretical and CFD values.

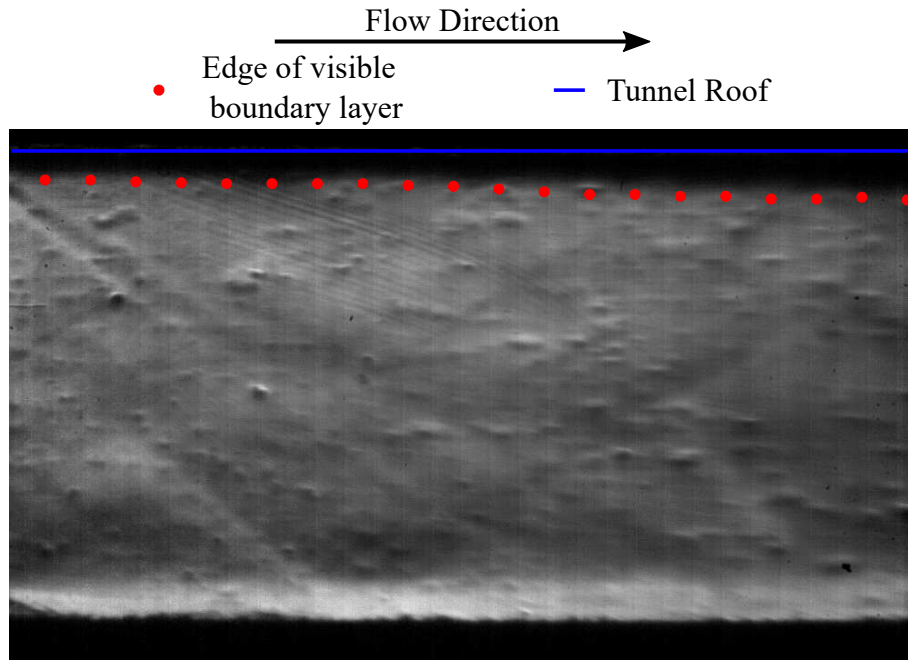


FIGURE 3.37: Illustration of the node points representing the boundary layer thickness extracted from the Schlieren images.

should take note of is that the wind tunnel design itself is not the only factor in the creation of a successful facility. The infrastructure that facilitates the use of the wind tunnel must also be carefully designed to ensure the end result is a correctly functioning wind tunnel.

The second section of this chapter focused on the characterisation of the facility. This was limited to Schlieren and pressure measurements due to the sensitivity of the facility to small blockages. The pressure measurements and boundary layer thickness measurements extracted from Schlieren were compared to CFD simulations of the same geometry. The CFD was limited to 2D however it provided a reasonable comparison for these purposes. The pressure measurements and the CFD results were found to disagree along the entire length of the test section. This was a result of the numerous errant shock waves generated by joints and imperfections in the real wind tunnel that were not present in the CFD. The comparison of boundary layer thickness was more successful. It was found that the boundary layer growth rate was very comparable between experimental data extracted from Schlieren imaging, CFD simulation and theoretical predictions. The absolute value was found to differ between the sets of data for a number of reasons. The theoretical value was fixed at 0 at the start of the image which is not true and is therefore a function of the methodology used rather than the equation used for the prediction. Regarding the Schlieren, this was also found to be lower than the CFD prediction and it is proposed that this is due to limitations in the sensitivity of the recorded images. The light intensity variation at the edge of the boundary layer will likely be very small and so the absolute thickness will be underpredicted by the Schlieren. These results do suggest that Schlieren could be used successfully to measure boundary layer thickness if configured accurately.

This would be an interesting area for future work, to show an accurate correlation of boundary layer thickness extracted from Schlieren imaging and other measurement sources such as pitot probes.

CHAPTER 4

EFFECT OF CAVITY GEOMETRY ON SUPERSONIC DUCT FLOW

4.1 SUPERSONIC CAVITY FLOW CHARACTERISTICS

4.1.1 CAVITY FLOW CLASSIFICATION

Cavity flows in the region of interest (Mach 1.7-2) exhibit fundamentally the same flow characteristics as subsonic cavities. The key fluid dynamic feature is the shear layer that detaches from the leading edge of the cavity. The behaviour of the shear layer downstream has a distinct impact on the cavity flow field as a whole. There are two distinctly different cavity flow fields known as open and closed cavities, as well as the case where the cavity is neither open nor closed and is known instead as transitional. Open and closed cavities are defined solely by the reattachment point of the shear layer. A cavity where the flow does not reattach to the cavity floor is an open cavity and one where the flow does reattach to the cavity floor is a closed cavity. The flow fields in these two types of cavity flows will clearly be different. Figure 4.1 illustrates the fundamental differences in the flow fields. The significant difference is that the open cavity has one large recirculation region in the centre of the cavity while a closed cavity has two smaller recirculation regions, one near the leading edge and one near the trailing edge.

The cavity geometry is the determining factor as to which of the aforementioned cavity flow fields are present. Typically for cavity geometries, the non-dimensional ratio of the cavity length divided by the cavity depth, $\frac{L}{D}$, is used to describe the geometry. A classification, based on this non-dimensional value, is available within the range of Mach numbers $1.50 < M < 2.86$ suggesting that cavity geometries with $\frac{L}{D} < 10$ will display open cavity flow fields while those with $\frac{L}{D} > 13$ will exhibit a closed cavity flow field. $\frac{L}{D}$ between these two values will likely exhibit transitional behaviour.[52] The fundamental trend shown of a smaller $\frac{L}{D}$ leading to an open cavity would seem logical as the shorter the distance relative to the depth of the cavity, the more likely it

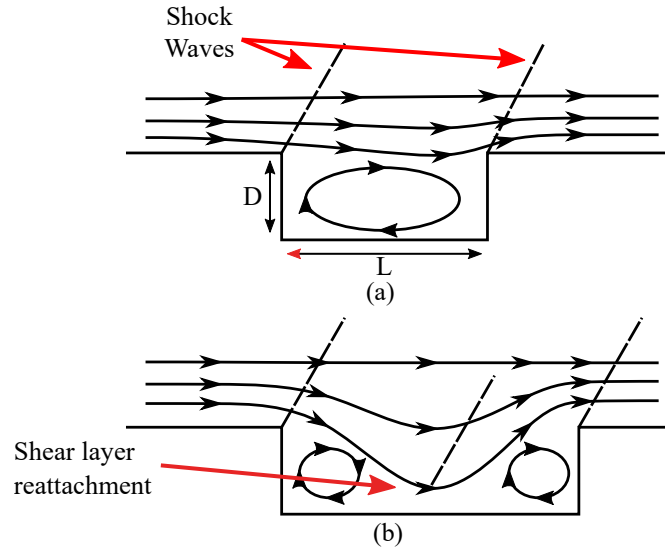


FIGURE 4.1: Diagram of the expected flow field in (a) open and (b) closed cavity flow fields

would be assumed that the shear layer would reach (and thus reattach) the trailing edge before the cavity floor, thus leading to an open cavity flow. The same logic could be applied to the opposite flow field. The research presented here is particularly interested in open cavity flows, this is due to the resonant modes produced by this type of flow field.

4.1.2 OPEN CAVITY RESONANCE MODES

Open cavities typically display two modes of resonance: shear layer mode resonance and wake mode resonance. This research is particularly interested in the shear layer resonance mode. This is due to a combination of the scale of the cavities used in this study, the wake mode tends to occur in longer cavities relative to the incoming momentum thickness of the boundary layer, and the inherent controllability of the shear layer resonance mode.

The longitudinal resonance mode is a result of the interaction of the shear layer with the cavity trailing edge, first documented in detail by Rossiter[53]. This phenomenon is a result of an acoustic feedback loop that occurs between the recirculating flow in the cavity, and the shear layer. As the shear layer separates from the cavity leading edge, small disturbances are amplified as they move downstream; a result of the Kelvin-Helmholtz instability. These structures interact with the cavity trailing edge, generating acoustic waves inside the cavity. These waves travel upstream within the cavity and perturb the shear layer at the leading edge resulting in further disturbances. It is this feedback loop that results in the phenomenon known as Rossiter mode resonance. Based on the work by Rossiter[53], the resonant frequencies exhibited by

an open cavity flow can be predicted through a relatively simple equation:

$$St = \frac{fl}{U_\infty} = \frac{m - a}{M + \frac{1}{k}} \quad (4.1)$$

where f is the resonant frequency of the cavity, l is the length of the cavity, U_∞ is the freestream velocity, m is the mode number, a is an empirical constant that accounts for the phase delay between the acoustic wave impinging at the upstream edge and the vortex shedding within the shear layer, k is the ratio of the vortex convection speed in the cavity to the freestream speed and M is the Mach number. One important point to note is that the resonant frequencies are not consistently present, they can switch between themselves or not be present at all at any one point in time. This was illustrated by Kegerise et al.[54] in their study where it was shown, through simultaneously acquired unsteady pressure measurements and Schlieren images, that the dominant resonant mode switches between the Rossiter mode frequencies.

HELLER MODIFICATION FOR SUPERSONIC FLOWS

The equation produced by Rossiter was later modified by Heller et al.[55] to better account for compressibility effects at high Mach numbers. The improvement is based on examining the impact of a change in speed of sound within the cavity. In Rossiter's earlier work it was assumed that the speed of sound was equal to the freestream speed of sound. Speed of sound in the cavity can be calculated by equation 4.2:

$$a_c = a_\infty \left[1 + r \left(\frac{\gamma - 1}{2} \right) M^2 \right]^{\frac{1}{2}} \quad (4.2)$$

where r is the recovery factor i.e. $r = \frac{(T_c - T_\infty)}{(T_0 - T_\infty)}$. In Rossiter's earlier model this recovery factor is assumed to be zero as the temperature of the flow in the cavity must be equal to the freestream temperature for the speed of sound to be equal. However, it is presented in the research by Heller et al.[55] that this is not the case at higher Mach numbers ($M > 1$), and that it is actually closer to 1 at $M \approx 2$. As a result, Heller et al.[55] suggested that an improvement was to assume the temperature in the cavity was equal to the freestream stagnation temperature (as suggested by a recovery factor value equal to 1). This assumption gives rise to equation 4.3 which includes the proposed modification:

$$St = \frac{f_m l}{U_\infty} = \frac{m - a}{\frac{M_\infty}{\sqrt{1 + \left[(\gamma - 1) \frac{M_\infty^2}{2} \right]}} + \frac{1}{k_c}} \quad (4.3)$$

where m is the resonant mode number, f_m is the resonant frequency, L is the cavity length, U_∞ is the freestream velocity, k_c is the vortex convection ratio mentioned above, M_∞ is the freestream Mach number and a is an empirical constant. This improvement

to the original formula was shown to correlate well in the Mach number region tested ($2 < M < 3$)[55] and is the equation that will be used for predictions of the frequencies expected in the current wind tunnel model.

4.1.3 PREVIOUS STUDIES ON CAVITY FLOW CONTROL

Cavity flows, particularly open cavity flows have been a field of great interest for a variety of applications since the first fundamental studies of these flow types. Applications in aerospace that have previously provided interesting research include but are not limited to: noise reduction of landing gear bays[56], reduction of unsteadiness in weapon bays[57] and supersonic combustion, in particular as flame-holders[58].

As previously mentioned, this research is particularly interested in the control of supersonic open cavity flows. The reason for this is the Rossiter mode resonance that they exhibit, the importance of which is that it has been shown to be controllable[59][60]. In this circumstance, this is referring to both the shear layer characteristics and the respective amplitudes of the resonant frequencies and how they can be manipulated. There have been numerous studies into the control of supersonic cavity flows, each with different flow control methodologies and motivations, however here only active flow control will be discussed as these studies are most relevant in comparison to this research.

Active flow control studies can be further subdivided. A simple representation of the breakdown is shown as a flowchart in figure 4.2. This breakdown is quite top-level and does not delve into much detail, however it does provide a useful breakdown in order to classify the currently published research that is relevant to this study. This research is primarily interested in the class highlighted in red; open-loop, pulsed flow control. However some examples of work carried out in the other areas will be discussed briefly in order to demonstrate the breadth of techniques that have been used to varying degrees of success. As shown in figure 4.2, active flow control can be split into two categories: open and closed loop control. Open loop is when no feedback, via some flow parameter, is available to tune the response of the flow control mechanism. Closed loop control refers to the case where there is some form of feedback from measurements of the flowfield itself, often a pressure measurement. Closed loop control is inherently more difficult, particularly at supersonic speeds[61]. Shaw and Northcraft[62] showed this was possible using a rotary-valve, pulsed blowing actuator capable of producing a single excitation frequency as a result of the valve rotating at a specified rotational speed (rpm). The issue with this technology however was that, due to the inertia of the valve, the response time to a commanded change in frequency was too slow to provide meaningful closed loop flow control at supersonic speeds. If mastered, there are benefits to closed loop control which include, but are not limited to: lower power requirements for the actuator and the ability to match the current dominant Rossiter frequency (not a consistent frequency as mentioned above) at any instant, and improving the time averaged effectiveness of the control method. The

methods employed in this work are considered to be open-loop methods.

There have been a variety of open loop flow control methodologies tested for supersonic cavity flow control e.g. steady upstream mass injection[63; 64; 65; 66], pulsed upstream jet injection[62][67] and energy deposition methods[59][60].

Although each flow control technology may operate in a different manner, there are only three fundamental ways in which each method can manipulate the cavity flow resonance characteristics. Rowley et al.[68] suggested that there are three discrete control philosophies that can be considered:

1. Modification of the upstream boundary layer/cavity shear layer thickness in order to modify the stability characteristics of the shear layer,
2. Actuation at an off-resonant frequency in order to disrupt the natural feedback loop resonant frequencies,
3. Adjust the reattachment/impingement location of the shear layer relative to the cavity trailing edge in order to disrupt the acoustic feedback loop.

From this list, the philosophy of interest to this work is that of actuating the flow control device at an off-resonant frequency in order to disrupt the natural feedback loop. On the same theme, a control methodology not mentioned by Rowley et al.[68] is to not disrupt the feedback loop, but instead actuate the flow control device at the cavity resonant frequency in order to enhance the cavity resonance. This is likely not mentioned as the usual aim of cavity flow control is to suppress resonance rather than enhance it. However for this research, enhancing the resonance is a possible goal as well as disrupting it. This methodology of flow control has previously been used with energy deposition flow control methods, specifically by Webb et al.[59][69] where localised arc filament plasma actuators (LAFPA) were used to modify the resonant characteristics of a cavity flow in a Mach 2.24 flow. They demonstrated that by actuating at different frequencies (relative to the cavity Rossiter frequencies) the LAFPA actuators could significantly modify the magnitude of the resonant frequency peaks, showing both the ability to suppress and enhance these resonant tones. This work illustrated that using energy deposition was a viable tool to control cavity flows at supersonic Mach numbers while employing the philosophy of disrupting/enhancing the feedback loop by actuating at specific frequencies. This is one of the key drivers that suggest using ns-DBD plasma actuators could be a possible option for supersonic cavity flow control. The implementation of this will be discussed in chapter 6, however it is important to make this connection here.

4.1.4 INTERACTION BETWEEN SHOCK TRAIN AND CAVITY

As mentioned in the introduction (chapter 1) the application of interest driving the various parts of this research is the improvement of Ramjet/Scramjet performance. This is approached in two different manners in this work: investigation of cavity flow control for implementation into a ramjet/scramjet isolator duct and separation

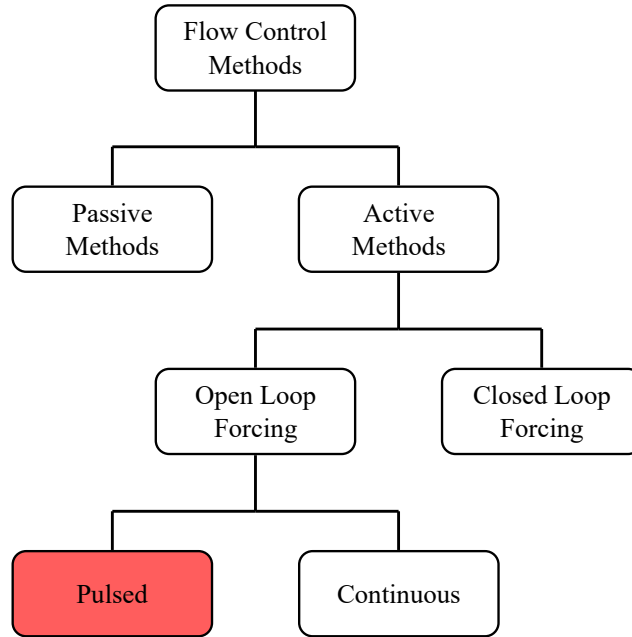


FIGURE 4.2: Illustration of the various levels of flow control classification

reduction on the axisymmetric intake cone using laser energy deposition. The first option is relevant to this chapter as the behaviour of the cavity in the supersonic duct is clearly important. A previous study[8] showed that a cavity can be used to delay unstart of a shock train in a rectangular duct. This was demonstrated by tracking the location of a shock train at different downstream back pressures and comparing the same conditions but with a cavity present. The study illustrated that a cavity could be used to delay unstart, but the mechanism that caused this was unclear and there was no clear suggestions as to what this may be.

This study however is not able to examine this in more detail, due to the facility being unable to create a repeatable back pressure for shock train location control. Instead this chapter will examine how the addition of a cavity can affect the flow field in a supersonic duct, particularly at start up. The problem of intake starting/unstarting is one that has prompted significant research into a variety of related areas such as: restarting an unstarted intake[70], unstart prevention through flow control[12][71], the impact of unstart on an aircraft[72]. The problem of inlet starting was first recorded in literature in the mid 1940's[73]. The fundamental difference between a started and unstarted inlet is the quantity of mass captured. A started inlet captures all of the incoming flow while an unstarted flow exhibits spillage, typically as a result of a shock formation upstream of the inlet entrance.

Starting behaviour can be predicted through examination of the area ratio in a similar manner as was discussed in section 3.1.2 regarding the starting problem for wind tunnel diffusers. The relationship between Mach number of an inlet and the minimum area ratio required for it to start was presented in analytical form by Kantrowitz et al.[73] Equation 4.4 shows this analytical relationship. The equation is straightforward

enough to derive by first taking the standard area-Mach relation and combining it with the starting shock present by assuming that the mass flow drop across the shock wave is solely a result of total pressure loss (assuming adiabatic flow).

$$\frac{A^*}{A_{Inlet}} = \frac{M^{\frac{\gamma}{\gamma-1}-1} \left[\frac{\gamma+1}{\gamma-1} \right]^{\frac{\gamma+1}{\gamma-1}} \left[1 + \frac{\gamma-1}{2} \right]^{\frac{-(\gamma+1)}{2(\gamma-1)}}}{\left[\frac{2}{\gamma+1} + M^2 \right]^{\frac{\gamma}{\gamma-1}} \left[\frac{2\gamma}{\gamma-1} M^2 - 1 \right]^{\frac{1}{\gamma-1}} \left[1 + \frac{\gamma-1}{2} M^2 \right]^{\frac{\gamma+1}{2(\gamma-1)}}} \quad (4.4)$$

The inverse of this equation is known as Hermann's swallowing function[74] and is plotted in figure 4.3. This equation illustrates the minimum area ratio between the inlet and the throat of the duct for which self-starting is possible. Also shown in figure 4.3 is the isentropic compression limit. There are three areas of interest in this graph: the area above the Kantrowitz limit where inlet starting is possible, the area between the two limits where a started inlet can exist but an unstarted inlet will not start, and the area below the isentropic compression limit where an inlet will be unstarted.

The relevance of the above information is that although the baseline tunnel has already been shown to start, the inclusion of a cavity geometry will modify the tunnel flow field. The shear layer above a cavity is likely to be considerably thicker than the undisturbed boundary layer. As such it is possible that the shear layer may move the wind tunnel from the region of figure 4.3 where the intake is started to the region where the intake is unstarted.

The paragraph above highlights the importance of this chapter to the research as a whole. There is no well documented analytic/empirical model available to predict the shear layer growth/thickness for a compressible cavity flow even though there have been significant experimental studies carried out in recent years (Beresh et al.[75]). As a result, this chapter will examine what scale of cavity is suitable and allows starting for this facility.

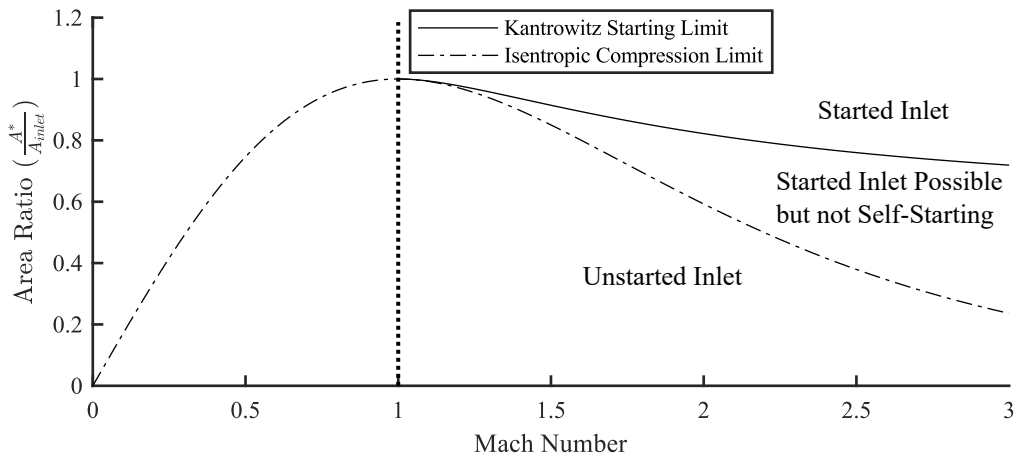


FIGURE 4.3: Hermann's swallowing function

4.2 INITIAL CAVITY WIND TUNNEL MODEL

The first section of this work was the design of appropriate cavity models. The aim was to investigate the interaction between the cavity model and the supersonic duct flow in the wind tunnel. The significant interest is how the cavity will affect the starting of the wind tunnel, as this is analogous to an intake starting. It is clear from previous work[75] that in general the cavity shear layer thickness will increase with cavity length, at least for a cavity operating in the open flow regime. This will be the key variable examined in this chapter, how the scale of the cavity relative to the duct has an impact on the duct starting characteristics. This will cover the impact of cavity length, depth and L/D and attempt to draw conclusions on what the relationship is between these and the inlet/wind tunnel starting characteristics. Before this can be discussed, the design of the cavity models used is discussed.

4.2.1 DESIGN REQUIREMENTS

Although the primary objective of this chapter is to examine the impact of a cavity on inlet startup, it is important that the cavity is designed to be suitable for the experiments that follow later. This implies that the cavity, at least the baseline, should be suitable for the flow control experiments that follow. As such, this section will first describe the design choices made for the baseline cavity, there will then be a brief discussion on how this baseline model was "iterated" to produce a number of different models with varying lengths, depths and cavity scale. Cavity scale here refers to the size of the cavity while maintaining the L/D. This is necessary as when the length is changed the depth will be held constant and vice versa, resulting in changing values for L/D. Therefore it was decided to run tests with the L/D held constant, but with length and depth reducing proportionally.

Section 4.1 provided some background into cavity flows and their control. This background, particularly equation 4.3, and the importance of the outcomes of the studies by Webb et al.[59][69] provide some guidance as to limits/requirements for the cavity model being designed. The first requirement was a limiting factor enforced by the nanosecond high voltage pulse generator. The generator available had a maximum pulse frequency of 3kHz. Given that one of the aims of the work was to use the ns-DBD plasma actuators to enhance/weaken the natural cavity resonance, it was important that the actuators could be operated at the resonant frequency of the cavity (see explanation in section 4.1.3 from previous studies). From equation 4.3 it is clear that cavity length has a significant impact on the expected resonant frequencies of the cavity flow field. As the model had to be designed and manufactured before the wind tunnel redesign was completed, the Mach number of the wind tunnel is assumed to be $M=2$, i.e. the design speed of the wind tunnel. The likelihood is that the Mach number in the wind tunnel will be slightly lower due to viscous effects not entirely accounted for, this is therefore a conservative approach as cavity resonant frequency is directly related to freestream speed. Therefore if freestream speed is lower than the

prediction then so is the cavity frequency, ensuring that the frequency is lower than the predicted frequency. The values of vortex convection velocity ratio, k_c , and empirical constant, a , have been debated in previous literature. k_c has been examined in-depth by Murray et al.[76] by measuring the vortex convection speed in the shear layer using planar laser imaging. They found that the commonly used value of $k_c = 0.57$ was accurate within the range of $1.8 < M_\infty < 2.8$. Therefore for this study that is the value that will be used. The most appropriate value for a is much less clear and understood. For this study the an initial value of $a = 0.25$ was used in the cavity design process as this is a commonly used value in literature[53][54][55][67]. Using equation 4.3 some limits could be set on the cavity dimensions. The cavity depth was set for these initial models as half the tunnel height. The importance of this was that the applicability of this work was eventually to confined flow in supersonic isolator ducts. It was therefore important to relate the cavity dimensions back to the duct in some manner so that future work could be scaled appropriately. Based on this depth, $D = 0.027\text{m}$, the Rossiter mode frequencies were predicted for an L/D range of 5 to 8. Earlier it was mentioned that the range in which an open cavity flow field occurs for the Mach number of interest here is 10. So in order to give some "safety" margin to this work it was decided to limit the maximum cavity L/D to 8 to ensure that an open cavity flow field was achieved. Table 4.1 shows the predicted Rossiter mode frequencies for the cavity lengths that give $5 \leq L/D \leq 8$ for the cavity depth used. Due to the maximum achievable actuator control frequency of 3kHz, forcing the actuator at the 4th Rossiter mode was unlikely to be achievable. However the first 3 predicted Rossiter modes are achievable for all of the cavities except for the length of 0.135m. It was therefore decided for the initial cavity models that lengths of 0.162m, 0.189m and 0.216m, and L/D of 6, 7 and 8 were to be used. Based on these predictions the first 3 Rossiter mode frequencies were achievable by the ns-DBD plasma actuators.

This requirement was the only fluid dynamic requirement on the model, the remaining requirements/restrictions were based on practicalities. The first was that the model material had to be a non-conducting material. This was necessary to house the ns-DBD plasma actuators. The material used was Sika block M960, a polyurethane plastic. This was chosen for a number of reasons:

- The material is non-conductive, the primary factor in its choice.
- It was readily available within the University, important as cost was a factor in the decision.
- Both the preferred external model manufacturer within the aerospace division and the University's own workshop had extensive experience milling this material. This was important to ensure that there were no issues during the manufacturing of the model.

The next requirement was that the model should be modular in order to test various lengths, depths and cavity scales desired. The model was to replace the tunnel

Cavity Length (m)	Mode Number			
	1	2	3	4
0.135	867	2022	3178	4333
0.162	722	1685	2648	3611
0.189	619	1444	2270	3095
0.216	542	1264	1986	2708

TABLE 4.1: Predicted Rossiter Modes for Cavities of Various Lengths

floor and it was important that the various cavity geometries could be interchanged without having to remove the entire tunnel floor. On this basis the model was split into three parts: upstream test section floor, downstream test section floor and the cavity insert itself. This ensured that the tunnel test section had a rigid frame while also ensuring that cavity geometries could be interchanged with minimal effort, an important factor to minimise wind tunnel downtime. The main requirement in terms of flow diagnostics was the location of accessible pressure ports. The interest in the pressure measurements was in the frequency content of the pressure signal in the cavity. It was shown in previous work that measuring the static pressure on the floor of the cavity was an effective method to do this.[8] In this work three locations along the floor of the cavity were used, however through carrying out the research it was found that the frequency content of the signals were the same in all three locations.[8] As such, for this work a single pressure port was used in the centre of the cavity floor. The cavity model was designed such that the transducer was threaded directly into the cavity insert with only a 2mm long, 1mm diameter tap between the face of the transducer and the cavity surface. Pressure taps would have been installed on the trailing edge of the model had space allowed, however due to the small scale of the wind tunnel facility there was not enough physical space to flush mount a transducer. Due to the high frequencies expected, there was no reason to include a pressure port with any significant length of tubing (5-10cm) on this face as the high frequencies would likely be filtered out. This is not a significant issue because, as made clear by Zhuang et al.[65], the Rossiter mode resonance is a global cavity instability. In their research it was shown that the resonant tones occur at the same frequency regardless of location.

4.2.2 END RESULT OF DESIGN PROCESS FOR BASELINE CAVITY

With the combination of the requirement defined above and the practicalities such as ensuring access for tightening bolts, manufacturing restrictions etc. the final design of the initial baseline cavity model was completed. Figure 4.4 shows a 3D view of the final design installed in the wind tunnel. Some of the key components of the wind tunnel have been highlighted to better differentiate between components. The orange components form the nozzle, the components highlighted in red form the diffuser, the green component is the upper wall of the wind tunnel (this remains the same between the baseline wind tunnel and the tunnel with cavity installed), the blue components

form the upstream and downstream test section floor, and the yellow component is the module inserted for the baseline cavity.

4.2.3 CAVITY MODEL VARIATIONS

The key objective here is to examine the impact of cavities with various lengths, depths and cavity scale to examine the impact on intake starting characteristics. The baseline model explained above served as the base to which all of the other cavities were mounted. It was decided that the baseline cavity was to be the largest cavity investigated as there was no benefit to increasing the size (with regard to the approximated resonant frequency limit discussed above).

Four data points were selected for each parameter (length, depth and cavity scale) in order to give a sufficient number of data points while avoiding too many different test cases to be run, i.e. the baseline cavity size and three other data points. In order to achieve a suitable distribution of data points the remaining three points were scaled based on the baseline cavity. The factors used were $\frac{3}{4}$, $\frac{1}{2}$ and $\frac{1}{4}$. Figures 4.5 and 4.6 illustrate this variation graphically.

To achieve the desired cavity geometries, blocks were mounted within the original cavity insert (shown in figure 4.4). An illustration of this is shown in figure 4.7 where the component highlighted in purple is an example of one such block, in particular this setup results in a cavity 162mm in length, 20.25mm in depth and $\frac{L}{D} = 8$.

After the blocks were sized and designed to provide the various cavity test cases it was concluded that for this set of experiments pressure measurements would not be recorded; and only Schlieren imaging would be used. The reason was that, as mentioned above, the pressure measurements need to be taken with a flush mounted transducer to ensure there is no low-pass filtering of the signal as a result of the tubing between the pressure port and the transducer surface. However with the constantly changing cavity length and depth this was not practical without manufacturing a new cavity insert model for each case (the yellow component in figure 4.4). The resulting cost of this was too high and the benefits did not outweigh this as the pressure measurements did not add significant research value. The aim of this chapter is primarily to provide input to chapter 6 regarding which cavity sizes are feasible to use for investigating cavity flow control. This will be done by examining what size of cavity will allow the wind tunnel to start. Schlieren measurements are sufficient since these will allow the starting behaviour of the tunnel to be investigated. The secondary aim was to examine the impact of cavities on intake starting characteristics. For this, the interaction between the cavity shear layer and the starting shock train is the key phenomenon to be examined. Again, this can be accomplished by examining Schlieren imaging of the flow field, pressure spectra from within the cavity will add little to this investigation. Clearly for the cavity flow control research (chapter 6), pressure measurements will be necessary.

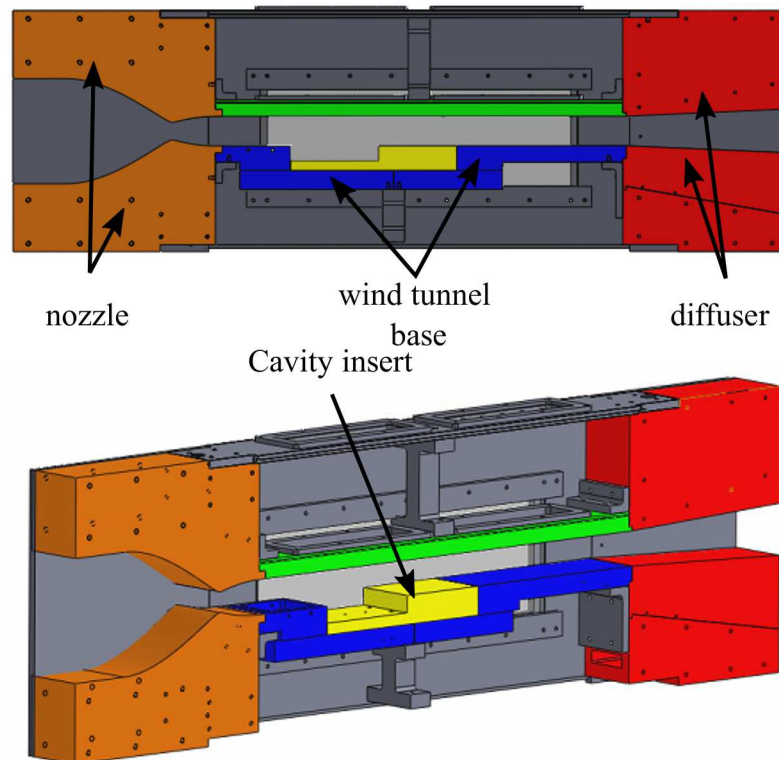


FIGURE 4.4: Cross-sectional view of baseline cavity model located in wind tunnel (top) and orthographic projection of wind tunnel with cavity model installed (bottom)

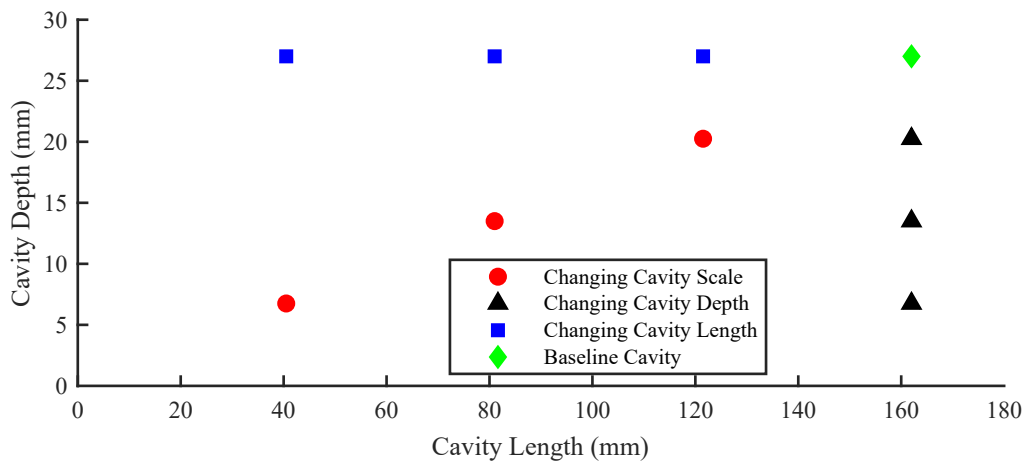


FIGURE 4.5: Graphical representation of the cavity geometries tested

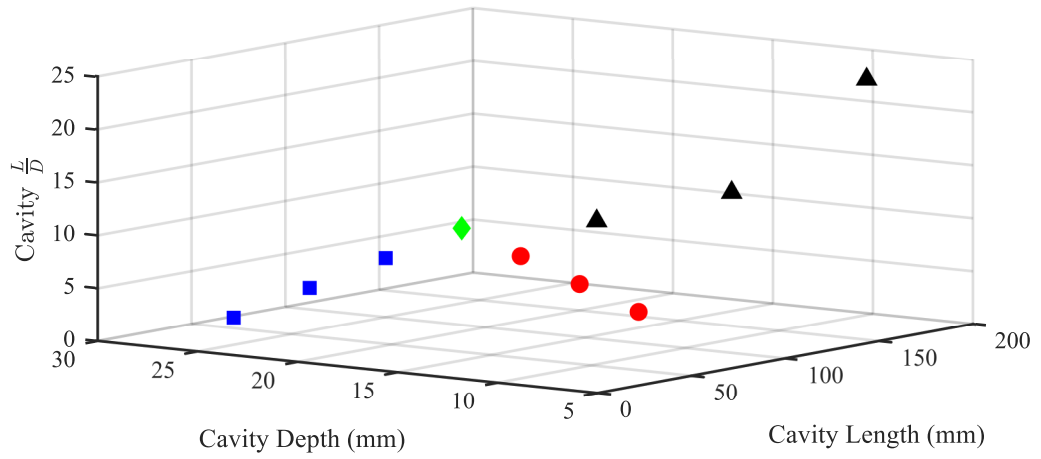


FIGURE 4.6: Graphical representation of the cavity geometries tested

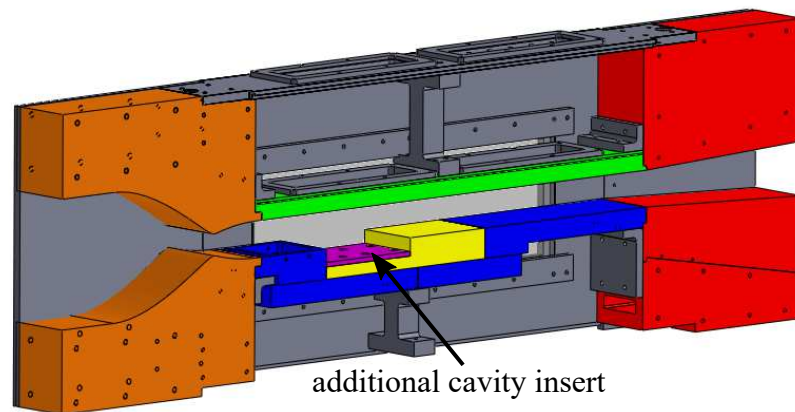


FIGURE 4.7: 3D model view of cavity installed in the wind tunnel with the modular block included for the case with the cavity geometry set to 162mm in length, 20.25mm in depth and $\frac{L}{D} = 8$

Now that the cavity models, both baseline and variation from baseline, have been explained, the results from the tests run with these can now be presented and analysed.

4.3 SCHLIEREN VISUALISATION

The key outcome of this chapter is to classify the range of cavities into two groups: those that allow the tunnel/intake to start and those which do not. The more complicated task is arriving at a conclusion as to why the cavities that allow the tunnel/intake to start do so and vice versa for those which do not. The Schlieren images presented, figures 4.8, 4.9 and 4.10, illustrate the various stages observed as the tunnel start up shock system travels downstream. This is assumed to be similar to how an intake shock train system would interact with a cavity.

Some of the features observed apply to all three sets of images. The white line at the top of the duct in each image highlights the edge of the duct. The time presented below each image, ΔT is the difference in time between image (a) of the set and the image in question. The absolute time is not presented as the Schlieren was not being synchronised with the wind tunnel valve and so did not start recording at the same instant, but at some arbitrary time before the wind tunnel valve opens. The first set of images, figure 4.8, is that with a cavity 81mm in length and 13.5mm in depth ($L/D = 6$). Figures 4.8a and 4.8b show the weak shock waves that are highlighted by arrow 1. As the tunnel starting shock system continues to move downstream the strong "normal" shock comes into view of the Schlieren imaging setup in figure 4.8c. Arrow sets 2 and 3, in figures 4.8c and 4.8d, highlight the triple point, common in the interaction of a normal shock with a boundary layer. As the system moves further in figures 4.8e and 4.8f it can be observed that the oblique separation shock becomes "fixed" at the cavity leading edge, the commonly expected flow feature at a cavity leading edge in supersonic flow. The separation on the upper surface continues to move downstream with the centre normal shock. However as a result of this the normal shock disappears due to the discrepancy in streamwise location of the two oblique separation shocks. This is highlighted by arrows 4 and 5 where there is no longer a visible normal shock and instead the two oblique shocks simply interact with one another. As the shock system moves further downstream and out of view this interaction point moves further away from the centreline and towards the upper surface of the duct. One interesting feature that is believed to be the driving factor behind the ability of the tunnel to start with a cavity installed is the movement of the shear layer. This can be highlighted by closer examination of figure 4.8f, the last image with the shock system in the Schlieren field of view, and figure 4.8h, an image recorded after the shock system has passed and the cavity flow has become much steadier. The red dotted lines drawn on top of each image is an estimate of the shear layer deflection angle from horizontal, determined through careful examination of the image. The angles of these lines are 8.58° and 3.36° for figures 4.8f and 4.8h

respectively. This would suggest that the cavity shear layer protrudes further into the centre of the duct the further downstream it travels.

The next set of Schlieren images, figure 4.9, shows similar features. This cavity is 40.5mm long and 27mm deep ($L/D = 1.5$); due to the shorter physical length it was possible to capture the flow field over the entire span of the cavity. As with figure 4.8, the first two images (a and b) show the initial weak shock waves that travel downstream prior to the strong, normal shock. Arrow set 2 highlights again the triple points where the oblique separation shocks and normal shock meets near the centre of the duct in figure 4.9c. In figure 4.9d the arrow highlights the movement of the shear layer towards the duct centreline as the leading oblique shock begins to travel across the cavity. Arrow 3 in image e shows again how the interaction point of the shock waves moves towards the upper surface of the wind tunnel as the upper separation shock moves downstream while the lower shock is “fixed” at the cavity leading edge. Arrow set 4 in figures 4.9e and 4.9f shows how, while the shock structure is over the cavity, the shear layer maintains an upwards trajectory (figure 4.9e); but when the shock structure moves past the cavity the shear layer angle begins to decrease. Figure 4.9g and arrow 5 show how as the shock structure moves even further downstream, the location of the upper separation shock moves far enough downstream that the lower separation shock at the cavity leading edge impinges at the same location. The usual reattachment shock also appears in this image at the trailing edge of the cavity as would be expected for this type of flow field. After this point in time there is no more evidence of a clear separation shock on the upper surface but just a reflected shock from the lower surface. Shown in figure 4.9h and arrow 6, is the same structure as observed in the steady state, final image of figure 4.8. Here the shear layer is very close to horizontal and shows very little intrusion into the central duct flow.

The comparison of these two sets of images suggests that the shear layer response to the starting shock system is the same. However the larger cavity will result in a greater maximum shear layer deflection as the shear layer has further to travel downstream before it meets the trailing edge. Although an interesting set of images, these do not necessarily help explain, at least in isolation, why some cavities do not allow the tunnel to start. Figure 4.10 presents a series of images from one of the test cases that does not allow the starting shock to travel down the tunnel, resulting in unstart of the wind tunnel. It is clear from examining these images that the shock does not travel past the cavity as it did with the other two cases shown. What is difficult to capture by viewing just a series of images is the oscillations experienced by the shock wave. Figure 4.11 illustrates the position of central normal part of the shock structure over a period of 0.14s. The shock position was tracked using an in-house MATLAB script. The script extracted horizontal intensity profiles from the Schlieren images over the approximate centre 20 pixels (10 above the centreline and 10 below) of the normal shock across the streamwise length of the image. It is only the approximate centre as it is specified by the user manually. An average of these profiles was taken and the maximum

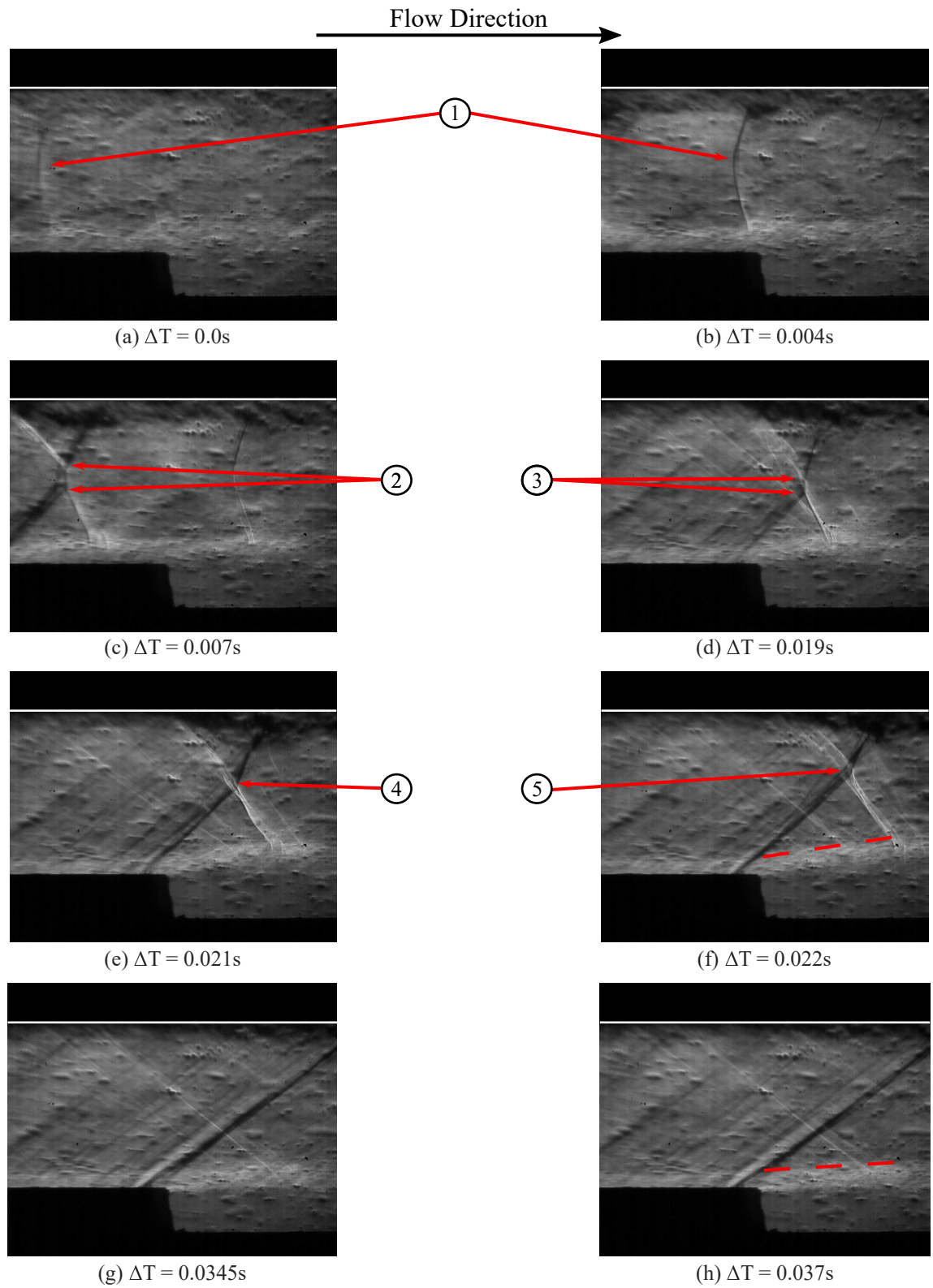


FIGURE 4.8: Series of Schlieren images at various stages in the indraft supersonic wind tunnel start up process (81mm long, 13.5mm deep cavity)

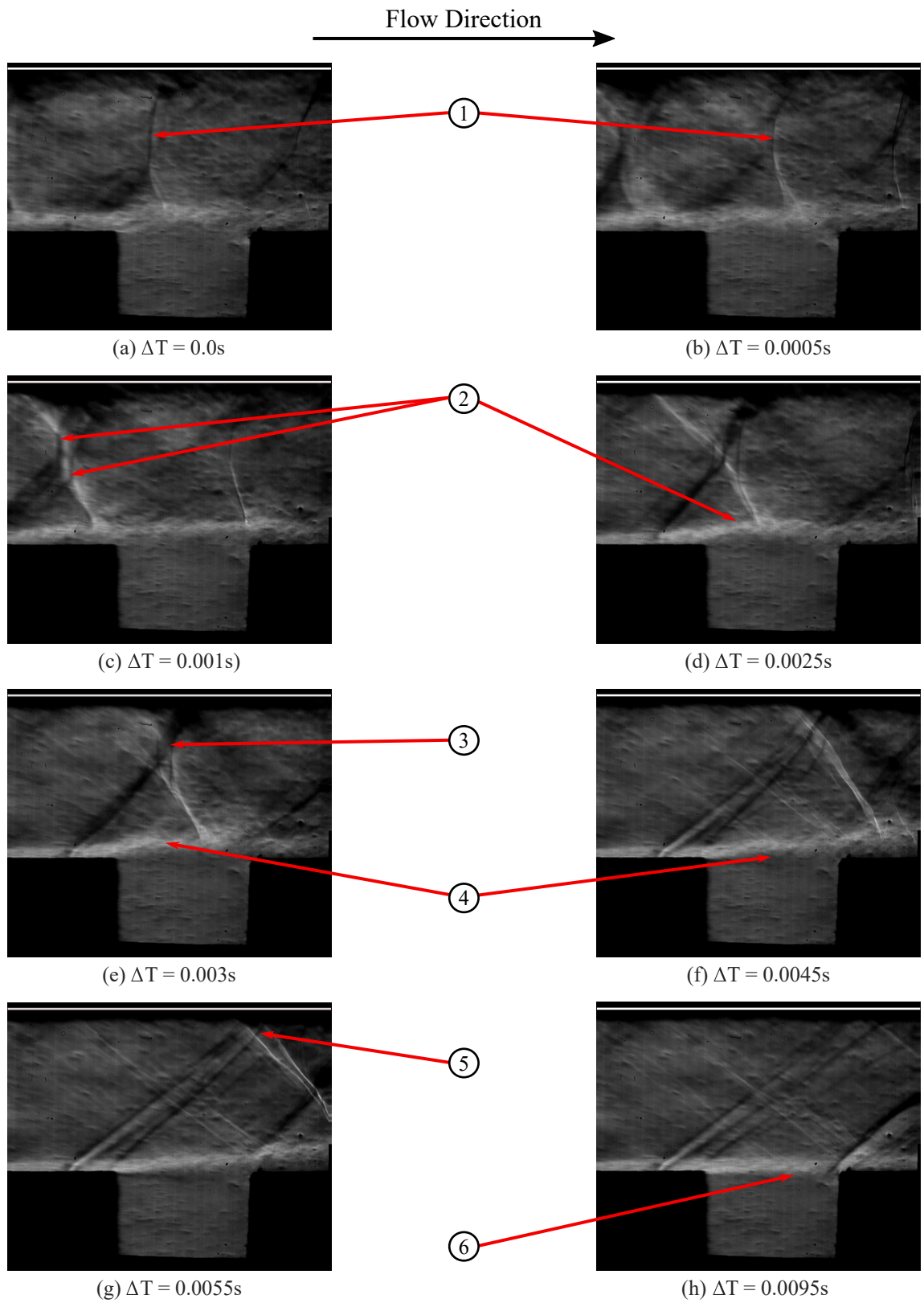


FIGURE 4.9: Series of Schlieren images at various stages in the indraft supersonic wind tunnel start up process (40.5mm long, 27mm deep cavity)

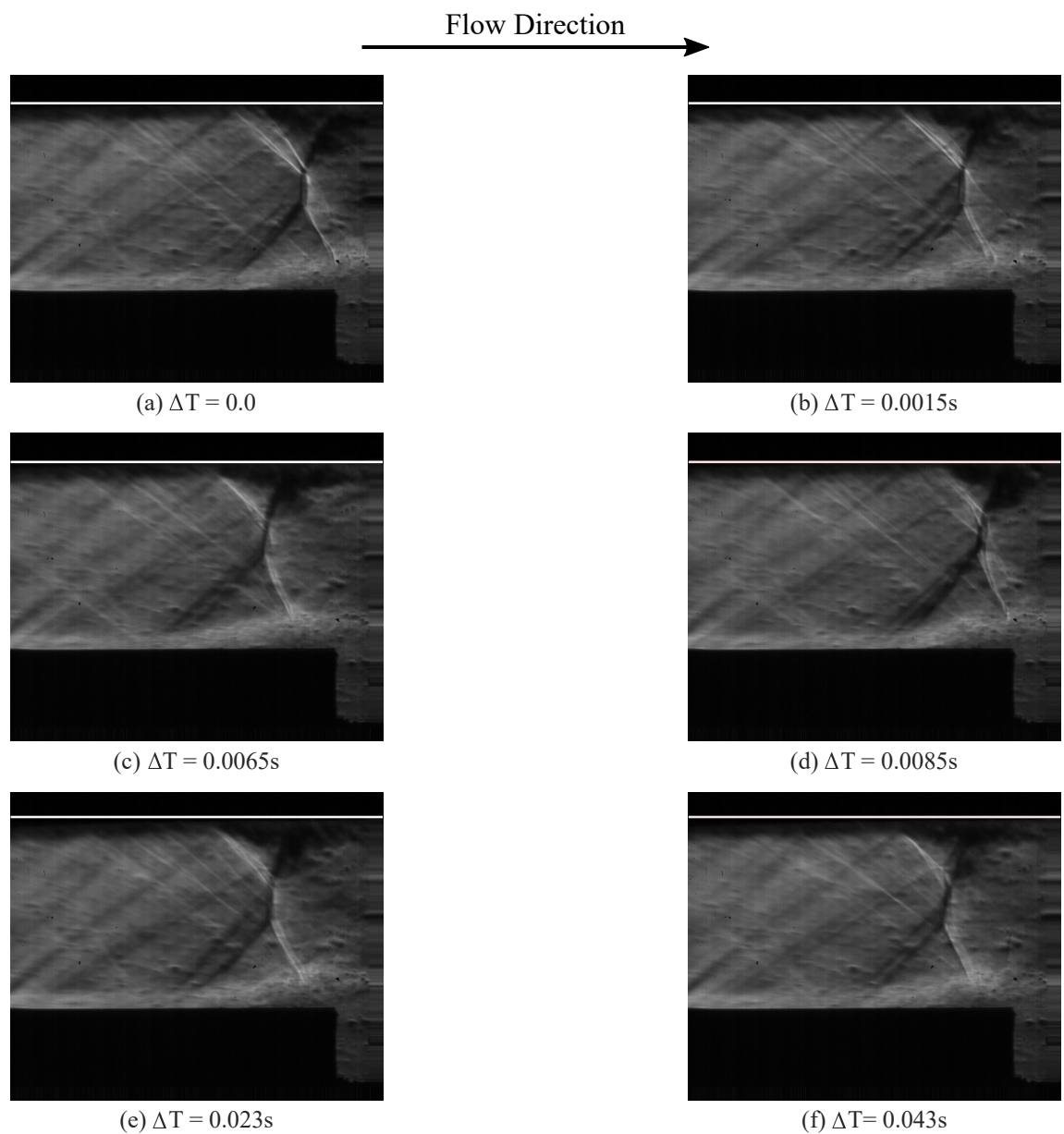


FIGURE 4.10: Series of Schlieren images showing the starting shock obstructed by the cavity shear layer/ shock-induced separation (121.5mm long and 20.25mm deep)

difference between two neighbouring pixels was calculated. By examining one of the images presented in figure 4.10, it is clear that the point with the biggest difference in neighbouring pixels intensity lies at the centre of the normal shock wave. Therefore this location was recorded and the information presented in figure 4.11. The pixel calibration was done using the known distance between the upper and lower surfaces of the wind tunnel to give a value of 0.1mm/pixel. The data presented illustrates the oscillation and also that the shock train oscillates around, broadly speaking, the same location. This is also clear in the image snapshots shown in figure 4.10, as in all of these images the normal shock appears to be in approximately the same location. An interesting comparison can be made when the images of figure 4.10 are compared with image (c) in figure 4.9 and figure 4.8. In the former two cases, where the tunnel starts successfully, the boundary layer separation observed appears to be noticeably smaller than that observed in the images in figure 4.10.

There could be a number of reasons for the increased boundary layer thickness but it is thought that it is likely to be a result of a greater adverse pressure gradient experienced in this case relative to the previous two. If this is the case, it is likely a result of an increased shear layer deflection into the central duct flow in comparison to those previous cases. The cause of this is not entirely clear.

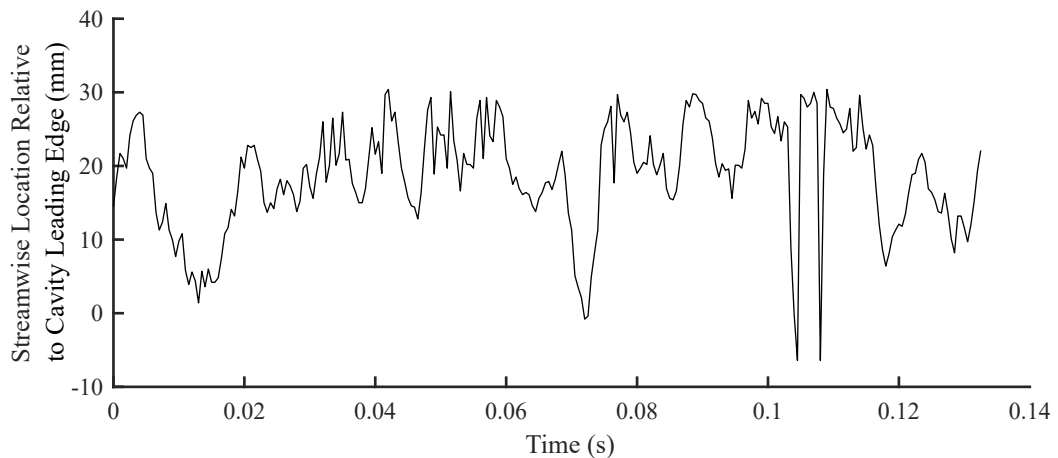


FIGURE 4.11: Illustration of unsteady start up shock location for unstarted wind tunnel/intake

4.4 CONCLUSIONS

There were two main aims of this chapter, to investigate the effect that the introduction of a cavity has on a supersonic duct flow and to attempt to classify the scale of cavity that will still allow a duct to start correctly.

Figure 4.12 illustrates the general trend in the results achieved, in terms of whether or not a cavity installed in the wind tunnel will allow it to start or if it will result in unstart. The blue areas are where the tunnel is observed to start and the red areas are where the tunnel is unstarted. The black points plotted are the actual data

points tested during this study. This is only an approximation but it does allow a clearer picture to be presented regarding what areas of the cavity geometry domain are viable for use within the wind tunnel/intake. The main conclusion that can be made here is that both cavity length and depth play a role in affecting the shear layer thickness/deflection into the core flow area (suggested to be the driving factor behind start/unstart with the cavity installed in the wind tunnel). It is also suggested here that, for open cavities, the starting behaviour of the tunnel may be more sensitive to cavity length than depth. This theory is suggested as there is an example of the deepest cavity used allowing the tunnel to start while this is not the case with the longest cavity. The longest cavity used does allow the tunnel to run but only once the depth has been reduced enough that the cavity flowfield is transitional/closed rather than an open cavity. None of the test cases with the cavity geometry at its longest (162mm) allowed the tunnel to start while still displaying an open cavity flowfield.

Regarding future work, a number of experiments could be carried out in order to provide more insight into this phenomenon. First, a wider range of cavities should be tested in order to fill out the "blanks" in figure 4.12. This would help to define a better boundary regarding what cavities could be used in the wind tunnel; this could possibly lead to some form of relationship between cavity length, depth, L/D or some combination of the three and some physical duct characteristic such as height. It would also be interesting to examine some form of quantitative data such as PIV to try and shed more light on the fluid features resulting from the interaction between the cavity and the starting shock waves. This may also help explain any empirical relationship that has been developed based on the previous suggestion. These avenues were not explored in this work as this chapter was not the primary focus of this research but instead a necessary prerequisite in order to conduct the following research. For this research, all that was required was to determine a limiting cavity case as an input for the design of the cavity geometries to be studied in more detail in chapter 6. How this fed into the design of these future cavity geometries will be discussed in chapter 6.

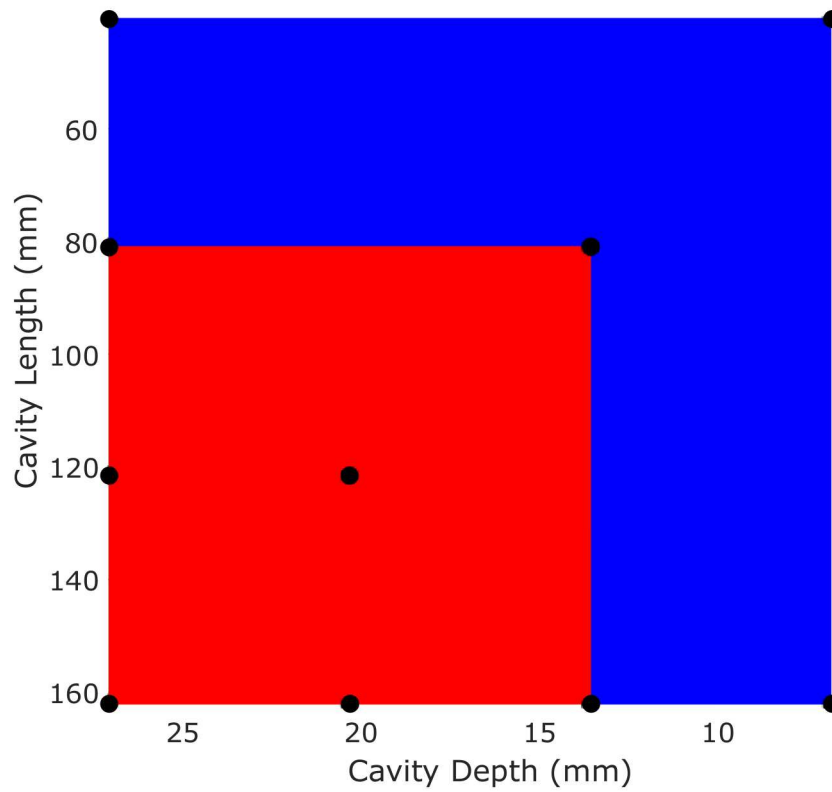


FIGURE 4.12: Visualisation of cavity classification where blue indicates a cavity that allows the intake to start and red indicates a cavity that unstarts the intake. The only points that are test data are the black circles overlaid on the colour plot. Points on the edge of red/blue indicate cavities where both an unstarted and a started intake were observed in different tests. This is simply a result of the unsteadiness of this interaction.

CHAPTER 5

CHARACTERISATION OF DIELECTRIC BARRIER DISCHARGE PLASMA ACTUATORS

The key goal of this work is to examine how/if energy deposition flow control could be used to improve ramjet performance. One proposal is to use surface plasma based flow control to influence the acoustic resonance modes in open cavity flows. For this work, the addition of a cavity to a ramjet is considered as it has been shown to help delay the onset of unstart. One drawback however due to the introduction of a cavity into a ramjet isolator is an increase in overall drag. Therefore it is proposed that plasma actuators could be used to reduce this negative consequence of adding a cavity to a ramjet design. However before this can be tested, the plasma actuators must be characterised.

There are multiple approaches when considering surface based plasma actuators: localised arc filament plasma actuators, dielectric barrier discharge (DBD) plasma actuators (nanosecond pulse and AC driven), DC driven plasma discharge, and pulsed plasma synthetic jets to name but a few. The current work focuses on the use of DBD plasma actuators, therefore the other actuator types mentioned will not be discussed in any detail. However if the reader is interested in more information on the other actuator types, Russell et al.[77] present an in-depth review of a variety of energy deposition flow control methods.

This chapter will focus on the characterisation of DBD plasma actuators using various experimental techniques: Schlieren, infrared thermography, high voltage electrical measurements and finally quantitative, calibrated Schlieren. The first three techniques are used to examine how different parameters describing the actuator construction can have an impact on the electrical efficiency of the actuator i.e. how much of the supplied electrical energy is converted into useful work and how much is wasted. The basic Schlieren technique will also be used in order to decide on the actuator most likely to be effective for the flow control application to the cavity flows being examined. Quantitative Schlieren will provide more insight into the fundamental

thermal behaviour of the actuators. As it will become clear in the background information to follow, DBD plasma actuator's flow control authority (particularly those driven by nanosecond pulses) is a result of thermal mechanisms. It is therefore thought to be important to gain as much understanding of the thermal perturbations created as possible.

5.1 DIELECTRIC BARRIER DISCHARGE (DBD) PLASMA ACTUATORS

Dielectric barrier discharge (DBD) plasma actuators create plasma based on a phenomenon called the dielectric barrier discharge effect that was first recorded by Ernsnt Werner Von Siemens in 1857 [78]. The dielectric barrier discharge phenomenon occurs due to the ionisation of molecules in the air as a result of the high voltages applied between the high voltage and ground electrode. For an AC driven plasma, electrons travel from the high voltage electrode and the surface of the dielectric barrier for the positive half of the AC cycle. For the other half of the cycle the electrons come from the dielectric surface and travel from there to the electrode. These electrons travel in so-called filaments (also known as streamers) that have a lifetime limited by the capacitance of the actuator[79]. This lifetime is limited since, as electrons build up on the surface of the actuator the electric field strength decreases until a point where no further discharges occur until the polarity of the electrode changes from positive to negative or vice versa. This self-termination is the reason behind the plasma being considered non-thermal as it means the plasma filaments do not overheat [80]. When the streamer collapses, although electrons no longer travel along it, there is still residual energy present in the same location. This is known as the microdischarge remnant and the phenomenon is the reason why distinct plasma filaments are visible in this kind of discharge. The residual energy results in repeated ionisation of the gas at these locations due to the reduced energy levels needed for ionisation. This ionisation and plasma creation impacts the surrounding flow as a result of the ionic wind generated. Ionic wind was a phenomenon first discovered by Hauksbee in 1709 but first explained in any detail by Faraday in 1838[81]. The phenomenon is fundamentally the result of particles ionised by the high voltage signal, colliding with and imparting momentum onto neutral gas particles.

In general, DBD plasma actuators have a very simple construction, shown in figure 5.1. The actuator consists of two electrodes, an anode and a cathode, separated by a dielectric material to form the dielectric barrier. There have been studies examining variations of this basic design and how these could impact the performance of the actuators. One example is the use of multiple ground electrodes as presented by Erfani et al. [82]. They showed how variations in depth of the ground electrodes within the dielectric material resulted in variations in plasma ignition time and the induced velcoties generated by the actuators. Another example is the serpentine actuator concept introduced by Riherd and Roy[83] where instead of straight electrodes, curved electrodes (serpentine in shape) were suggested. They illustrated that this change

in shape allowed the actuators to excite a wider range of flow phenomenon than a standard linear actuator.

Significant research has been carried out into the use of DBD plasma actuators for low speed flow control. An in-depth review of these and other types of surface plasma actuators is presented by Moreau[81]. However for this work, the application is at much higher velocities and there are limits to what can be achieved by AC driven plasma actuators at these speeds.

AC-DBD's are limited in their performance by the ion charge density in the region of the actuator. Macheret et al.[84] provide an interesting quantification of the relative strength of the electrohydrodynamic (EHD) effects responsible for the created ionic wind. Equation 5.1 comes from relating fluid momentum and the electrostatic force:

$$Z_{EHD} = \frac{en_+\Delta\phi}{\rho U_\infty^2} \quad (5.1)$$

where e is the electron charge, n_+ is the density of positive ions, $\Delta\phi$ is the voltage drop in charge region, ρ is density and U_∞ is flow speed. Z_{EHD} is the ratio of electrostatic effects to the fluid momentum and Macheret et al.[84] suggest that these two properties should be approximately equal i.e. $Z_{EHD} \approx 1$ in order for an actuator to exert a significant flow control effect. They suggest that a maximum flow speed of 72m/s is the limit at which this requirement is no longer met. This would suggest that AC-DBD's have very limited use at higher velocities. The author believes this to be somewhat misleading as the actuators fundamentally generate an ionic wind in the vicinity of the boundary layer. In this region, even in high speed flows, the gas velocity is significantly lower than the freestream. As such, this suggestion of 72m/s may be used to describe the flow velocity in the region of operation of the plasma actuator but should not be used as a measure of the freestream speeds at which these actuators can effectively be used. However this work will focus on a variety of DBD plasma actuators that have shown more promise in being used effectively for flow control at supersonic speeds, nanosecond (ns) pulse driven DBD plasma actuators.

5.1.1 NANOSECOND DIELECTRIC BARRIER DISCHARGE (NS-DBD) PLASMA ACTUATORS

ns-DBD plasma actuators are similar to AC-DBD actuators in that they create plasma using the same fundamental principle, dielectric barrier discharge, and they share the same actuator geometry as shown previously in figure 5.1. The difference is that ns-DBD plasma actuators are driven with very short duration pulses (tens of nanoseconds at most) in comparison to the essentially constant voltage supply (usually with sinusoidally varying polarity) that is used to drive the AC-DBD plasma actuators.

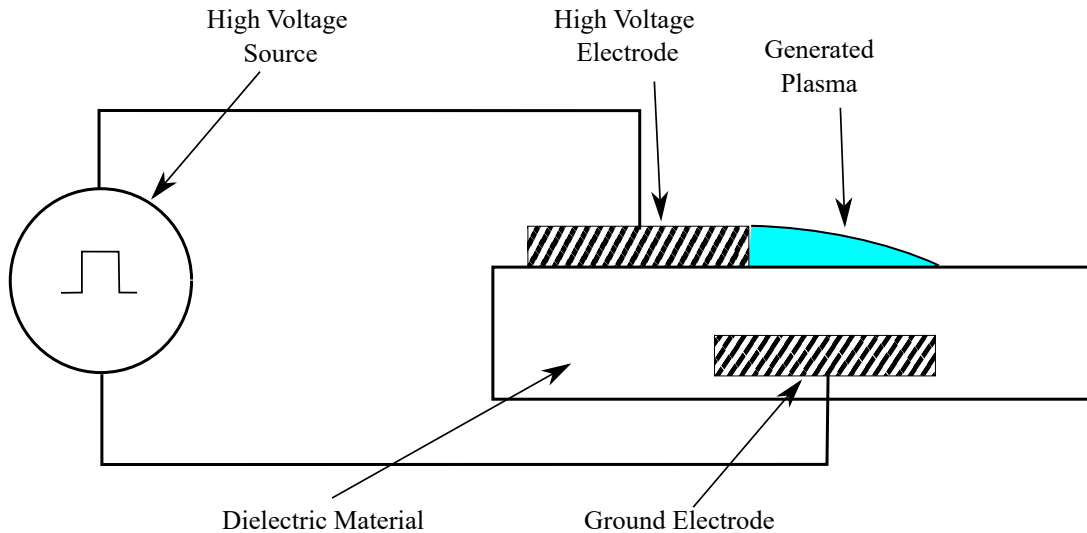


FIGURE 5.1: General diagram of a DBD plasma actuator

One of the first published papers on using nanosecond voltage pulses to drive DBD plasma actuators was presented by Likhanskii et al. [85]. The suggestion was made that DBD actuator operation could be improved by using a pulsed voltage supply with megahertz repetitions. This suggestion was based on the fundamental mechanism explained above of how electrons travel from the electrode to the dielectric surface and that highly repetitive forcing frequencies would ensure that electrons on the dielectric surface were replenished quickly. This theory was tested in a later work by Opaitis et al. [86] who used nanosecond high voltage pulses combined with a sinusoidal voltage signal. Their study demonstrated the effectiveness of using this type of driving signal to create plasma. However, the first study to show a true understanding of how nanosecond pulse generated plasma can exert flow control was by Roupassov et al. [87]. Through the use of smoke visualisation it was demonstrated that ns-DBD plasma actuators produced practically zero induced velocity. Through further investigation, the study showed that the nanosecond pulses created pressure waves as a result of rapid gas heating. The fundamental physics of how this occurs was presented by Popov. [88] where the mechanism of the rapid heating of air in gas discharges (plasma generation) is examined. It was explained how the high voltage excites nitrogen molecules to a higher discrete energy level (Bohr[89] explains these energy levels). These excited nitrogen molecules then react with oxygen molecules in the air (oxygen quenching) and release heat energy in the process. At the same time atomic oxygen is formed and reacts with oxygen molecules in the air to create ozone (a popular use of DBD plasma actuators outwith the field of aeronautics). This rapid heating and the associated pressure rise occurs in such a small period that it is less than the acoustic timescale. Therefore, this sudden pressure rise results in the pressure waves observed by Roupassov et al. [87]. This phenomenon was investigated further by Takahisma et al. [2] in order to achieve a better understanding of the plasma characteristics that contribute to the pressure wave formation. It was shown that the pressure waves observed by Roupassov et al. [87] were actually a combination of many individual

waves, one for each of the plasma filaments. The imaging presented in the work of Roupasov et al. [87] looked along the length of the actuator and so could not capture this distinction. Figure 5.2 illustrates these waves, one for each plasma filament as the Schlieren view point is across the actuator not along it.

ACTUATOR CHARACTERISATION

Actuator characterisation is a topic of great interest since improving the effectiveness of these actuators is key for their implementation to a wide variety of applications. Characterisation can generally be split into two areas: electrical and geometric. Electrical characterisation refers to the voltage supply itself and the examination of how various electrical parameters can affect the performance of the actuators. The geometric parameters in question are of the actuator itself e.g. actuator length, dielectric thickness, gap between electrodes etc.

First, focusing on the electrical characteristics, Benard et al.[90] present a study examining how the polarity of the input pulse could impact the performance. This is not of great interest for this study as the equipment available is only capable of producing positive polarity pulses. Their study suggested that positive polarity pulses resulted in a plasma dominated by filaments in comparison to the more diffuse plasma produced by negative pulses. Positive polarity pulses were found to produce stronger pressure waves and also that positive pulses tended to be more efficient. However Dawson et al. [91] disagree with the last statement and suggests that negative pulses deposit more energy into the gas (and are therefore more efficient for the same energy input). Therefore this is still an area that is open for debate. Takashima[92] provided an examination on the impact of pulse frequency showing that increasing the pulse frequency leads to a more filamentary plasma. This would seem sensible as the earlier description of the discharge process suggested that plasma filaments tend to form in the same location due to the residual energy remaining in the air when a filament is extinguished. If the time between pulses is reduced, as frequency increases, then it would seem sensible that the residual energy in these channels should have less time to dissipate. The result being that filaments would likely occur in the same

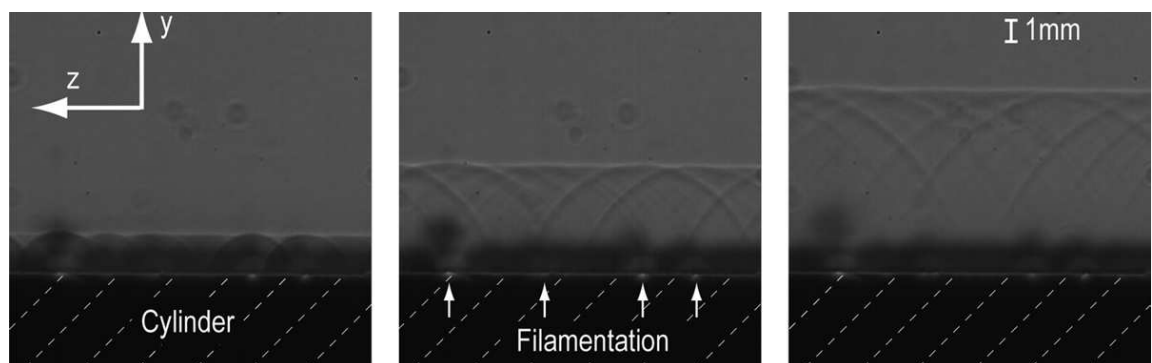


FIGURE 5.2: Schlieren imaging across a plasma actuator illustrating that each plasma filament creates a pressure wave[2]

location more often and thus the plasma would appear to exhibit more obvious plasma filaments.

Pulse width was another parameter investigated by Benard et al.[90] Using nanosecond voltage pulses, a pressure wave forms from each edge of the pulse, both the rising and falling edge. This was illustrated by Benard et al.[90] as, when the pulse width was large enough that the time between the rising and falling edge was larger than the acoustic time scale, two pressure waves were visible from one voltage pulse. However, when the pulse width was shorter than the acoustic time scale, both the current spikes (one for each edge) and the rapid heating associated with each one of them contributed to a single pressure wave. This “double pulsing” of the actuator is an interesting phenomenon that could, depending on the application area, prove useful in allowing multiple frequency components to be excited simultaneously from one actuator.

The impact of altering the geometric parameters has also been examined in great depth. Aba’a Ndong et al.[93] presented an interesting study into some of these parameters. In particular, the focus was examining the impact of actuator length and the gap between electrodes. Measurements of current were used to illustrate that as the actuator length increased, the current was found to decrease. This result was confirmed by Dawson et al.[94] and the impact on pressure wave strength, a decrease in strength was confirmed. This again, seems logical, since spreading the same quantity of energy across a longer distance would reduce the energy at any one location and thus reduce the overall pressure wave strength. Research into the impact of changing the gap between electrodes provided some insightful results. As the gap was increased two distinct current peaks became clear. Aba’a Ndong et al.[93] suggested that this was the capacitive current (resulting from the change in voltage) and the discharge current (present when the plasma ignites and the electrons begin to “flow” from the electrode to the dielectric). Separating the electrodes further has the effect of decreasing the local electric field strength and thus the ignition is delayed in comparison to when the electrodes are closer together. This is the reason why the two distinct current sources are not visible in the cases with no electrode gap. However there was no clear trend presented in the relationship between electrode gap and current amplitude (and thus energy deposited and pressure wave strength) so this is a possible avenue for exploration of future studies.

One of the goals of this chapter is to quantify the electrical conversion efficiency of the actuators. This refers to the relationship between electrical energy supplied and the useful thermal energy added to the gas. There have been some preliminary studies carried out in this area, the work of Avallone et al.[26] and Van den Broeke et al.[95] being the most significant. These studies have provided useful insight into methods that can be used to quantify this efficiency. However, other than dielectric thickness, there has been no significant effort to examine how other geometric properties such as actuator length, electrode widths and electrode gap impact the actuator efficiency. This is the area that part of this chapter will investigate.

5.2 QUANTITATIVE SCHLIEREN EXPERIMENTAL TECHNIQUE

The temperature profile resulting from the plasma discharge of the actuators is investigated in this chapter. These actuators' operation, when driven by ns voltage pulses, is highly related to the heat addition into the gas (the cause of the pressure waves). As such it is thought to be important to gain a better understanding of the temperature changes experienced as a result of the actuators' operation. One way in which this can be done is through the use of the quantitative Schlieren technique. As will be shown from the results obtained from this technique, this could potentially be used to examine the actuators' efficiency in converting electrical to thermal energy.

Schlieren is widely thought of as a qualitative technique. However, since the variation in intensity of a Schlieren image is a result of refractive index changes in the flow field which in turn are a result of density changes in the flow field, it is a reasonable suggestion that this information could be extracted. This suggestion was first made by Schmidt and then Schardin in the 1930's/1940's [3]. It was not until the early 2000's that the technique gathered any significant interest, largely as a result of improved computing power and resources.

Hargather et al. [3] present a detailed comparison of a number of quantitative Schlieren techniques: calibrated Schlieren, background oriented Schlieren (BOS) and "rainbow Schlieren". It was found that both calibrated and BOS were capable of producing results to a similar level of accuracy. "Rainbow Schlieren" was found to give no significant benefit when compared to calibrated Schlieren but had significantly more difficulties regarding setup. Likewise it was found that BOS was very sensitive to setup with very little margin for error. As a result of these conclusions, calibrated Schlieren was the technique chosen for the present study.

5.2.1 CALIBRATED SCHLIEREN

Calibrated Schlieren uses a very similar setup to conventional Schlieren for the recording of data. In comparison to the conventional setup shown in figure 2.1, the significant change to the setup is the replacement of the knife-edge with a graded filter. The reason for the replacement of the knife-edge with a graded filter is to increase the range over which light refraction angles can be measured [3]. The knife-edge produces a more sensitive image (shown by the larger maximum gradient in figure 5.3c compared to the graded filter) but the graded filter has a larger measurement range (shown by the longer distance from the lens center where the intensity varies). The result of this comparison is that the graded-filter allows measurement of the refraction angle of the light over a much larger area but with a greater uncertainty. This is acceptable as the knife edge would allow such a narrow field of measurements as to be an impractical choice.

From a fundamental point of view, equation 5.2 represents the relationship between

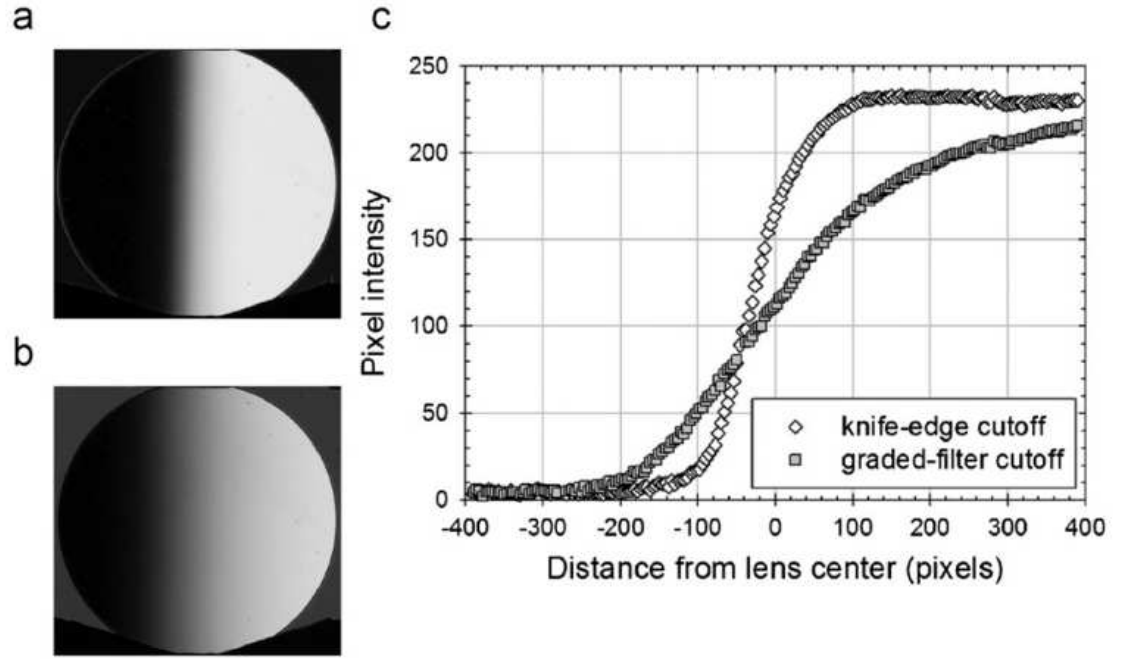


FIGURE 5.3: Comparison of range and sensitivity for a knife-edge cutoff and a graded filter cutoff[3]. The recorded Schlieren images show the image intensity across a knife edge in image (a) and the graded filter in image (b). Image (c) plots the variation in pixel intensity across the lens for each of images (a) and (b).

the angle of refraction and the refractive index gradient, integrated in the z -direction, in both the x and y axis:

$$\begin{aligned}\epsilon_y &= \frac{1}{n} \int_0^z \frac{\partial n(x, y)}{\partial y} dz = \frac{z}{n_\infty} \frac{\partial n(x, y)}{\partial y} \\ \epsilon_x &= \frac{1}{n} \int_0^z \frac{\partial n(x, y)}{\partial x} dz = \frac{z}{n_\infty} \frac{\partial n(x, y)}{\partial x}\end{aligned}\quad (5.2)$$

where ϵ is the refraction angle, n is the refractive index and subscript ∞ represents the surrounding, quiescent gas. The x axis is along the discharge, y is the vertical direction and z is along the electrode (optical axis). For the above relationship to be useful, a method of obtaining refraction angle based on the image intensity has to be obtained. This can be done by using a source that provides a known light refraction angle, a lens. The refraction angle resulting from the light passing through the lens can be calculated based on the focal length, f , and an arbitrary radius on the lens surface, r , as shown by equation 5.3[3]:

$$\epsilon \approx \tan \epsilon = \frac{r}{f}\quad (5.3)$$

It is important to use a physically small lens with a long focal length for good quality calibrated Schlieren. This is for two reasons: this combination leads to $r \ll f$ which is important for the small angle assumption made in equation 5.3 and it also leads

to being able to ignore uncertainties due to aberration as a result of the distance between the focal plane of the lens and the camera lens. A plano-convex lens (CVI Laser Optics, model: PLCX-25.4-5151.0-C, focal length: 10 m, outer radius: 12.7mm, surface accuracy: $\frac{\lambda}{10}$) was used as a calibration lens/graded filter.

In order to calibrate the images a Schlieren image was recorded of the calibration lens. From this image an intensity profile was extracted across the diameter of the lens. At each location along the profile, the image intensity was plotted against the calculated refraction angle. The refraction angle was recorded relative to the centre point of the lens. This results in equation 5.4 being used to calculate the refraction angle at each location:

$$\epsilon_{image} = \epsilon - \epsilon_0 = \frac{1}{f}(r - r_0) \quad (5.4)$$

where the subscript 0 refers to the centre of the lens. Figure 5.4(a) shows a Schlieren image containing the calibration lens and all of the extra points plotted along with the cubic polynomial calibration fit generated (figure 5.4(b)). The result is a calibration that allows the conversion of image pixel intensity to refraction angle from the range of -1.2312×10^{-3} to 0.9742×10^{-3} radians.

Once the calibration is complete the calibration lens is removed from the frame and the images are recorded. As illustrated by equation 5.4, the image of the actuator in operation is subtracted from a reference image to obtain the difference in intensity. From this and the calibration curve shown in figure 5.4 the refraction angle can be calculated. To ensure repeatability an ensemble average refraction angle was calculated across three different tests. This refraction angle can then be used to solve for local refractive index by differentiating equations 5.2 and combining them to give

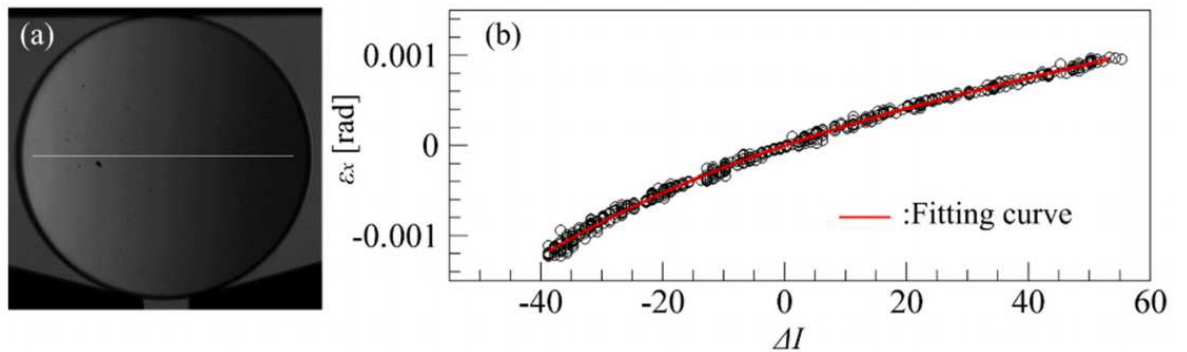


FIGURE 5.4: Schlieren image showing the variation in intensity across the calibration lens and the calibration fit between intensity and refraction angle generated from the image[4]

equation 5.5:

$$\frac{\partial^2 n(x, y)}{\partial x^2} + \frac{\partial^2 n(x, y)}{\partial y^2} = \frac{n_\infty}{z} \left(\frac{\partial \hat{\epsilon}_x(x, y)}{\partial x} + \frac{\partial \hat{\epsilon}_y(x, y)}{\partial y} \right) \quad (5.5)$$

This is an elliptic (as the roots of the equation would be imaginary) partial differential equation for refractive index, in the commonly used form known as the Poisson equation. In this case, the equation was solved using the Successive Over Relaxation Method. The solution of equation 5.5 is the local refractive index which can then be converted to local density using the Gladstone-Dale law, equation 5.6:

$$n = k \cdot \rho + 1 \quad (5.6)$$

where k is the Gladstone-Dale constant for air.

ERRORS OF CALIBRATED SCHLIEREN

There are a couple of error sources associated with the manner in which this technique has been applied here: error associated with the curve fitting for the calibration curve and the error related to how the centre of the calibration lens was defined. With regard to the polynomial fit used for the calibration curve; it is clear that the fit is a good one purely from examination of figure 5.4(b). However the error associated with the fit cannot be ignored, no matter how small it may seem. The standard root mean square error for a curve fitting is shown in equation 5.7:

$$\sigma = \sqrt{\frac{\sum_{i=1}^N (f(x_i) - y_i)^2}{N}} \quad (5.7)$$

Now if this is applied to the current problem, the equation becomes:

$$\sigma_{cal,y} = \sqrt{\frac{\sum_{i=1}^N (\epsilon_{exp,y}(\Delta I)_i - \epsilon_{fit,y}(\Delta I)_i)^2}{N}} \quad (5.8)$$

$$\sigma_{cal,x} = \sqrt{\frac{\sum_{i=1}^N (\epsilon_{exp,x}(\Delta I)_i - \epsilon_{fit,x}(\Delta I)_i)^2}{N}}$$

where N is the number of samples recorded along the intensity profile extracted, and subscript *exp* and *fit* are the experimental and the calibration fit refraction angle values respectively.

Regarding the lens centre error, the lens centre is taken as the point on the profile where the image intensity matches that of the background intensity. The background light

intensity is clearly not constant throughout the image and so there is the possibility of the centre being inaccurate. This error is formed by the product of two components: the sensitivity of refraction angle to changes in lens centre (i.e. the partial derivative of refraction angle relative to lens centre) and the standard deviation in refraction angle based on the standard deviation in the background intensity. Equation 5.9 presents the error calculation containing the contribution from both the lens centre uncertainty and the curve fitting uncertainty:

$$\begin{aligned}\sigma_{\epsilon,y} &= \sqrt{(\sigma_{cal,y})^2 + \left[\left(\frac{\partial \epsilon_{image,y}}{\partial r_{0,y}} \right) \cdot \sigma_{r0} \right]^2} \\ \sigma_{\epsilon,x} &= \sqrt{(\sigma_{cal,x})^2 + \left[\left(\frac{\partial \epsilon_{image,x}}{\partial r_{0,x}} \right) \cdot \sigma_{r0} \right]^2}\end{aligned}\tag{5.9}$$

5.3 MANUFACTURING AND DESIGN OF ACTUATORS

The manufacturing of the actuators is a key component in the reliability of the results. A common technique when making DBD plasma actuators for testing is to use copper and Kapton (or similar polyimide material) adhesive tapes on a non-conductive material such as a plastic of some sort to make the actuator. The issue with this sort of construction is both the accuracy and repeatability of the actuators created. It is not a simple process to accurately cut these tapes to identical lengths and then locate them in the same position relative to one another, multiple times in a row. This, based on the author's experience, would be necessary as through the process of testing the actuators some are likely to malfunction or breakdown through use. Therefore it was decided for this study to use a more reliable method for creating the actuators. In this case it was decided to use photolithography to create the actuators.

5.3.1 PHOTOLITHOGRAPHY

Photolithography has been used since the 1800's, however the process was developed into a useful tool in the 1950's when it was further developed and patented by US military [96]. The basic principle is that a copper clad board is coated (usually applied by the manufacturer) with a UV resistant material. This material is then rendered soluble where desired through exposure to UV light. The soluble material is then removed leaving only the desired copper remaining on the board.

5.3.2 APPLICATION OF PHOTOLITHOGRAPHY TO DBD ACTUATORS

In this case the board used was FR4 where the FR stands for flame retardant. The material, which will be used as the dielectric in this case, is composed of several layers of glass fibre epoxy laminate. The board is coated in $35\mu m$ of copper on both sides with a positive UV resist pre-applied. In order to isolate the regions of copper that were to remain, the high voltage and ground electrodes, masks were created that would protect these regions from UV light when the board is exposed. This results in

the UV resists remaining insoluble and the copper remaining on the board in these areas during the development stage.

These masks were created in solidworks, CAD software, in order to ensure the accuracy of the printed masks. Clearly this will limit the accuracy of the lengths used to the accuracy of the printer used, however there is still an improvement in the reliability and reproducibility of the actuators measurements as the same mask will be used for all actuators of the same geometry.

The mask was then secured, front and back, to the copper clad board and exposed to UV light for 30 seconds. The board is then placed in a developer bath; this solution dissolves the resist that was made soluble through exposure to the UV light. The copper exposed by this resist removal is then dissolved by spraying the board with a ferric chloride solution. It takes approximately 1 minute for the copper to be removed (per side). Following this, the UV resist remaining on the board is removed with acetone solution.

The end result is a copper clad board with copper remaining only for the high voltage and ground electrodes. This process can be used to create any number of actuators with the exact same dimensions and locations. An example of a board produced using this method is shown in figure 5.5.

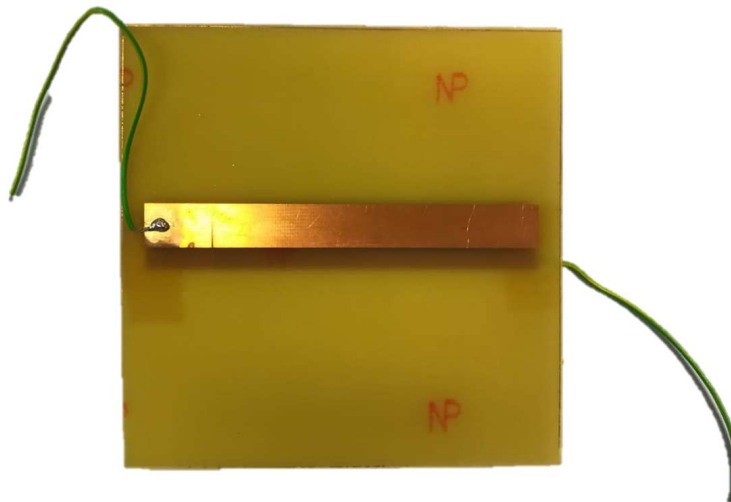


FIGURE 5.5: An example of a DBD actuator created using photolithography.

5.4 ACTUATOR PARAMETERS TO BE INVESTIGATED

For this study, table 5.1 presents the parameters investigated and the various values of each parameter that were used. As each parameter is varied the rest remain consistent to the baseline actuator, the parameters of which are highlighted in bold in the aforementioned table. This covers all of the relevant geometric parameters describing these DBD plasma actuators. The range of values used was due to a number of reasons. For dielectric thickness the limit was the availability of material, since only certain

thicknesses, namely those presented, were available for use. In terms of electrode length, the limit was again manufacturing related. The photolithography facilities were limited in the maximum length that could be created. For the remaining parameters, a wide range of values were used that would hopefully provide useful data to make conclusions whilst not creating a large number of cases to be tested.

Actuator Geometric Parameter	Values Used (mm)
Electrode Lateral Separation	0.5, 0, 1, 2, 3, 4
Ground Electrode Thickness	5, 10, 15, 20, 30, 40
High Voltage Electrode Thickness	2, 5, 10, 20
Electrode Length	60, 75, 90, 120, 135, 150
Dielectric Thickness	0.4, 0.8, 1.6

TABLE 5.1: Summary of geometric actuator parameters varied

5.5 CHARACTERISATION OF NS-DBD ACTUATORS

5.5.1 TEST CONDITIONS

All of the characterisation tests that follow were conducted under the same conditions. Standard atmospheric conditions were present i.e. sea level temperature and pressure and the characterisation was done in stagnant air. The voltage applied was maintained at 12kV, based on that being the minimum supply voltage available from the high voltage pulse generator. The lowest possible voltage was used in order to minimise deterioration of the actuators being tested. The pulse frequency was maintained at 1kHz. The frequency was not varied as a parameter during the actuator characterisation as the focus was on geometric parameters and also due to the flow field dictating the frequencies used during the flow control experiments i.e. it was not an independent variable.

5.5.2 QUALITATIVE SCHLIEREN IMAGING

The first set of tests carried out for the characterisation process was conventional Schlieren. This was used to examine the pressure waves generated by the plasma actuators. This allows the measurement of the wave speed and strength. This method was used successfully by Dawson et al.[94]. The method relies on the same principle as the calibrated Schlieren discussed earlier; image intensity is dependent on the refractive index which itself is dependent on density. The density behind the pressure wave is an indication of the wave strength and therefore so is the intensity peak behind it. On this basis, the brightest region in the Schlieren will occur directly behind the

pressure wave and so provides both a good indication of its location and strength. This point was extracted by taking an intensity profile along the vertical axis of the plasma actuator (the direction in which the pressure wave travels), centered in the end of the high voltage electrode as this is where the pressure wave is generated from. The maximum intensity along this profile was extracted and its location recorded. In order to achieve a clear image, the pressure wave strength and speed were based on phase averaged images. This was across 40 phases with each phase representing an actuator pulse.

In order to obtain the shock strength, the maximum intensity extracted was normalised by the average background intensity (taken from an image in quiescent air). The wave speed was calculated using the position of the actuator and a calibration image. An example of the intensity profiles at each average image location are shown superimposed in figure 5.6. The averaged Schlieren images have been superimposed on one another to visualise the progression of the pressure waves, this is shown in figure 5.7. Each wave location is associated with an intensity profile from figure 5.6.

The obvious peaks shown in figure 5.6 are the points from which the pressure wave strength is calculated. Figures 5.8, 5.9, 5.10, 5.11 and 5.12 show the variation in wave strength with varying high voltage electrode width, ground electrode width, electrode separation, dielectric thickness, and electrode length, respectively. The first two parameters, high voltage electrode width and ground electrode width shown in figures 5.8 and 5.9, respectively, show no significant trends. There is a clear variation in the pressure wave strength as these parameters are varied but the level of variation is relatively insignificant in comparison to variation observed across the other parameters. Also the variation appears to be random, at least for the sample size available.

The other parameters investigated each demonstrate some interesting results. Examining the electrode separation, the first 4 cases of 0mm, 0.5mm, 1mm and 2mm separation show little variation and there is no discernible trend observed. As the

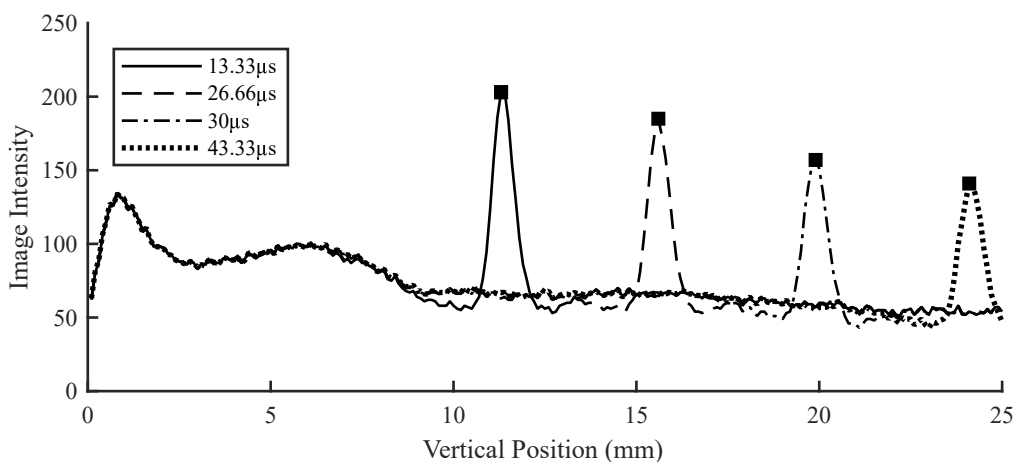


FIGURE 5.6: Intensity profile of phase averaged Schlieren images, one for each phase averaged frame in which the pressure wave is present

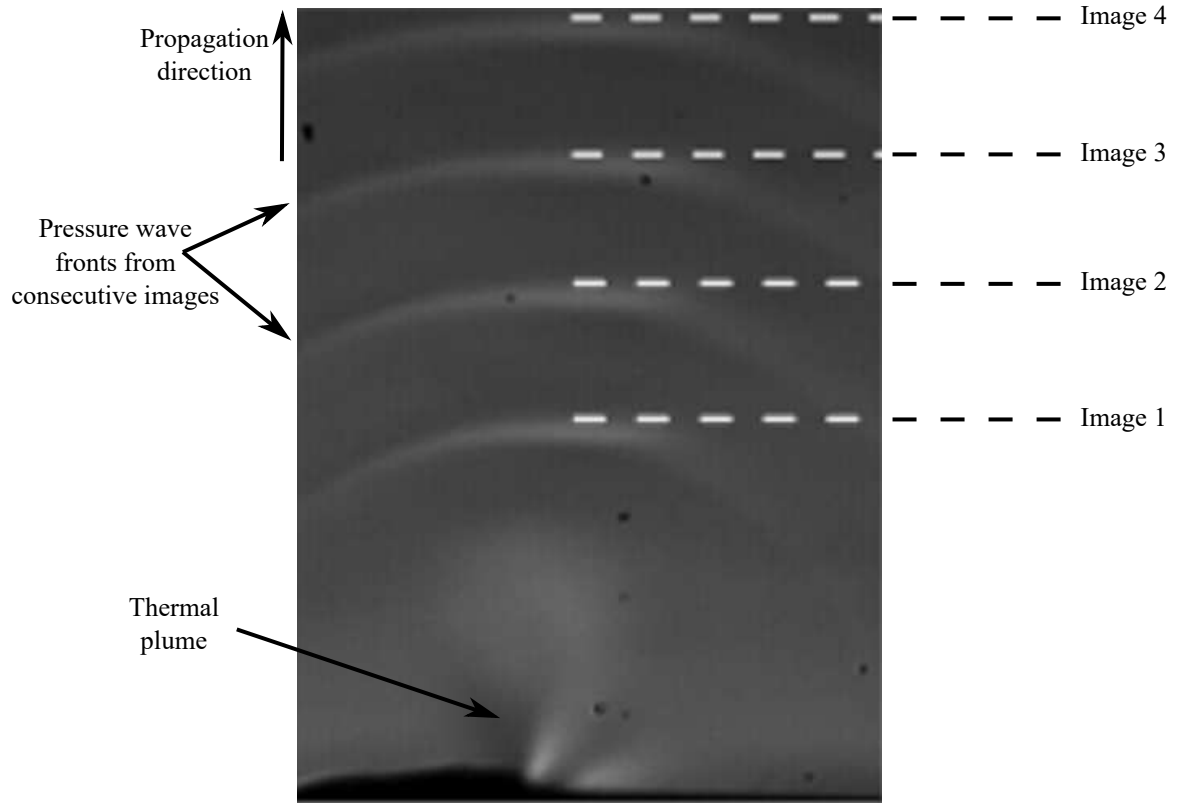


FIGURE 5.7: Combined Schlieren image showing pressure wave propagation away from DBD surface

separation is increased to 3 and 4mm there is a significant change in the pressure wave strength and the decay in the pressure wave strength. The noticeable decrease in strength is thought to be a result of the separation of the capacitive and discharge currents as observed by Aba'a Ndong et al.[93] (see section 5.1.1 for more information). With a larger gap, the electric field strength drops and the ignition of the plasma takes longer in comparison to those with a smaller gap. Due to the short length of the pulses used here ($\approx 10\text{ns}$), it is possible that the length of the voltage pulse available during discharge is significantly shorter than with a smaller electrode gap. This would result in less energy deposited into the flow and thus a weaker pressure wave. The reduction in the decay of the pressure wave strength is likely to be a result of how acoustic waves (will be highlighted shortly that all of these actuators produced acoustic waves) are attenuated through atmospheric absorption. This attenuation is often quoted in a value of Decibels per metre (dBm^{-1}) and is dependent on pressure, temperature and humidity. This value in dB is independent of the acoustic amplitude, the pressure wave strength in this case. Therefore, due to the logarithmic nature of the dB scale, the decay in amplitude of a signal will decrease as the signal decreases in strength. This goes some way to explaining why the decay in the pressure wave strength is lower when the initial wave strength is also lower.

The next interesting result, and most important result of this characterisation, is the variation due to changes in dielectric thickness shown in figure 5.11. This figure shows

significant increase in pressure wave strength as dielectric thickness is decreased. The reason for this result will be explained in more detail when examined alongside the electrical results presented in section 5.5.3.

The final parameter of interest is the change in pressure wave strength due to variation in electrode length, shown in figure 5.12. The first observation regarding this figure is that the pressure wave strength is significantly lower than those of the previous tests. This is a result of the direction in which the Schlieren images were captured relative to the ns-DBD actuators. As was shown in figure 5.2, the pressure wave observed in the Schlieren images taken along the electrode is actually the superposition of a large number of individual pressure waves (one for each plasma filament). This is not an issue when characterising actuators that have the same electrode length; however this becomes a problem when the length is varied, as the superimposed pressure wave observed would include contributions from a larger number of pressure waves for longer electrodes and vice versa for shorter electrodes. This would skew the results in favour of the larger electrodes producing stronger pressure waves even if this was not the case in reality. Therefore for the case where the electrode length is varied, the Schlieren images were recorded in the direction across the electrodes rather than along them. This was not ideal as, in this direction, the observed waves are less distinct in the Schlieren imaging due to only imaging a single pressure wave. However it was still possible to draw some conclusions from the results. Figure 5.12 shows that there is a general trend of decreasing wave strength as the electrode length is increased. This is a logical result as the energy supplied to the actuator is identical regardless of the actuator size. For a longer actuator, with a longer plasma discharge width, the energy is spread across a larger discharge area leading to a less intense discharge. Therefore, for a fixed energy source, the strongest pressure wave will result from the actuator with the smallest electrode length.

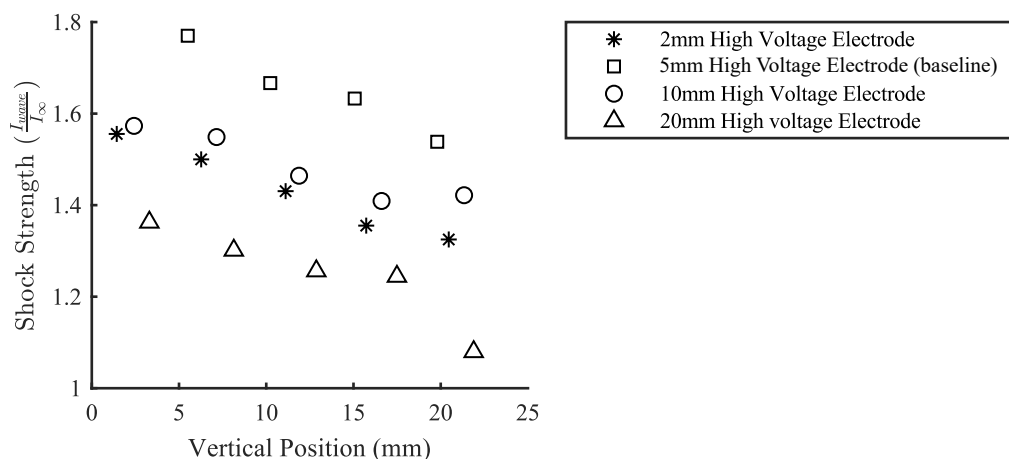


FIGURE 5.8: Variation in pressure wave strength with varying high voltage electrode width.

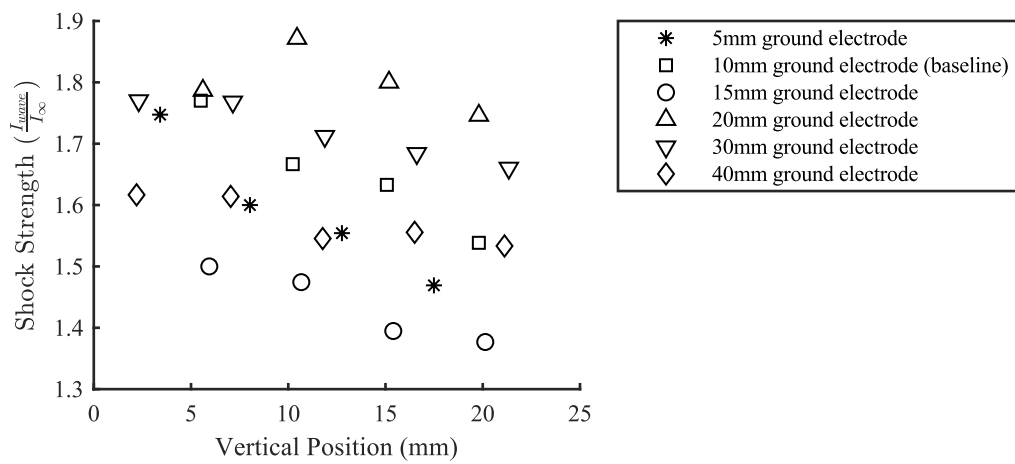


FIGURE 5.9: Variation in pressure wave strength with varying ground width.

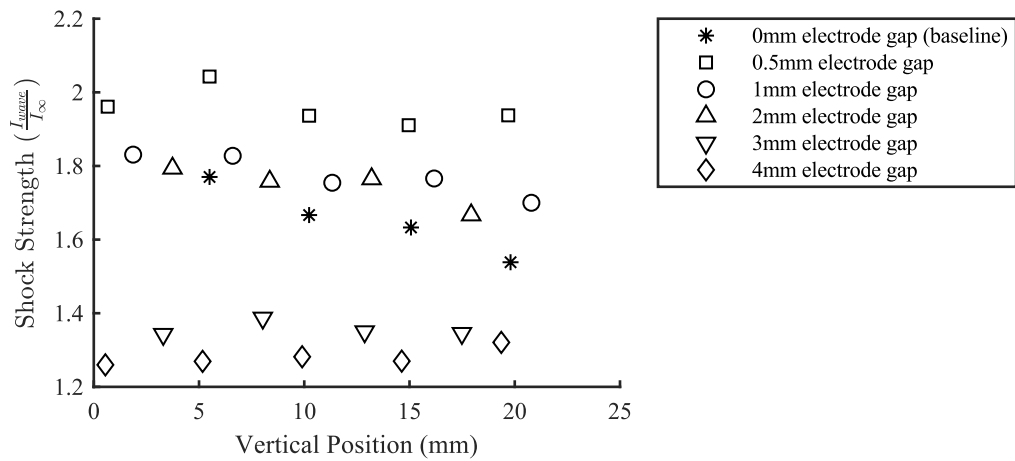


FIGURE 5.10: Variation in pressure wave strength with varying electrode gap.

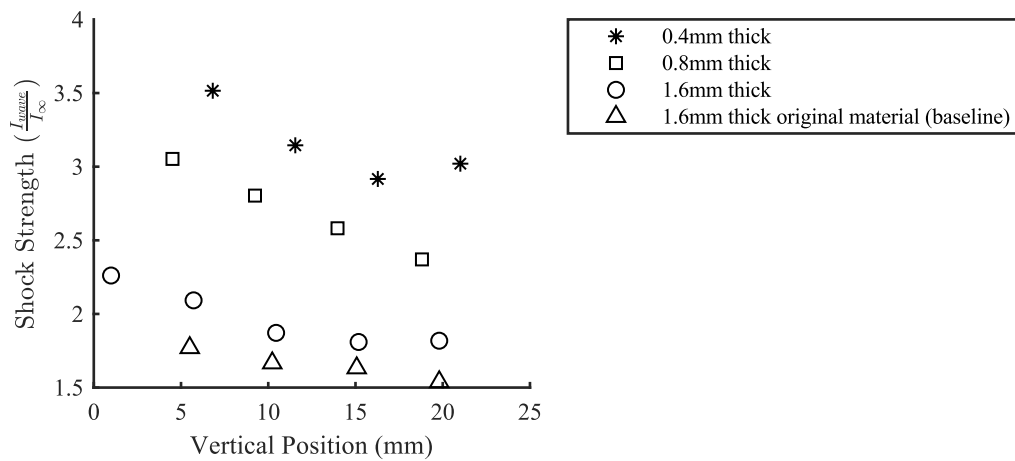


FIGURE 5.11: Variation in pressure wave strength with varying dielectric thickness.

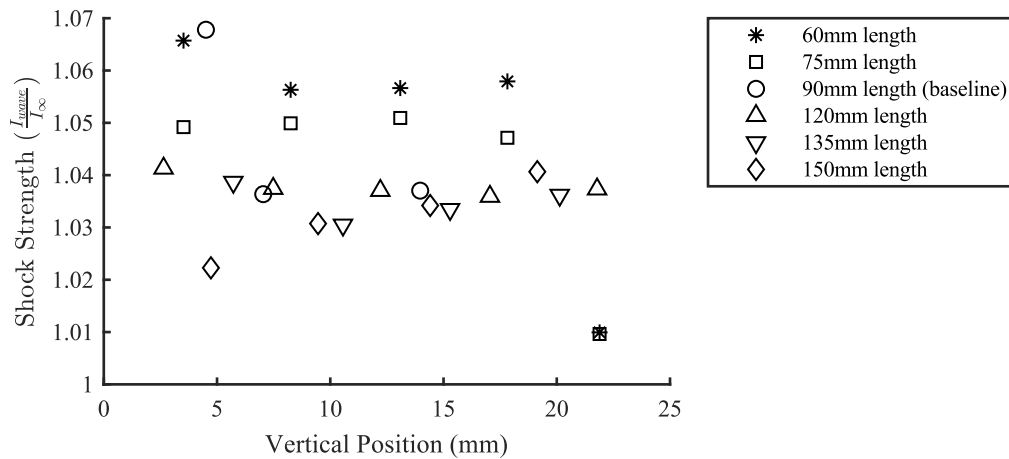


FIGURE 5.12: Variation in pressure wave strength with varying electrode length.

5.5.3 ELECTRICAL MEASUREMENTS

The method by which the electrical measurements were recorded and calibrated was explained previously in section 2.1.4. The focus here is to calculate the electrical energy actually dissipated in the actuator. This is done by measuring the input voltage pulse and also any pulse reflected back by the ns-DBD actuator.

To verify that the current shunt and oscilloscope used were working as expected it was decided to take some measurements with the nanopulse generator connected across a resistor. This removed any unknowns associated with the complex electrical characteristics of a ns-DBD plasma actuator and provided some important results that were used during the analysis of the plasma actuator electrical signals. Figure 5.13 shows a plot of the calibrated voltage signal recorded with the purely resistive load. The first peak shown is the output from the generator, the second peak is due to the resistive load breaking down. In theory all of the supplied voltage should be dissipated across the resistor and there should be no voltage pulse travelling back through the ground of the coaxial cable. However, current “leaks” through the resistor as a result of the high voltage and continues to travel along the ground of the coaxial cable. Although this was unintended, it did allow a useful measurement to be made i.e., the time taken for the initial pulse to travel from the shunt to the load and back again. As highlighted in figure 5.13, the time taken for the pulse to travel from the shunt to the load and back again is 35.3ns. This can be compared to the expected propagation speed of an electrical signal along the coaxial cable. The 75Ω coaxial cable has a velocity of propagation equal to 66% of the speed of light. Combined with the distance between the shunt and the load, which is 3.2m, this leads to $\Delta T = 32.3ns$. Although very similar, the measured and calculated values are not perfectly aligned. However, the calculated value does not account for the distance travelled by the signal across the load or for any uncertainty in the velocity of propagation (no quoted uncertainty available for the coaxial cable). The values however are of similar magnitude and so, for the rest of this work, the measurement is assumed to be accurate. The importance

of this for the actuator measurements will become clear as the measurements recorded across the ns-DBD actuators are examined in the following section.

For each actuator a number of tests were recorded and the average voltage signal was calculated. Figure 5.14 shows three tests for one particular actuator and the resulting average signal. Figure 5.15 shows a close up view of the circled area from figure 5.14. This illustrates that the voltage pulses are near identical, the only difference being a phase difference which is likely a result of the triggering of the oscilloscope used to capture the signals. From this it was concluded that any of the signals could be used since the difference between them is small, however a simple average could not be used due to the phase difference between each signal.

The key difference between the measured voltage across the resistive load in comparison to that measured across the ns-DBD load is the oscillatory signal that follows the initial voltage pulse. This was initially thought to be due to stray inductance from the current shunt device, and it was thought possible to fit a curve to the oscillations and remove them from the voltage signal. The result is shown in figure 5.16 where the blue line represents an attempt to fit an exponentially decaying sine wave to the observed oscillations. As a result it became clear that the oscillations were not a result of any stray inductance in the current shunt but instead a result of reflection from the generator itself.

An important point to remember is the impact that the termination of a coaxial cable can have on the response. If the impedance of load at the receiving end of a coaxial cable is not equal to the impedance of the cable, then some of the voltage pulse will be reflected back in the direction it came from. In this case, this phenomenon occurs when the supplied voltage pulse interacts with the DBD but also when the reflected pulse generated by this interacts with the generator. With this in mind, the ΔT between each of the vertical dotted lines visible in figure 5.16 is equal to the time taken for the pulse to travel between the current shunt and the load and back again, as highlighted previously in figure 5.13. Therefore the oscillatory behaviour is highlighting that the generator is not impedance matched correctly with the coaxial cable, resulting in the voltage pulse being reflected back down the cable towards the DBD. This will happen until the energy dissipates, shown by the approximately exponential decay in the signal amplitude. With this assumption in place, a method is proposed for calculating the electrical energy per pulse that is consumed by the actuator i.e. the difference in the input voltage pulse and the first reflected pulse. From Transmission line theory[97], the energy in a voltage pulse can be calculated using equation 5.10:

$$E_{in} = \int P_{in} dt = \int V_{in} I_{in} dt = \int_{t_1}^{t_2} \frac{V_{in}^2}{Z} dt \quad (5.10)$$

t_1 and t_2 refer to the time at the start and end of the voltage pulse respectively. This

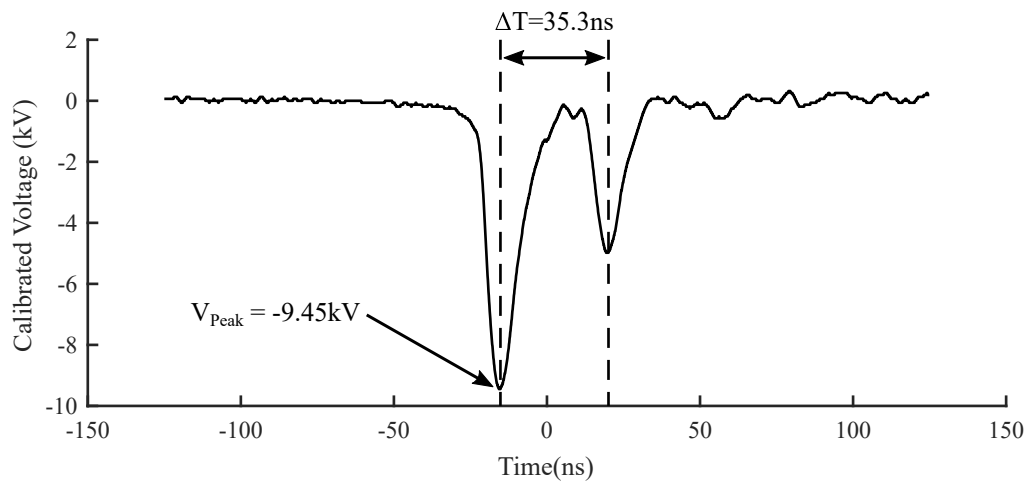


FIGURE 5.13: Calibrated voltage pulse output from nanopulse generator (purely resistive load)

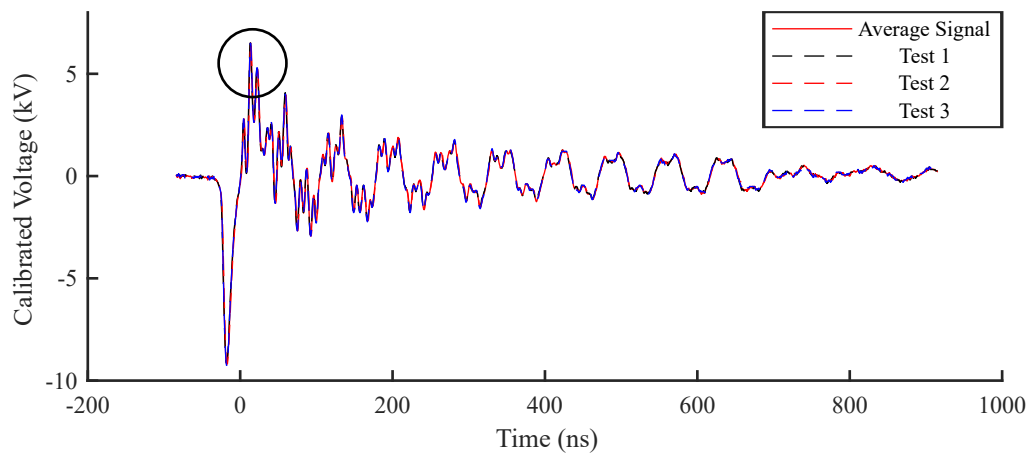


FIGURE 5.14: Comparison of calibrated voltage signals (ns-DBD load)

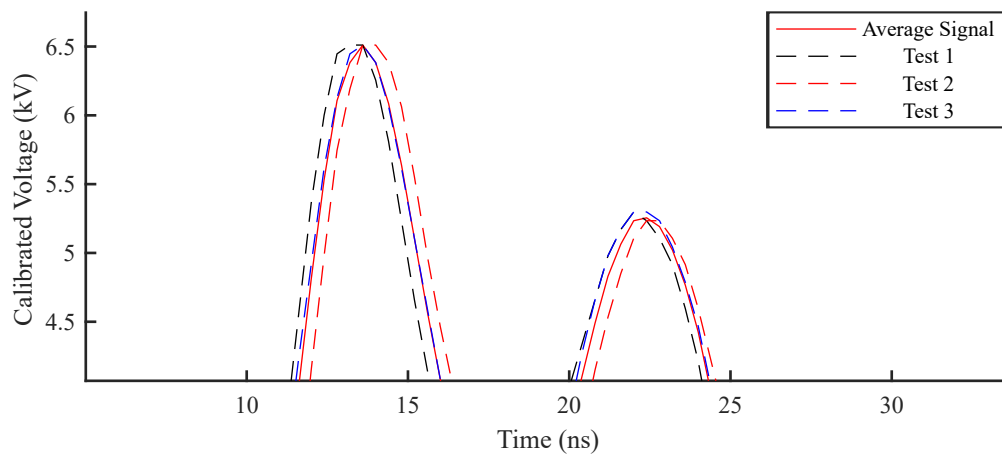


FIGURE 5.15: Close up comparison of calibrated voltage signals (ns-DBD)

integral can be evaluated numerically through trapezoidal integration. Trapezoidal integration involves discretising the area of a graph of interest and calculating the area under the graph between these points by approximating the area under the graph as a trapezoid. However before this can be used, the end of the voltage pulses, both input and reflected, need to be defined. The input pulse has a well defined shape where the beginning and end of the pulse is clear, however this is not the case for the reflected pulse due to the interaction with further reflections. An assumption was made that the reflected pulse could be considered to end where the fitted sine wave, illustrated in figure 5.16, crossed the y-axis. This assumption was made for two reasons: the half period of the sine wave and the voltage pulse width are approximately equal and this method could be applied to voltage pulses consistently across all DBD configurations tested. This was important as it allowed the results to be compared, and even if it did introduce an error into the calculation, the error would be consistent across the test cases and so would not influence the conclusions.

Using the same test case as presented in figure 5.16, figure 5.17 visually illustrates the area considered for trapezoidal integration. From this integration, the difference between the input and the reflected voltage pulses is considered as the electrical energy consumed by the DBD actuator. Figures 5.18, 5.19, 5.20, 5.21 and 5.22 show the variation in electrical energy consumed per pulse by varying the high voltage electrode width, ground electrode width, electrode separation, dielectric thickness, and electrode length respectively. The error bars included in the plot represent the uncertainty of the measurements due to the oscilloscope being used. For all except the dielectric thickness variation (figure 5.21) there is no significant variation in the measured energy per pulse. This confirms the results of the wave strength characterisation in section 5.5.2. The lack of variation in energy consumed for the cases with varying electrode length supports the conclusion that the pressure wave strength is inversely proportional to electrode length with constant energy. For the dielectric thickness (see figure 5.21), there is a measureable increase in energy consumed as dielectric thickness decreases. This agrees with the increase in pressure wave strength witnessed at lower

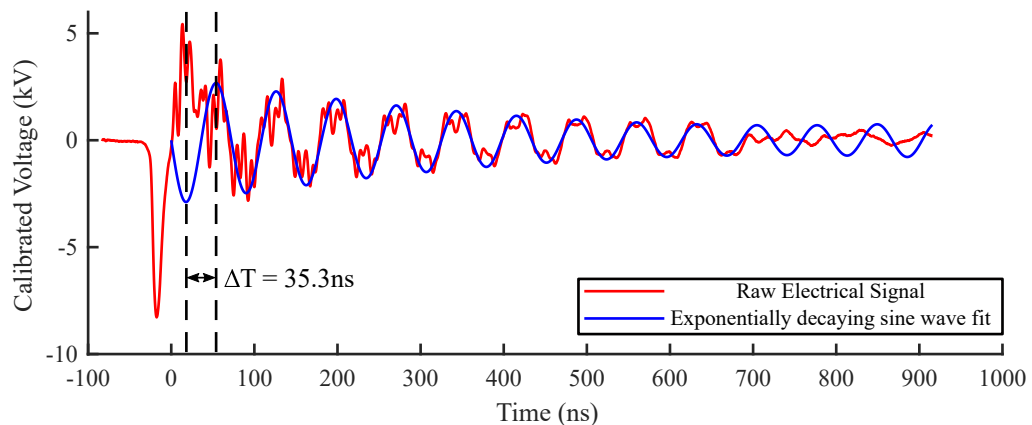


FIGURE 5.16: Example of calibrated voltage signal across an ns-DBD actuator and a exponentially decaying sine wave fit superimposed

dielectric thicknesses i.e. the pressure wave strength is proportional to the energy consumed by the actuator. This result can be explained if the electrical characteristics of the actuator are considered. The first point to note is that for all cases the impedance of the actuator is greater than that of the coaxial cable supplying the voltage, this can be assumed due to the change in polarity of the reflected pulse. Therefore, a reduction in the actuator impedance should result in a smaller proportion of the voltage pulse being reflected back along the supply line. Underwood et al.[98] developed a lumped element circuit model for ns-DBD plasma actuators. This model treated the dielectric material as a simple capacitor. The capacitance, C , of any general capacitor can be written as equation 5.11:

$$C = \frac{\epsilon_0 \epsilon_r A}{d} \quad (5.11)$$

where ϵ_0 is the permittivity of free space (a constant), ϵ_r is the relative permittivity of the substance (dielectric constant of the dielectric used in this case), A is the area of the two plates that make up the capacitor (area of the actuator in this case) and d is the distance between the two plates (dielectric thickness in this case). The important parameter is the impedance of the actuator; for a capacitor the impedance is inversely proportional to the capacitance. Therefore in this case, as dielectric thickness decreases the capacitance of the actuator increases which, in turn, results in a decrease in actuator impedance. This conclusion agrees with the results of the electrical measurements and helps to confirm that the measurements show the correct trends.

The next step is to examine the thermal measurements made for the actuators that will help to demonstrate how effective the actuators are at converting this electrical energy consumed into useful thermal energy. For this work this has been done using two different techniques: IR thermography and calibrated quantitative Schlieren. The aim of using IR thermography is to measure the thermal energy lost by measuring

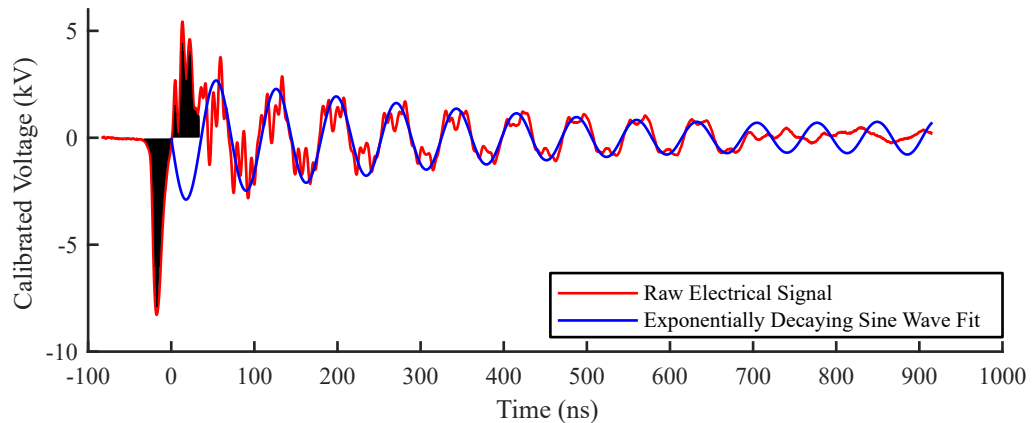


FIGURE 5.17: Example of voltage pulse area considered for trapezoidal integration in order to calculate pulse energy

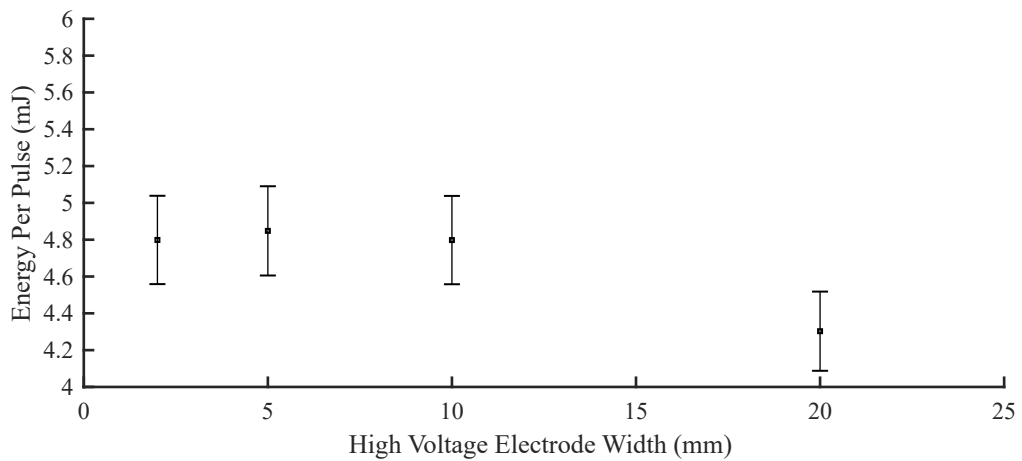


FIGURE 5.18: Variation in electrical energy consumed per pulse with varying high voltage electrode width

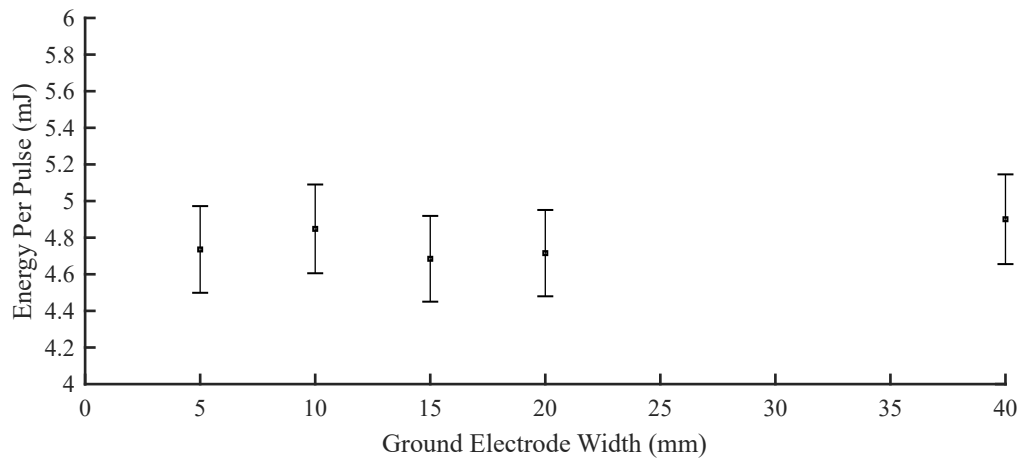


FIGURE 5.19: Variation in electrical energy consumed per pulse with varying ground electrode width

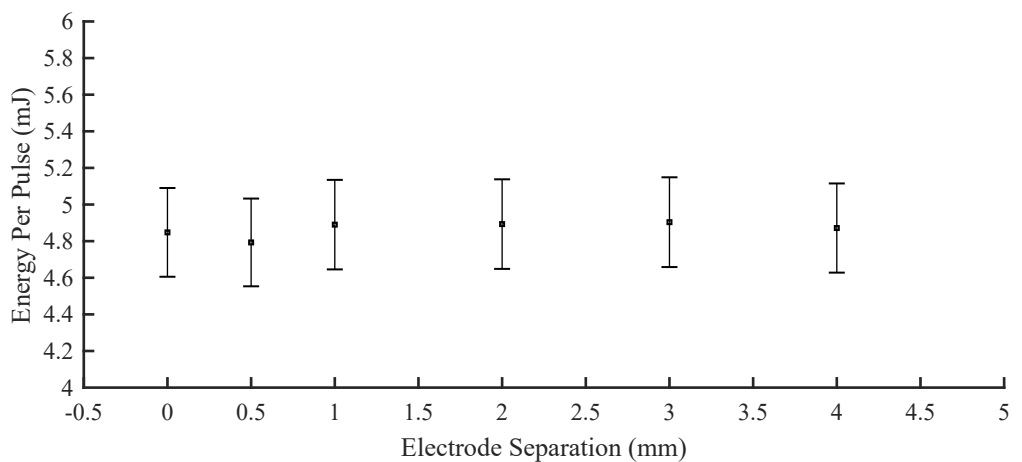


FIGURE 5.20: Variation in electrical energy consumed per pulse with varying electrode separation

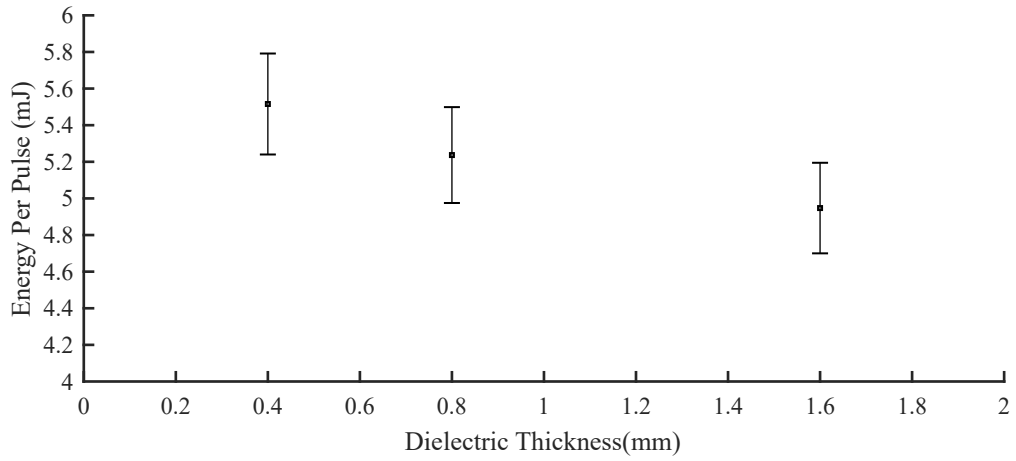


FIGURE 5.21: Variation in electrical energy consumed per pulse with varying dielectric thickness

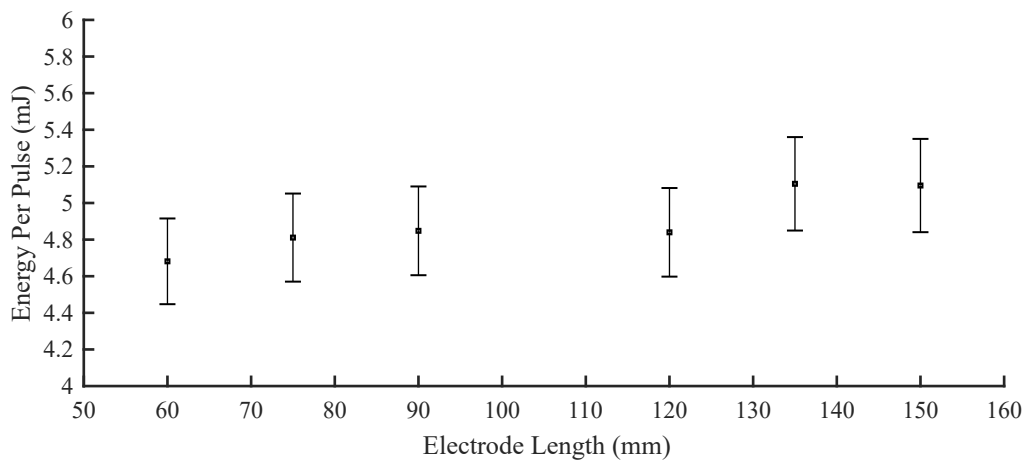


FIGURE 5.22: Variation in electrical energy consumed per pulse with varying electrode length

the surface temperature of the DBD and calculating the heat flux through the surface. The calibrated Schlieren on the other hand aims to measure the temperature of the air above the actuator surface. These temperatures can be converted into thermal energy. This is an important actuator performance metric as this thermal energy is what is responsible for the generation of the pressure waves that give these actuators their control authority.

5.5.4 INFRARED THERMOGRAPHY

The details of the infrared thermography measurement technique including information regarding the camera are provided in section 2.1.5. This section will focus on the results and the comparison of the results to the wave strength and electrical measurements presented previously.

The aim of this section is to quantify the amount of thermal energy transmitted through the dielectric barrier by conduction. As the infrared images are captured with the actuator upside down (plasma formed on the lower surface) there is no significant thermal energy loss as a result of convection. Therefore the only significant loss of thermal energy is the thermal energy conducted through the dielectric barrier. To calculate the thermal energy transferred through the dielectric barrier, the heat flux will need to be calculated at each point in the plasma discharge at a resolution of 0.00144m resolution (the pixel resolution of the IR camera). This heat flux can be summed across the discharge to provide the heat transfer power at each instant of the discharge. This power is then integrated in time (trapezoidal integration was used) to calculate the energy transferred by conduction through the dielectric barrier over the duration of the plasma discharge. This energy loss is compared to the electrical energy consumed by the actuator (based on the results of section 5.5.3) over the same interval in order to calculate a measure of the actuator efficiency.

Figure 5.24 presents two different temperature profiles at specific points. One profile is an example of the temperature profile observed at the edge of the high voltage electrode. The temperature profile used along the length of the discharge is an average across the length of the actuator electrode. This average profile is the temperature profile used to calculate the heat flux and thus the energy loss. The second profile is the temperature profile observed on the reverse side of the actuator. This is important as it confirms that the semi-infinite slab assumption is valid in this case. The semi-infinite slab assumption states that the temperature on the opposite side of the material in question remains at a constant temperature. This can be shown to be numerically accurate by rearranging the equation for the penetration depth, equation 5.12:

$$d = \sqrt{\pi\alpha t} \quad (5.12)$$

where d is the penetration depth, α is the thermal diffusivity coefficient and t is

time. For the thinnest actuator used, 0.4mm dielectric thickness, this time is 0.0548s. The experimental data provided shows that in this case the temperature on the reverse of the actuator remains unchanged throughout the discharge, 0.12s. As the temperature remains constant throughout the discharge, the semi-infinite slab model can be assumed for the remainder of this work.

Figure 5.23 provides a wider view of how the temperature varies along the plasma discharge. This plot illustrates that the variation in temperature during the discharge depends on the distance from the edge of the high voltage electrode. There is a rapid drop-off in temperature as we move further away from the edge of the high voltage electrode.

From temperature profiles such as that presented in figure 5.24 the heat flux through the surface of the dielectric is calculated. The heat flux per unit area can be calculated using the conduction equation shown in equation 5.13:

$$Q = \frac{k\Delta T}{D} \quad (5.13)$$

where ΔT is the difference in temperature between the two surfaces of the actuator, k is the thermal conductivity of the material (0.343W/mK for FR4[99]) and D is the dielectric thickness. The temperature on the reverse side is taken as the initial temperature of the actuator. The calculated heat flux is then summed along the length of the discharge and the length of the electrode. The heat flux is then converted to an energy loss through numerical integration. Figures 5.25, 5.26, 5.27, 5.28 and 5.29 show the variation in thermal energy loss through conduction throughout the discharge with varying high voltage electrode width, ground electrode width, electrode separation, dielectric thickness, and electrode length, respectively. The error bars included in these plots includes uncertainties due to: the pixel dimension uncertainty, the IR camera temperature uncertainty and the uncertainty in the measurement of the dielectric thickness.

Examining these results there is one significant point to take away; the method as it is applied here is not reliable. For the dielectric thickness variation, the apparent heat flux through the surface is so large that a negative efficiency is calculated i.e. more energy is lost to conduction through the dielectric than was consumed. This is a clear indicator that either the IR results or the electrical measurements cannot be trusted. The conclusion made here is that the IR measurements are unreliable. The electrical measurements, the pressure wave strength measurements and the basics of the DBD lumped electrical model[98] all exhibit a certain level of agreement from a qualitative point of view. The increase in electrical energy consumed by the actuator as the dielectric thickness decreases suggests that there is a decrease in actuator impedance. This agrees with the fundamental equations for the capacitance of the actuator and the associated impedance. The significant increase in pressure wave strength as dielectric

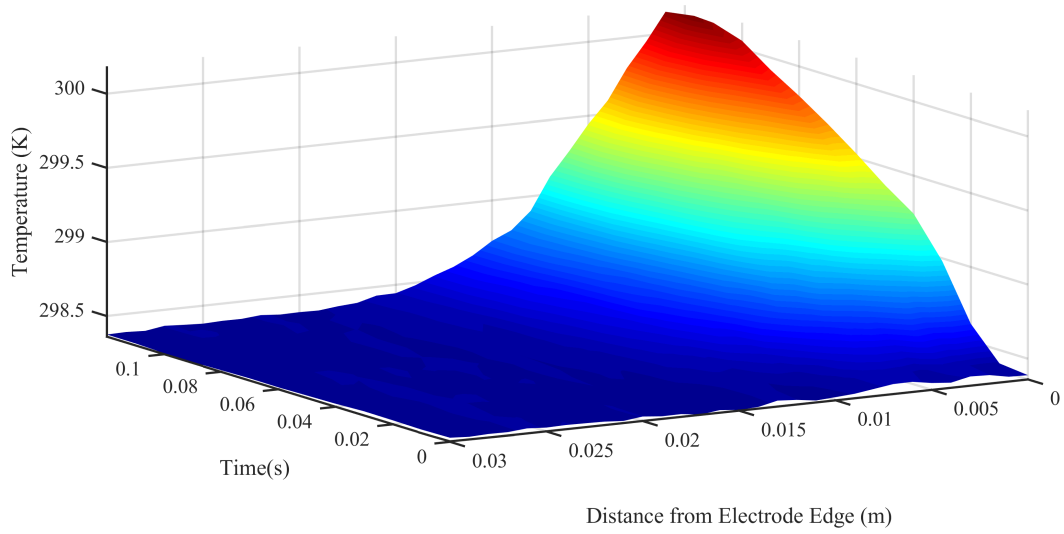


FIGURE 5.23: Temperature profile along the length of the plasma discharge

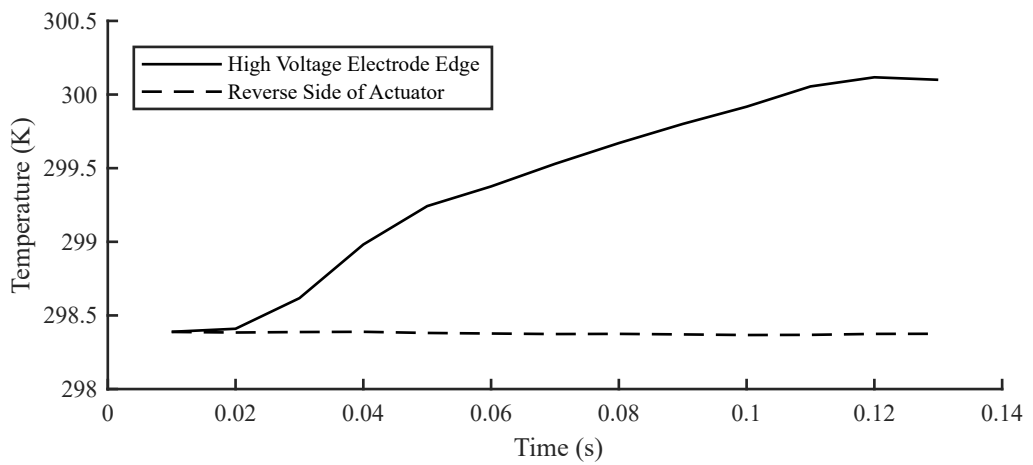


FIGURE 5.24: Temperature profile at two different points: the edge of the high voltage electrode and the reverse side of the actuator

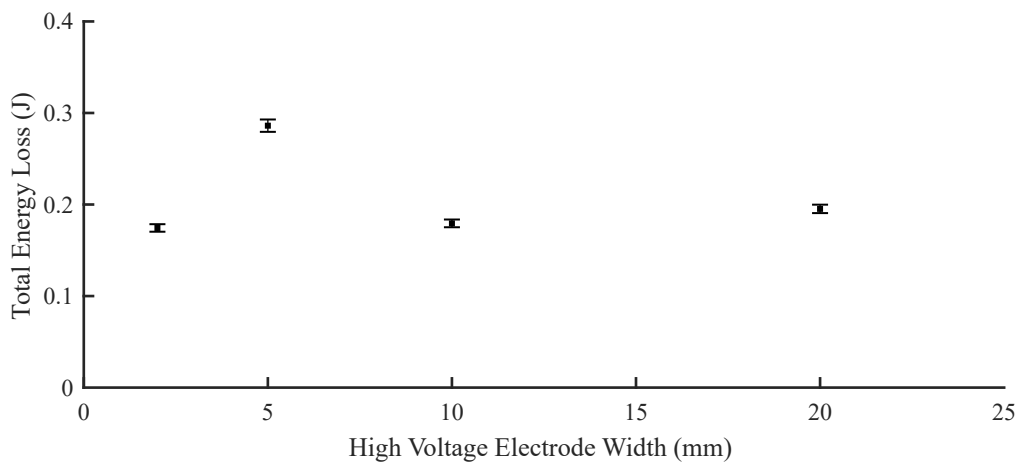


FIGURE 5.25: Variation in thermal energy lost over the course of the discharge with varying high voltage electrode width

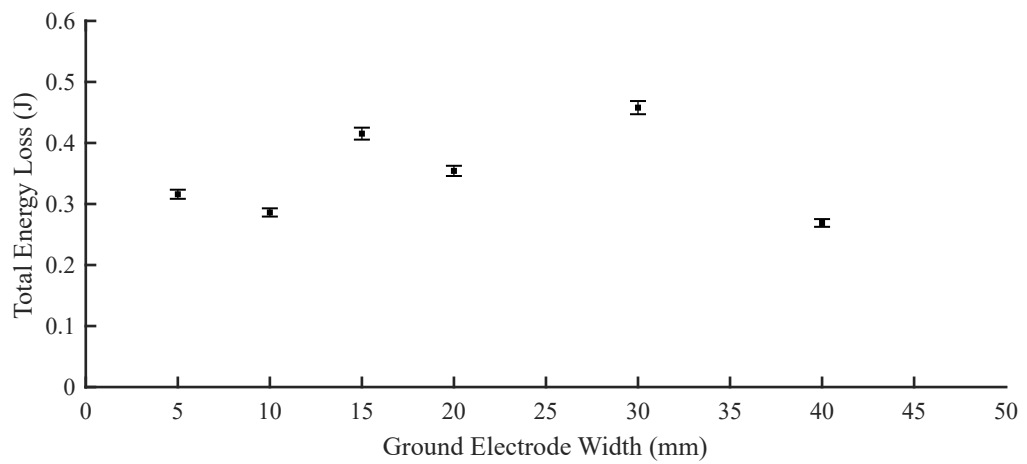


FIGURE 5.26: Variation in thermal energy lost over the course of the discharge with varying ground electrode width

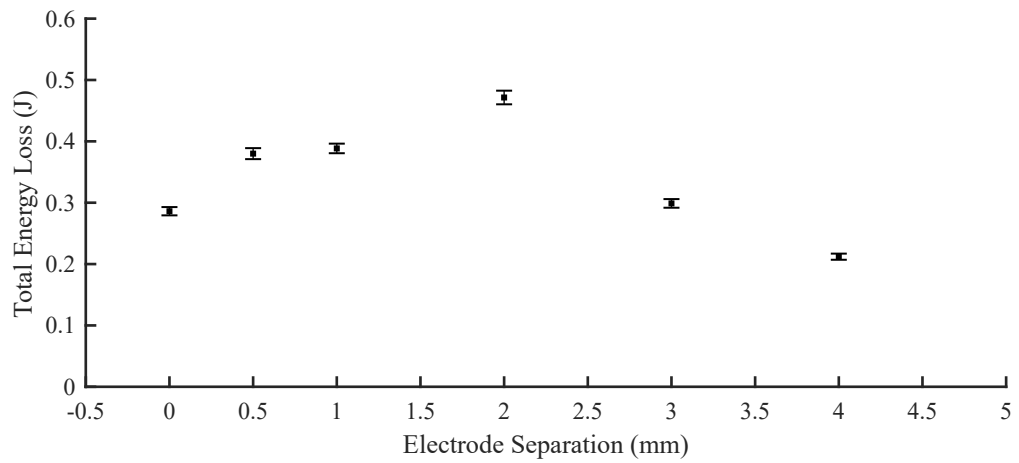


FIGURE 5.27: Variation in thermal energy lost over the course of the discharge with varying electrode separation

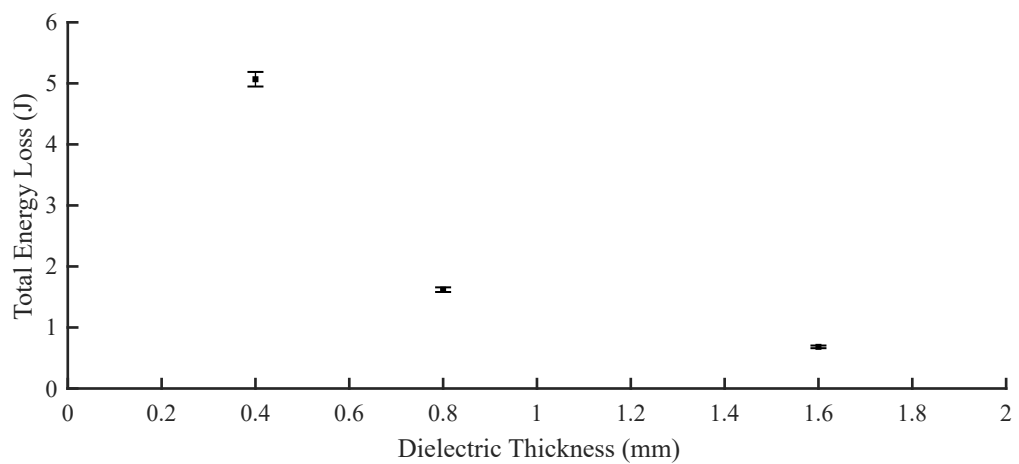


FIGURE 5.28: Variation in thermal energy lost over the course of the discharge with varying dielectric thickness

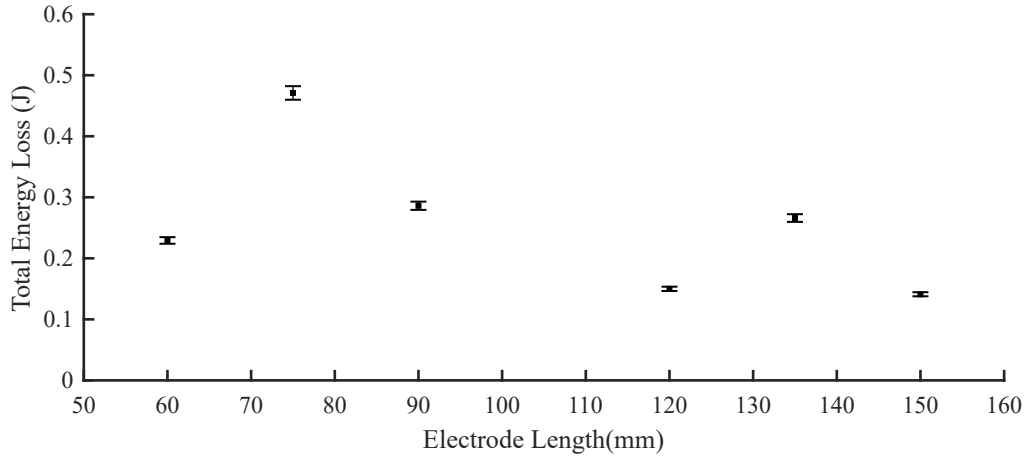


FIGURE 5.29: Variation in thermal energy lost over the course of the discharge with varying electrode length

thickness was decreased would also suggest that the actuator efficiency increases with decreasing dielectric thickness. It certainly does not agree with the decrease in efficiency suggested by the IR measurements.

This thought process lends itself to the argument that the IR data recorded was not reliable and that the electrical measurements (despite its limitations due to the pulse reflections from the generator) and the conventional Schlieren imaging were more useful. There are a number of reasons why this could be the case. The first was highlighted in section 2.1.5; the inherent inaccuracy of the camera. In figures 5.25 - 5.29 errorbars are included in the results. These errors were derived based on the standard error equation 5.14. Based on equation 5.13 the error can be reduced to equation 5.15:

$$R = R(X, Y, \dots)$$

$$R = \sqrt{\left(\frac{\partial R}{\partial X} \cdot \delta X\right)^2 + \left(\frac{\partial R}{\partial Y} \cdot \delta Y\right)^2} \quad (5.14)$$

$$\frac{\delta Q}{|Q|} = \sqrt{\left(\frac{\delta T}{\Delta T}\right)^2 + \left(\frac{\delta D}{D}\right)^2}$$

$$\frac{\delta Q}{|Q|} = \sqrt{\left(\frac{\delta Q}{\Delta Q}\right)^2 + \left(\frac{\delta X}{X}\right)^2} \quad (5.15)$$

The decision that had to be made regarding the calculation of these errors was how to consider the quoted error of the IR camera. The camera has a quoted error of $\pm 2\%$. However, what is not clear is if this value should be considered for each individual measurement or for the ΔT across the actuator. In figures 5.25 to 5.29 the errors indicated are based on the assumption that the $\pm 2\%$ error in the temperature measurement

is applied to the ΔT across the actuator and not to each individual measurement. If instead the error was to be applied to each measurement individually, i.e. before ΔT was calculated, then the reason for the unreliable temperature measurements becomes clear. With this method of accounting for the uncertainties, the variation in temperature is of a similar magnitude to the IR uncertainties.

Another possibility, although it is thought it would have less of an impact, is that plasma discharge introduces a significant change into the measured emissivity of the dielectric material. The emissivity of a surface is a measure of how well the surface emits IR radiation, a perfect black body emitter has an emissivity of 1. The dielectric was known to have an emissivity of approximately 0.95. It is possible that this value changes when the ns-DBD is supplied voltage and plasma is generated. No definitive answer to what the emissivity of a surface plasma could be equal to was found and so the effect of this possible error source is difficult to quantify. However, it is thought that any change in the emissivity as a result of this is small. This is based on the temperature profile provided as an example in figure 5.24. From a time of 0s to 0.2s, the temperature begins to rise, but only slightly as would be expected given that the plasma discharge has just begun. If there was any significant variation in the emissivity due to the plasma discharge, then a more significant increase or a visible decrease in temperature would be expected. Therefore if the emissivity does change due to the plasma discharge, it is assumed to be of a small enough magnitude such that it does not significantly contribute to the errors observed in these measurements.

The two sources of errors described above go some way to explaining why the IR measurements presented do not correlate well with previous measurements (electrical and conventional Schlieren imaging). As such, for the remainder of this chapter and the rest of this work, the IR measurements here are assumed to be unreliable. The following section provides an alternative method for measuring these temperatures in an attempt to more accurately quantify the actuators thermal efficiency.

Parameter Value (mm)	0	0.5	1	2	3	4
Efficiency (%)	41.0	20.7	20.6	3.6	39.1	56.5

TABLE 5.2: Effect of electrode separation on actuator efficiency

Parameter Value (mm)	5	10	15	20	40
Efficiency (%)	33.3	41.0	11.4	24.9	45.1

TABLE 5.3: Effect of ground electrode width on actuator efficiency

Parameter Value (mm)	2	5	10	20
Efficiency (%)	63.7	41.0	62.6	54.6

TABLE 5.4: Effect of high voltage electrode width on actuator efficiency

Parameter Value (mm)	60	75	90	120	135	150
Efficiency (%)	51.0	2.1	41.0	69.0	47.9	72.3

TABLE 5.5: Effect of electrode length on actuator efficiency

Parameter Value (mm)	0.4	0.8	1.6
Efficiency (%)	-818	-209	-37.8

TABLE 5.6: Effect of dielectric thickness on actuator efficiency

5.5.5 CALIBRATED SCHLIEREN

Calibrated Schlieren was used to measure the temperature change in the air surrounding the actuator. The suggestion is that the addition of thermal energy to the air is the method by which the pressure change is generated which in turn results in the observed pressure waves. Therefore, an effective measure of the efficiency of the actuators would be the ratio of the input electrical energy to the thermal energy added to the surrounding air. The fundamentals of the technique are explained in detail in section 5.2.1 and so will not be explained here. The focus in this section is on the calibration carried out for the technique and the results of applying the technique to certain plasma actuators. From the results gathered previously using conventional Schlieren and current shunt electrical measurements, it is clear that the only parameter investigated to have a significant impact on the measured actuator response (wave strength and energy consumption) is the dielectric thickness. Therefore only the cases with varying dielectric thickness are examined using the calibrated Schlieren technique.

QUANTITATIVE SCHLIEREN CALIBRATION

To provide proof that the calibrated Schlieren technique was setup and applied accurately in this study it was decided to carry out some validation work with a well documented temperature source/field. The calibration conducted investigated the temperature profile in the direction normal to a vertically mounted heated flat plate. This was done by comparing the calibrated Schlieren measurement results with the theoretical results of the temperature profile across the boundary layer formed as a result of natural convection from the heated flat plate.

The theoretical results are based on work carried out by Ostrach [100] where it was shown that the temperature profile across the thermal boundary layer could be given by equation 5.16:

$$T_{BL} = H(\eta) \cdot (T_s - T_\infty) + T_\infty$$

where:

$$\eta = \left(\frac{Gr}{4}\right)^{\frac{1}{4}} \cdot \frac{y}{x} \quad (5.16)$$

$$Gr = \frac{g \cdot \beta \cdot (T_s - T_\infty) \cdot x^3}{\nu^2}$$

where Gr is the Grashof number, y is the distance along the plate, x is the distance perpendicular to the surface of the plate, g is the gravitational constant and is taken as 9.81m/s^2 , β is the coefficient of thermal expansion (which if an ideal gas is assumed is equal to $\frac{1}{T}$), and ν is the kinematic viscosity. The Grashof number is a ratio of the buoyancy to viscous forces (in a similar way that Reynolds number is the ratio of inertial to viscous forces). $H(\eta)$ is a function tabulated by Ostrach [100] for a number of different Prandtl numbers (Pr). The Prandtl number is calculated as in equation 5.17:

$$Pr = \frac{C_p \mu}{\kappa} \quad (5.17)$$

At sea level atmospheric temperature and pressure, the Prandtl number is approximately 0.71. The closest available look up table for $H(\eta)$ is for $Pr = 0.72$ [100] and so this table was used to calculate the appropriate values of $H(\eta)$.

To obtain the thermal profile, the plate was heated using a silicone rubber heater powered by a DC power supply to a stable temperature of $T_s = 326\text{K}$. It took approximately 15 minutes for the temperature to stabilise. The temperature was measured using the same IR camera as in the previous work (see section 2.1.5 for details of the camera). Room temperature and pressure were measured to be 287.8K and 102.47kPa , respectively. Once the temperature of the plate had stabilised Schlieren images were recorded and calibrated as described in section 5.2.1. From the calibrated density profiles, the temperature was calculated based on the ideal gas laws and this profile could then be compared to the theoretical profile described above. Figure 5.30 shows the Schlieren image (left) and the temperature profiles extracted from the image superimposed on the theoretical temperature profile. It is clear that there is little difference between the calibrated Schlieren temperature profile and the theoretical temperature profile. The largest variation between the two datasets is 0.7%.

This process provides evidence that the calibrated Schlieren has been setup and operated correctly. Therefore it can be assumed that measurements recorded of the temperature profiles above the DBD actuators are also likely to be accurate.

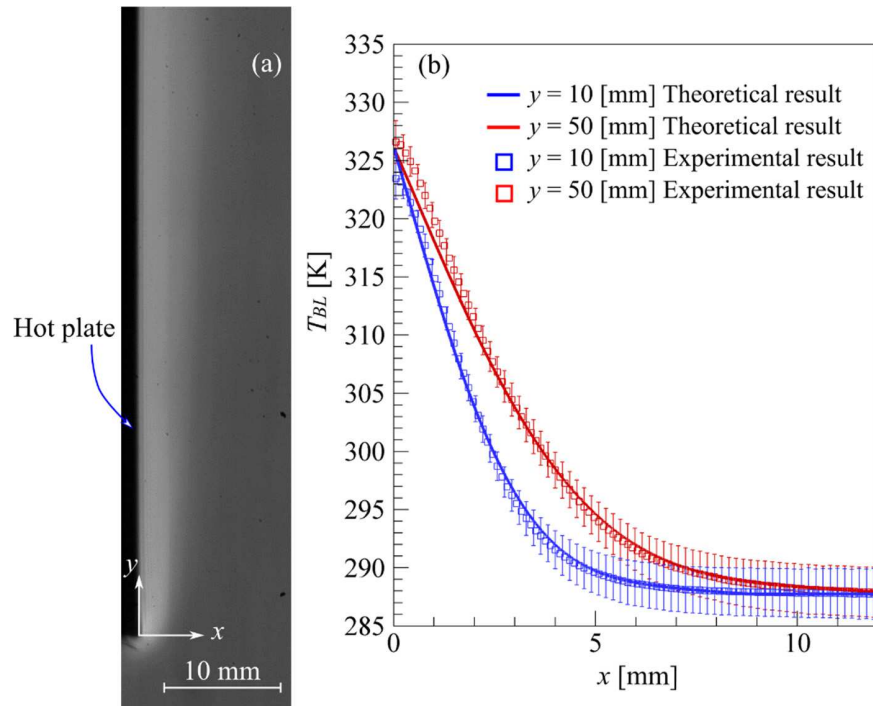


FIGURE 5.30: Schlieren image and extracted temperature profiles illustrating the check carried out to ensure the calibrated Schlieren was set up and operated accurately

TEMPERATURE VARIATION DUE TO DBD PLASMA DISCHARGE

Now that it has been shown that the proposed method can produce accurate results, the temperature response of the air to the actuators can be examined. The first thing to look at is a visualisation of how the temperature field above the surface of the actuators changes during the course of the plasma discharge. Figures 5.31, 5.32 and 5.33 show the temperature field above actuators with 0.4mm, 0.8mm and 1.6mm dielectric thickness respectively, at discrete points in time during the 0.1s plasma discharge. There are a variety of insights that can be taken from this data, both quantitative and qualitative. The focus is first on the qualitative information that can be gathered on the mechanisms behind the heating of the air. Figure 5.31 will be the focus for the qualitative discussions as the changes in temperature are larger which make any features clearer. The first point of interest is that, particularly early in the discharge period, there are two clear sources of heat energy being added to the flow. The first is at approximately 1.5 to 2mm from the edge of the high voltage electrode and the second is at approximately 4 to 5mm downstream of the high voltage electrode. This is highlighted in images (a) - (c) by the small, comparatively low temperature region near the actuator surface approximately 3mm downstream of the high voltage electrode. It is believed that these two locations are likely to be the beginning and end of the plasma streamers generated by the actuators. This thermal hotspot at 1.5 to 2mm is aligned with the origin of the hemispherical wave and this has been shown previously to originate from the beginning of the plasma filaments [2]. Another observation is the significant vertical growth of the temperature distribution

at this location. This can partially be explained by convection, however the growth is too rapid for that to be the only cause. It is likely that this vertical temperature profile is a result of the induced flow behind the generated pressure waves. The other interesting feature is the horizontal movement of this thermal plume originating at 1.5 to 2mm. There are two possible reasons for this movement, however it is not clear what is the reason behind this. The first is the induced flow generated behind the hemispherical pressure wave. As the induced flow follows the direction of the pressure wave, the induced flow is in every direction. If this were the only factor then it would be expected to remain centered on the origin of the pressure wave. The reason being that it would experience an induced flow in both the positive and negative x-directions and this is clearly not the case. The other, seemingly more likely, explanation is that the actuator generates a weak ionic wind. It was explained in section 5.1.1 that ns-DBD actuators have shown to produce practically no ionic wind. This temporal variation in temperature distribution suggests however that there is some ionic wind generated by these actuators. The magnitude of this ionic wind is indeed very small, somewhere in the region of 1 to 2mm/s based on the movement of the observed thermal plume. This is the only conceived explanation as to why the thermal plume travels in the manner observed and while it is a negligible flow, it is an interesting observation. This small ionic wind would also explain why the area of lower temperature discussed above disappears 70ms into the discharge as the time scales are too low for the reason to be diffusion (diffusion time constant is in the order of 100's of seconds when derived from the 1D time-dependant conduction equation).

With the quantitative results in mind, it is suggested here that not all of the thermal energy added to the flow by the plasma discharge can be considered to contribute to the flow control authority. The hypothesis here is that the thermal "bump" generated in the vicinity of the plasma streamer start (where the hemispherical wave is generated) is actually the mechanism that gives ns-DBD actuators their flow control authority. Therefore it may be sensible to ignore the thermal energy added at the downstream end of the plasma streamer. This is unproven and it is difficult to separate thermal contributions from each area; and as such for the remaining of this analysis this hypothesis will be ignored. This is an interesting area for future study; to confirm the hypothesis that the thermal "bump" is the mechanism responsible for the flow control and to investigate actuator efficiency by systematically ignoring energy added at the termination of the plasma streamer.

Moving on from the qualitative results, the same temperature distributions can be examined quantitatively to provide more insight into the variations between different actuators. The vertical temperature profiles at a number of different distances from the edge of the high voltage electrode are examined. Figures 5.34, 5.35 and 5.36 show the temperature profiles at $x = 0, 1, 2, 3, 4$ and 5mm for actuators with a dielectric thickness of 0.4, 0.8 and 1.6mm respectively. Comparing locations for the same actuator, the general trends stay the same, namely, upstream of what is thought to be the beginning

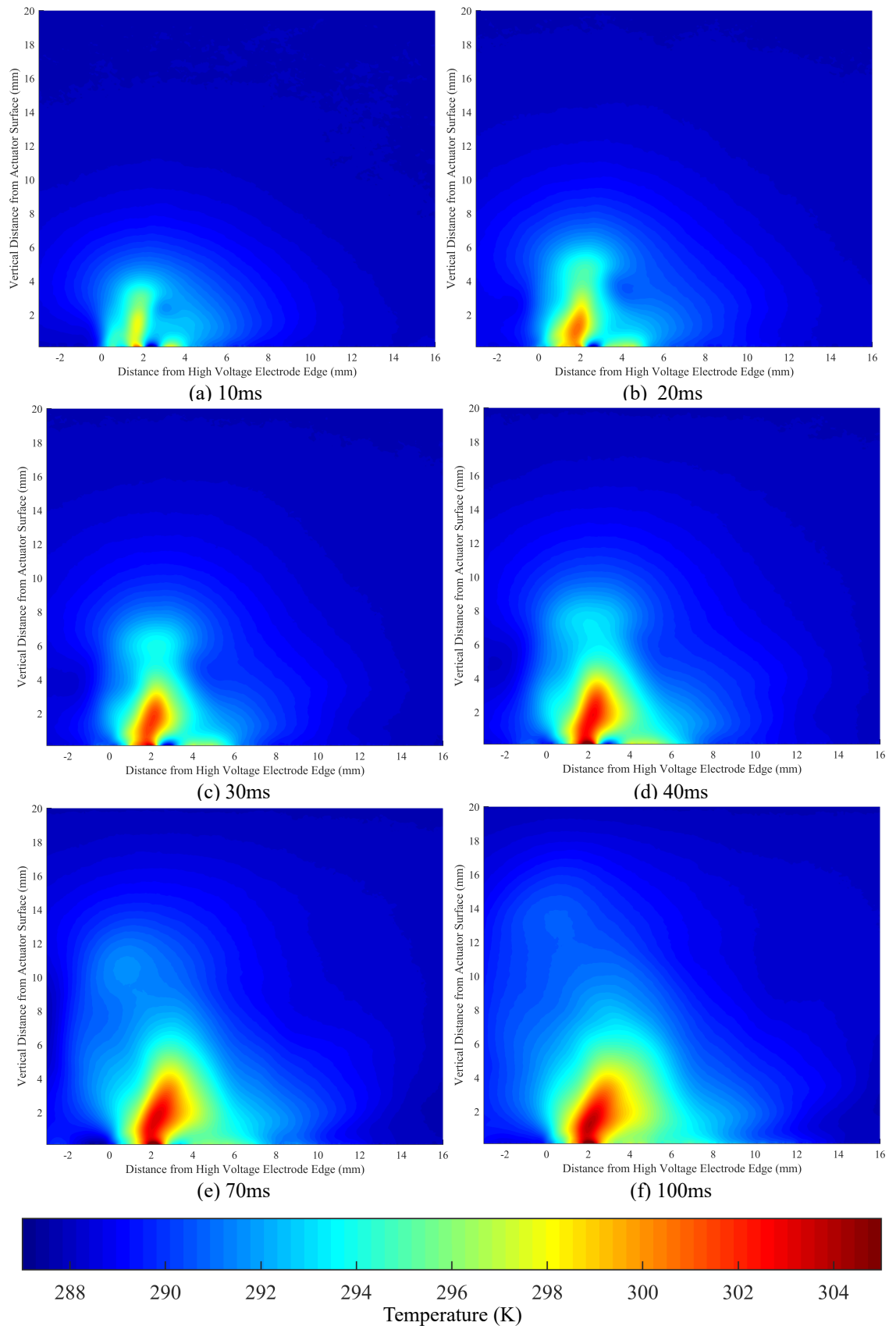


FIGURE 5.31: Set of images that show the evolution of the temperature profile above the DBD plasma actuator with 0.4mm dielectric thickness at (a) 10ms (b) 20ms (c) 30ms (d) 40ms (e) 70ms and (f) 100ms from the beginning of the plasma discharge.

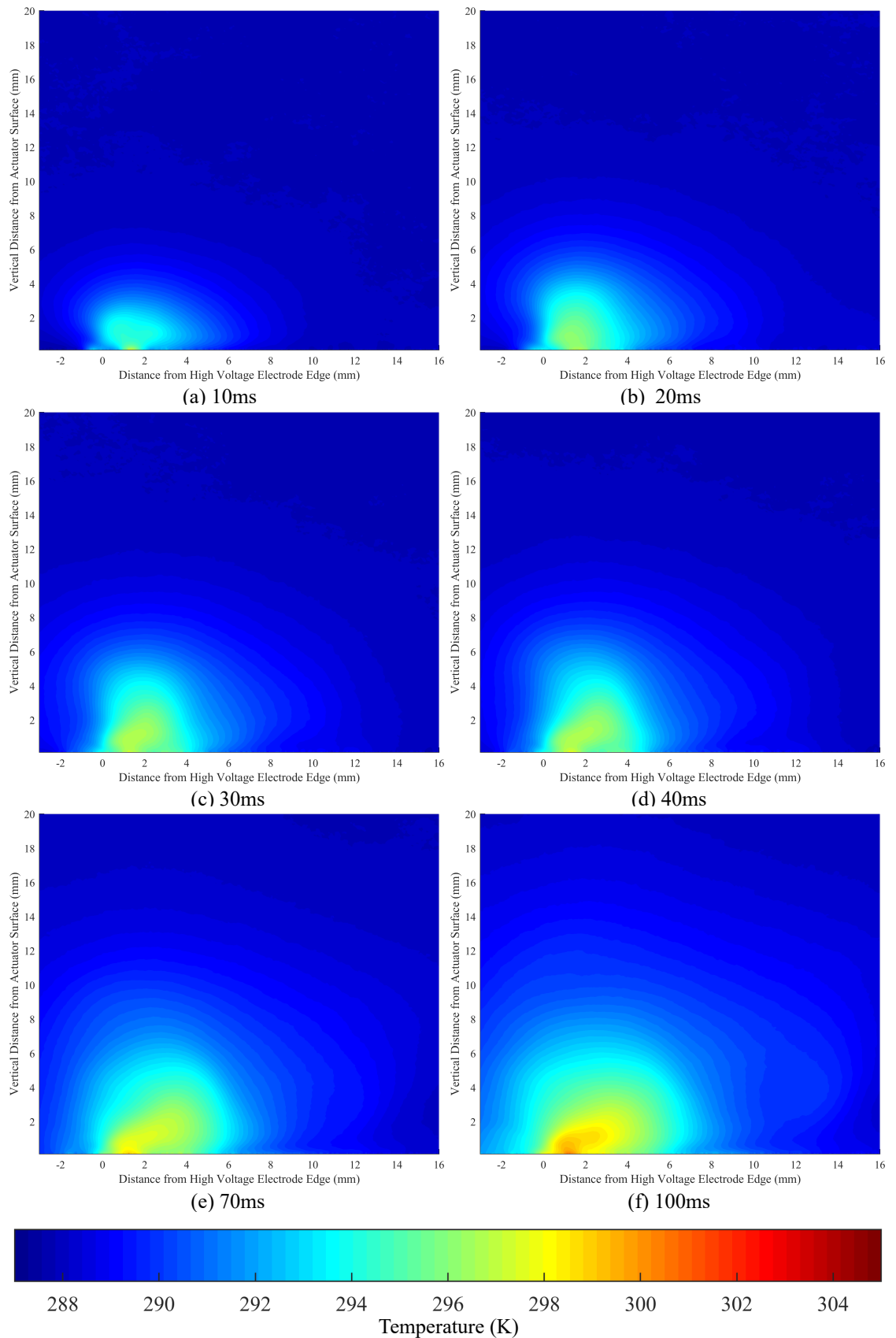


FIGURE 5.32: Set of images that show the evolution of the temperature profile above the DBD plasma actuator with 0.8mm dielectric thickness at (a) 10ms (b) 20ms (c) 30ms (d) 40ms (e) 70ms and (f) 100ms from the beginning of the plasma discharge.

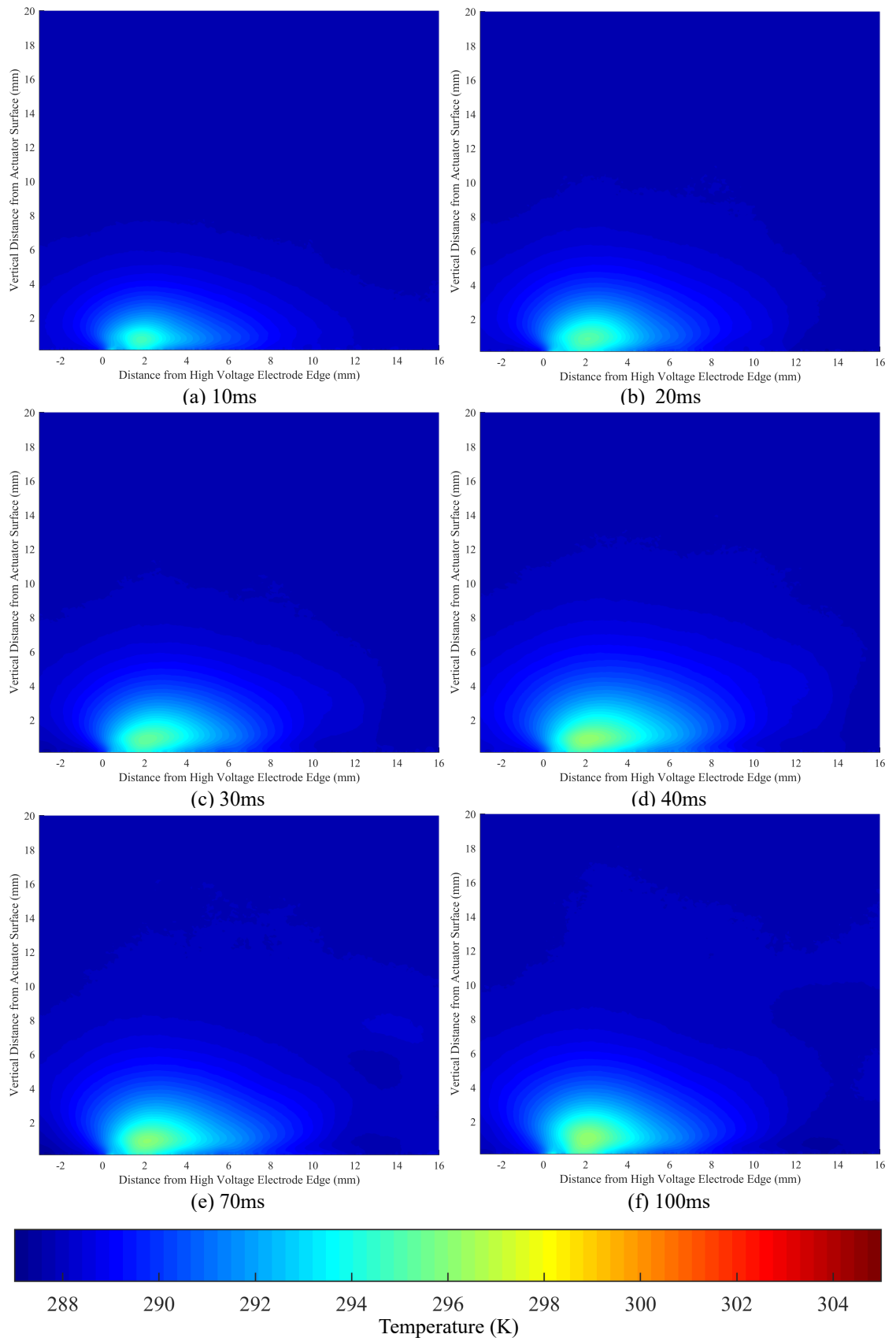


FIGURE 5.33: Set of images that show the evolution of the temperature profile above the DBD plasma actuator with 1.6mm dielectric thickness at (a) 10ms (b) 20ms (c) 30ms (d) 40ms (e) 70ms and (f) 100ms from the beginning of the plasma discharge.

of the plasma streamer there is little change in air temperature across all of the tested actuators. This agrees with the hypothesis that there is a low velocity ionic wind present during the discharge. There is a trend present in the data of the 0.8mm thick actuator that is not present in the other actuators, there is no readily available explanation for this. Figure 5.35 shows that there is an increase in temperature with time across all of the measurement locations. Based on the temperature profile at $x = 0\text{mm}$ (as this profile is relatively stable for the other two actuators after the first 0.01s) it would appear that something causes an increase in temperature from approximately 0.04s over the entire imaged area. It is thought that this is likely to be a result of the imaging method and not a physical phenomenon displayed by the actuator. The importance of this observation will become clear in a later calculation. Another interesting observation is the apparent stagnation of the temperature change. This highlights an issue with the commonly used practice of characterising these type of actuators in quiescent conditions: the temperature field appears to reach an equilibrium condition that would in theory limit the observed functionality of the actuators. These actuators function on the principle of adding thermal energy to a flow and the rapid heating which creates a pressure wave. However, as the temperature of the surroundings increases due to this actuation, the effect of the actuators will diminish. This phenomenon would not occur during use as forced convection (due to the flow in which the actuators are used) would inhibit this increase in temperature and so the strength of the pressure waves generated would not decrease with discharge time as is likely the case here. If the actuators being used could be operated for a longer time (5-10s) during a test, the impact of this would likely become clearer. However, the material integrity of the dielectric currently being used is not sufficient enough for this length of test to be carried out. This also suggests that the actuator effectiveness will depend on atmospheric temperature (for the same input electrical energy), proving this would be another interesting area for further research.

Figure 5.37 shows, at a number of discrete discharge times (1, 10 and 50ms), the streamwise temperature profile 1mm above the actuator surface. The vertical location selected is arbitrary as the general streamwise temperature distribution will not vary significantly within the heated region. The significant increase in thermal energy added to the air using the actuator with 0.4mm dielectric thickness is clearly highlighted again in this data. An interesting observation is that this additional energy appears to be more focused on the point at 1.5 to 2mm unlike the other actuators where the peak temperature region is more widely spread. This goes some way to explaining the significant increase in pressure wave strength as the increase in thermal energy relative to the other actuators is primarily focused on the region where the pressure wave is generated.

The final information to be extracted from the calibrated Schlieren results is a measure of the thermal conversion efficiency i.e. the ratio of the thermal energy added to the air compared to the electrical energy added (presented in section 5.5.3). The energy added to each pixel can be estimated from the measured temperature by using

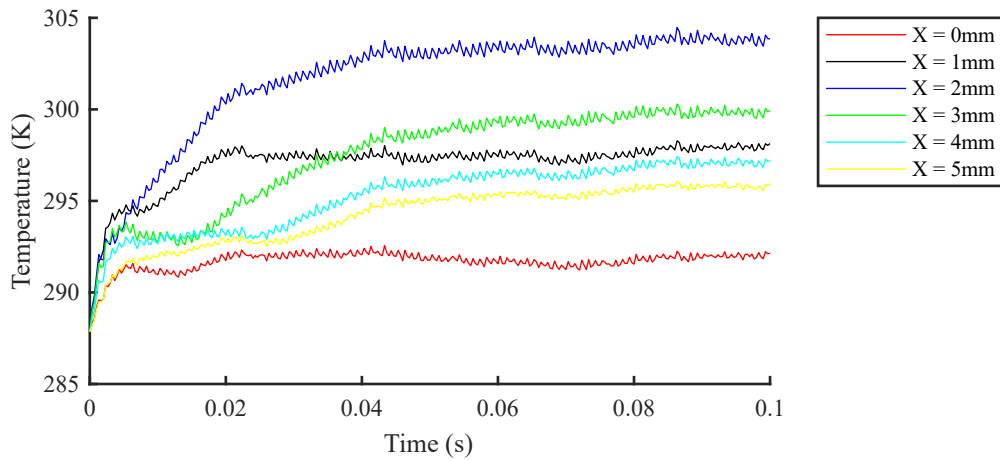


FIGURE 5.34: Temperature profile 1mm above an ns-DBD plasma actuator with 0.4mm dielectric thickness at $x = 0, 1, 2, 3, 4$ and 5mm downstream of the high voltage electrode.

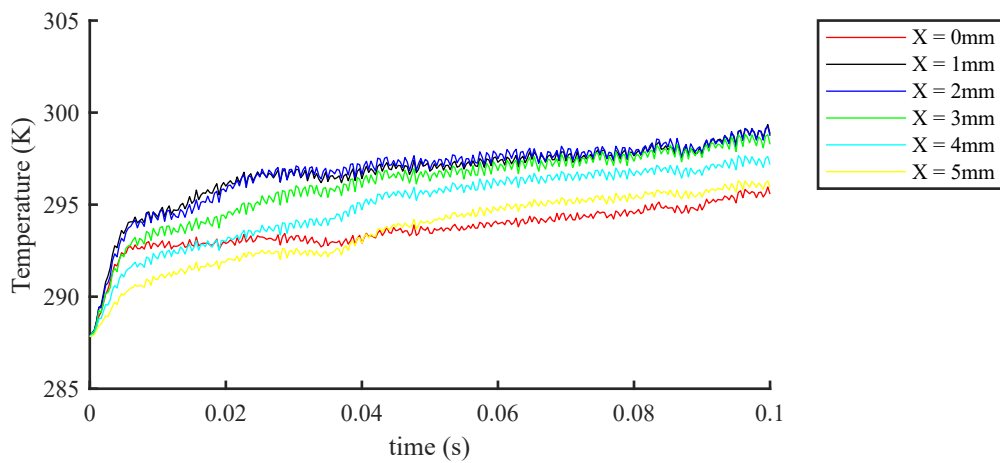


FIGURE 5.35: Temperature profile 1mm above an ns-DBD plasma actuator with 0.8mm dielectric thickness at $x = 0, 1, 2, 3, 4$ and 5mm downstream of the high voltage electrode.

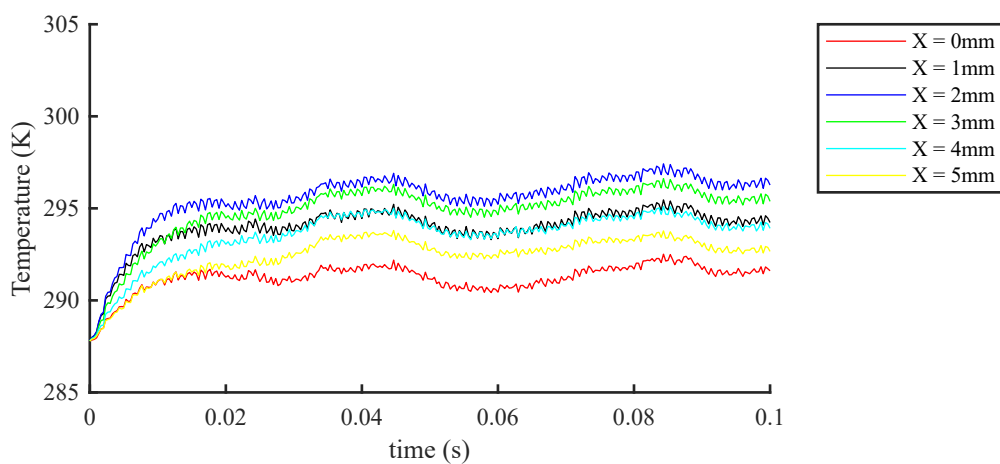


FIGURE 5.36: Temperature profile 1mm above an ns-DBD plasma actuator with 1.6mm dielectric thickness at $x = 0, 1, 2, 3, 4$ and 5mm downstream of the high voltage electrode.

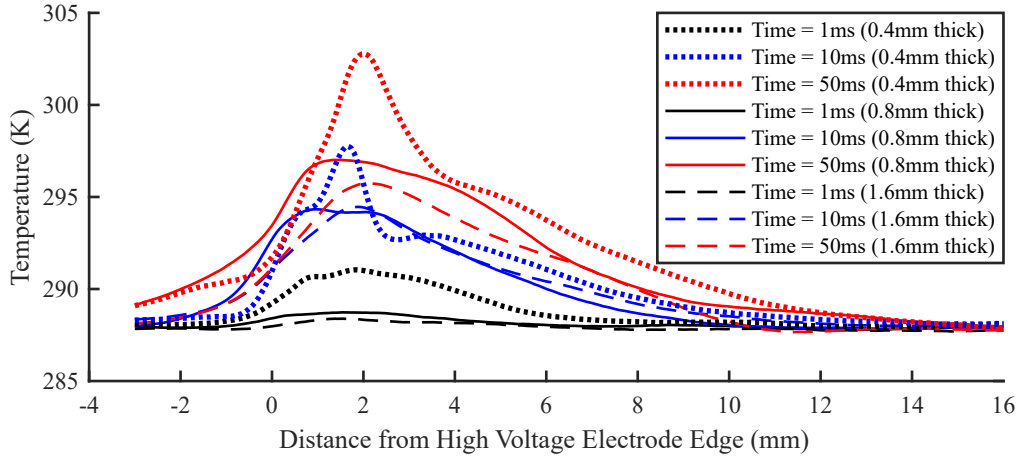


FIGURE 5.37: Temperature profile 1mm above the actuator surface at 1, 10 and 50ms for actuators with 0.4mm, 0.8mm and 1.6mm dielectric thickness.

equation 5.18:

$$E = C_p m \Delta T \quad (5.18)$$

where E is the thermal energy, C_p is the specific heat capacity of air, m is the mass of air per pixel and ΔT is the measured change in temperature. Mass here is calculated based on the volume of each pixel (the pixel area, 0.0598mm²/px, multiplied by the length of the actuator, 90mm) and the density of quiescent air calculated from the perfect gas law using static pressure and temperature measurements recorded at the time of the calibrated Schlieren imaging. Figure 5.38 shows the cumulative energy added across the entire imaging area as a function of time. The observation regarding the trend of increasing temperature throughout the imaging area for the 0.8mm thick dielectric is apparent here too. The 0.8mm dielectric thickness case cumulative energy continues to rise when the other two actuators remain constant. As a result of this, when quantifying the thermal conversion efficiency, the energy value used is at 0.04s as this is the point at which the issue arises with the 0.8mm thick case. The resulting electrical energy added (based on the energy measured for a single pulse multiplied by the number of pulses in 0.04s at a 1kHz pulse rate), thermal energy measured in the air and the thermal conversion efficiencies are summarised in table 5.7.

There are two key observations here, the first is that, based on the conventional Schlieren and electrical measurements, the thermal conversion efficiency of the actuator increases with decreasing dielectric thickness. The other important observation is that the conversion efficiency is very low and this raises questions over the efficacy of this technique. These questions are not regarding the accuracy of the temperature measurements as it is clear, based on the flat plate calibration, that the technique displays an acceptable degree of accuracy. The issue is whether or not measuring the temperature added to the flow can be used as a measure of the actuator efficiency. The

Thickness (mm)	Electrical Energy (mJ)	Thermal Energy Present in Air (mJ)	Thermal Conversion Efficiency (%)
0.4	220.64	0.07234	0.033
0.8	209.48	0.0481	0.023
1.6	197.88	0.03	0.015

TABLE 5.7: Summary of the electrical energy consumed, the thermal energy added to the surrounding air and the associated efficiency of energy conversion for ns-DBD plasma actuators of varying dielectric thickness.

results measured from the conventional Schlieren, the electrical measurements, and the calibrated Schlieren do agree with one another and the overall result, that efficiency improves with decreasing dielectric thickness, agrees with results of previous work [95]; however there is still more work to be done in an effort to better understand the impact of actuator design on the energy efficiency of the actuator. The outcome that is clear from the result is that, for a given voltage supply used, a very important characteristic to design around is the actuator impedance. If the actuator impedance can be matched to the system, then the electrical energy consumed by the actuator will increase significantly. This can be predicted based on equation 5.11 and an interesting area of future work would be to design a number of actuators with impedance values predicted from this equation and then test the quantity of electrical energy consumed relative to that supplied. This would not only aid in the design of future ns-DBD plasma actuators, but also prove/disprove that this equation holds true (as long as the impedance of the voltage supply is accurately measured).

5.6 CONCLUSIONS

This chapter had two goals: the characterisation of the ns-DBD plasma actuators and to examine the thermal behaviour of the actuators during operation. The characterisation was split into characterisation of the actuator “strength”, measured by the generated

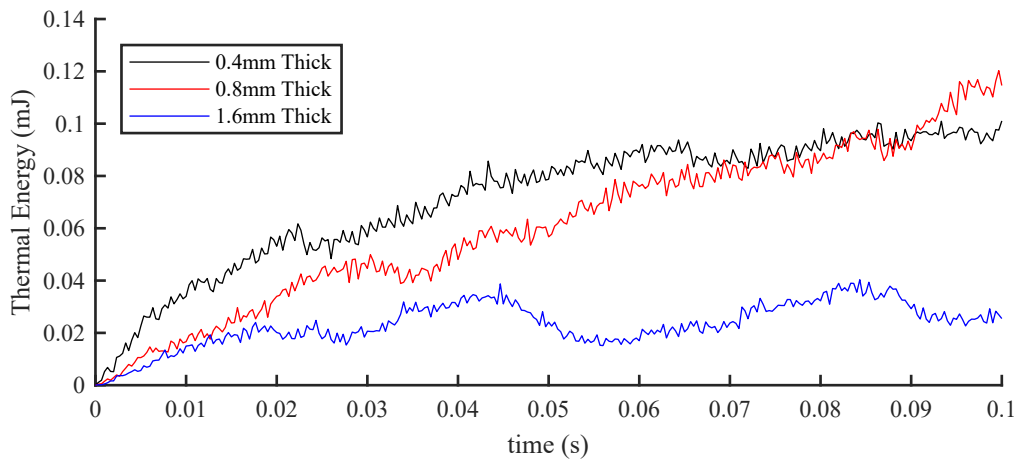


FIGURE 5.38: Cumulative energy added across the imaging area for each of the dielectric thicknesses tested (as a function of time)

pressure wave strength, and the characterisation of the actuator efficiency.

The actuator efficiency focused on a comparison of the electrical energy delivered to the actuator and the thermal energy lost during operation. The initial target was to achieve this by measuring the thermal energy conducted through the surface of the dielectric barrier as, with the actuator oriented upside down as was done during the test, this is the only significant source of thermal losses. However it was found that with the temperature variation observed, the available IR camera was not accurate enough to provide meaningful data. Another attempt was made to quantify the thermal environment around the actuators by using quantitative Schlieren to measure the thermal energy deposited into the air and compare this to the electrical energy consumed. Through comparison to a well known flow field the calibrated Schlieren is known to be accurately set up. However the efficiency values determined using this method were very low. It is therefore the conclusion that measuring the thermal energy deposited in the actuators surroundings is not a viable method of characterising the actuator efficiency.

Although the calibrated Schlieren measurements were not useful for the calculation of actuator efficiency, they did provide some useful insight into the thermal behaviour of the actuator surroundings during operation. The most important observation here is that there is thermal energy added to the flow at both the beginning of the plasma and its termination at the dielectric surface. This is an important observation to be considered for future studies which examine the thermal energy of the fluid around an ns-DBD plasma actuator. The energy added at the termination of the plasma should be considered as a loss as the pressure waves are generated at the start of the plasma and as such only the heat generated here, at the high voltage electrode, contributes to the generated pressure wave.

The fundamental goal of this chapter was to provide the best actuator design for application to the next chapter examining the use of ns-DBD plasma actuators for flow control. This "best" actuator was the combination of features that produces the strongest pressure wave. The section below explains the actuator parameters chosen and the rationale behind the decisions.

5.6.1 FINALISED ACTUATOR DESIGN

The final section of this chapter, that will feed into the following chapter, is using the information provided above to choose the parameters of the actuator used for the supersonic flow control study. It is clear from the data presented that the only two parameters with non-negligible influence on the strength of the pressure waves generated are the dielectric thickness and the electrode length. The electrode length will be fixed to the width of the wind tunnel (minus a margin to ensure the high voltage electricity does not arc to the wind tunnel walls) as the desire is to create a flow field as close to a 2D flow field as possible. Therefore the electrode length will be set to 90mm (the baseline value) as the tunnel is 101.6mm wide and this will

provide sufficient margin between the tunnel side walls and the edge of the electrode to prevent the actuators arcing to the wind tunnel. The dielectric thickness used will be 0.4mm as this provides the strongest pressure waves for a given voltage signal. The remaining parameters, electrode widths and electrode separation, are set to 5, 10 and 0mm for the high voltage electrode width, ground electrode width and electrode separation. The electrode separation was minimised as it has been shown [93] that larger values of separation can result in the plasma discharge taking longer to initiate for each voltage pulse. This results in less of the supplied voltage pulse being used for the plasma generation, and thus pressure wave generation. Although this does not appear in the results measured here, it was thought prudent to use the best design, even if based on previous results. The electrode width values used were arbitrarily set to the baseline actuator values as there was no evidence that these parameters had an impact on the strength of the generated pressure wave or any suggestion from previous work.

This actuator design will now be taken into the next chapter; in which it is applied as a supersonic flow control method for cavity flow control in internal duct flows.

CHAPTER 6

SUPERSONIC CAVITY FLOW CONTROL

6.1 SUPERSONIC CAVITY CONTROL

Chapter 4 provided an initial insight into how cavity flows interact with a shock train in a duct flow. This chapter is focused on examining how these cavity flows can be manipulated by ns-DBD plasma actuators. There are a variety of applications where controlling cavity flows are of interest such as cargo/landing gear bay doors and mixing enhancement in supersonic combustion. Fundamentally, the majority of cavity flow control applications are interested in altering the resonance characteristics of the cavity. It is this resonance that has a major influence on the general flow characteristics.

Successful supersonic cavity flow control has been demonstrated in past research using both passive and active flow control methods. A number of studies have successfully proven to mitigate the amplitude of Rossiter mode oscillations through passive flow control methods such as: vertical rods upstream of the cavity [101], subcavities upstream and downstream of the main cavity [102] and trailing edge geometry modification [103]. The methods employing vertical rods and subcavities function by manipulating the upstream shear layer that then interacts with the cavity. The vertical rods have the effect of thickening the shear layer and making it more turbulent due to the structures shed from the rod. These two effects in combination result in a shear layer that is less receptive to the excitation from the Rossiter feedback loop. [101] The suggestion for the subcavities is that they lift the shear layer up in comparison to the baseline configuration due to the shock structure generated by the subcavity. [102] This would likely reduce the amplitude of the pressure fluctuations present in the feedback loop and the shear layer would be less likely to be excited by the acoustic waves impinging on the leading edge of the cavity. The modification of the trailing edge results in weaker acoustic waves since a much smaller portion of the energy is directed back downstream towards the cavity leading edge as part of the feedback mechanism.

The two significant downsides with passive flow control in general are that they cannot be modulated i.e. the scale of the flow control cannot be altered and, they are specifically designed for one flow condition and therefore, at off-design conditions, the flow control performance decreases and introduces extra drag into the system. A third drawback is that they cannot be switched off i.e. the impact on the cavity resonance will always be present, even when it is unrequired. Therefore the ideal flow control is an active system. A number of examples of active flow control have been successfully demonstrated such as leading edge blowing[104], microjets located at the leading edge[65] and localised arc filament plasma actuators (LAFPA) located along the leading edge[59]. The mechanism for the leading edge blowing and microjets are fundamentally based on the same principle as the vertical rods and upstream subcavity explained above. They have the effect of thickening the boundary layer (due to mass flow injection and streamwise vorticity generation) and, to a lesser extent, lifting the boundary layer up relative to the cavity. Both of these lead to a less receptive cavity shear layer and reduce the effectiveness of the Rossiter mode feedback loop. The LAFPA flow control method functions instead on introducing a competing periodic oscillation into the shear layer that disrupts the natural resonance and reduces the amplitude of the resonant frequency and of the overall sound pressure level (OASPL).

The latter of the active flow control methods is used here as the inspiration for using ns-DBD plasma actuators to control supersonic cavity flows. This is the aim of this next section of work.

6.1.1 APPLICATION OF SUPERSONIC CAVITY FLOW CONTROL

As is the case with all of the topics examined in this work, the interest here is in the potential application to the intakes of ramjet propulsion systems. It has been shown previously[8] that a cavity located in a supersonic duct flow, here representing the isolator of a ramjet, can delay the upstream movement of a shock train within the duct when compared to a clean duct flow. The published research[8] does not provide an insight into the reason as to why the cavity modifies the shock train behaviour. It is suggested here that it is a result of the local cross-sectional area change in the duct when the shock train reaches the cavity. This could result in a larger Mach number locally than in the rest of the duct which in turn would allow the shock train to support a larger back pressure and halt the movement upstream. This correlates with Webb et al.[8] where, although there was no in depth discussion, it was suggested that the resonance in the cavity was the reason for the change in shock train behaviour; as the Rossiter resonance results in the shear layer moving deeper into the cavity, increasing the local cross-sectional area "seen" by the flow. This leads us to the reason for examining the flow control of a supersonic cavity, controlling the Rossiter resonance.

There are some drawbacks in including a cavity in an isolator of a ramjet propulsion

system, one of which is the increase in drag associated with the cavity. It has been shown that the Rossiter mode resonance can significantly increase drag in supersonic cavity flows (up to 250%[105]). However it has been suggested that for this shock-trapping capability of a cavity in a supersonic duct flow to exist, Rossiter mode resonance is necessary. Therefore the goal for the application of flow control to a cavity in a supersonic duct would be either enhancing the resonance characteristics of a non-resonating cavity when its shock-trapping capability is required (e.g an increase in pressure detected at the combustor on a real ramjet engine) or disrupting the resonance of naturally resonating cavity when its influence is not required. If successful, either of these techniques would result in a setup where the unwanted drag due to the cavity can be minimised when the cavity does not need to act as a shock-trap. This study will focus on the latter of the two suggested control methods, disrupting a naturally resonating cavity based on the principle explained in the previous section of introducing a competing periodic oscillation into the cavity shear layer.

6.1.2 CAVITY MODEL

The results gathered in Chapter 4 provide some limitations of cavity sizes that will allow an established supersonic flow to form in the wind tunnel. This established flow is crucial to understanding the impact of ns-DBD plasma actuators on the cavity flow. As a result of these earlier results, three cavities were manufactured to test. The length for all three cavities was kept constant, and equal to the height of the test section, H . Three depths of cavities were initially tested: $0.125H$, $0.25H$ and $0.5H$. This gave L/D ratios of 8, 4 and 2 respectively. During testing however it was found that the $0.125H$ cavity was a transitional cavity and so the flow control method, applicable to open cavity flows, could not be tested on this particular setup. The dimensions of the cavities were kept relative to the test section duct height as in reality this ratio is important in terms of what scale of cavity can be used in a supersonic duct flow whilst still allowing the duct to start (see results of Chapter 4).

There are two reasons for the variation in depth of the cavity as opposed to the length. The first is that for the application of interest, "shock-trapping", it is thought that the depth could play a crucial role. This is due to the author's hypothesis that the change in cross-sectional area at the cavity leading edge (relative to the downstream shock train) is the feature that results in the "shock-trapping" phenomenon. Therefore it was thought necessary to examine how the flow control would impact cavities of different depths. Secondly, from the results of chapter 4, the scale of the cavity shear layer is somewhat dependant on the depth of the cavity. It has been suggested previously[101] that thicker shear layers are less receptive to the Rossiter mode resonance and so it was thought important to examine how a variation in shear layer might impact the flow control effectiveness.

Therefore the test cases in this chapter will focus on the two newly designed cavities

that exhibited an open cavity flow field. The measurements recorded for each case are explained below.

6.1.3 EXPERIMENTAL MEASUREMENTS RECORDED

To examine the effectiveness of an ns-DBD plasma actuator as a flow control device for supersonic cavity flow, a number of experimental techniques are used. For flow visualisation the conventional Schlieren setup is employed. This allows any visual change to the cavity flow field as a result of the ns-DBD flow control to be observed. The Schlieren imaging was carried out at a relatively low frame rate of 2kHz for the majority of the testing so as to allow a large enough field of view to be useful. Some limited testing was done at 37.5kHz where the field of view was much smaller. These tests were conducted with a field of view directly above the ns-DBD location in an attempt to examine the frequency domain of the image intensity when the actuator is pulsing. The hope would be to observe the actuator forcing frequency in the Schlieren imaging frequency analysis. Alongside the Schlieren imaging, two techniques were used to directly measure the dominant frequencies present within the cavity. The first is static pressure measurements from Kulite transducers mounted in the floor of the cavity. A single transducer in the floor of the cavity was deemed sufficient as previous studies have shown that the frequency response in the measured static pressure shows the same results at the leading edge, trailing edge and cavity floor.[59] The second, more novel method of measuring the resonant frequencies is a laser vibrometer.

A kulite functions, fundamentally, by measuring the pressure driven oscillations across a diaphragm using strain gauges and, through a calibration process, converting the generated electrical signals to pressures. The larger the pressure the greater the deformation of the diaphragm. To mimic this, a piece of retro-reflective tape was placed across the tapping made for the pressure transducer and the vibrations of it measured using a vibrometer. The oscillation frequencies of this make-shift diaphragm are caused by the same pressures that would be measured by the kulite. The vibrometer measures the size of the vibration in the same manner as the kulite does therefore, although this will give no pressure information, it will allow measurement of the resonant frequencies present in the cavity and the relative magnitude of these frequencies as evaluated in the frequency domain.

Other than proving that the vibrometer works, the main reason for using the vibrometer was to allow measurements to be recorded while the ns-DBD plasma actuators were running. As was observed during the IR measurements taken in a previous chapter (see chapter 5) the ns-DBD actuators emit significant electromagnetic interference (EMI). It was found during testing that the USB connection between the National Instruments DAq system and the PC used would drop out during the operation of the plasma actuators due to this interference. Attempts were made to shield the system from the interference but none were successful. However the laser vibrometer was not as affected by this interference and so could still be operated while the ns-DBD plasma

actuators were active. The final technique used here is surface oil flow visualisation. The primary goal of the oil flow is to characterise the 3-dimensional nature of the cavity and to highlight where within the cavity flow could be considered 2D. However the oil flow was compared between the various test cases as well to examine if any significant differences are observed with and without flow control. Finally, the oil flow results are also compared to CFD results of the cavity flow by examining the relative locations of the downstream vortex edge within the cavity. This can be shown in the oil flow by examining where the oil collects at the downstream region of the cavity and can be compared to static pressure profiles extracted from the CFD on the cavity floor.

Detailed information for each of the techniques used is available in chapter 2 presented previously. The remainder of this chapter will present the data gathered and discuss primarily the influence of the ns-DBD actuators on the supersonic cavity flow while also presenting justification for the use of a laser vibrometer to measure surface pressure frequencies.

6.2 VIBROMETER EVALUATION

The first step was to evaluate the performance of the vibrometer in measuring the resonant frequencies experienced within the cavity flows. This was done using the cavity with an $L/D = 4$ (54mm in length and 13.5mm in depth). There were 4 different available sources that could provide data regarding the resonant frequencies of the cavity. The first is the theoretical prediction of the cavity resonant frequencies, the Heller modified Rossiter equation[55] (see equation 4.3). Based on the wind tunnel freestream velocity, the cavity length and empirically defined values for phase delay factor and the vortex convection speed. The value of the two empirical constants were taken to be 0.25 and 0.57 respectively as these are the most widely agreed upon numbers used in literature. The wind tunnel freestream velocity is calculated from the wind tunnel Mach number and the static temperature. The static temperature in the wind tunnel is calculated from the stagnation temperature (assumed to be equal to atmospheric temperature due to the fundamental operation of the wind tunnel and the assumption of isentropic expansion through the nozzle). The Rossiter frequencies were calculated for two different Mach numbers, 1.8 and 2.0. This was done in order to give a range of possible values that the tunnel could be operating in as the measurements within the wind tunnel suggested that it was operating at Mach 1.8 however the CFD suggested that the nozzle would provide a flow at Mach 2.0 (see chapter 3 for more detail). The second theoretical source of cavity resonance data is CFD modelling. The modelling methodology is largely the same as was demonstrated in Chapter 3 (see chapter 2 for details regarding the fundamental modelling methods). The difference with the CFD in this chapter was that it was run unsteady rather than as a steady simulation. This was necessary since the cavity flow is fundamentally an unsteady process and as such had to be modelled in this way. The issue with unsteady

CFD simulation is often the computational resource needed to run the simulation for an appropriate length of time. Using STAR CCM+, the only available unsteady solver is an implicit unsteady solver and so this was used for the simulation. It is suggested in the STAR CCM+ manual that the time step should be calculated through the ratio of the base grid size divided by the reference velocity of the flow. This requirement is based on the assumption that the Courant-Friedrichs-Levy (CFL) number should be kept to a maximum of 1 for implicit unsteady simulations. The CFL number is a term that appears due to the discretisation of the governing equations and if it is greater than 1, can lead to indefinite growth in the solution. The grid size was not changed from the mesh convergence study performed in Chapter 3 and the reference velocity is taken as the freestream velocity within the tunnel. The result is a timestep of $3.125\mu\text{s}$. Due to the very small time step required, a limited length of real time could be simulated. This is simply a limitation of the computational power available and the time available to run the simulation. The issue here is that the frequency resolution of the frequency domain analysis carried out on the CFD results is dependant on the overall sample time, the frequency resolution is the reciprocal of the time period sampled. This places a limitation on the relevance of the CFD data, however it will still provide useful results to confirm those of the other available sources.

From the CFD data, the pressure measurements and the vibrometer measurements a power spectral density was calculated using the Welch method in order to provide the frequency response within the cavity. If we first examine each set of results individually, starting with the theoretical Rossiter modes, calculated using equation 4.3. Table 6.1 shows the range of these calculated modes where the lower limit corresponds to Mach 1.8 and the upper limited corresponds to Mach 2.0.

The next set of results to present are those gathered from the frequency domain analysis of the CFD simulation output. The raw data used is a time history of pressure recorded in the centre of the cavity floor. This location was used since it was the position at which the experimental measurements were also recorded. Figure 6.1 presents the output of the frequency domain analysis. The first thing to note is that the frequency resolution of this data set is extremely limited by the very low real time sample length. The sample time was limited to 2.1875ms which, in turn, leads to a frequency resolution of only 457Hz in the frequency domain. Therefore although it is possible to extract the peak resonant frequencies from the CFD, the limitations of this

Rossiter Mode	Resonant Frequency Range (Hz)
1	2095-2166
2	4889-5055
3	7682-7944
4	10833-10475

TABLE 6.1: Rossiter resonant frequencies calculated from the Heller modified Rossiter equation.

data must be made clear. With this in mind, an immediate observation is that the two resonant peaks observed in the CFD data correspond reasonably well to the 2nd and 3rd Rossiter modes presented in table 6.1.

The next set of data examined is the vibrometer measurements. As mentioned above, the vibration data recorded was from a membrane in the form of retroreflective tape placed across a pressure tapping in the centre of the cavity floor. The orientation of the vibrometer was ensured to be vertically downwards (checked using a digital inclinometer) towards the cavity floor. This was done so that the laser beam was perpendicular to the cavity floor surface, resulting in a strong signal returning to the vibrometer. The results of the vibration measurements analysed in the frequency domain are shown in figure 6.2.

There are two important observations that can be made here. The first is that the significant resonant peaks within the PSD plot align well with the predicted Rossiter modes and the information extracted from the CFD simulations. This suggests that the vibrometer measurements can be trusted to give accurate measurements of the resonant frequencies within the cavities as the theoretical results are well known to provide accurate predictions of the observed values during testing. The second observation is that there is a noticeable peak at 21Hz that is not predicted by the CFD or the theoretical equations. This peak is part of the structural response of the wind tunnel and not the fluid mechanics of the system. Figure 6.3 shows the structural response from a bump test conducted on the wind tunnel. This involved striking the wind tunnel with a mallet and monitoring the vibrational response. The resonant frequency observed here is approximately 11Hz. It is believed that the 21Hz peak in the vibration measurements recorded within the cavity correspond to this structural resonance.

The final source of data is the Kulite pressure measurements. These were recorded with a Kulite pressure transducer from a pressure tapping in the centre of the cavity

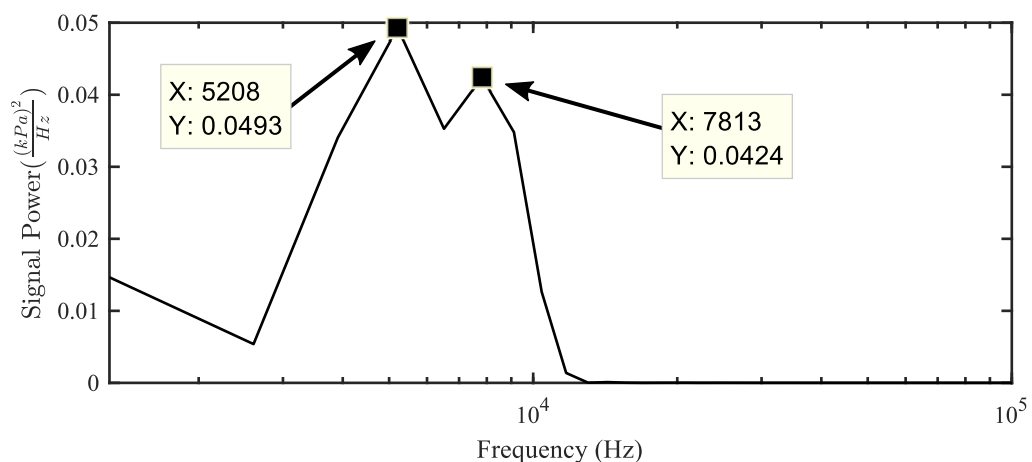


FIGURE 6.1: Frequency domain analysis of unsteady pressures at the centre of the cavity floor, extracted from CFD simulations.

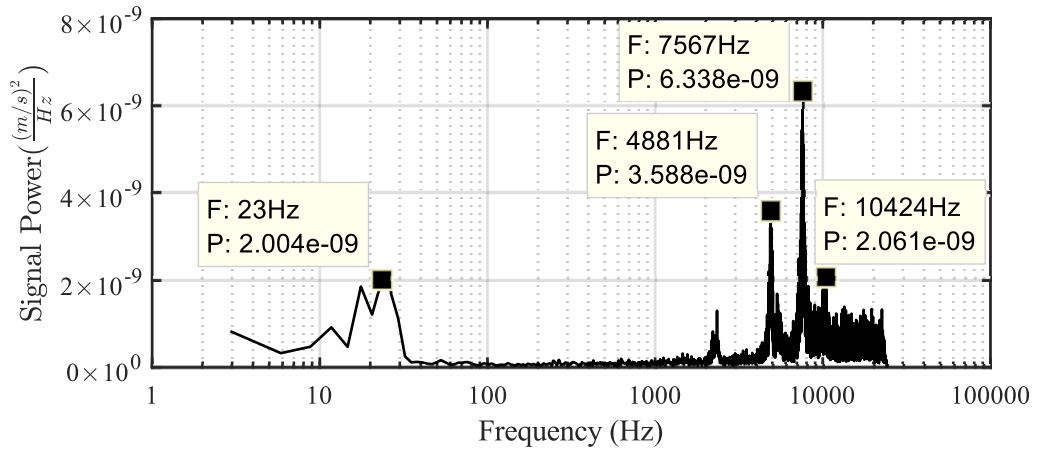


FIGURE 6.2: Frequency domain analysis of vibration measurements recorded at the centre of the cavity floor.

floor. The tapping was 23mm in depth and 2mm in diameter. The resulting frequency response from the pressure measurements is shown in figure 6.4.

The immediate observation is that the peak resonant frequencies observed for these measurements do not necessarily agree with those of any of the previous three sources. If the four sources are plotted side by side this becomes clear, see figure 6.5. Although the second peak resonant frequency appears to agree with the fourth predicted Rossiter mode, this is believed to be coincidental and not a true measurement. Based on the fact that three out of the four measurements agree reasonably well, it is assumed that the fourth measurement is where the fault lies.

The reason for the difference in the pressure measurements was found to be a result of a phenomenon called “Organ pipe resonance”. This is a form of acoustic resonance that is observed within pipes i.e. in this case the tapping between the cavity floor and the surface of the pressure transducer. The frequency of this acoustic resonance can be calculated based on the speed of sound and the length of the pipe by

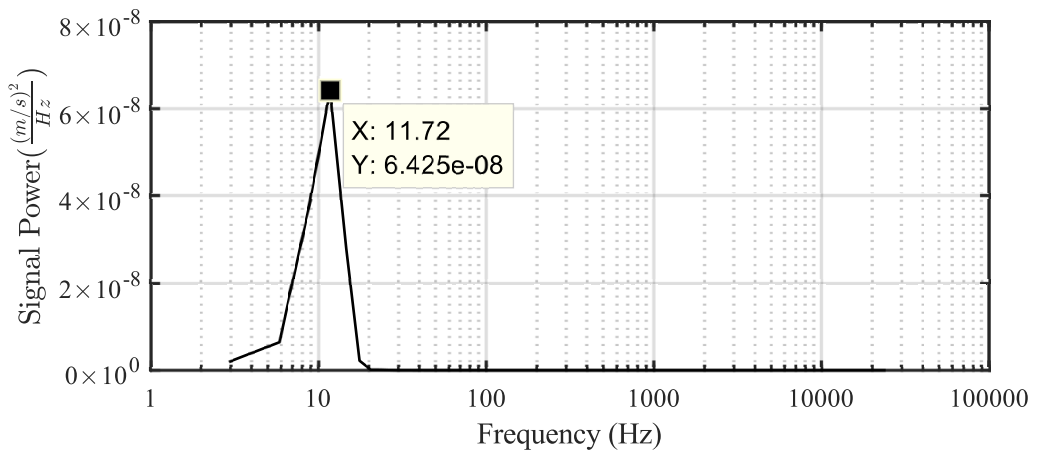


FIGURE 6.3: PSD of the laser vibrometer data recorded during a bump test conducted on the wind tunnel structure.

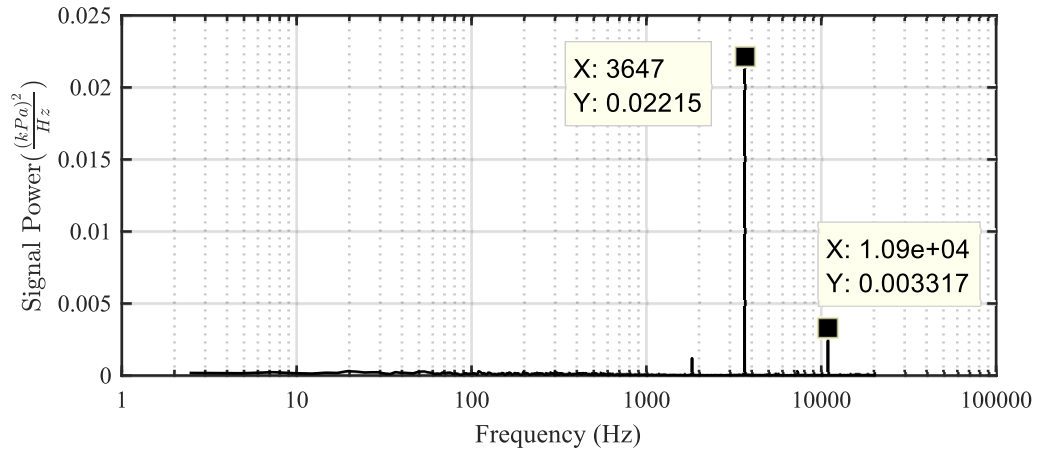


FIGURE 6.4: Frequency domain analysis of pressure measurements recorded at the centre of the cavity floor.

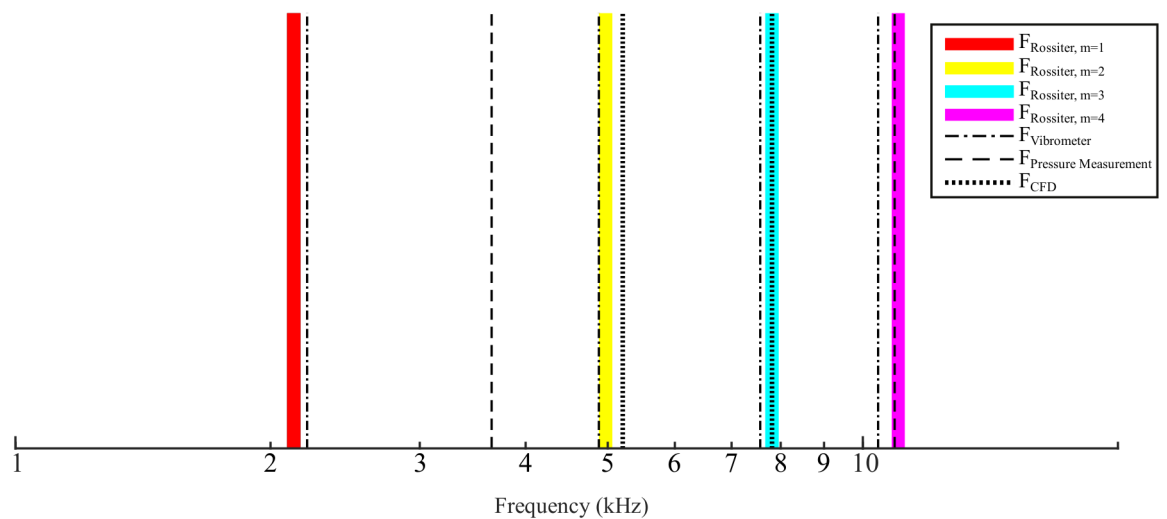


FIGURE 6.5: Side by side comparison of cavity resonant frequencies observed using different techniques.

equation 6.1:

$$f = \frac{nV}{4(l + \Delta l)} \quad (6.1)$$

where n is the mode number, V is the speed of sound and l is the length of the pipe. The term Δl is called an end correction. This is necessary as the pipe has an additional virtual length due to the fact that air immediately outside of the pipe is also involved in the acoustic oscillation. From theory, this end correction is equal to $0.03D$ where D is the diameter of the pipe (the diameter of the tapping in this case). If the first two modes of this organ pipe resonance are calculated for the tapping length used, the first two resonant frequencies are found to be 3612Hz and 10836Hz. If these two frequencies are included in the side by side comparison of the cavity resonant frequencies plotted previously, see figure 6.6, an interesting and useful result is observed. These two calculated frequencies align very well with the peak resonant frequencies observed in the pressure data. This results in the cavity resonant tones being unable to be separated from the noise in the remainder of the frequency domain analysis as it is dominated by these organ pipe resonant frequencies.

Based on these different sets of results, it is believed that the vibration measurements can be considered to provide an accurate measurement of the cavity resonant tones. This is not only an interesting result in its own right as it has never been used before as a technique for measuring fluid mechanic driven resonant frequencies, but is also helpful for the remainder of this work. It will allow the potential impact of the ns-DBD flow control on the cavity resonant frequencies to be examined which is not possible with the pressure measurements as explained earlier. The next step is to examine the baseline cavity flow field and the impact of ns-DBD flow control in more detail.

6.3 OIL FLOW VISUALISATION

The oil flow visualisation was performed with the aim of examining the three dimensionality of the flow field. Images were also recorded for ns-DBD flow control cases. Figure 6.7 presents a time history of the oil flow during the wind tunnel start up. The final two images provide a representation of the steady state flow within the cavity.

The main observations to be made regarding figure 6.7 is the largely 2D nature of the cavity. The only non-uniform regions are those near the cavity walls at the top and bottom of each image and the region in the vicinity of the screws that hold the cavity floor in place. The disturbance near the screws is likely to be a combination of the disturbance due to the screw itself but also as a result of the unsteady flow near the corner. In the region where the vibrometer and pressure measurements have been recorded, the flow is uniform and two dimensional. Figure 6.8 shows the comparison of the approximate location of the trailing edge of the vortex structure within the cavity extracted from the oil flow and the location of the same feature extracted from

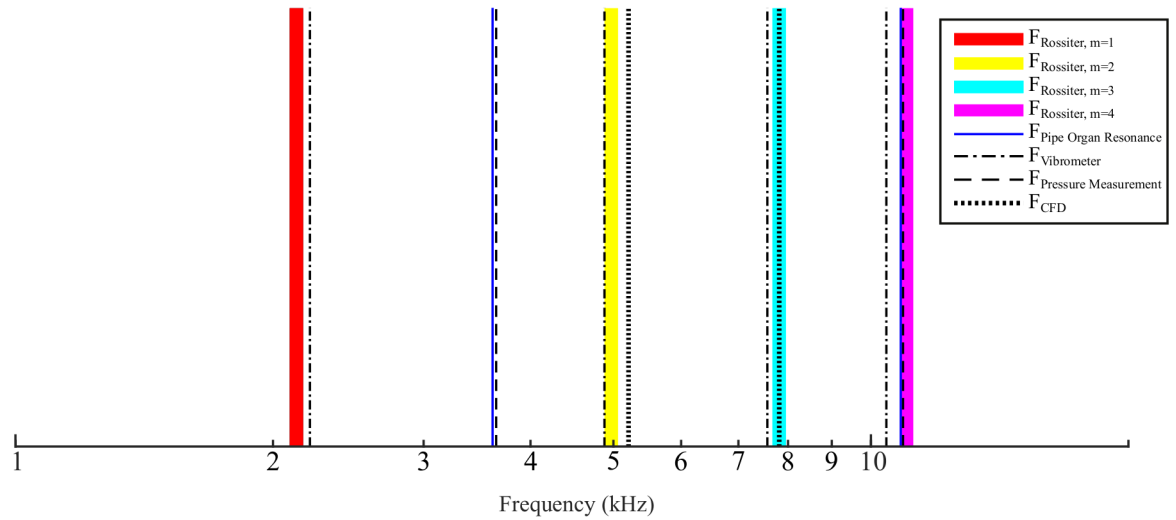


FIGURE 6.6: Side by side comparison of cavity resonant frequencies observed using different techniques.

the CFD. The location extracted from the oil flow is based on the area where the oil begins to collect in the downstream region of the cavity floor. The location extracted from the CFD is chosen as the location where the low pressure visible within the cavity begins to rise i.e. where the flow begins to move towards stagnation conditions near the cavity trailing edge. Another point that should be noted is the triangular region in the centre of the cavity. This was simply a portion of tape that was used to protect the pressure tapping in the centre of the cavity floor. This minimised the impact that this tapping might have on the oil flow visualisation and prevented any oil from clogging this tapping for future use. The oil flow experiences minor disturbances due to the presence of this slight protrusion on the cavity floor but the effect is minimal and is not believed to change the global results.

The next step was to examine if any significant difference was visible in the average oil flow image as a result of ns-DBD flow control. Figure 6.9 presents the steady state oil flow visualisation for each of the ns-DBD control frequencies examined. The focus is on the central region of the cavity where the flow is uniform and unaffected by the screws/side-walls of the cavity. In this region there is no observable change between the baseline case and any of the cases with pulsed ns-DBD flow control. There is no evidence of any disturbances introduced into the flow as the key observable feature, the downstream edge of the vortex, does not change from case to case.

These results were not unexpected as it is likely that any impact that the ns-DBD actuators may have on the cavity will be limited to the cavity shear layer. It is thought unlikely that the flow properties relating to the vortex within the cavity will change as a result of the ns-DBD flow control. However it was useful to examine the cases using this visualisation technique incase there were some unexpected results due to the ns-DBD operation for example additional disturbances near the edge of the cavity (in the region between the edge of the ns-DBD electrode and the cavity wall).

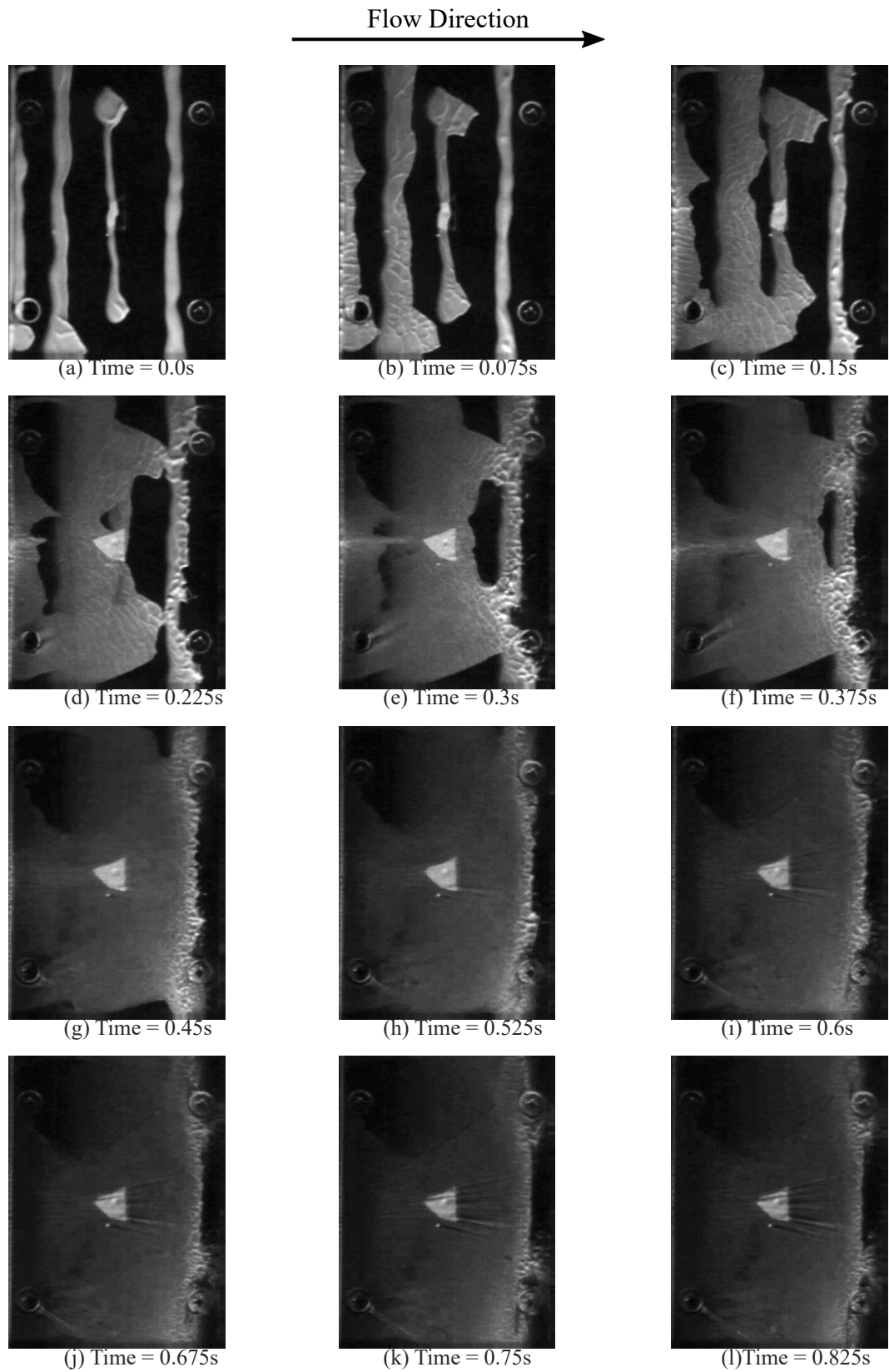


FIGURE 6.7: Oil flow visualisation of the cavity floor at various stages in the wind tunnel starting process, including the final steady state flow field.

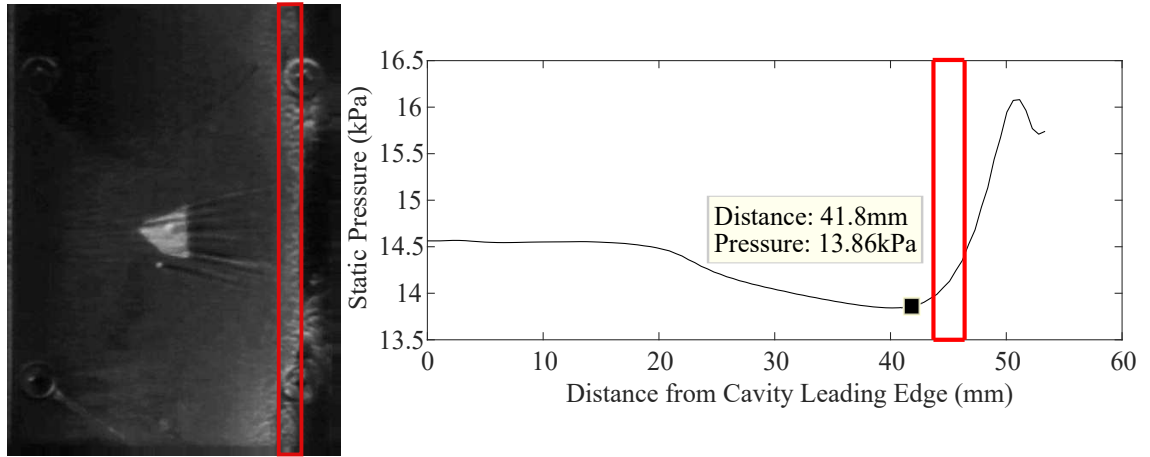


FIGURE 6.8: Comparison of the separation point predicted from the 2D CFD simulations and the separation location extracted from the oil flow visualisation. The red region on both the oil flow image and the CFD static pressure plot shows the separation location as suggested by the oil flow.

6.4 SCHLIEREN IMAGING

6.4.1 HIGH FREQUENCY SCHLIEREN IMAGING

Initially, the high frequency images in the region directly above the ns-DBD actuator were examined. This high frequency imaging was restricted to a small field of view due to the restrictions imposed by the hardware when recording with a frequency large enough to accurately capture useful information in the frequency domain for this flow field. However, this type of image acquisition can show the region of influence of the DBD actuators by highlighting the areas that the frequency of forcing is visible in the frequency domain. Figure 6.10 illustrates the response in the frequency domain at each of the forcing frequencies tested. For each case there is a high amplitude region at the discharge location of the DBD actuator. This highlights the region where the impact of the DBD actuator will be strongest as the amplitude of the forcing is most significant here.

The other key feature highlighted in figure 6.10 is that the region above the actuator, in what would be the freestream flow of the wind tunnel, experiences forcing to varying degrees. For larger forcing frequencies, particularly 2 and 3kHz, the actuators influence (high amplitude regions) appears further away from the actuator surface than the lower frequencies. This is shown by the white fringes in the PSD visualisation above the actuator surface for these two frequencies. These fringes visualise the propagation of the blast waves generated by the ns-DBD actuators. The reason for the appearance of this feature is not clear but it is thought to be a result of the image acquisition than a physical feature produced by the plasma actuators. The sensitivity of the Schlieren system may have shifted slightly during the number of test cases used and so this is thought to be the likely cause of this effect. In reality, at higher frequencies the surface of the actuator generates more heat than at lower forcing

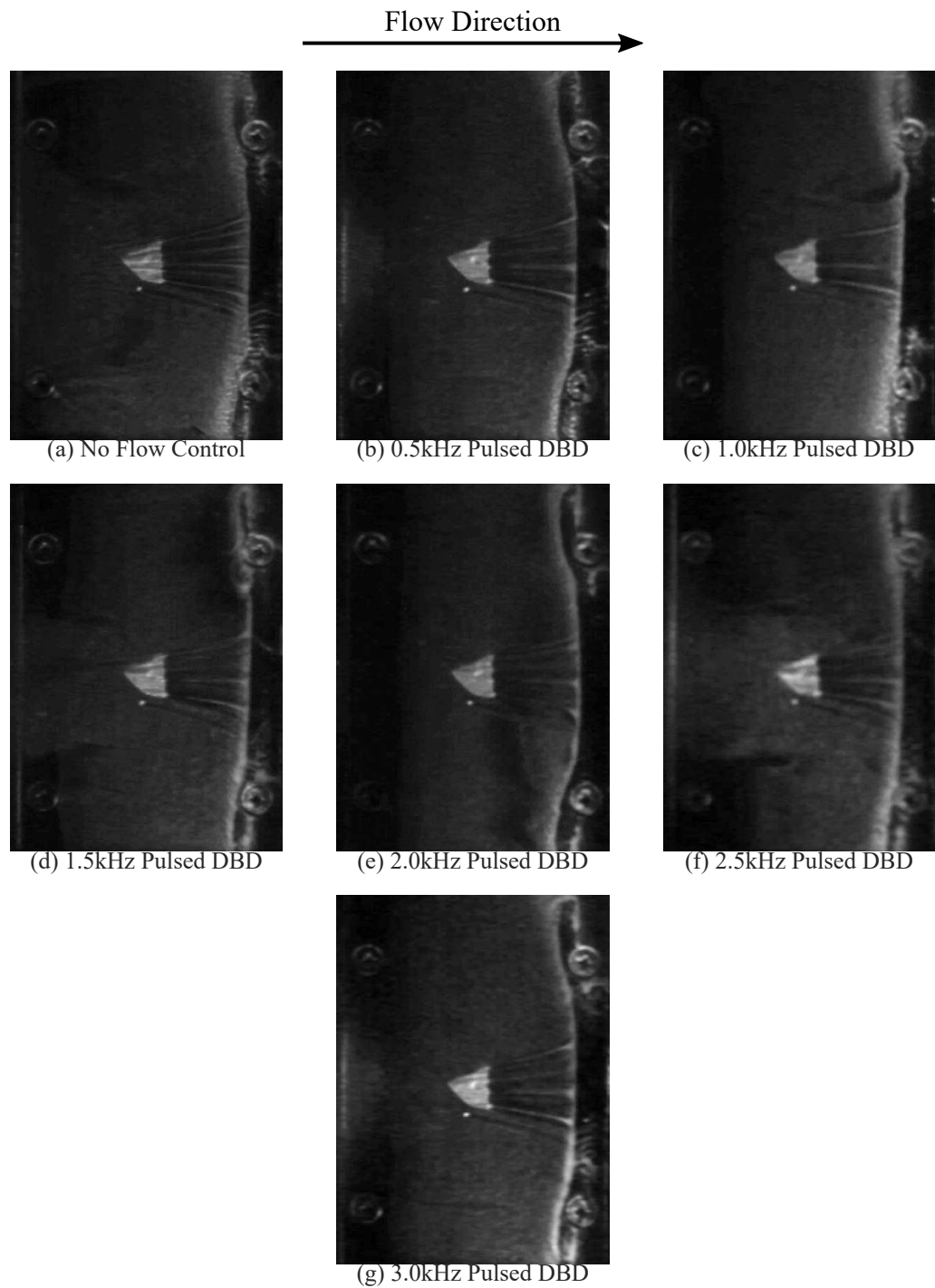


FIGURE 6.9: The steady state oil flow visualisation for each of the flow control forcing frequencies examined.

frequencies. This would result in a blast wave with decreasing strength rather than increasing strength, which is the suggestion of these images. The intensity of these fringes relative to that at the actuator surface is also significantly less, therefore it is assumed to be of no consequence for the remainder of this work.

The aim of this set of results was to examine the main region in which the ns-DBD actuator exert an observable degree of flow control. The results suggest that there is a sizeable area close to the wall affected by the discharge. This suggests that the actuator could influence the boundary layer as it approaches the cavity leading edge and becomes the cavity shear layer. The control strategy is to introduce competing frequencies into this fluid layer, disrupting the natural resonance that occurs within the cavity.

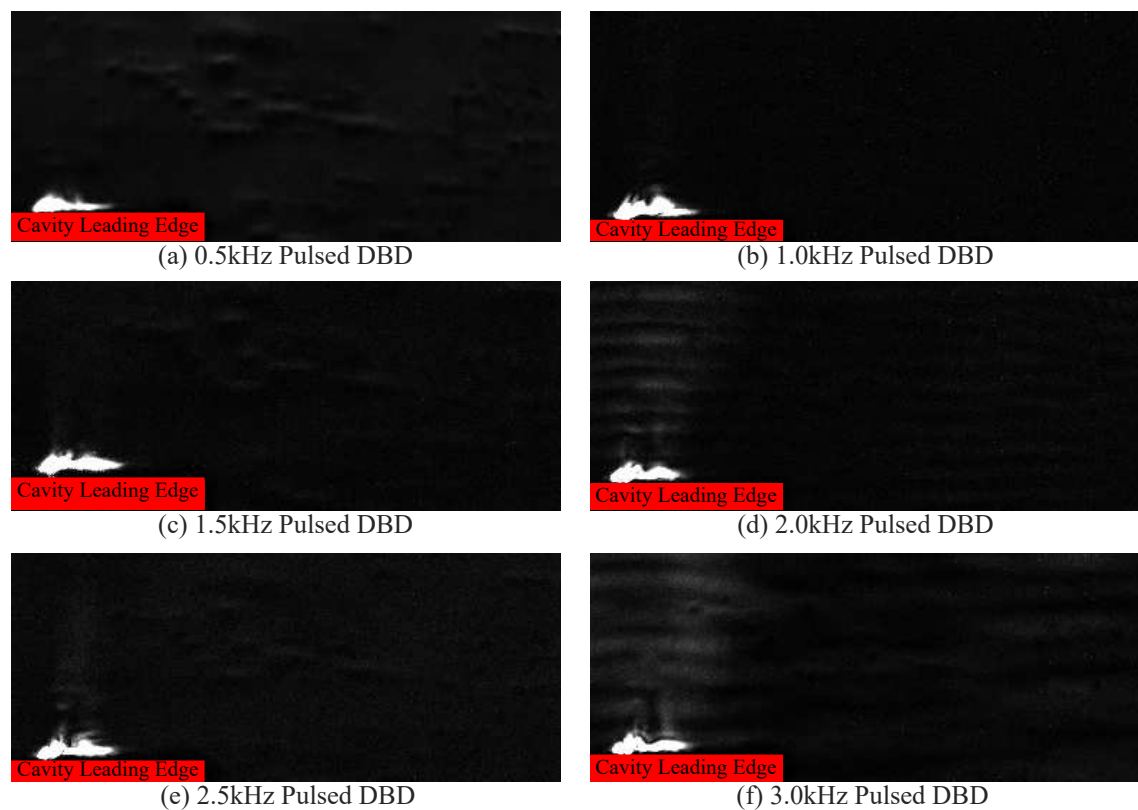


FIGURE 6.10: Visualisation of the frequency domain extracted from Schlieren imaging of the region above the ns-DBD plasma actuator electrodes.

6.4.2 TIME AVERAGED SCHLIEREN

The next set of results examined were the time averaged Schlieren images. As these were recorded at a significantly lower frequency (2kHz) they provided visualisation for a much larger region of the flow. The images display the entire cavity flowfield along with the area upstream and downstream of the cavity also visible. Figure 6.11 presents a time averaged Schlieren image for each of the forcing frequencies tested. All sets of images show the same fundamental flow features. Arrow 1 highlights the reflection of a shock wave generated where two sections of the wind tunnel floor

meet. Arrow 2 shows the separation shock that is generated where the boundary layer transforms into the cavity shear layer at the cavity leading edge. Finally, there is the aforementioned shear layer highlighted by arrow 3 in image (a).

Examining the different forcing cases, there is no clear influence on flow field as a result of the ns-DBD actuator operation. There is no noticeable change in the growth rate or elevation of the shear layer and there is also no significant difference in the cavity leading edge shock structure. Time averaged Schlieren provides limited data to investigate the flow field, however if there was any significant change in the flow structure as a result of the ns-DBD flow control it would be apparent in the time-averaged imaging. These results suggest that the ns-DBD have no observable impact on the cavity flow in the configuration that is being tested. The vibrometer measurements are examined next as they will provide a more sensitive, quantitative view of the changes, if any, which occur to the cavity resonance during the operation of the ns-DBD actuators.

6.5 VIBROMETER MEASUREMENTS

As discussed in section 6.2, the vibrometer is used to measure the vibrations of a membrane in the centre of the cavity. The amplitude of these vibrations will be proportional to the amplitude of the frequencies present in the pressure fluctuations within the cavity. As such, although the actual pressures can not be measured here, the general trend of any change in the pressure oscillation amplitude can be measured by comparing the vibration spectrum across various test cases. If the amplitude of a component of the PSD calculated in the frequency domain changes, then this corresponds to a change in the amplitude of the pressure oscillation.

Figure 6.12 presents the average PSD recorded at the centre of the cavity floor for each of the forcing frequencies tested. These plots show that the amplitude of each of the four resonant frequencies highlighted do not change significantly. There are slight variations observed such as the amplitude of the 7.6-7.7kHz mode varying between 5.15×10^{-9} and 1.41×10^{-8} , however these variations are small and would not constitute a result of any real significance in comparison to other attempts at flow control applied in a similar manner[8]. These results combined with those presented earlier of the oil flow visualisation and the time averaged Schlieren imaging suggest that the configuration of ns-DBD plasma actuator used in this application has little to no effect on the overall flow field within the cavity.

6.6 CONCLUSIONS

The primary aim of this chapter was to investigate the effect of applying ns-DBD flow control to supersonic cavity flows. During this testing, the application of a laser Doppler vibrometer for measuring pressure driven resonant frequencies was tested. It has been shown through comparison of the laser Doppler vibrometer results with

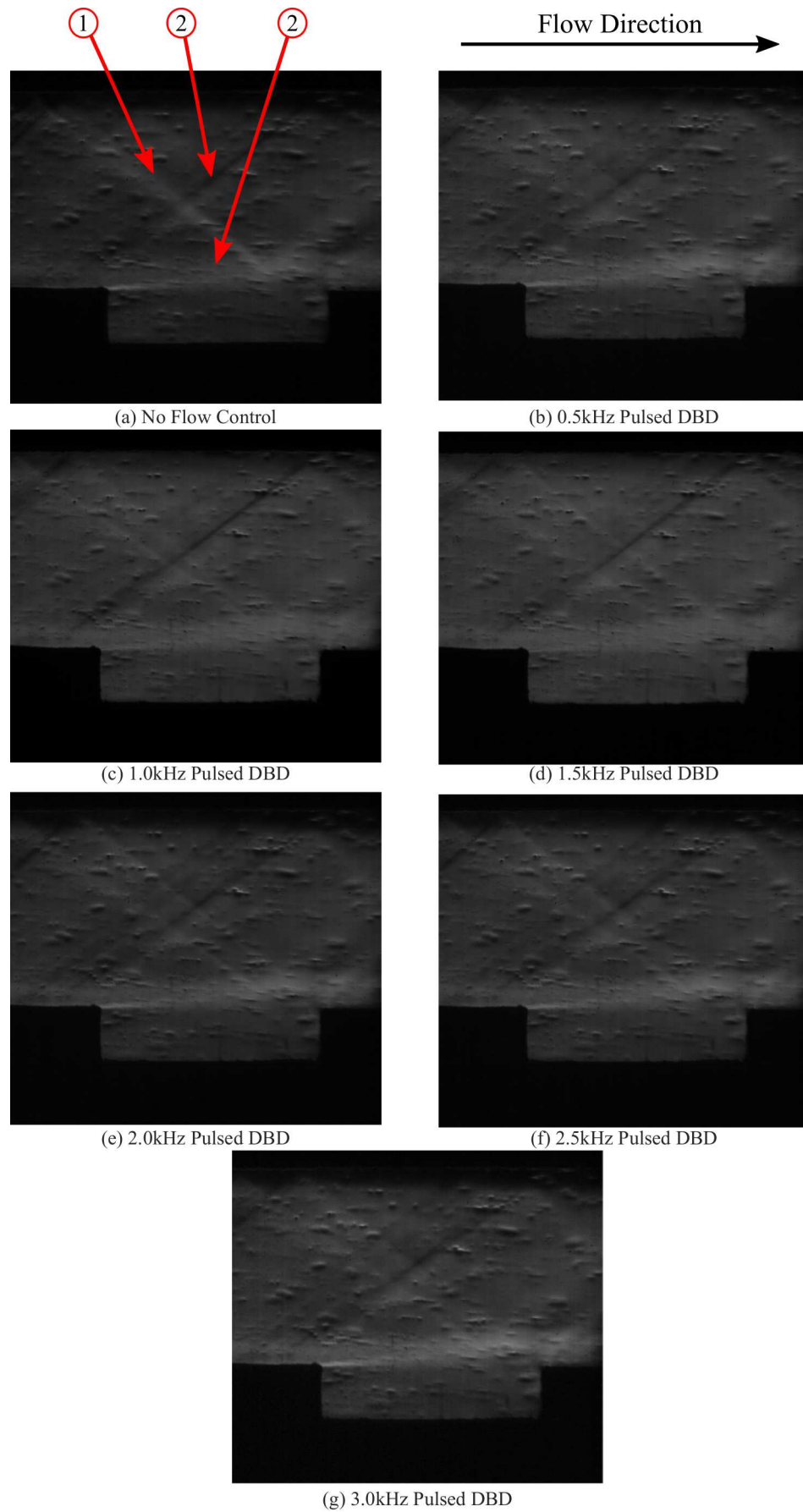


FIGURE 6.11: Time averaged Schlieren imaging across the entire cavity flow field for each of the forcing frequencies examined.

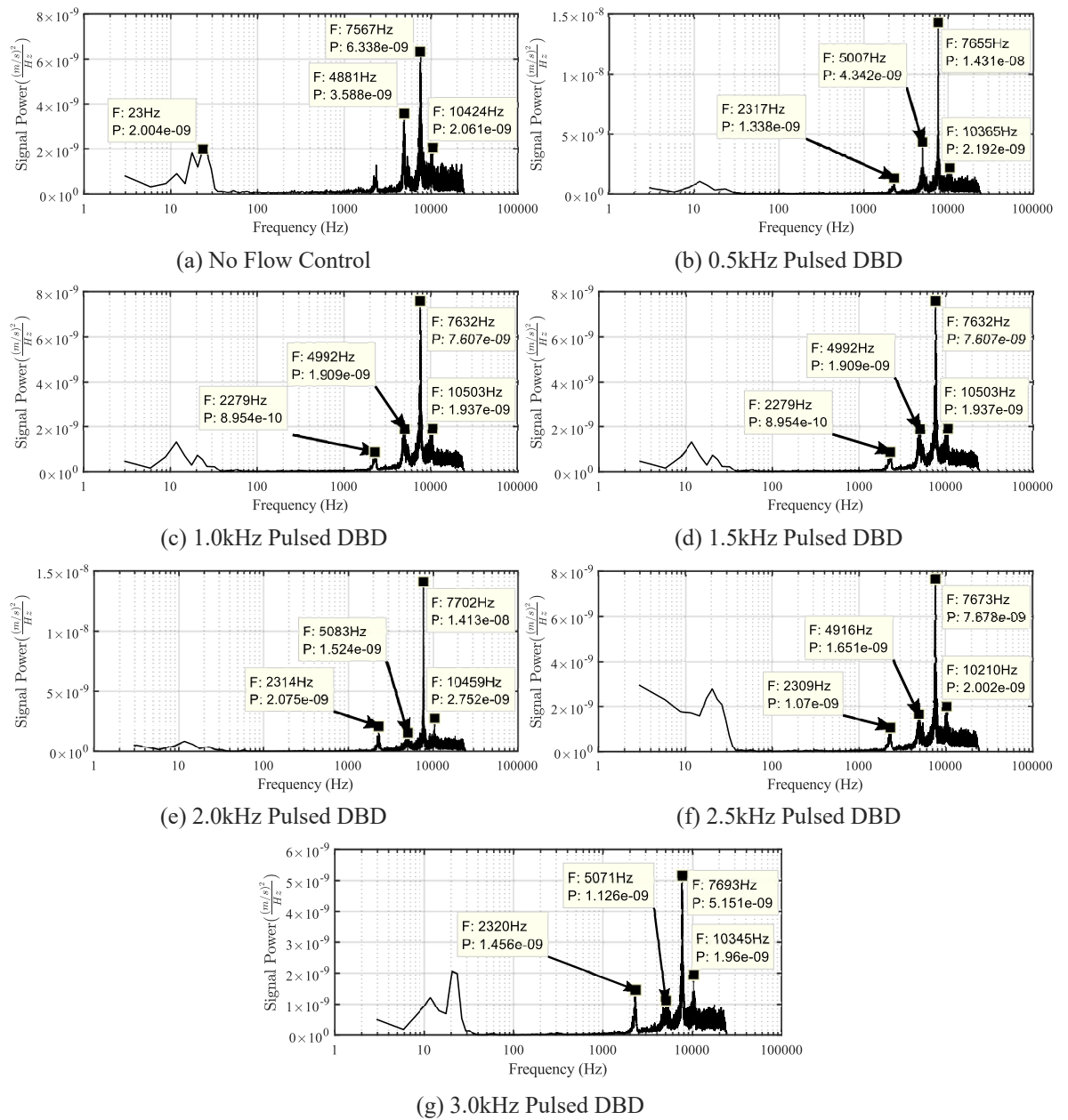


FIGURE 6.12: PSD of the vibration measurements captured from the centre of the cavity floor for each of the various forcing frequencies tested.

theoretical predictions and CFD results, that this method does provide accurate results for the configuration used. The Rossiter modes were found to be consistent between all of the data sets. This presents a novel approach to the measurement of resonant frequencies within a cavity that could prove useful to future studies. There is however further work required to completely test this new method. Important future work on this topic should include comparison against other experimental sources such as transducer measurements or fast response PSP. It would also be interesting to attempt to calibrate the velocity signals measured by the vibrometer using known pressure measurements in order to allow the vibration data to be converted to absolute pressure values.

The flow control itself was found to be ineffective in the setup used for this study. In terms of the proposed reasons for the lack of effect on the flow, there are three properties of the flow control that should be discussed: the region of application, the mechanism of the flow control and its effectiveness for this application, and the strength of the application. Regarding the region of application, it has been shown previously that energy deposition based flow control applied directly upstream of a supersonic cavity can produce effective flow control[8]. It is therefore a safe assumption that the location of the flow control was not the reason for the lack of influence. The second point is the mechanics of the flow control application, in this case a source of pulsed energy deposition that results in a localised temperature increase along with an associated blast wave. The pulsed nature of flow control for this application has been widely demonstrated in numerous studies, using a variety of methods such as jets and LAFPA's and so this is not deemed to be the reason as to why the method was unsuccessful either. One possible failure in the mechanics of the application is that the energy deposition runs the entire width of the cavity, rather than in discrete lengths. Previous studies of energy deposition based methods have suggested that the pulsed nature of the flow control is the reason for its effectiveness, however it is possible that this is actually a result of vorticity generated between these discrete lengths of plasma rather than the pulsed forcing.

The final point, the strength of the interaction, is believed to be the fundamental reason as to why the actuators have proven ineffective in this scenario. The strength of the interaction of these actuators is directly related to both the amplitude of the nanosecond voltage pulses and also the thickness of the dielectric material used. However, these two requirements are somewhat contradictory to one another as the thinner the dielectric, the lower the breakdown voltage of the actuator and thus the lower the voltage that can be safely used to generate the plasma. Higher voltages can be used but require thicker dielectrics which generally result in a weaker generated pressure wave. Therefore (with the current materials available to use) the strength of the interaction created is limited. With the currently available materials the pressure waves generated are simply acoustic waves i.e. the pressure differential generated across the wave is small. For some applications such as boundary layer separation control this has proven to be sufficient, however for this application it is now believed

that this is not the case.

These results do not preclude the use of ns-DBD plasma actuators for this flow control application, however there are two key features that should be examined to prove/disprove that they can in fact be effective. The first is to investigate the effect of a ns-DBD actuator with numerous discrete lengths that act in the same manner as physical tabs used for flow control. The second aim would be to identify materials for the construction of the actuators (along with a more powerful pulse generator) that allow a larger voltage to be used, thus producing stronger pressure waves. These stronger pressure waves may prove to be sufficient for the actuator to display a measure of control on the supersonic cavity flow examined.

CHAPTER 7

LASER ENERGY DEPOSITION FOR THE SUPPRESSION OF SEPARATION ON AN AXISYMMETRIC CONE INTAKE

The previous chapters have focused on ns-DBD plasma actuators and their application supersonic cavity flow control. The aim, as discussed in the introduction, is to investigate techniques that can improve ramjet intake performance. This chapter looks at a different method of accomplishing the same goal; using laser energy deposition to improve ramjet intake pressure recovery.

7.1 SUPERSONIC INTAKES AND THE APPLICATION OF FLOW CONTROL

It is important to understand the background regarding the operating principles of modern supersonic intakes and the associated difficulties. The overall aim of any supersonic intake is to decelerate the incoming flow to subsonic speeds. A well designed intake will aim to accomplish this with minimal loss in total pressure. There are always losses in supersonic intakes as compression is achieved (to varying degrees) as a result of shock waves, and shock waves are associated with increasing entropy. A large proportion of the total pressure loss experienced by an intake is due to the terminating normal shock that will finally decelerate the flow from supersonic to subsonic. The earliest supersonic intakes, known as pitot intakes, used just a single normal shock to decelerate the flow to subsonic speeds which, although functional, was not an efficient approach [73]. Modern supersonic intakes use a series of ramps to compress the air more gradually through a series of oblique shocks, but still terminated by a normal shock. This improves the total pressure recovery due to the non-dimensional relationship between total pressure drop across a normal shock and upstream Mach number (shown in a previous chapter, see figure 3.7). These types of intakes operate in three different modes: subcritical, critical and supercritical. Each of these modes is defined by the location of the terminating, normal shock relative to the intake cowl. Critical operation refers to the design point of the intake, at which the normal shock is located at the lip of the intake cowl. Supercritical

operation occurs when the normal shock is located within the supersonic diffuser and occurs when the pressure at the entrance to the combustor is lower than the design condition. At this condition the normal shock is located within the internal section of the intake. Although at this condition the intake will operate less efficiently than the design condition; the condition remains a stable operating point. Subcritical operation refers to the case where the normal shock is located upstream of the intake cowl and can occur if the pressure at the combustor is larger than can be supported by the design compression system. At this condition flow spillage occurs around the intake increasing drag. This mode is not a stable condition and is associated with flow instabilities. All of these conditions are shown diagrammatically in figure 7.1.

As highlighted above, an issue with the subcritical operation mode are flow instabilities. These stem from the interaction between the boundary layer and the generated shock waves. This interaction leads to shock-induced separation which can have significant effects on the performance of the intake, see figure 7.2 for a representation of this type of flow field. One of the key flow phenomenon resulting from the interaction between compressible flow features, such as shock waves and the boundary layer, is inlet buzz. Buzz here refers to a self-sustaining shock oscillation that can lead to, amongst other things, a drop in intake pressure recovery. This phenomenon was first observed by Oswatich[106] in 1947 but the two different types of inlet buzz were later explained in more detail by Ferri et al.[107] and Dailey[108]. The two different types of inlet buzz are known as the Ferri criterion or "little buzz" and the Dailey criterion or "big buzz". "Little buzz" was suggested to be a result of the shear layer originating at the triple point of the cone tip shock and the separation shock. This shear layer will generate vortex structures within the intake and reduce the intake mass flow. "Big buzz" is a result of the interaction between the boundary layer on the central compression cone and the terminating shock wave when the intake is operating in subcritical mode.

The key source of the two above phenomenon is the boundary layer separation present on the external compression ramp. Therefore it is clear that if the boundary layer separation could be reduced, the impact of these two instabilities would also be reduced. This is the intake performance improvement opportunity that this chapter will focus on, the reduction of separation on the external compression ramp using active flow control.

A number of different methods for flow control have already been considered for this application. A variety of passive flow control techniques have been applied to shock-boundary layer interactions in general such as microramps[109][110] and vortex generators[12]. In particular, vortex generators were investigated experimentally by Vyas et al.[111] as a method to improve supersonic intake performance with regard to reducing the impact of these instabilities and improving pressure recovery by energising the low momentum boundary layer. They found that, when placed in certain locations, vortex generators could result in a thinner boundary layer and a

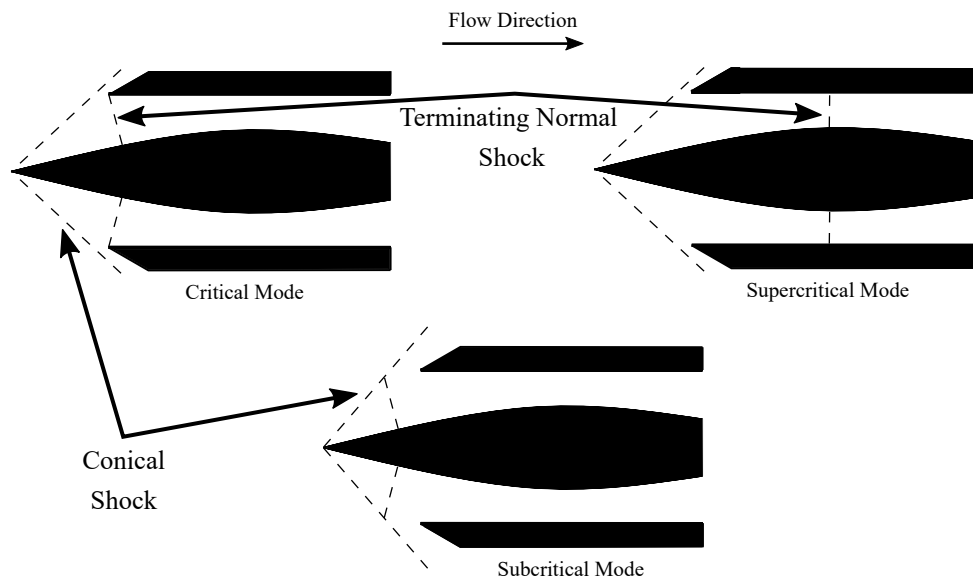


FIGURE 7.1: Illustration of the three supersonic intake modes of operation

reduction in shock structure unsteadiness. However it was found that the pressure recovery of the intake did not improve but actually worsened. Another common flow control method that has proved effective in improving the operability of supersonic intakes is boundary layer bleeding[112],[113]. This usually involves introducing pores onto the surface of the compression ramp to remove the low momentum boundary layer flow. A significant consequence of this method in reality however is that the inlet area has to be increased in order to provide the same mass flow to the engine core. This would result in an increase in the weight and drag associated with the propulsion system[111]. This work will look at an alternative to the flow control methods explained above: upstream laser energy deposition.

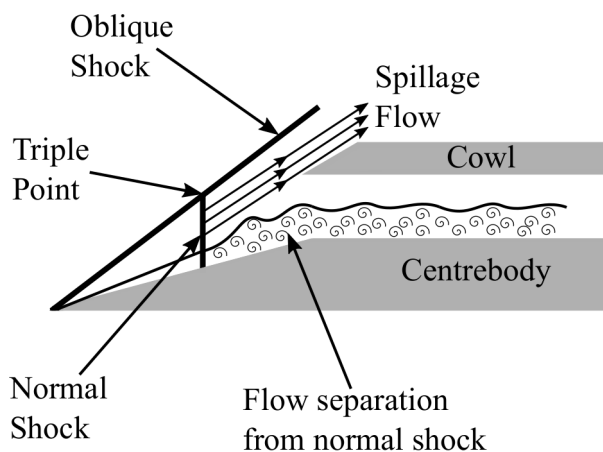


FIGURE 7.2: Illustration of the compressible, viscous flow field observed for an intake operating in the subcritical regime.

7.2 LASER ENERGY DEPOSITION FOR FLOW CONTROL

Laser induced gas breakdown was first observed by Damon et al.[114] in 1963. Laser energy deposition can control flows either through the interaction of generated blast waves with the flow or through its heating effects on other flow characteristics.[77] Laser light can add significant energy to fluid flow due to initiating gas breakdown; the process can be broken down into 4 separate steps. The first two steps refer to the gas breakdown itself while the last two describe how this can affect the fluid flow. The first step is the ionisation of the initial molecule of gas. A molecule will be ionised when struck by multiple individual laser photons; multiple photons are required due to the high ionisation energy of these molecules.[115] It has been shown by Panarella et al.[116] that the ion density (i.e. number of ions per unit volume) is proportional to the laser light intensity (see equation 7.1). For this reason it is preferred that when using laser energy deposition, the laser light is focused using a lens. This will increase the laser light intensity at the point of breakdown for the same laser power.

$$N_i \propto N_a (Ih\nu)^{N_0} \quad (7.1)$$

Once the first molecule has been ionised, and therefore released an electron, step 2 can take place. The electron that is released can absorb light energy and this “excited” electron will then collide with another molecule and ionise it. This collision will release further electrons and the process can repeat itself. The combination of this ionisation and the ongoing multi-photon ionisation is known as cascade ionisation.[117] These two steps describe the process by which the laser energy generates the first plasma in the fluid flow. The plasma region created absorbs the laser light and the next “layer” of gas molecules between the plasma and the laser source ionises in the same manner as the first. This process repeats itself over and over again to form a distinct region of plasma in the fluid. As the plasma absorbs the laser light, the temperature rapidly increases and this generates a blast wave. This rapid heating that results in a blast wave is a very similar process as that observed for the ns-DBD’s in chapter 5.

It has been shown[118] that equation 7.2 can be used to approximate the laser power needed for laser induced breakdown in air:

$$P_t = \frac{K_c I_i (\omega^2 + \nu_m^2)}{0.11 \tau \nu_m} \quad (7.2)$$

where P_t is the threshold power, K_c is the critical number of electron generations, I_i is the energy spent per ion pair generation, ω is the frequency of the laser, ν_m is the collision frequency and τ is the duration of the laser pulse.

Laser energy deposition when used for flow control can be split into two distinct variations: continuous and pulsed. The method of gas ionisation and blast wave generation described above describes the pulsed mode of operation. The continuous

mode was first studied by Generalov et al.[119] and the initial ionisation to create the plasma region is done in the same manner as the pulsed method described above. However once the plasma has been generated, it is then maintained continuously by the laser. The laser energy absorbed by the plasma region is convected downstream by the fluid and forms a heated wake behind it [77]. This method has only seen successful application to the field of blunt body drag reduction. Significant drag reductions have been observed [120] for blunt bodies at supersonic speeds. It was suggested that the cause of the drag reduction is the thermal wake modifying the “virtual” shape of the blunt body encountered by the flow. This reduces the strength of the shock structure generated by the object and reduces the drag.

This study is more interested however in pulsed laser energy deposition and so this topic will be the focus. The area of blunt body drag reduction has been considered for the application of pulsed energy deposition as well. It was shown that up to a 21% drag reduction was achievable by laser energy deposition pulsed at 80kHz [121]. The same study found that the level of drag reduction was dependent on the frequency of the laser energy deposition. This may suggest that the continuous laser energy deposition method is superior for drag reduction as it appears from the study by Sasoh et al. [121] that drag reduction increases with frequency. If the trend were to continue towards an infinite pulse frequency, i.e. continuous laser energy deposition, it would prove that continuous laser energy deposition was superior for drag reduction.

A computational study on the same topic was carried out by Hong et al.[122] They found that the laser pulses created a persistent region of low density gas upstream of the blunt object’s bow shock. This causes the bow shock to locally move upstream in this region, increasing the stand-off distance from the blunt body and thus decreasing the drag. Similar results were found in a number of different studies[123][124][125]. These studies all confirm that pulsed laser energy deposition can be used for drag reduction.

Another area of application for laser energy deposition was the Edney IV shock-shock interaction. This term describes the interaction between a bow shock and an impinging oblique shock. This interaction leads to a jet of supersonic flow impinging on the surface of the object which results in significant peaks in local surface pressure and temperature. Adelgren et al.[126] examined both a blunt body case and the Edney IV interaction, however with only a single laser pulse, not repetitive pulses. They were able to achieve a 30% and 40% reduction in surface pressure for the blunt body case and the Edney IV interaction case respectively. A significant factor that was still not well understood from either this study or that of Sasoh et al.[121](discussed above), was the effect of the pulse-pulse interaction of the laser on the achieved results. The importance of this will become clear later in this chapter.

An important area of study relevant to this particular work is the use of laser energy deposition to affect flow separation. Both Osuka et al.[127] and Erdem et al.[128] investigated how pulsed laser energy deposition could improve the separation char-

acteristics of a flared cylinder. It was found in both studies that the heated bubble generated by the laser produces toroidal vortices as it interacts with the shock system around the cylinder. These vortices are produced due to the difference in orientation of the density gradients and the pressure gradients as the low density bubble interacts with the shock wave. The vortices energise the low momentum flow in the boundary layer and delay separation.

Another interesting outcome of both of these studies was the ability of the pulsed laser energy deposition to reduce oscillation in the shock structure. The results of Erdem et al.[128] highlighted that the effect of the laser energy deposition varied with the laser frequency. The suggestion was that at very high repetition rates the oscillation magnitude was decreased significantly however at some lower frequencies the amplitude of oscillation was amplified. This was thought to be due to the laser energy amplifying natural, resonant frequencies in these regions. Similar conclusions were arrived at in work by Tamba et al.[129] and Iwakawa et al.[130].

This last area of study forms the basis for the work carried out here. The aim is to use the pulsed laser energy deposition to control separation characteristics, it was highlighted above that it has the capability to do so. However the aim of this work will be to improve the performance of a ramjet intake by reducing the impact of flow instabilities, Ferri and Dailey criteria, through the use of laser energy deposition. The baseline flow field of the investigated intake will first be examined. The flow field will then be compared to that with laser energy deposition added upstream of the intake at a variety of different pulse frequencies.

7.3 WIND TUNNEL FACILITY

This chapter of work was carried out at Nagoya University, whereas the results presented thus far were all conducted at the University of Glasgow. Therefore it is important to provide a brief explanation of the facility used. The facility used was a supersonic indraft wind tunnel that provides a flow of Mach 1.92 ± 0.04 in an 80 x 80 mm test section. Test section static pressure was measured at 13.8kPa while ambient temperature measurements were used to predict a test section temperature of 169K, assuming an isentropic process through the nozzle. The laser energy deposition was provided by an Nd:YVO₄ laser with a wavelength of 1064nm and an energy per pulse of up to 7.2mJ/pulse. For this study, the laser energy per pulse was fixed at 5.6mJ and the pulse frequency was varied between 1 and 60kHz. The laser was guided to the test section by a series of mirrors and through a lens with 60mm focal length in order to focus the laser light to aid the laser induced gas breakdown.

The diagnostic equipment used, Schlieren and pressure measurements, were discussed in a previous chapter (see section 2.1) and so will not be discussed again here.

7.3.1 INTAKE MODEL

The model used for this study featured a single, central compression cone housed in a 149mm long cowl. The half angle of the central cone was 12.5° and the diameter was 11mm. The central compression cone extended out 14mm from the cowl face. The physical locations of each of these measurements are shown relative to a schematic of the model in figure 7.3. The ratio of the inlet area to the throat area within the cowl is 0.71. If figure 4.3, shown in chapter 4 is examined at Mach 1.92, an intake with an area ratio ($\frac{A_T}{A_{inlet}}$) of 0.71 lies in the region where both an unstarted and a started inlet can exist. Intakes are often designed in this region rather than the self-starting region as the area ratios required for self-starting are often too large to be of any practical significance. However because of this the initial starting of the intake is an issue as, at the design condition, the intake will not necessarily self start. In reality there are a number of ways in which this is handled; overspeeding and variable area geometries are the most common. Overspeeding refers to an intake subjected to a freestream Mach number larger than the design value which decreases the area ratio defined by the Kantrowitz limit which can allow an unstarted inlet to start. Variable geometry can be used to either reduce the inlet area or increase the throat area during start up in order for the inlet to be above the Kantrowitz limit. However for this model overspeeding is not possible as the wind tunnel operates at a fixed Mach number and variable geometry is too complex to be a realistic option. A third, very simple option exists however known as the overboard spillage method[131]. This technique can be used if the intake is not fully enclosed on all sides; in this case the central compression cone is external to the intake cowl for 14mm. The fundamental reason why this technique works is that the Kantrowitz limit will only apply from the inlet to the fully enclosed section of the intake. Veillard et al.[131] provide an equation to predict the Kantrowitz limit for such an intake, see equation 7.3:

$$\left(\frac{A_T}{A_I}\right)_K = \left[\frac{\gamma-1}{\gamma+1} + \frac{2}{(\gamma+1)M_1^2}\right]^{\frac{1}{2}} \left[\frac{2\gamma}{\gamma+1} - \frac{\gamma-1}{(\gamma+1)M_1^2}\right]^{\frac{1}{\gamma-1}} \quad (7.3)$$

where $\left(\frac{A_T}{A_I}\right)_K$ is the new Kantrowitz limit for an intake with an external compression cone and M_1 is the Mach number downstream of the conical shock (see table 7.1 for calculated value of 1.72 in this case). From this equation, the Kantrowitz limit for a self-starting inlet is equal to 0.76. Therefore the area ratio of 0.8 for the configuration used is above the newly defined Kantrowitz limit based on overboard spillage and as such will self start when the wind tunnel reaches steady operation during a test.

It was important that the intake could operate in the different modes of operation as described in the previous section, particularly in subcritical mode as this is the operating state where Ferri and Dailey instabilities are experienced. In order to achieve this an adjustable plug is installed at the rear of the intake that allows the exit area to be adjusted. The plug is moved laterally in order to alter the exit area, A_e , and thus change the ratio of throat to exit areas. This plug restricts the mass

flow through the intake and can thus be used to move the intake operating point between supercritical, critical and subcritical as required. The primary goal here is to examine the impact of laser energy deposition on the intake performance at subcritical conditions, so only one intake operating condition is considered. Figure 7.4 presents a schematic of the intake model with the plug feature highlighted alongside the location of pressure measurements taken and the field of view available for the Schlieren visualisation.

7.4 RESULTS POST-PROCESSING

Using the facility and test model outlined above, the goal is to examine the impact of pulsed laser energy deposition on the separation characteristics of this intake model. In particular, the goal is to establish how varying frequency of laser energy deposition can affect the influence of the flow control on the intake separation. The impact of flow separation on the intake performance will then be analysed using pressure measurements to highlight how the change in separation can have a significant impact on the pressure recovery of the intake.

7.4.1 CONVENTIONAL SCHLIEREN PHOTOGRAPHY

As in previous chapters, conventional Schlieren photography is used extensively here to examine the flow field and how the laser energy deposition affects it. The flow fields examined in this study are unsteady and therefore the presentation of the Schlieren images must account for this. This means that the temporal variation of the Schlieren images will be the primary focus here as this is the key to understanding the influence of the heated bubble generated by the laser energy deposition. This will involve a number of different processing methods in order to extract useful information from the flow.

DEVIATION FROM MEAN IMAGE

One method that is used to examine the time varying aspects of the flow field is to examine how each instantaneous image differs from the mean image. This is done by first calculating the mean image for each test case. Each instantaneous image in the test is then subtracted from this mean image and the absolute value of the difference recorded. Although the resulting intensities per pixel do not represent any physical

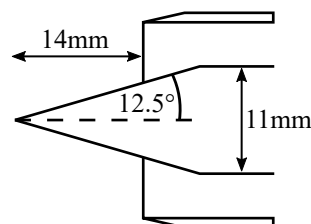


FIGURE 7.3: Illustration of relevant dimensions highlighted on model schematic.

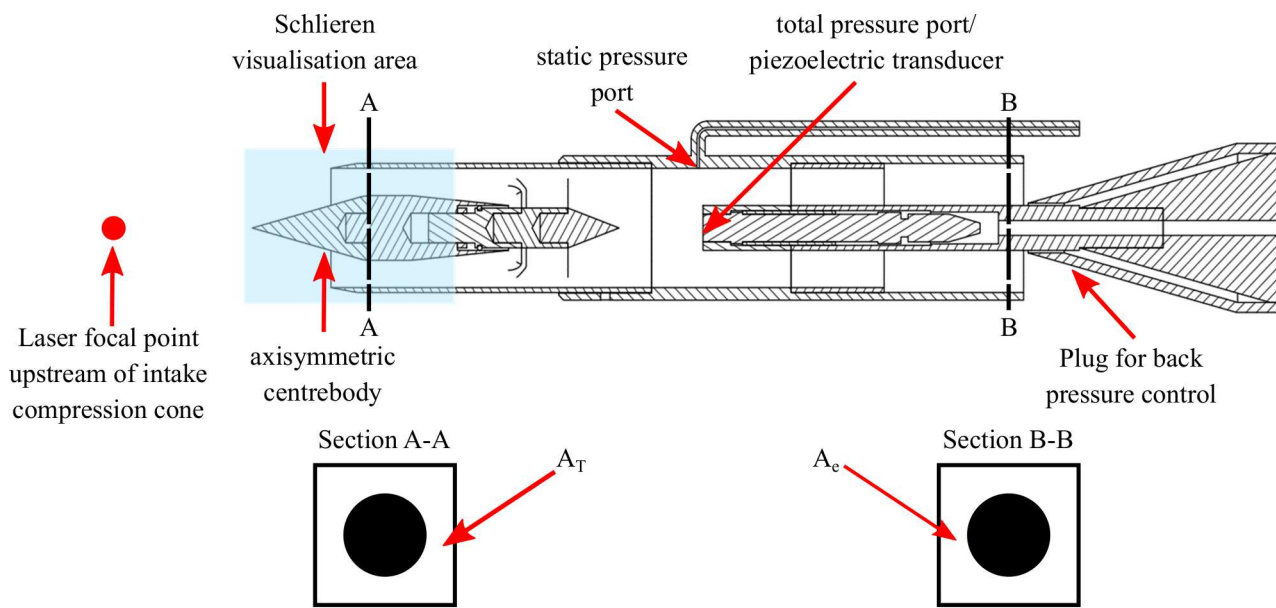


FIGURE 7.4: Schematic of Intake model

quantity, they do give an indication of areas with changing density gradients. These areas can then be attributed to different features such as shock oscillation and, more importantly, regions of separated flow.

FREQUENCY DOMAIN ANALYSIS

One area that is key to examine is the frequency response of the flow field to the flow control input. Frequency domain information can be extracted from the Schlieren imaging by examining how the intensity of each pixel varies with time. In this instance the power spectrum density (PSD) of each pixel is calculated across the entire image. The PSD is calculated as opposed to the FFT due to the fact that, as with the majority of cases that occur in reality, there is a non-negligible level of noise associated with the measurements. As such if a single FFT was calculated across the length of the single calculated then there would be a large amount of noise in the signal. A PSD can alleviate the impact of noise on the frequency domain results due to the averaging carried out as part of the process. In this work the Welch method[132] for calculating the PSD of a signal was used. This calculates the finite Fourier transform of a number of segments of the signals, the length of each signal segment is based on the window size used. This provides a number of periodograms equal to the number of segments used which are then averaged to give the PSD of the signal.

The calculated PSD will be used to examine the Schlieren frequency content of the baseline intake and is then compared to the frequency content measured for the intake with flow control applied. The first set of data analysed is the PSD along a line drawn 1mm above and parallel to the surface of the central compression cone. The second is the PSD along the centre line of the visible portion of the intake isolator. Figure 7.5 illustrates the regions described above.

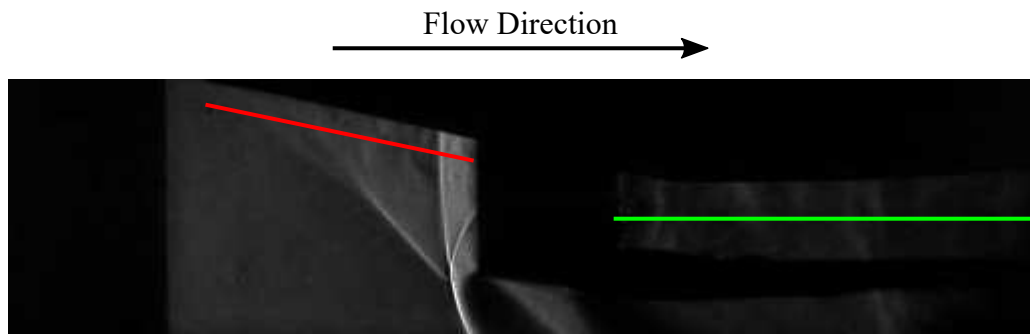


FIGURE 7.5: Illustration of regions along which the PSD was calculated where the red line is the segment parallel to the compression cone (1mm from the surface) and the green line is the segment along the centre line of the isolator.

FEATURE TRACKING

The last set of data that has been extracted from the conventional Schlieren imaging is the temporal tracking of the separation location along the surface of the compression cone. This was done in order to track how the separation location varies as the thermal bubbles interact with the tip shock wave of the compression cone. This information was extracted from the Schlieren images simply by observing the Schlieren images frame by frame for 1.2ms of real time and manually recording the pixel location of the separation. This was then calibrated using two different known distances from the image (centreboddy length and centreboddy diameter), both of which gave the same pixel resolution to a thousandth of a mm at 0.1mm/px. This physical distance was converted to a non-dimensional location along the ramp by normalising the distance by the length of the ramp. From the time varying position the mean non-dimensional separation location was calculated.

It should be noted that the pixel location chosen for each frame to denote the separation location was done by examination of the images. This introduces a certain element of objectivity into the results as the actual separation location could be a number of pixels to the left/right of the actual location presented. However the choice of pixel was done in the same manner for each test case and so if there are any errors introduced into the analysis it is assumed that the error would be consistent across all of the cases examined.

7.4.2 PRESSURE MEASUREMENTS

UNSTEADY PRESSURE MEASUREMENTS

In order to capture any unsteady effects of the applied flow control, high frequency measurements of the internal total pressure were recorded. These measurements were captured using a piezoelectric sensor that captured any total pressure fluctuations relative to the steady state value. These fluctuations can be used to examine the impact of the flow control on the frequency response of the inlet. As was the case with the Schlieren imaging described above, this is done by calculating the PSD of the pressure

fluctuation signal.

STEADY PRESSURE MEASUREMENTS

Alongside the unsteady pressure measurements, the steady total pressure was also recorded. The response time of this transducer is too low to provide any unsteady information but it can provide information on the overall performance of the inlet. The average total pressure during the test at each flow control condition can be calculated. This total pressure, given that the upstream total pressure and incoming Mach number are consistent between tests, can be used as a measure of the inlet efficiency and how this changes relative to the baseline flow when laser energy deposition is applied as flow control.

7.5 RESULTS

The first step is to discuss the fundamental flow field as captured in the raw Schlieren images, as an understanding of the important features present is key when examining the effect of flow control. Figure 7.6 presents a Schlieren image showing the baseline intake flow. The normal shock on the external compression ramp and the spillage flow highlighted confirm that the intake is operating in the subcritical mode as desired. The separated flow that is present along almost the entire length of the external compression cone can also be clearly observed. The final feature worth highlighting is the shock structure present in the isolator. This is present due to the acceleration of the flow back to supersonic speeds after passing through the normal shock on the compression ramp. It is barely visible, suggesting that it is a relatively weak normal shock and that the flow is only just supersonic upstream of it.

The next step is to examine the raw Schlieren data as the thermal bubble generated by the laser energy deposition interacts with the intake flowfield. Figure 7.7 presents a set of Schlieren images that illustrate the various steps in the cycle of interaction between the intake flowfield and the thermal bubble. In order to achieve the required frame rate to accurately resolve the unsteady flow field, a result of the pulsed energy deposition, the field of view had to be reduced. As such, the edge of the image for these images is aligned with the centreline of the intake. This was not a concern however as the intake flow field is symmetrical and examining half of the flow field will be sufficient. These images were captured at a frame rate of 130081Hz i.e. an image was recorded every $7.69\mu\text{s}$. The first is taken as the reference point for the remaining images in figure 7.7 i.e. the time stamp on each image is the time between that image and the original image presented. At $0\mu\text{s}$ the thermal bubble can be observed at the tip of the compression cone. In the following image, at $7.69\mu\text{s}$, the bubble has transformed into a toroidal vortex structure due to the baroclinic interaction between the low density bubble and the shock structure. By $30.75\mu\text{s}$ the effect of the vorticity is becoming clearer as the flow begins to reattach along the compression cone. $130.69\mu\text{s}$ after the thermal bubble reached the cone the flow is fully attached along almost the entire

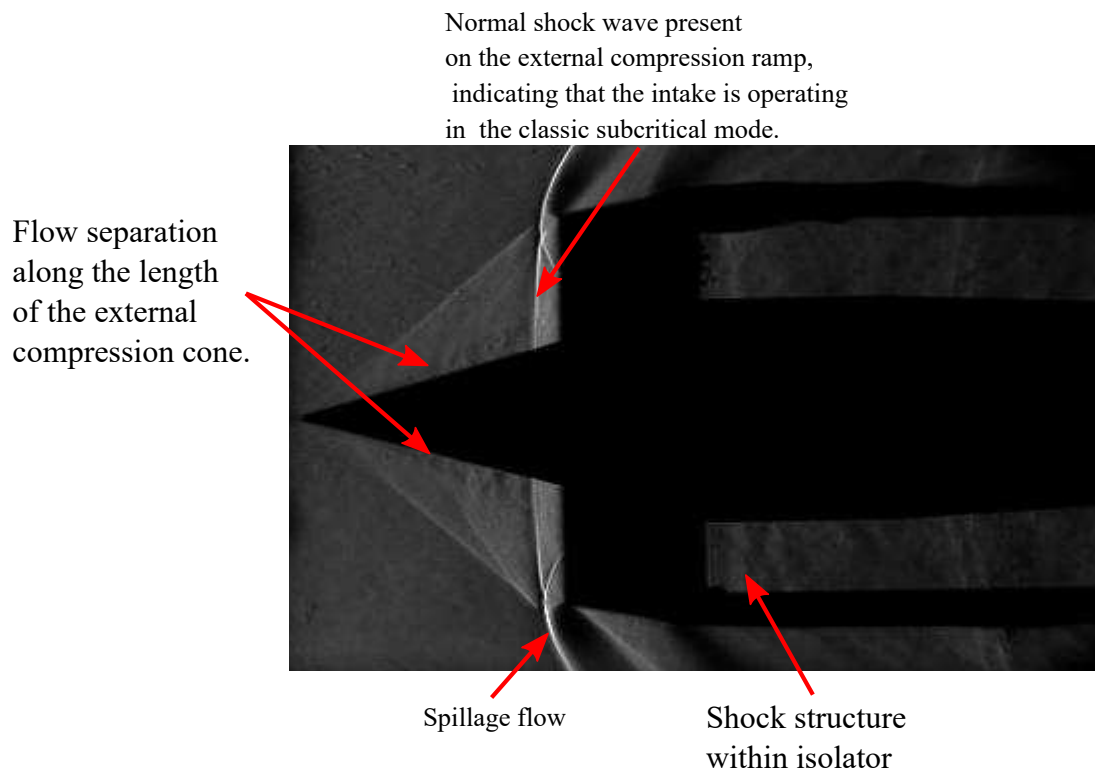


FIGURE 7.6: Schlieren image indicating the key features observed in the baseline flow field.

length of the centrebody. As the vortex structure travels downstream into the isolator the separation begins to reappear until $253.69\mu\text{s}$ at which the flowfield once again resembles the baseline flow field.

7.5.1 FREQUENCY DOMAIN ANALYSIS

PRESSURE MEASUREMENTS

Examining the unsteady measurements first, this measure of the total pressure fluctuation can be converted to the time domain as described above. Figures 7.8 to 7.13 present the calculated PSD for the various cases of laser energy deposition studied, from no laser energy deposition to 60kHz pulsed laser energy deposition.

If first the baseline case is considered (figure 7.8), there are a number of observations made. The first is that there is a large peak at 0.1kHz. This results from a combination of the filtering used and the DC offset present in the signal. A low pass filter was used with a cut-off frequency of 0.1kHz to reduce the impact of the DC offset. This peak is not a physical frequency in the pressure and so is ignored for the remainder of the results. The key feature of interest is the peak at 11.87kHz. This appears to be the fundamental natural frequency in the total pressure during operation. There are two more clear peaks at 33.75kHz and 55.58kHz that display lower amplitudes than that of the peak at 11.87kHz. The potential importance of the frequency observed at 11.87kHz will become apparent as the cases with pulsed laser energy deposition

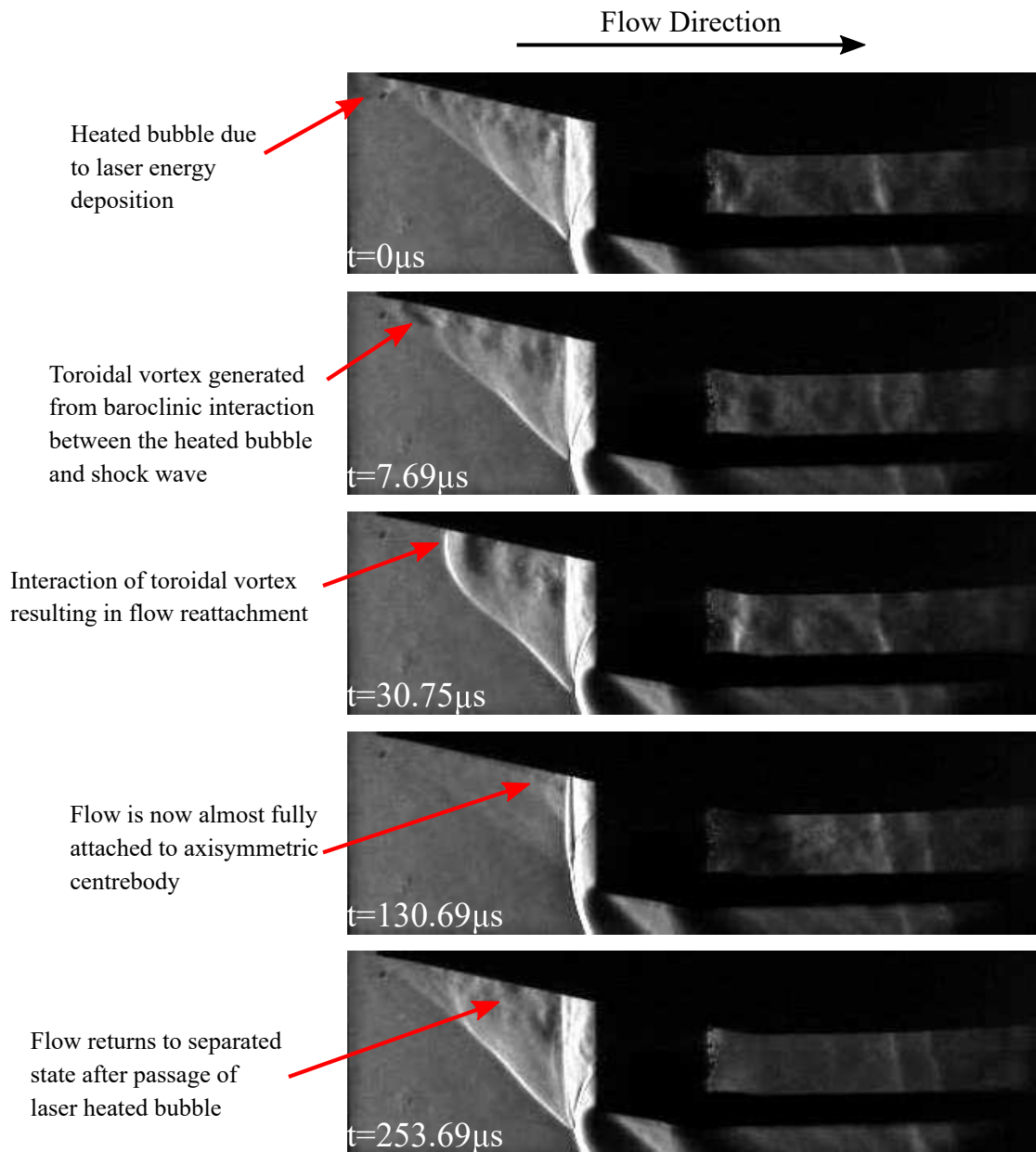


FIGURE 7.7: Time series of Schlieren images that illustrate the various stages in the interaction between the supersonic intake flowfield and the laser generated, thermal bubble.

are examined. Another interesting observation is that after the significant peak observed at 11.87kHz, the general broadband noise observed in the signal decreases significantly. It is believed that this is likely related to the turbulent energy cascade. High frequency fluctuations are related to smaller scale structures and vice versa. Therefore as the lower frequencies are dominated by larger structures, which as per the turbulent energy cascade will tend to have more energy, they will tend to exhibit larger amplitudes in the PSD in comparison to the higher frequencies.

Now moving on to the cases where pulsed laser energy deposition is added; there are a number of interesting features observed across the various cases. If the cases are examined in order of decreasing laser energy frequency, the 60kHz laser energy deposition case (figure 7.13) is first to be examined. The important conclusion is that there is no significant change to the PSD compared to the baseline intake case (figure 7.8). There is a peak at 60kHz, corresponding to the laser frequency, however it is notably smaller than the natural resonant frequency which occurs at 12.01kHz (presumed to be equivalent to the 11.87kHz peak observed in the baseline). This result is repeated in figures 7.11 and 7.12 i.e. the excitation frequency is present but the impact on the original baseline PSD is insignificant.

Now if the cases where the laser energy deposition frequency is set to 1kHz and 10kHz (figures 7.9 and 7.10 respectively) are examined, there is a much starker contrast in comparison to the baseline spectrum. The reason for the large peaks at 1kHz and some of its harmonics is not clear as there are no clear natural frequencies in this area. It is possible that this excitation frequency is amplifying the noise that is apparent between 0.1 and 10kHz. The most significant change occurs when an excitation frequency of 10kHz is examined. This is suggested to be a result of the clear peak already present in this region of the spectrum for the baseline case. The amplification of this frequency is significant, approximately 200 times larger than the natural frequency. The importance of the change occurring at 10kHz will become apparent later in the chapter when all of the results from the various techniques have been presented.

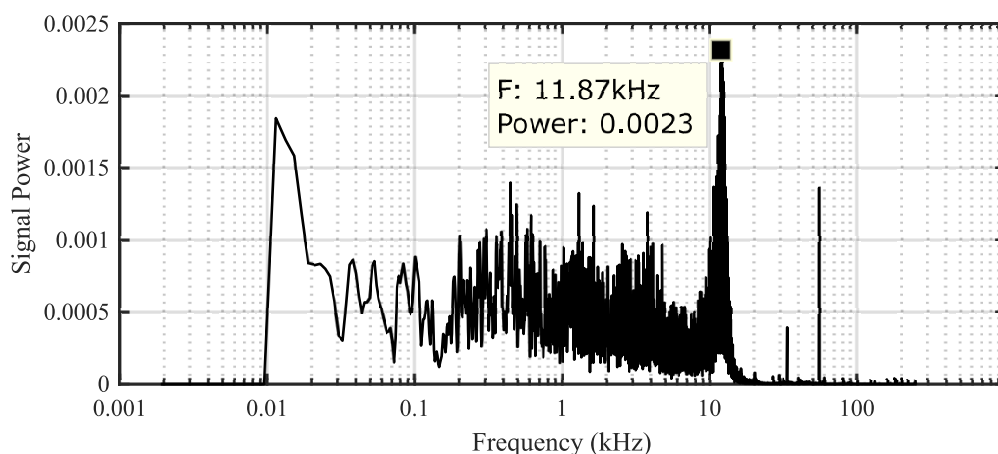


FIGURE 7.8: Power spectral density (PSD) of total pressure fluctuations within the intake with no laser energy deposition.

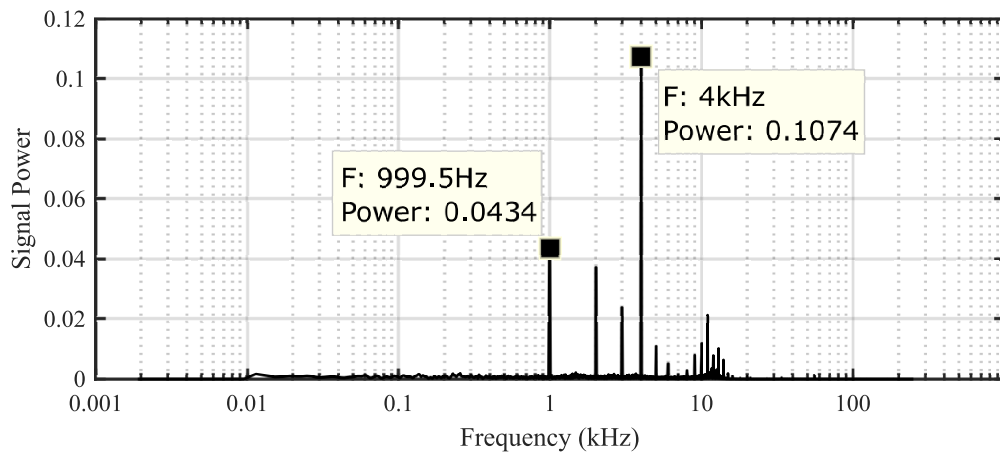


FIGURE 7.9: Power spectral density (PSD) of total pressure fluctuations within the intake with laser energy deposition pulsed at 1kHz.

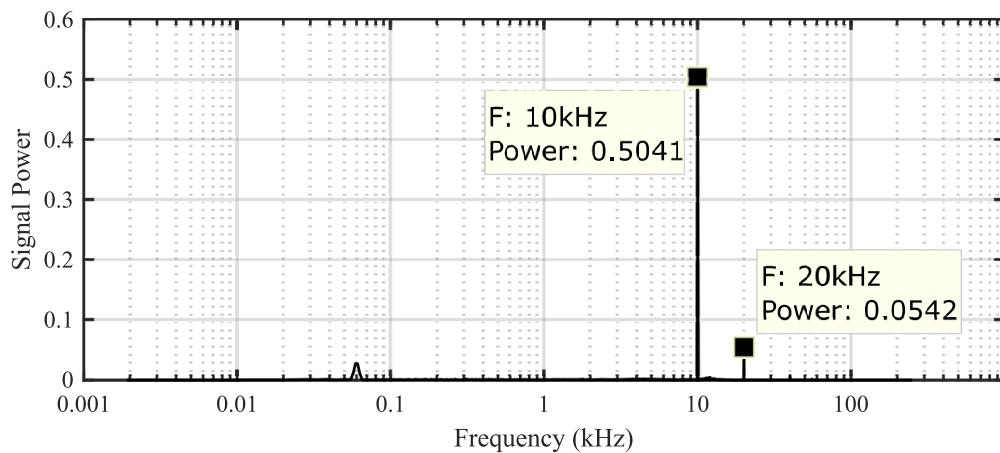


FIGURE 7.10: Power spectral density (PSD) of total pressure fluctuations within the intake with laser energy deposition pulsed at 10kHz.

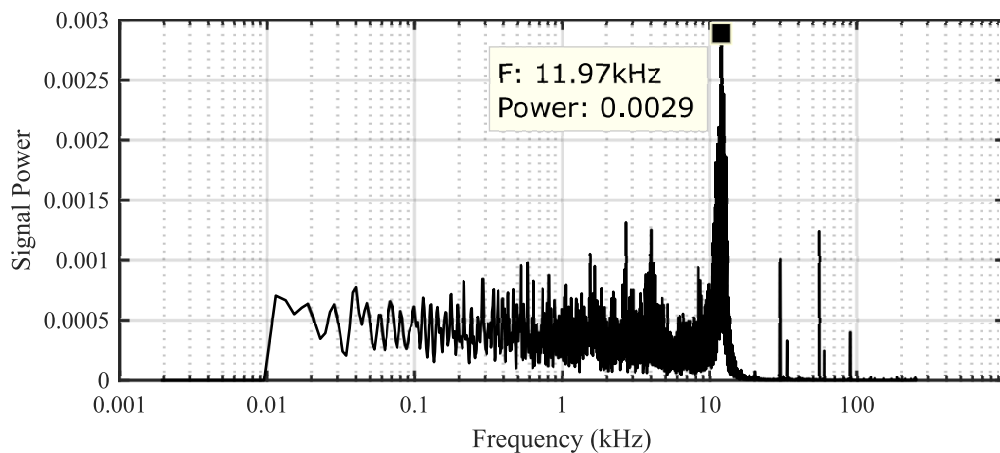


FIGURE 7.11: Power spectral density (PSD) of total pressure fluctuations within the intake with laser energy deposition pulsed at 30kHz.

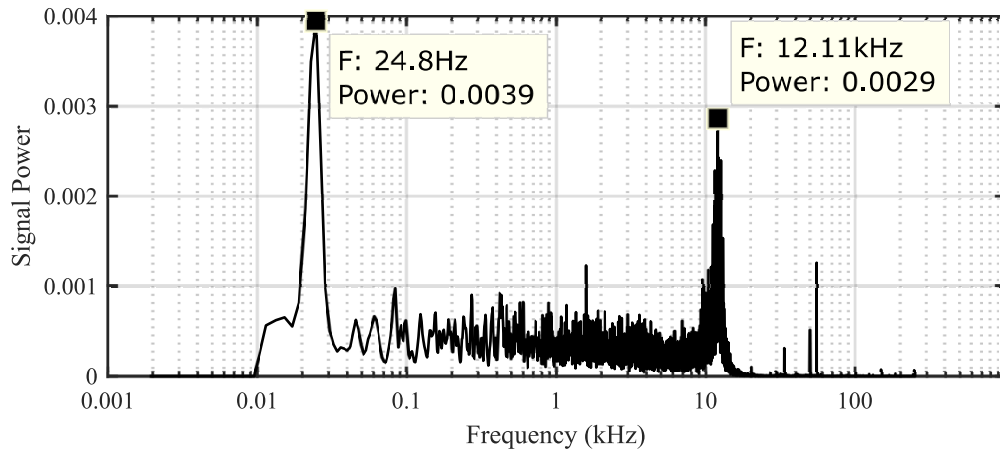


FIGURE 7.12: Power spectral density (PSD) of total pressure fluctuations within the intake with laser energy deposition pulsed at 50kHz.

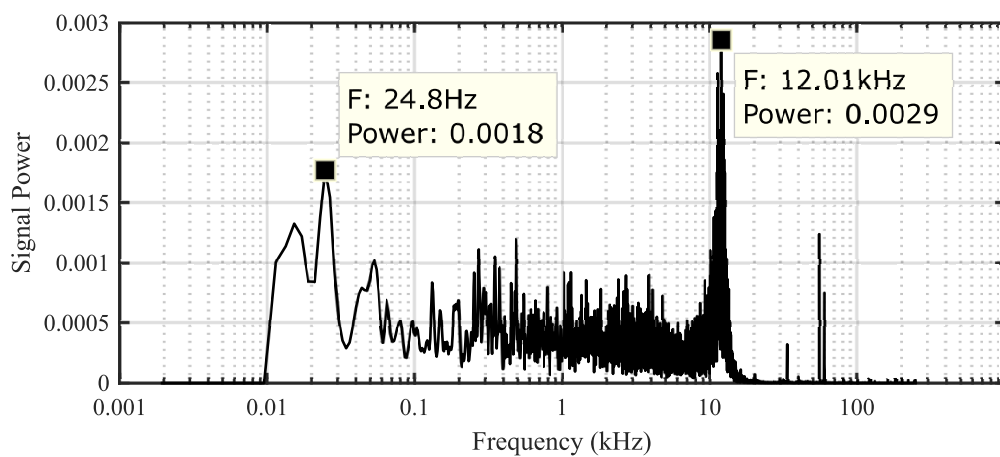


FIGURE 7.13: Power spectral density (PSD) of total pressure fluctuations within the intake with laser energy deposition pulsed at 60kHz.

CONVENTIONAL SCHLIEREN PHOTOGRAPHY

As with the unsteady pressure measurements, the Schlieren images recorded were used to produce a PSD for each of the laser excitation frequencies used. The temporal data used for the calculation of the PSD was the variation in pixel intensity. Figure 7.14 presents the PSD along the centreline of the intake isolator for each excitation frequency. Figure 7.16 presents the PSD along a line drawn 1mm above and parallel to the external compression ramp surface for each excitation frequency.

The results of this analysis allow for the majority of the same conclusions as the pressure measurements. First examine the PSD of the image intensity along the isolator centreline, figure 7.14. The area of this profile is around the region 0-2mm from the beginning of the isolator. This is the only region of the isolator where significant oscillations are observed. It is thought that these oscillations originate from the feature highlighted in the red circle shown in figure 7.15. This appears to be a weak shock wave formed as the subsonic flow behind the external normal shock accelerates due to the area contraction present within the isolator.

For the cases with an excitation frequency of 50kHz and 60kHz, figures 7.14e and f respectively, the results appear very similar to that of the pressure measurements. The only change in comparison to the baseline case, figure 7.14a, is the slight change in the amplitude of the broadband noise between 0 and 10kHz. However this reduction is very small and of no real significance. The case with an excitation frequency of 1kHz, figure 7.14b, shows a similar result to that of the pressure measurements; there are a number of peaks at different frequencies between 0 and 10kHz. The 10kHz excitation case, figure 7.14c, also displays the same result as was observed in the pressure measurements. There is a distinctive peak around 10kHz that is much larger than that apparent in any of the other cases.

There are some deviations in these results when compared to the time domain analysis of the pressure measurements. The first is that the naturally occurring peak around 10kHz observed in the pressure measurements of the baseline case is not apparent in the baseline case for the Schlieren imaging. The other difference in comparison to the pressure measurements occurs in the 30kHz excitation case. In figure 7.14d there are two distinct peaks located at 27kHz and 30kHz respectively. There is no indication of any significant peak in the pressure measurement PSD presented earlier for the same case, figure 7.11.

The Schlieren imaging frequency domain analysis along the external compression ramp, figure 7.16, displays much the same results as those discussed above. The baseline and 1kHz cases, figures 7.16a and b respectively, display the same features as above; no significant natural frequencies (in comparison to the excited cases) and the 1kHz excitation has little impact other than a slight amplification of frequencies in the 0-10kHz region. The 10kHz case, figure 7.16c, shows the same peak at 10kHz along with a peak around 20kHz that is assumed to be a harmonic. Similar to the

results of the profile taken along the isolator, the 30kHz case (figure 7.16d) shows two apparent peaks, one at 27kHz and one at 30kHz. At this location these frequencies are also observed for the 50kHz case, figure 7.16e, however not at 60kHz.

The data presented does not capture the intake's fundamental resonant frequencies as a result of the two buzz phenomena. Some simple analytic calculations can be carried out to predict the resonant frequencies expected to be observed. Newsome[133] provided a relationship (equation 7.4) that can be used to predict the resonant frequencies of a duct configuration as used here:

$$f_n = (2n - 1) \frac{c}{4L} (1 - M_i^2) \quad (7.4)$$

where n is the mode number, c is the speed of sound, L is the length of the duct and M_i is the Mach number of the flow within the duct (assuming that the flow has passed a terminal normal shock before entering the duct itself). To use this equation the Mach number within the duct must be known.

The flow observed in the Schlieren images is an example of a conical flow, for which the Taylor-Maccoll[134] equation, equation 7.5, provides a solution which allows the calculation of the Mach number:

$$\begin{aligned} \frac{(\gamma - 1)}{2} \left[V_{max}^2 - V_r^2 - \left(\frac{dV_r}{d\theta} \right)^2 \right] \left[(2V_r) + \left(\frac{dV_r}{d\theta} \cot(\theta) \right) + \left(\frac{d^2V_r}{d\theta^2} \right) \right] \\ - \left[\frac{dV_r}{d\theta} \left(V_r \frac{dV_r}{d\theta} + \frac{dV_r}{d\theta} \frac{d^2V_r}{d\theta^2} \right) \right] = 0 \end{aligned} \quad (7.5)$$

where V_{max} is the maximum velocity achievable from an initial condition (i.e. the velocity if the flow was theoretically expanded to zero temperature), V_r is the radial component of the velocity downstream of the conical shock wave, V_θ is the flow normal to the conical shock wave and r, θ are the radial coordinates with the origin at the tip of the cone. There are a number of assumptions made, the significant ones being:

- The flow is steady, isentropic and the cone is at zero angle of attack.
- The fluid properties are constant along each "ray" that extends out from the origin between the shock wave and the cone surface (see figure 7.17).
- The flow is axisymmetric around the cone axis.
- The fluid properties only vary with θ (complimentary to the assumption of constant properties along each ray i.e. in the direction of the r ordinate).

This equation has no known analytic solution but it can be solved numerically if the second order form of the equation is converted into two first order equations; one that

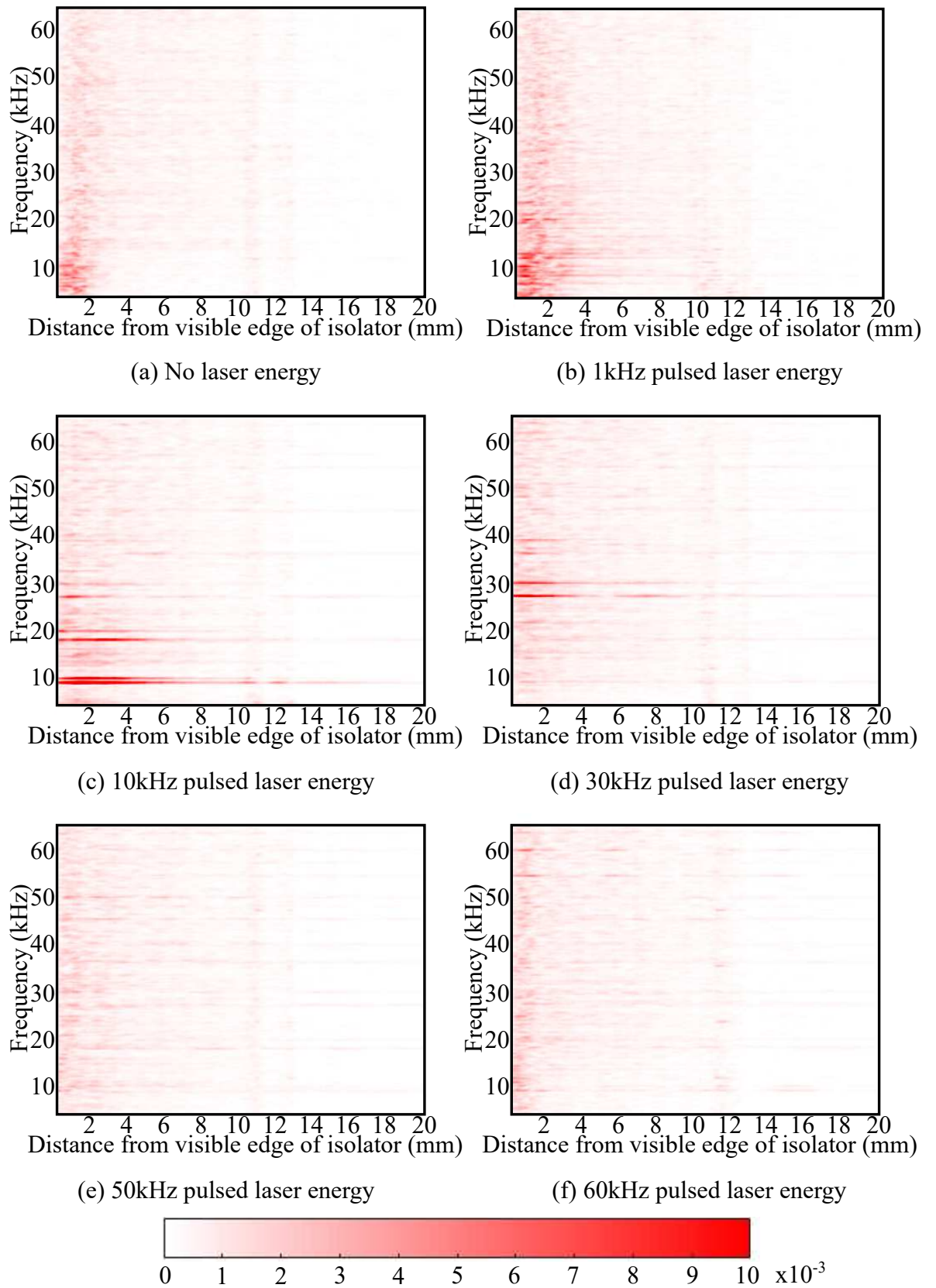


FIGURE 7.14: Power spectral density (PSD) of Schlieren imaging intensity along the centreline of the intake isolator.

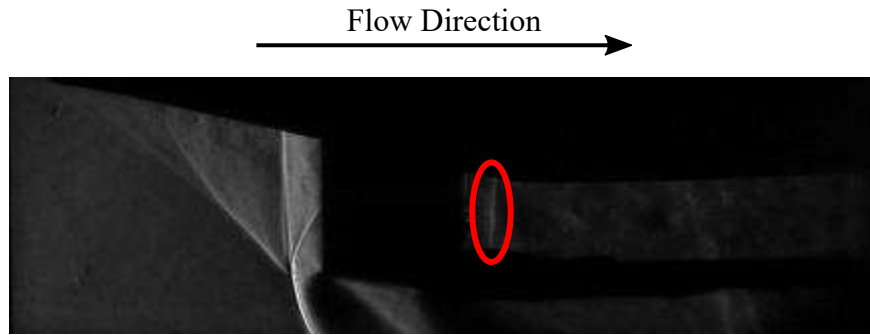


FIGURE 7.15: Schlieren image of the baseline flow with the flow feature highlighted that is thought to be responsible for the oscillations observed within the isolator.

equates to the first order derivative of V_r and another which equates to the second order derivative. This leads to the equations in the form shown in equation 7.6:

$$\frac{d^2 V_r}{d\theta^2} = \frac{A}{\frac{(\gamma-1)}{2} \left[V_{max}^2 - V_r^2 - \left(\frac{dV_r}{d\theta} \right)^2 \right] - \left(\frac{dV_r}{d\theta} \right)^2}$$

$$A = \left(\frac{dV_r}{d\theta} \right)^2 V_r - [(\gamma-1)V_r(B)] - \frac{(\gamma-1)}{2} [B] \frac{dV_r}{d\theta} \cot(\theta) \quad (7.6)$$

$$B = V_{max}^2 - V_r^2 - \left(\frac{dV_r}{d\theta} \right)^2$$

$$V_\theta = \frac{dV_r}{d\theta}$$

Details on the fundamental numerical method used to solve these equations is available in Anderson[1]. The difference here is that the shock angle is measured from the Schlieren images. Figure 7.18 shows an example of the angle considered as the cone shock angle from the Schlieren images. The value used in the calculation is a result of an average angle calculated over 100 images. The measured cone shock angle can then be used as an input into oblique shock equations to calculate the Mach number downstream of the shock wave and the flow deflection angle. From this and the ambient conditions, the radial and normal velocity components can be calculated. The measured shock angle and the two velocity components are then input into the Taylor-Maccoll equations and these are integrated numerically in steps of the spherical ordinate θ to calculate the velocity components at each incremental value of θ . The value of θ at which $V_\theta = 0$ is the cone surface, as the flow perpendicular to the wall must be zero for an impermeable surface. The velocities calculated for each step in the θ range between the shock wave and the cone can then be used to calculate Mach number.

This analysis provides a Mach number after the cone shock, however the flow passes through the normal shock observed on the external compression ramp before passing into the duct. The Mach number entering the duct is therefore calculated from normal shock relations based on the Mach number upstream of the normal shock taken as the average Mach number calculated across the θ range (calculated from the

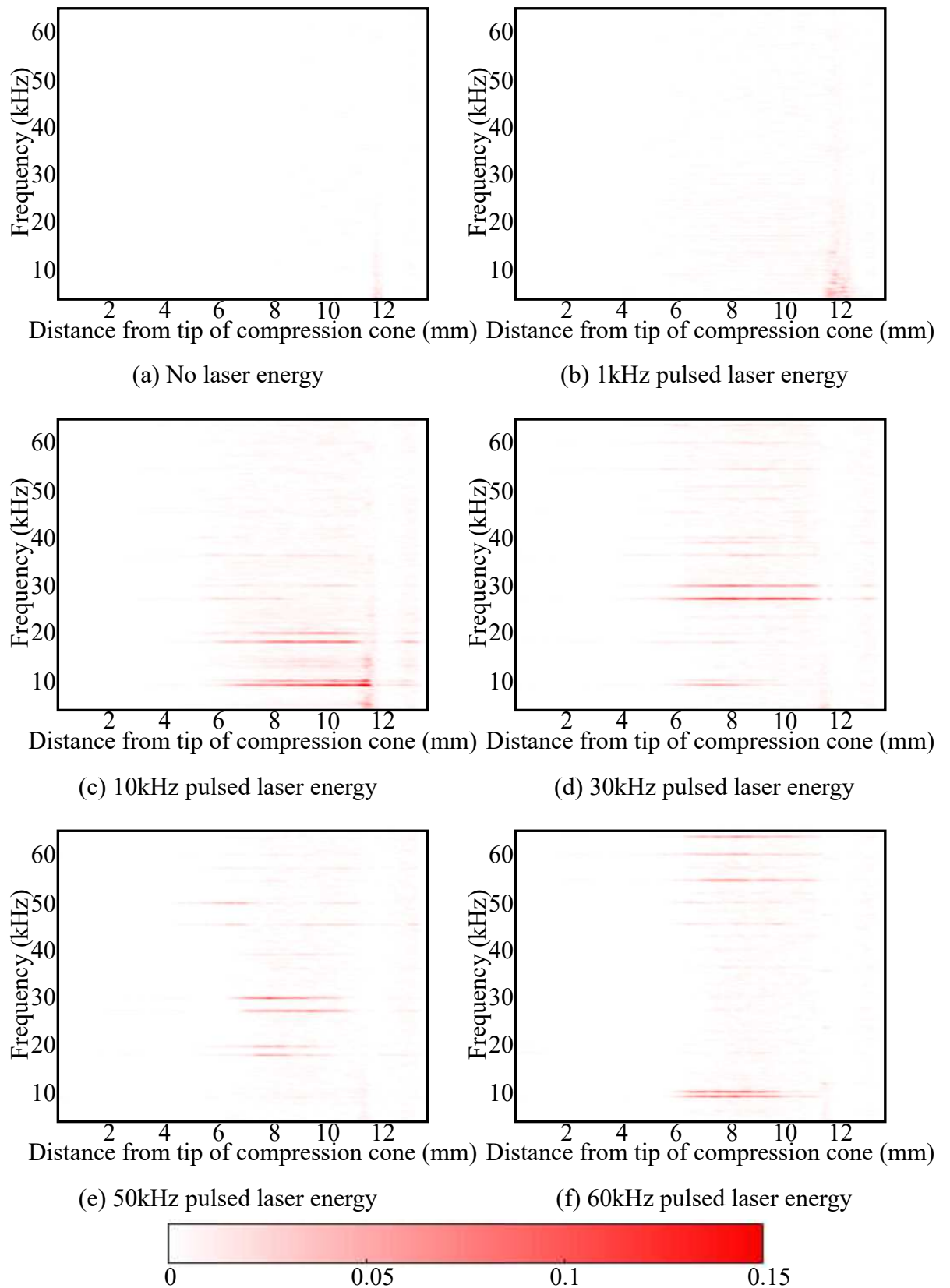


FIGURE 7.16: Power spectral density (PSD) of Schlieren imaging intensity 1mm above the external compression ramp.

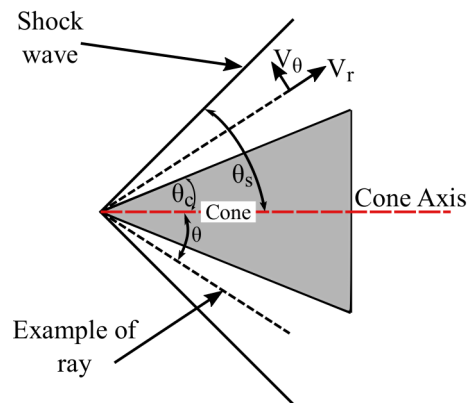


FIGURE 7.17: Diagram illustrating key geometric parameters that are used in the Taylor-Maccoll equation.

Taylor-Maccoll analysis).



FIGURE 7.18: An illustration of the measured cone shock angle overlaid on a Schlieren image.

Table 7.1 presents the Mach number results based on the analysis described above. The results are presented for two different shock wave angles: the measured shock wave angle and the shock wave angle that would result in a flow deflection equal to the 10° half angle of the cone. The latter is provided in order to provide a range, within which the result is likely to be due. The measured shock wave angle will be subject to a degree of measurement uncertainty due to the “qualitative” manner in which it was measured, however the flow deflection angle will be larger than the 10° half angle of the cone as a result of the viscous effects.

Shock Angle Source	Measured from Schlieren	Calculated based on cone angle
Shock Angle (°)	34.1	32.3
Flow Deflection Angle (°)	13.5	12.5
Average Mach downstream of Conical Shock	1.72	1.75
Static Temperature Downstream of Conical Shock (K)	177.4	175.6
Mach in the Isolator (downstream of the normal shock)	0.64	0.63
Static Temperature Downstream of Normal Shock (K)	264.3	262.5

TABLE 7.1: Mach number variation downstream of the conical shock and downstream of the normal shock.

Based on the resulting duct Mach number calculated above, table 7.2 presents the first 8 resonant frequencies predicted by equation 7.4.

These predicted resonant frequencies can be compared to the measured values by examining a section of the FFT data that captures the outer edges of the compression cone tip shock wave and the normal shock wave. In these locations the power spectrum calculated will be less affected by the noise generated by the separation along the compression cone surface. Figure 7.19 illustrates the section of the Schlieren images used for this PSD calculation.

The PSD calculated for this location for the baseline case and each of the laser pulse frequencies is presented in figure 7.20. Here it is immediately clear that the resonant frequency calculated earlier for mode 4 or 5 (see table 7.2) is observed where the profile examined across the Schlieren image meets the oblique shock. The resonant frequency calculated from the PSD is 3252Hz which, considering the limited resolution available for the Schlieren PSD, is very close to the frequency predicted earlier. Regarding the impact of the laser energy deposition on the resonant frequency, the only excitation

n	1	2	3	4	5	6	7	8	9
Resonant Frequency [Hz] (measured shock angle)	968	1614	2260	2905	3551	4197	4842	5488	6134
Resonant Frequency [Hz] (shock angle from cone half angle)	986	1643	2300	2958	3615	4272	4930	5587	6244

TABLE 7.2: Resonant frequencies within the isolator, predicted from equation 7.4, for the two different isolator Mach numbers calculated (see table 7.1).

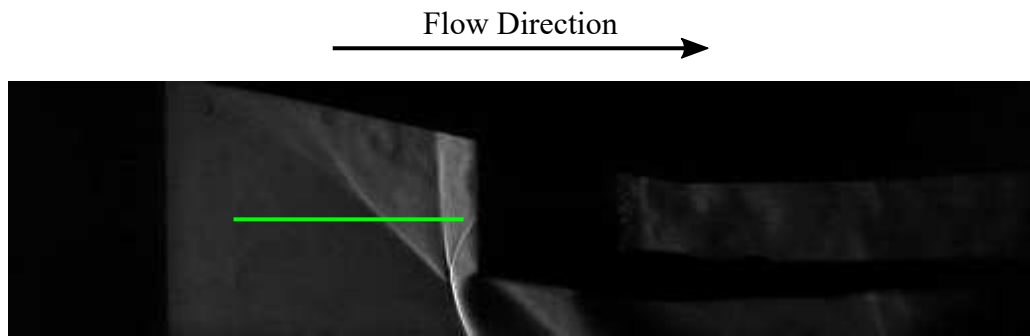


FIGURE 7.19: Schlieren image with the profile highlighted that was used for the calculation of the intake resonant frequency modes.

frequency that has a significant impact on the magnitude of this resonant frequency is 10kHz. When the laser is pulsed at this frequency the amplitude of the resonant frequency drops significantly and a sizeable oscillation appears in the normal shock at the excitation frequency. The 1kHz, 30kHz and 50kHz excitation frequencies have little impact on the amplitude of this resonant mode. The 60kHz case appears to suppress the resonant frequency slightly however more broadband noise appears around the resonant mode. Due to the limited resolution of the PSD it is possible that this broadband noise is actually one single frequency that lies between two of the available bins calculated for the PSD. Although the 50kHz and 60kHz cases do not significantly reduce the amplitude of the resonant mode, it is observed that the location is shifted downstream by approximately 0.5-1mm relative to the baseline case. This is thought to be a result of the average separation location moving further downstream (see section 7.5.2 for confirmation of this) relative to the baseline and as such the oblique shock will also move further downstream.

Figure 7.21 shows the PSD intensity across the entire Schlieren image at the resonant frequency, 3252Hz, identified above. This set of images confirms the previous observations, that the 10kHz excitation frequency is the only condition that shows significant mitigation of the resonant mode observed in the oblique shock oscillation.

7.5.2 SCHLIEREN IMAGING ANALYSIS

The Schlieren imaging was examined in the frequency domain in section 7.5.1, here the focus will be on how the laser energy affects the intake flow field, in particular the separation characteristics. The first step taken was to examine the flow field from a purely qualitative point of view. In attempt to better highlight areas of interest some processing was carried out on the images. This involved subtracting the mean Schlieren image from each instantaneous image and taking the absolute value as the "new" pixel intensity. This highlights regions where there is significant fluctuation in the image intensity with time and thus significant fluctuation in the density gradients.

Figure 7.22 shows these images for the baseline and 1kHz laser pulse frequency cases

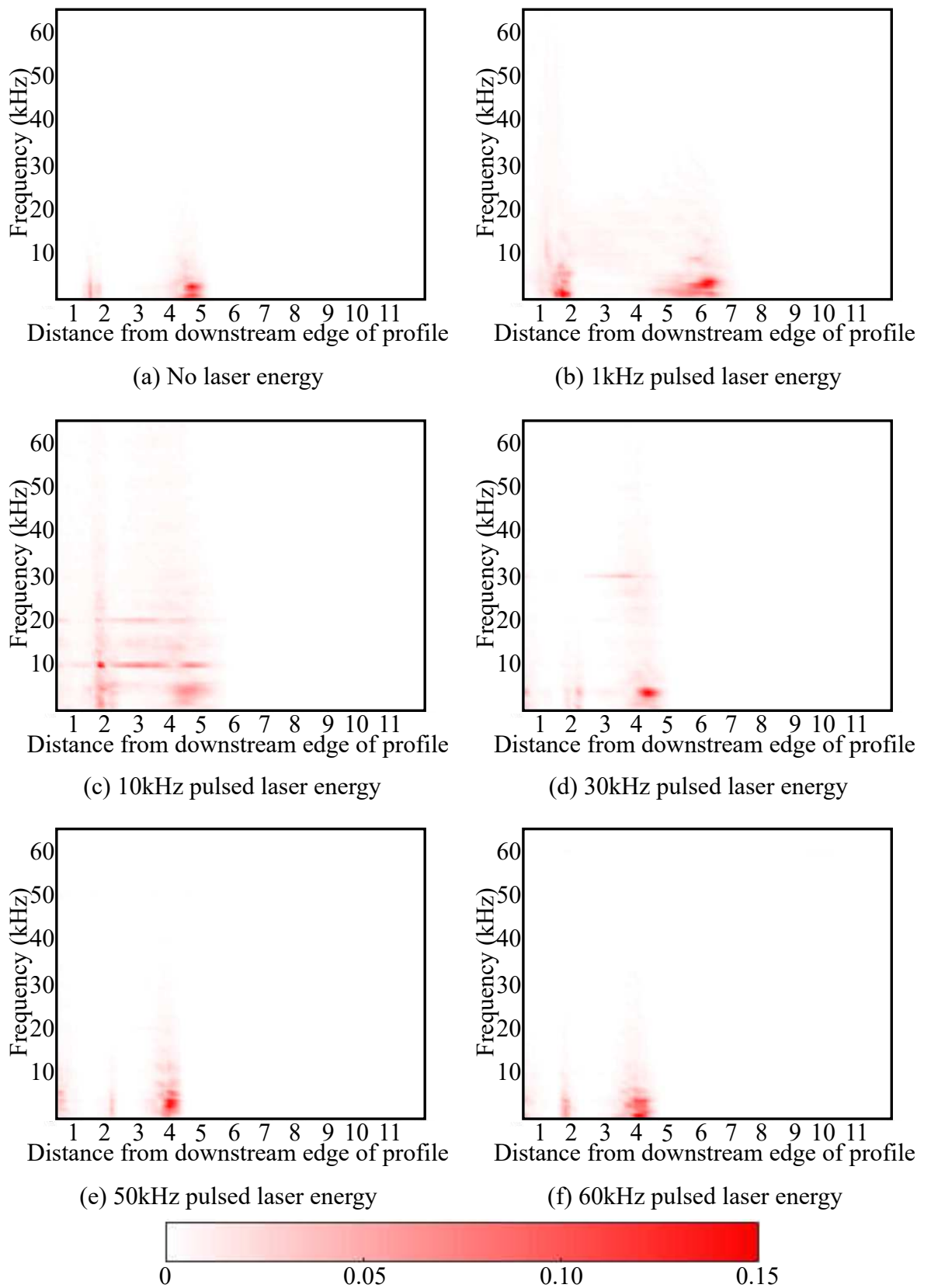


FIGURE 7.20: PSD for each of the test cases in the location shown in figure 7.19.

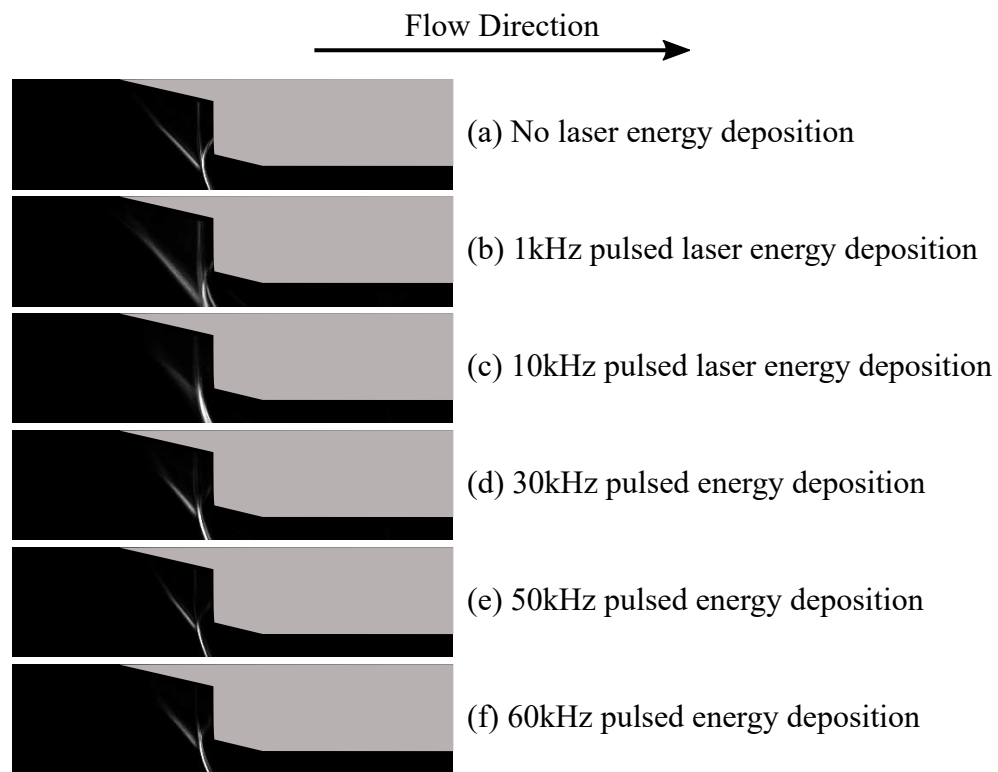


FIGURE 7.21: PSD intensity at the identified intake resonant frequency across the entire Schlieren image for each excitation frequency.

and figure 7.23 shows these images for the 10kHz and 30kHz laser pulse frequency cases. All of the image sets presented were recorded over 2.61ms. The baseline case, figure 7.22a, appears to display a low amplitude oscillation in the separation shock. Although the shock wave has a visible deviation from the mean image, the region of high intensity is small, indicating limited movement of the shock wave. Within the intake isolator, there is a region of unsteadiness (assumed due to the fluctuation intensity/density gradients) at the upstream section, however these fluctuations appear to reduce in amplitude the further the flow travels down the isolator. Figure 7.22b presents the images for the 1kHz excitation case and there are a number of clear features that appear as a result of the laser heated bubbles interacting with the shock system. The image set is split into three distinct flow regimes: A, B and C. Section A refers to the area where the separation on the external compression ramp begins to be suppressed. This separation suppression is a result of the baroclinic interaction which occurs as the low density, heated bubble interacts with the shock wave near the tip of the compression cone. This effect is discussed in more detail by Ogino et al.[135], but fundamentally, the baroclinic interaction describes the interaction between the pressure gradient due to the shock wave and the density gradient due to the laser heated bubble. Baroclinicity refers to the misalignment of the density and pressure gradients resulting in the production of vorticity. In this case the result is that the heated bubble deforms to form a torus that travels along the external compression cone. This torus has a vorticity resulting from this baroclinic interaction. The vorticity present is thought to be the mechanism responsible for the separation suppression.

For the ducted intake used the Reynolds number is calculated as 1.3×10^5 or 3.1×10^5 if the central cone diameter or the external duct's hydraulic diameter are taken as the characteristic length respectively. This places the intake in the transitional regime between a laminar and turbulent boundary layer. It is likely that near the tip of the cone the boundary layer is laminar and therefore susceptible to flow separation. The vorticity generated through the baroclinic interaction will energise the boundary layer and likely promote early transition to a turbulent boundary layer. This results in a boundary layer that is more resistant to separation in comparison to the baseline case. This is shown clearly in section B of figure 7.22b where there is a distinct reduction in the region of separated flow on the external compression cone. Finally, in section C, there are two flow features to highlight. The first is the reappearance of the separation along the length of the compression cone. This is as expected once the torus of vorticity has passed along the cone. The second interesting feature is the region of steady/attached flow which appears inside the intake isolator. This is a result of the reduced unsteadiness of the incoming flow; due to the separation suppression on the compression cone. It is this reduction in unsteadiness in the isolator that is thought to be the reason for the increase in pressure recovery of the entire intake (see results presented in section 7.5.3).

Figure 7.23a, 10kHz laser pulse frequency, shows fundamentally the same steps except that there is less time between the periods of separation suppression. The flow field is different when the 30kHz case is considered, figure 7.23b. For this case there are no clearly defined stages in the intake flowfield. This is due to the lack of any definitive structures forming and disappearing within the images as was the case with the 1kHz and 10kHz cases. The features that are present, such as the separation shock and the separated region, are also not as bright as the features that form in the 1kHz and 10kHz, suggesting that the mean flowfield and the instantaneous flow field are more similar here than in the 1kHz and 10kHz cases. The flow field appears to reach a somewhat steady state where the origin of the separation shock is further downstream than the baseline case.

To shed more light on the relative effect of each laser energy deposition frequency, an attempt was made to extract quantitative data from the intake flow field. The separation location was recorded for 1.2ms for each laser pulse frequency using the Schlieren images. Figure 7.24 presents the time varying separation location recorded for each pulse frequency, from which a number of conclusions can be drawn. The first is that for the 1kHz and 10kHz excitation frequencies there is a clear oscillation in the separation location. For the 10kHz case, this oscillation in separation location occurs at the same frequency as the excitation frequency. For the 1kHz excitation, this appears to also be the case however the sample time is too short to confirm this for certain. Due to the smaller time between the oscillations for the 10kHz case, the separation location never travels back up the compression ramp to the baseline position as is the case with the 1kHz case. A very different behaviour is observed for the 30, 50 and 60kHz excitation frequencies. For these cases there is no clear oscillation in the separation

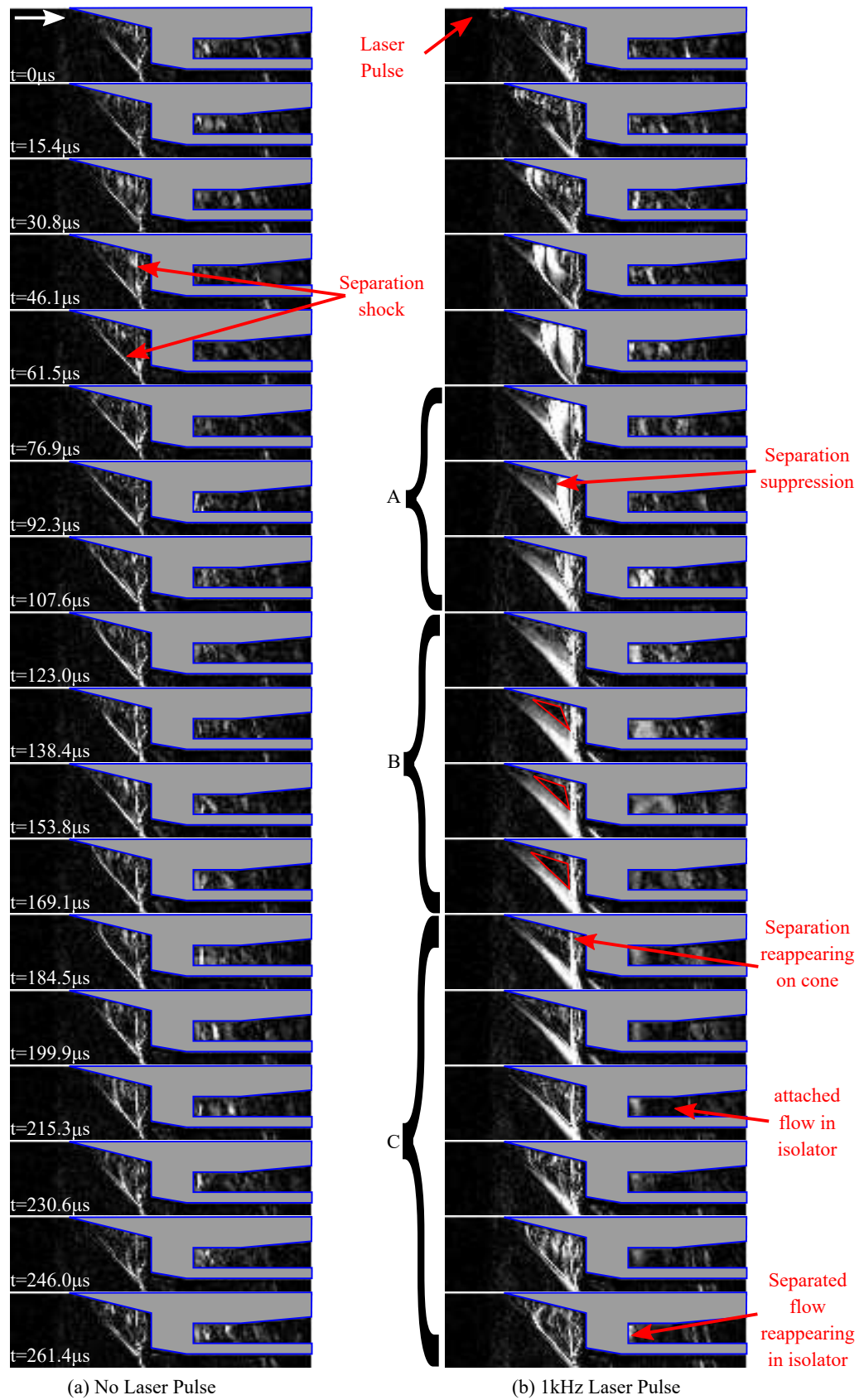


FIGURE 7.22: Post-processed Schlieren images showing the observed deviation from the mean image intensity for the baseline case and the 1kHz laser pulse frequency case.

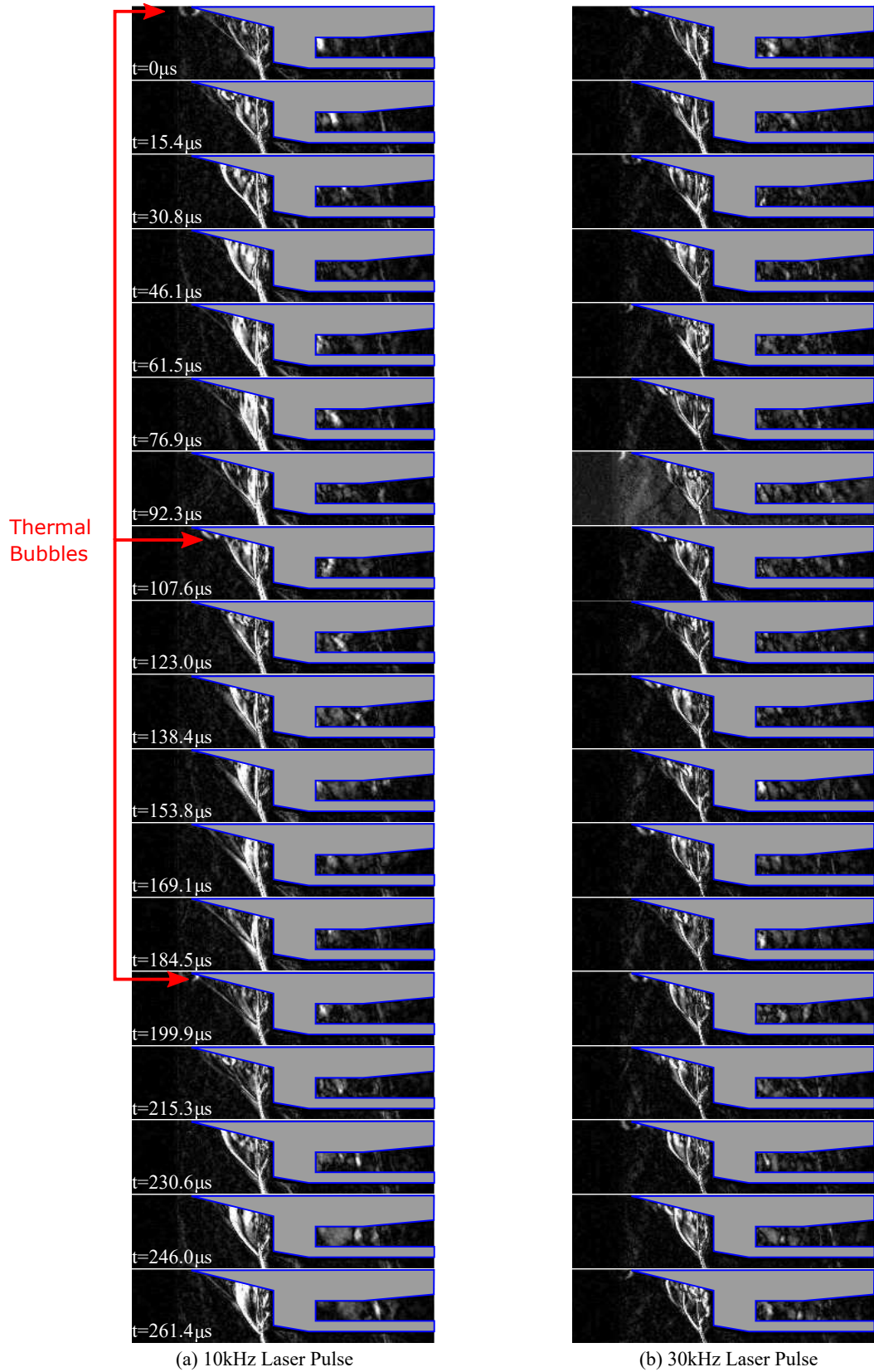


FIGURE 7.23: Post-processed Schlieren images showing the observed deviation from the mean image intensity for the 10kHz and 30kHz laser pulse frequency cases.

location but instead a steady (relative to the oscillating cases) offset is observed relative to the baseline case. The reason for this is thought to be that at higher frequencies the laser heated bubbles responsible for the variation in separation characteristics begin to interact with one another. Figure 7.25 shows the average non-dimensional separation location based on the time history shown in figure 7.24. This suggests that, of the frequencies tested, 10kHz was the optimal for this particular configuration in order to minimise the region of separation. These results suggest that the optimal frequency to minimise the separation region is dependent on the freestream velocity. The frequency at which the heated bubbles will begin to interact with one another will increase with increasing freestream velocity and vice versa with decreasing freestream velocity.

7.5.3 PRESSURE RECOVERY COMPARISON AND RESULTANT IMPACT ON THEORETICAL THRUST

The best measure available of the intake efficiency is the total pressure recovery. A 100% efficient intake would have no total pressure recovery loss i.e. solely isentropic compression. However in reality this does not happen due to the shock waves that decelerate the flow. Total pressure recovery can be used as a measure of the efficiency of the intake at each operating condition i.e. at each laser pulse frequency. Figure 7.26 shows the percentage change in pressure recovery relative to the baseline (no laser) case. These pressures are mean values based on measurements recorded over the entirety of each test. The total pressure is recorded at the centreline, downstream of the isolator section of the intake, and the static pressure is recorded at the side wall of the isolator at the same streamwise location as the total pressure measurement (see figure 7.4 for the pressure port location). The trend in the pressure recovery increase (relative to the baseline intake without laser energy deposition), ΔP , shown in figure 7.26 is the same trend displayed in the mean separation locations presented in figure 7.25. This shows that the separation suppression provided by the pulsed laser energy deposition is responsible for the total pressure recovery increase observed in

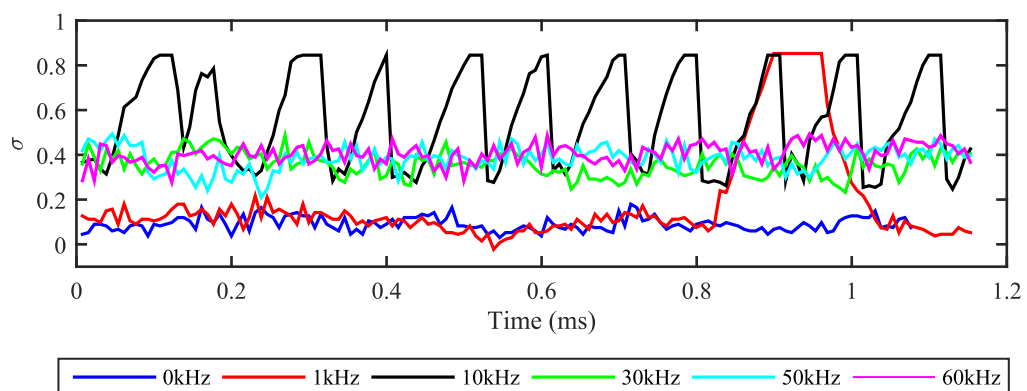


FIGURE 7.24: Variation in non-dimensional separation location (σ) with time.

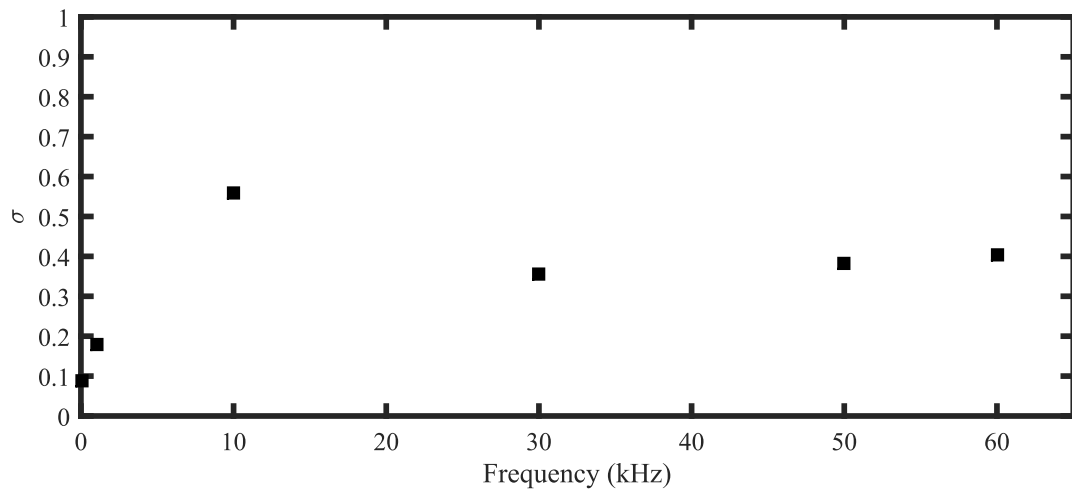


FIGURE 7.25: RMS average non-dimensional separation location (σ).

the intake.

IMPACT OF TOTAL PRESSURE RECOVERY CHANGES ON A HYPOTHETICAL ENGINE

To provide an example of how these pressure recovery improvements could impact engine performance, a hypothetical engine is considered. This is a limited study in that it will focus on one specific engine operating at a specific condition, however it will provide an example of the scale of the potential impact that this flow control method could have. To provide a straightforward method for the calculations, some assumptions had to be made:

- The nozzle expands to ambient pressure.
- The expansion that occurs within the nozzle is isentropic.
- The heat addition due to fuel burn in the combustor results in a choked flow at the exit of the combustor/entrance to the nozzle.

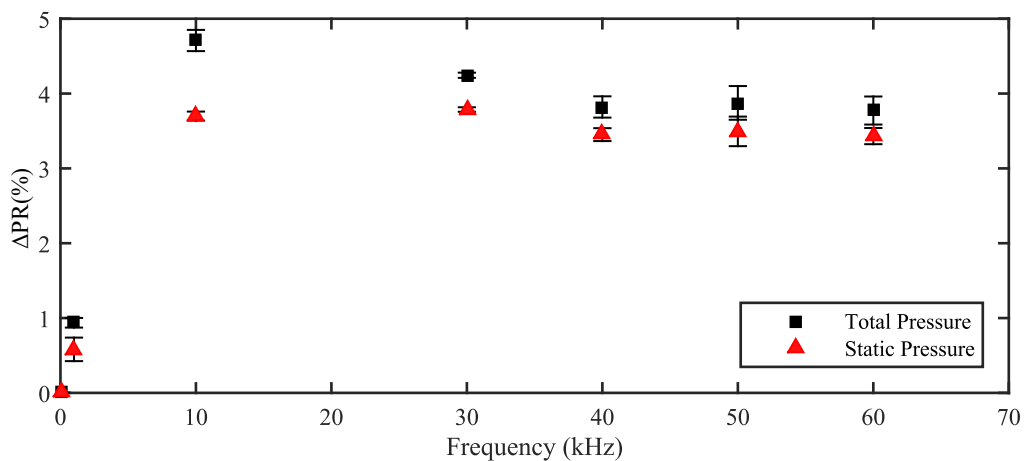


FIGURE 7.26: Percentage change in pressure recovery, relative to the baseline case, due to pulsed laser energy deposition.

- The spillage drag does not change with the addition of the pulsed laser energy. This is likely to be untrue however it is assumed that the difference would be negligible.
- The oblique shock angle that forms the conical shock has the same shock angle for all test cases. This was determined from measurements to be accurate to within 0.5° (i.e. maximum of 0.5° difference between any of the test cases).

In order to be as consistent as possible, the sizing of the hypothetical ramjet will be based on the wind tunnel model used for the testing. As it is unknown how the phenomenon observed would scale, it was thought prudent to avoid adding another uncertainty into these calculations. This set of assumptions will allow the calculation of the fuel flow rate required for the baseline ramjet (no pulsed laser energy) to achieve choked flow at station 4, the entry to the combustor. From this baseline, the impact of the total pressure recovery improvements due to the laser energy deposition will result in a lower required fuel flow rate than the baseline case.

The first step is to calculate the Mach number at the entry to the combustor, M_4 . This can be done using the static and total pressure measurements recorded at the locations shown in figure 7.4. M_4 can be calculated using the isentropic relationship between static and stagnation pressure:

$$M_4 = \sqrt{\left[\left(\frac{P_{04}}{P_4} \right)^{\frac{\gamma-1}{\gamma}} - 1 \right] \frac{2}{\gamma-1}} \quad (7.7)$$

Now, assuming that the combustor can be treated as an example of Rayleigh flow (non-adiabatic flow through a constant area duct with heat addition), the stagnation temperature ratio necessary to provide a choked flow at station 5, the exit of the combustor/entrance to the nozzle, may be calculated using equation 7.8. In reality this is not true however for this hypothetical calculation it will be assumed as the error associated with this assumption will affect the result both with and without laser energy deposition:

$$\frac{T_{05}}{T_{04}} = \left(\frac{1 + \frac{\gamma-1}{2} M_5^2}{1 + \frac{\gamma-1}{2} M_4^2} \right) \left(\frac{M_5}{M_4} \right)^2 \left(\frac{1 + \gamma M_4^2}{1 + \gamma M_5^2} \right) \quad (7.8)$$

Since the stagnation temperature does not vary across shock waves T_{04} is known as it is equal to T_{01} . Therefore from this and equation 7.8, T_{05} may be calculated. From here, the required fuel flow rate can be determined based on the conservation of energy i.e.:

$$f = \frac{C_p(T_{05} - T_{04})}{\Delta H} \quad (7.9)$$

where f is the fuel flow fraction (i.e. fuel mass flow rate over air mass flow rate), C_p is

the specific heat of air at a constant pressure and ΔH is the enthalpy of combustion of the fuel (assumed to be Hydrogen in this case). This fuel fraction can then be converted into a mass flow rate by multiplying the result by the mass flow rate entering the combustor, \dot{m}_4 . This is calculated through equation 7.10:

$$\dot{m}_4 = \frac{\gamma}{\left(\frac{\gamma+1}{2}\right)^{\frac{\gamma+1}{2(\gamma-1)}}} \left(\frac{P_{04} A_4}{\sqrt{\gamma R T_{04}}} \right) \frac{A^*}{A_4} \quad (7.10)$$

From the calculation process defined above, the fuel flow rate required to choke the nozzle geometry for each case can be calculated. These results are presented in figure 7.27 and illustrate how the fuel flow required to achieve the same outlet condition at the combustor changes with the same approximate trend as the total pressure recovery variation. It is observed that there is a significant reduction in the required fuel flow corresponding to the laser frequencies which provided the largest increase in pressure recovery. However, the higher frequencies, which still provided a pressure recovery improvement, mostly required an increased fuel flow.

7.6 CONCLUSIONS

The results presented in this chapter provide interesting insights into the impact of pulsed laser energy deposition on a supersonic intake flow field. The measurable impact on the intake operation, the total pressure recovery, showed a distinct improvement when forced at a particular frequency, 10kHz. Through the calculation process outlined this was shown to result in a potential fuel mass flow rate reduction of 3.7%. This is a significant improvement to the ramjet performance however the overall gain would have to be balanced against the energy used to power the laser in the first place. Therefore the overall benefit for the system would be less apparent than the 3.7% suggested above.

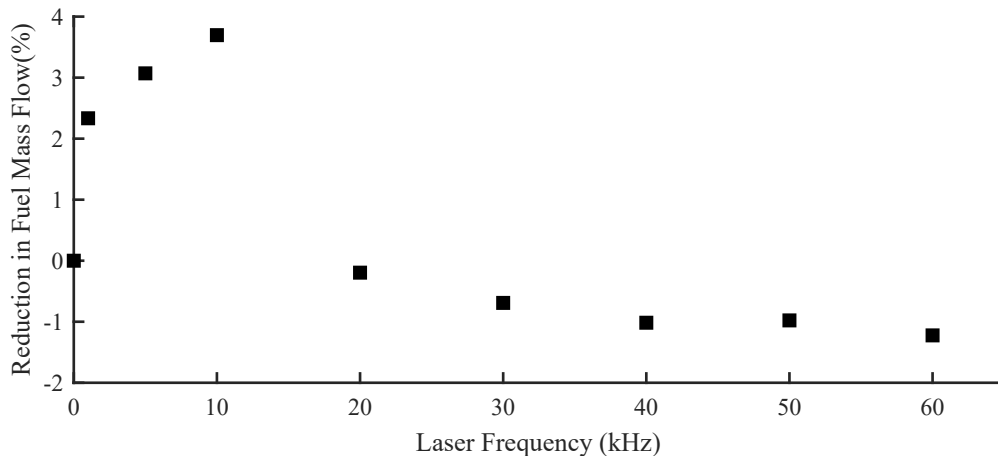


FIGURE 7.27: Percentage reduction in fuel mass flow rate required to achieve a choked flow at the exit of the hypothetical ramjet combustor.

10kHz was found to be a natural resonant frequency in the baseline case however the exact source of this oscillation is thus far not clear. This frequency does not align with any of the expected oscillation frequencies due to “little” or “big” buzz. It is observed in the baseline case for the total pressure measurement, however it is not as distinctly apparent in the oscillations recorded in the Schlieren image intensity. Excitation at 10kHz resulted in a significant amplification of this frequency observed in the frequency analysis of both the Schlieren images and the total pressure fluctuation measurements. This frequency was also shown to be the most effective at mitigating the natural “little” and “big” buzz frequencies observed in the tip shock and the normal shock on the external compression ramp. The reason for the effectiveness of this particular frequency is not clear, however it is clear that this frequency of laser excitation has the most significant impact on the separation characteristics on the external compression ramp (see figures 7.24 and 7.25).

The profile of the separation location follows the profile shown by the total pressure recovery data (figure 7.26) which would appear to confirm that the separation suppression is the reason for the total pressure recovery improvement. The reason as to why, for the frequencies tested, 10kHz was the optimal control frequency is not immediately clear. There are two possibilities considered that would explain the reasoning for this optimal frequency. The first is that the laser pulses are exciting the natural frequency observed in the total pressure fluctuation measurements at 10kHz. However it is not clear what is the source of this natural frequency and it may just be a coincidence. The second is that the optimal frequency is dependant on the freestream Mach number. The dependance would be a result of how the thermal bubbles generated by the laser pulses interact with one another. For the same Mach number, at a low frequency the bubbles do not interact with one another however the time between each thermal bubble and the next interacting with the external compression system is too long and the separation suppression is not apparent for an extended period of time. At a high frequency the bubbles begin to interact with one another and the region of attached flow resulting from one thermal bubble is affected by the following thermal bubble too soon, reducing the overall length of the attached region. The ideal frequency, for this theory, would be such that the cycle of flow reattachment followed by the reappearance of separation completes just as the next thermal bubble begins to interact with the external compression system.

In order to prove which of these theories is correct some further work is required. To prove, or disprove, the second theory further tests are required at varying Mach numbers. If this theory is correct then the optimal frequency should decrease with decreasing freestream Mach number and increase with increasing Mach number. Furthermore, the first theory could be tested using intakes with different geometric parameters at the same Mach number as this will likely alter any naturally occurring oscillation frequency. If the optimal frequency follows the natural frequency, at the same freestream Mach number, then this theory would be confirmed. Which method is chosen to determine the cause of the improvement would depend on the facility

available. If the work was continued at the same facility at Nagoya University then the second method would have to be used as the indraft wind tunnel available is only capable of operating at one supersonic Mach number.

CHAPTER 8

CONCLUSIONS AND FUTURE WORK

The findings of this body of work is broken down into three distinct research areas: (1) considerations that should be made for future wind tunnel design; (2) outcomes of the ns-DBD characterisation; (3) the effectiveness of using ns-DBD plasma actuators for cavity flow control; and (4) the application of laser energy deposition to improve ramjet intake performance. The findings for each of these areas are summarised in the sections that follow.

8.1 CONCLUSIONS

8.1.1 SUPERSONIC WIND TUNNEL DESIGN

The initial part of this work centered on modifying the existing supersonic indraft wind tunnel facility to make it function properly. A number of different theories were considered as to why the facility was not working correctly. This was based on a combination of available wind tunnel measurements and the underlying theory of supersonic wind tunnel design. The modifications made included redesigning the diffuser, redesigning the nozzle, replacing the control valve, shortening the test-section, and re-locating the wind tunnel relative to the pipework of the entire Acre roading facility. The redesign of the diffuser and nozzle are believed to have been improvements to the wind tunnel operation in general, however they were not the key factors preventing the tunnel from operating correctly.

The pipework was found to be the key factor that, when changed, allowed the wind tunnel to function correctly. It was found that a combination of the large number of right angled turns in the pipework, the length of the pipework and the small diameter of some of the piping sections were the issue. These factors combined to produce a facility with a small conductance, a key parameter in vacuum applications. It was shown that by reducing the length of the pipework, limiting the sections of pipework with a small diameter, and limiting the number of right angled turns the tunnel would

operate correctly. The result of these changes was that the calculated conductance increased by almost a factor of 4 from $3.49m^3s^{-1}$ to $13.119m^3s^{-1}$.

The key outcome to take from this section of work for future researchers involved in wind tunnel design is to properly account for the conductance of the pipework between the wind tunnel facility and the downstream vacuum chamber. This work has shown that it can be a severely limiting factor if not correctly accounted for.

8.1.2 NS-DBD ACTUATOR CHARACTERISATION

The aims of the section of work that focused on the characterisation of DBD plasma actuators can be split into primary and secondary objectives. A primary objective was one that was necessary to achieve in order to move forward with the other areas of research (cavity flow control). The only objective that fell into this category was the characterisation of the pressure wave strength produced by the actuators. This was achieved through the use of a conventional Schlieren setup and the optimal actuator design was chosen for future steps. This study showed that there were only two geometric parameters with a significant influence on the pressure wave strength: dielectric thickness and electrode length. As such the thinnest dielectric that was available, 0.4mm thick, was chosen for the actuator being applied as flow control. The result of the study of the electrode length showed that shorter actuators produced stronger pressure waves for the same voltage supply. However the length of the actuator was restricted for the application to supersonic cavity flows. The electrode length was kept as close to the full width of the cavity as was practical and so it was not possible to take advantage of the impact of a shorter electrode.

Secondary objectives were those that posed an interesting and potentially useful area of research, but if unsuccessful would not limit the scope of the rest of the studies within this project. Two objectives fell into this category: a study of the electrical efficiency of ns-DBD plasma actuators and a study of the key thermal features generated as a result of the plasma discharge. The study into the electrical efficiency was carried out by measuring the thermal energy lost through the dielectric barrier and comparing this to the electrical energy supplied. The thermal energy was calculated based on the surface temperature of the dielectric, measured using an IR camera. The electrical energy supply was measured using the back-current shunt technique. The study produced results with mixed success. The electrical measurements were shown to be accurate based on the comparison to the known supply voltage without the DBD actuators. However it was found that the electrical supply was not impedance matched with the transmission line used to supply the actuator. This resulted in exponentially decaying reflections in the measured voltage pulses that introduced uncertainty into the results. This did raise some introducing questions that could be answered in future work (see future work section below).

The IR results were not reliable for a number of reasons. Primarily, it was found that the temperature differences measured were of a similar magnitude to the accuracy

of the camera and thus the results could not be reliably used, for most cases. The temperature differences for the test cases involving the varying dielectric thickness were large enough that the camera uncertainty was less of an issue. This did allow the confirmation of results of a previous study conducted into a similar area. This suggests that, with an sensitive/accurate enough camera, useful results could be recorded regarding the other geometric parameters investigated.

The final objective, studying the key thermal features generated as a result of the plasma discharge, was achieved through the use of calibrated Schlieren. This allowed the measurement of the temperature field within the entire Schlieren field of view. The technique was calibrated by measuring the thermal boundary profile generated by a heated flat plate, a well documented test case. This technique provided some interesting insight on how the temperature field changes above the actuators during the discharge. One such observation was that heat was generated at the termination of the plasma discharge as well as the start of it. This is thought to be another source of loss that could contribute to actuator efficiency as the pressure wave is generated at the start of the plasma discharge and as such the heat at the termination does no useful work.

The calibrated Schlieren was also used to try and measure the efficiency of the actuator by assuming that the useful work added to the air could be used as a measure of the actuator efficiency. However, it was found that the measured thermal energy added to the air was significantly lower than that of the electrical energy supplied. This is an area where further work could be done to attempt to correlate the thermal energy added to the flow to pressure wave strength and actuator efficiency.

8.1.3 NS-DBD PLASMA ACTUATORS FOR SUPERSONIC CAVITY FLOW CONTROL

The aim of this section of work was to apply the characterised DBD plasma actuators as a flow control device for a supersonic cavity flow. The desired outcome was the reduction or amplification, either would prove that the ns-DBD's could exert some flow control authority, in the amplitude of the resonant tones observed within the cavity. This was investigated through both qualitative, Schlieren and oil flow, and quantitative methods, laser vibrometry and pressure measurements (when possible).

Unfortunately, the ns-DBD plasma actuators were not shown to be successful in this capacity. Schlieren and oil flow were used to examine the steady state flow field. Neither of these techniques displayed any significant variation in the flow field as a result of the ns-DBD actuators. The quantitative measurements recorded using the laser vibrometer resulted in the same conclusion. There was no significant variation in the amplitude of the resonant frequencies observed within the cavity.

However, there was one positive outcome achieved as a result of this section of work. Through comparison with theoretical values and numerical predictions (CFD); it was

found that a vibrometer could be used to effectively measure the resonant, pressure driven frequencies within the cavity. This technique has not been shown to be used successfully before and provides a novel approach to gather information on the resonant behaviour of these types of cavity flows. This also presents an opportunity to potentially apply the technique to other similar problems.

8.1.4 APPLICATION OF LASER ENERGY DEPOSITION TO IMPROVE RAMJET INTAKE PERFORMANCE

Laser energy deposition has been shown to be effective previously for supersonic flow control, however this work was interested in quantifying further the potential gain that this can provide to a Ramjet propulsion system and to further examine the fluid mechanics of the flow control.

This work provides a useful insight into the dependency of the success of the laser flow control on the laser frequency. It was shown that there is an optimal laser pulse frequency to use, in terms of largest pressure recovery improvement. For the conditions examined here this was found to be 10kHz. There are two possible reasons provided for this frequency resulting in the biggest benefit to the system. 10kHz was found to be a naturally resonant frequency in the baseline, no flow control, condition examined. The source of this frequency is not clear as it does not match either of the well-known "little" or "big" buzz intake frequencies. The laser energy could be exciting the source of this naturally resonant frequency and this maybe the reason for the improvement in pressure recovery. The other possible mechanism is that at higher laser frequencies, at this freestream Mach number, the laser generated, heated bubbles begin to interact with one another and diminish the intake separation improvement caused by the laser energy. The Schlieren imaging recorded suggested that this was the case and the post-processing showed that the 10kHz pulse frequency provided the biggest improvement in the separation characteristics for this intake. This is due to the heated bubbles interacting with one another at frequencies higher than 10kHz and reducing the positive impact that they have.

The impact of the laser energy deposition was quantified by the measurement of the total pressure recovery observed within the intake model. Through the calculation process outlined in chapter 7, it was shown that, for a specific set of conditions, this could provide a benefit of up to 3.7% reduction in fuel mass flow required for the same generated thrust. It is highlighted that this figure only applies to a very specific set of conditions, however it does provide an idea of the potential efficiency gains that this flow control could provide for an operational Ramjet propulsion system.

8.2 FUTURE WORK

As highlighted throughout the course of this work, there are a number of areas that are worthy of further examination.

8.2.1 NS-DBD ACTUATOR CHARACTERISATION

1. Investigate effect on thermal loss due to various geometric and electrical parameters with hardware that has an appropriate level of accuracy.
2. Examine the electrical and thermal properties, using the techniques as presented in this work, of an actuator with impedance that matches that of the voltage supply.

8.2.2 NS-DBD CAVITY FLOW CONTROL

1. Attempt to use a more powerful voltage supply, and a DBD capable of supporting the high voltage, to control a cavity under the same conditions.
2. Test various different geometries of DBD actuators such as a tabbed configuration to examine the impact on the flow control authority.
3. Test the application of laser energy deposition for the same flow control application. One option is the use of an array of focused laser energy to influence the flow along the width of the cavity.
4. Attempt to calibrate a laser vibrometer and membrane combination to a known pressure. This will allow not only the frequency and relative amplitude of the signal to be examined as was the case here, but also the absolute pressure to be measured.

8.2.3 LASER ENERGY DEPOSITION TO IMPROVE RAMJET INTAKE PERFORMANCE

1. Conduct an experiment with varying Mach number in order to examine if the Mach number does influence the optimal laser pulse frequency.

BIBLIOGRAPHY

- [1] J. D. Anderson, *Modern Compressible Flow with Historical Perspective*. McGraw-Hill, 2003.
- [2] K. Takashima, Y. Zuzeeq, W. R. Lempert, and I. V. Adamovich, "Characterization of a surface dielectric barrier discharge plasma sustained by repetitive nanosecond pulses," *Plasma Sources Science and Technology*, vol. 20, 2011.
- [3] M. J. Hargather and G. S. Settles, "A comparison of three quantitative schlieren techniques," *Optics and Lasers in Engineering*, 2012.
- [4] T. Ukai, A. Russell, H. Zare-Behtash, and K. K., "Temporal variation of the spatial density distribution above a nanosecond pulsed dielectric barrier discharge plasma actuator in quiescent air," *Physics of Fluids*, 2018.
- [5] R. S. Fry, "A century of ramjet propulsion technology evolution," *Journal of Propulsion and Power*, vol. 20, pp. 27–58, 2004.
- [6] E. Curran, "Fluid Phenomena in Scramjet Combustion Systems," *Annual Review of Fluid Mechanics*, vol. 28, pp. 323–360, 1996.
- [7] C. S. Billig, F. S. and P. P. Pandolfini, "Design techniques for dual mode ram-scramjet combustors," *AGARD 75th Symposium of Hypersonic Combined Cycle Propulsion*, vol. 23, 1990.
- [8] N. Webb and M. Samimy, "Shock-Trapping Capability of a Cavity in a Supersonic Flow," *46th AIAA Plasmadynamics and Lasers Conference*, 2015.
- [9] S. B. Verma and A. Hadjadj, "Supersonic flow control," *Shock Waves*, vol. 25, pp. 443–449, 2015.
- [10] Y. Lee, M. Kang, H. Kim, and T. Setoguchi, "Passive control techniques to alleviate supersonic cavity flow oscillation," *Journal of Propulsion and Power*, vol. 24, 2008.
- [11] K. H. Lo and K. Kontis, "Supersonic flow over rounded contour bumps with vortex generators or passive longitudinal jets." *Experimental Thermal and Fluid Science*, vol. 85, pp. 213–228, 2017.

- [12] A. Valdivia, K. B. Yuceil, J. L. Wagner, N. T. Clemens, and D. S. Dolling, "Control of Supersonic Inlet-Isolator Unstart Using Active and Passive Vortex Generators," *AIAA Journal*, vol. 52, no. 6, pp. 1207–1218, 2014.
- [13] W. Wong, "The application of boundary layer suction to suppress strong shock-induced separation in supersonic inlets." *Experimental Thermal and Fluid Science*, vol. 85, pp. 213–228, 2017.
- [14] V. Narayanaswamy, L. L. Raja, and N. T. Clemens, "Control of unsteadiness of a shock wave/turbulent boundary layer interaction by using a pulsed-plasma-jet actuator," *Physics of Fluids*, vol. 24, 2012.
- [15] Boom Supersonic, "Our partnership with japan airlines," *Boom Supersonic*, May 2018. [Online]. Available: boomsupersonic.com
- [16] Reaction Engines, "Reaction engines participating in uk mod - funded research programme to develop hypersonic propulsion systems," *Reaction Engines*, Jul 2019. [Online]. Available: www.reactionengines.co.uk
- [17] Rolls Royce, "Rolls-royce to develop hypersonic technology with uk mod," *Rolls Royce*, Jul 2019. [Online]. Available: www.rolls-royce.com
- [18] J. Rienitz, "Schlieren experiment 300 years ago," *Nature*, vol. 254, pp. 293–295, 1975.
- [19] P. Krehl and S. Engemann, "August toepfer - the first who visualized shock waves," *Shock Waves*, vol. 5, pp. 1–18, 1995.
- [20] J. P. Marat, *Recherches physiques sur le feu*. Chez C. A. Jombert, 1780.
- [21] H. Kleine, H. Grönig, and K. Takayama, "Simultaneous shadow, schlieren and interferometric visualization of compressible flows," *Optics and Lasers in Engineering*, vol. 44, no. 3, pp. 170 – 189, 2006, optical Methods in Heat Transfer and Fluid Flow.
- [22] R. Gardon, "Variation of densities and refractive indices in tempered glass," *Journal of the American Ceramic Society*, vol. 61, 2006.
- [23] K. H. Lo, H. Zare-Behtash, and K. Kontis, "Control of flow separation on a contour bump by jets in a mach 1.9 free-stream: An experimental study," *Acta Astronautica*, vol. 126, pp. 229–242, 2016.
- [24] I. Bajsic, J. Kutin, and T. Zagar, "The response time of a pressure measurement system with a connecting tube," *Instrumentation Science and Technology*, vol. 35, pp. 399–409, 2007.
- [25] F. Avallone, C. S. Greco, F. F. J. Schrijer, and G. Cardone, "A low-computational-cost inverse heat transfer technique for convective heat transfer measurements in hypersonic flows," *Experiments in Fluids*, vol. 56, 2015.

- [26] F. Avallone and G. Correale, "Method to quantify the electrical efficiency of a ns-DBD plasma actuator," in *10th Pacific Symposium on Flow Visualization and Image Processing*, 2015.
- [27] M. Planck, *Ueber eine Verbesserung der Wien'schen Spectral-Gleichung*. J.A. Barth, 1900.
- [28] J. Stefan, K. Staatsdruckerie, Ö. A. der Wissenschaften, and A. A. de Ciencias, *Über die Beziehung zwischen der Wärmestrahlung und der Temperatur*, ser. Sitzungsberichte der Kaiserlichen Akademie der Wissenschaften in Wienn. Aus der k.k. Hof-und Staatsdruckerei, 1879.
- [29] T. Astarita and G. M. Carlomagno, *Infrared thermography for thermo-fluid-dynamics*. Springer, 2013.
- [30] S. L. Chang and K. T. Rhee, "Blackbody radiation functions," *International Communications in Heat and Mass Transfer*, vol. 11, pp. 451–455, 1984.
- [31] S. P. Langley, "The bolometer and radiant energy," *Proceedings of the American Academy of Arts and Sciences*, vol. 16, pp. 342–358, 1880.
- [32] B. T. Meggit, *Chapter 17 - Fiber Optics in Sensor Instrumentation*. Butterworth-Heinemann, 2010.
- [33] W. Y. K. Chan, P. A. Jacobs, and D. J. Mee, "Suitability of the $k - \epsilon$ turbulence model for the scramjet flowfield simulations," *International Journal for Numerical Methods in Fluids*, vol. 70, pp. 493–514, 2012.
- [34] F. Gnani, H. Zare-Behtash, C. White, and K. Kontis, "Numerical investigation on three-dimensional shock train structures in rectangular isolators," *European Journal of Mechanics / B Fluids*, vol. 72, 2018.
- [35] CD-Adapco, "Star-ccm+ user documentation," CD-Adapco, Tech. Rep., 2015.
- [36] J. Boussinesq, "Essai sur la théorie des eaux courantes," *Mémoires présentés par divers savants à l'Académie des Sciences*, vol. 23, 1877.
- [37] B. H. Anderson, J. Tinapple, and L. Surber, "Optimal Control of Shock Wave Turbulent Boundary Layer Interactions Using Micro-Array Actuation," *3rd AIAA Flow Control Conference*, pp. 1–14, 2006.
- [38] J. Hadamard, "Leçons sur la propagation des ondes et les equations de l'hydrodynamique," *Nature*, vol. 71, pp. 196–197, 1903.
- [39] T. M. Cain, W. K. E. Huntington-Thresher, and P. G. Mariott, "Final report on the centrebody nozzle design," *Fluid Gravity Engineering*, Tech. Rep., 1994.
- [40] H. P. Liepman, "An analytic design method for a two-dimensional asymmetric curved nozzle," *Air Research and Development Command USAF*, 1953.

- [41] M. Tucker, "Approximate calculation of turbulent boundary-layer development in compressible flow," *NACA-TN-2337*, 1951.
- [42] E. W. E. Rogers and B. M. Davis, "A note on turbulent boundary-layer allowances in supersonic nozzle design," *Aeronautical Research Council Technical Report*, 1957.
- [43] J. Ruptash, "Supersonic wind tunnels - theory, design and performance," Ph.D. dissertation, University of Toronto, 1952.
- [44] R. E. Wilson, "Turbulent boundary layer growth with favorable static pressure gradient at supersonic speeds," *Proceedings of the 2nd Midwestern Conference on Fluid Mechanics*, 1952.
- [45] B. S. Stratford and G. S. Beavers, "The calculation of the compressible turbulent boundary layer in an arbitrary pressure gradient - a correlation of certain previous methods," *Aeronautical Research Council Technical Report*, 1961.
- [46] T. L. Ho and E. G., "Design of a nozzle contraction for uniform sonic throat flow," *AIAA Journal*, vol. 38, pp. 720–723, 2000.
- [47] P. W. Runstadler, *Diffuser Data Book*. Creare, inc., 1975.
- [48] F. E. C. Culick and T. Rogers, "The response of normal shocks in diffusers," *AIAA Journal*, vol. 21, pp. 1382–1390, 1982.
- [49] A. Kantrowitz, "The formation and stability of normal shock waves in channel flows," *NACA-TN-1225*, 1947.
- [50] D. Halwidl, *Development of an Effusive Molecular Beam Apparatus*. Springer Spektrum, 2016.
- [51] E. Sherriff, "Conductance of bends and concentric tubes of a vacuum system," *Journal of Scientific Instruments*, vol. 26, pp. 43–44, 1949.
- [52] R. L. Stallings and F. J. Wilcox, "Experimental cavity pressure distributions at supersonic speeds," *NACA-TN-2683*, 1987.
- [53] J. Rossiter, "Wind-tunnel experiments on the flow over rectangular cavities at subsonic and transonic speeds," p. 36, 1966.
- [54] M. A. Kegerise, S. Spina E. F., Garg, and C. L. N., "Mode-switching and nonlinear effects in compressible flow over a cavity," *Physics of Fluids*, 2004.
- [55] H. H. Heller, D. G. Holmes, and E. E. Covert, "Flow-induced pressure oscillations in shallow cavities," *Journal of sound and vibration*, vol. 18, pp. 545–553, 1971.
- [56] Y. Li, X. Wang, and D. Zhang, "Control strategies for aircraft airframe noise reduction," *Chinese Journal of Aeronautics*, vol. 26, no. 2, pp. 249 – 260, 2013.
- [57] L. Cattafesta, D. Shukla, G. S., and R. J., "Development of an adaptive weapons-bay suppression system," *5th AIAA/CEAS Aeroacoustics Conference and Exhibit*, 1999.

- [58] K. Yu, K. Wilson, and K. Schadow, "Effect of flame-holding cavities on supersonic-combustion performance," *Journal of Propulsion and Power*, 2001.
- [59] N. Webb and M. Samimy, "Supersonic Cavity Control Using Plasma Actuators," *53rd AIAA Aerospace Sciences Meeting*, 2015.
- [60] E. Lazar, G. Elliott, and N. . Glumac, "Control of the Shear Layer Above a Supersonic Cavity Using Energy Deposition," *AIAA Journal*, vol. 46, no. 12, pp. 2987–2997, 2008.
- [61] L. N. Cattafesta, Q. Song, D. R. Williams, C. W. Rowley, and F. S. Alvi, "Active control of flow-induced cavity oscillations," *Progress in Aerospace Sciences*, vol. 44, pp. 479–502, 2008.
- [62] L. Shaw and S. Northcraft, "Closed loop active flow control for cavity resonance," *AIAA*, vol. 99, 1999.
- [63] A. Vakili and C. Gauthier, "Control of cavity flow by upstream mass-injection," *Journal of Aircraft*, vol. 31, 1994.
- [64] P. Bueno, O. Unalms, N. Clemens, and S. Dolling, "The effects of upstream mass injection on a mach 2 cavity flow," *40th AIAA Aerospace Sciences Meeting and Exhibit*, 2002.
- [65] N. Zhuang, F. S. Alvi, M. B. Alkisar, and C. Shih, "Supersonic Cavity Flows and Their Control," *AIAA Journal*, vol. 44, no. 9, pp. 2118–2128, 2006.
- [66] T. Ukai, H. Zare-Behtash, K. H. Lo, K. Kontis, and S. Obayashi, "Effect of dual jets distance on mixing characteristics and flow path within a cavity in supersonic crossflow," *International Journal of Heat and Fluid Flow*, vol. 50, 2014.
- [67] D. Williams, D. Cornelius, and C. Rowley, "Supersonic cavity response to open loop forcing," in *First Berlin Conference on Active Flow Control*, 2006.
- [68] C. W. Rowley and W. D. R., "Dynamics and control of high-reynolds number flow over open cavities," *Annual Review of Fluid Mechanics*, vol. 38, 2006.
- [69] N. Webb and M. Samimy, "Control of a Non-Resonating Supersonic Cavity Using Plasma Actuators," *54th AIAA Aerospace Sciences Meeting*, 2016.
- [70] P. Senthilkumar and T. M. Muruganandam, "Experimental studies on unsteady start/unstart of high speed air intakes with moving cowl," in *29th International Symposium on Shock Waves 1*. Cham: Springer International Publishing, 2015, pp. 699–704.
- [71] S. Im, H. Do, and M. Cappelli, "The manipulation of an unstarting supersonic flow by plasma actuator," *Journal of Physics D: Applied Physics*, vol. 45, 2012.
- [72] S. Takasaki, A. Fujimoto, B. J. Churchill, and T. Takasu, "Inlet unstart influence on aerodynamic characteristics of next generation supersonic transport (sst)," *SAE Transactions*, vol. 107, pp. 1638–1644, 1998.

- [73] A. Kantrowitz and C. Donaldson, "Preliminary investigation of supersonic diffusers," Langley Memorial Aeronautical Laboratory, Tech. Rep., 1945.
- [74] N. Ratanak, "Analysis of a channeled centrebody supersonic inlet for f-15b research," *48th AIAA Aerospace Sciences Meeting*, 2010.
- [75] S. Beresh, J. Wagner, and C. K., "Compressibility effects in the shear layer over a rectangular cavity," *Journal of Fluid Mechanics*, 2016.
- [76] R. Murray and G. Elliott, "Characteristics of the compressible shear layer over a cavity," *AIAA Journal*, vol. 39, no. 5, pp. 846–856, 2001.
- [77] A. Russell, H. Zare-Behtash, and K. Kontis, "Joule heating flow control methods for high-speed flows," *Journal of Electrostatics*, 2016.
- [78] W. Siemens, "Ueber die elektrostatische Induction und die Verzögerung des Stroms in Flaschendrähnen," *Poggendorffs Annalen der Physik und Chemie*, 1857.
- [79] B. Eliasson and U. Kogelschatz, "Modelling and applications of silent discharge plasmas," *IEEE Transactions on Plasma Sciences*, 1991.
- [80] A. Fridman, A. Chirokov, and A. Gutsol, "Non-thermal atmospheric pressure discharges," *J. Phys. D*, vol. 38, p. 1, 2005.
- [81] E. Moreau, "Airflow control by non-thermal plasma actuators," *Journal of Physics D: Applied Physics*, vol. 40, pp. 605–636, 2007.
- [82] R. Erfani, H. Zare-Behtash, C. Hale, and K. Kontis, "Development of DBD plasma actuators: The double encapsulated electrode," *Acta Astronautica*, vol. 109, pp. 132–143, 2015.
- [83] M. Rihard and S. Roy, "Serpentine geometry plasma actuators for flow control," *Journal of Applied Physics*, 2013.
- [84] S. O. Macheret, M. N. Shneider, and R. B. Miles, "Scramjet Inlet Control by Off-Body Energy Addition: A Virtual Cowl," *AIAA Journal*, vol. 42, no. 11, pp. 2294–2302, 2004.
- [85] A. V. Likhanskii, M. N. Shneider, S. O. Macheret, and R. B. Miles, "Modeling of Interaction Between Weakly Ionized Near-Surface Plasmas and Gas Flow," *44th AIAA Aerospace Sciences Meeting and Exhibit*, pp. 1–26, 2006.
- [86] D. F. Opaitis, G. Neretti, A. V. Likhanskii, S. Zaidi, M. N. Shneider, and R. B. Miles, "Experimental Investigation of DBD Plasma Actuators Driven by Repetitive High Voltage Nanosecond Pulses with DC or Low-Frequency Sinusoidal Bias," in *38th AIAA Plasmadynamics and Lasers Conference*, no. June, 2007, pp. 1–21.
- [87] D. V. Roupasov, A. A. Nikipelov, M. M. Nudnova, and A. Y. Starikovskii, "Flow Separation Control by Plasma Actuator with Nanosecond Pulsed-Periodic Discharge," *AIAA Journal*, vol. 47, no. 1, pp. 168–185, 2009.

- [88] N. A. Popov, "Investigation of the mechanism for rapid heating of nitrogen and air in gas discharges," *Plasma Physics Reports*, vol. 27, no. 10, pp. 886–896, 2001.
- [89] N. Bohr, "On the Constitution of Atoms and Molecules, Part II Systems Containing Only a Single Nucleus," *The London, Edinburgh, and Dublin Philosophical*, vol. 26, pp. 1–25, 1913.
- [90] N. Benard, N. Zouzou, A. Claverie, J. Sotton, and E. Moreau, "Optical visualization and electrical characterization of fast-rising pulsed dielectric barrier discharge for airflow control applications," *Journal of Applied Physics*, vol. 111, no. 2012, 2012.
- [91] R. Dawson and J. Little, "Effects of pulse polarity on nanosecond pulse driven dielectric barrier discharge plasma actuators," *Journal of Applied Physics*, vol. 115, no. 2014, 2014.
- [92] K. Takashima, Z. Yin, and I. V. Adamovich, "Measurements and kinetic modeling of energy coupling in volume and surface nanosecond pulse discharges," *Plasma Sources Science and Technology*, vol. 22, 2013.
- [93] A. C. Aba'a Ndong, N. Zouzou, N. Benard, and E. Moreau, "Geometrical optimization of a surface DBD powered by a nanosecond pulsed high voltage," *Journal of Electrostatics*, vol. 71, no. 3, pp. 246–253, 2013.
- [94] R. Dawson and J. Little, "Characterization of nanosecond pulse driven dielectric barrier discharge plasma actuators for aerodynamic flow control," *Journal of Applied Physics*, vol. 113, 2013.
- [95] J. Van den Broecke, G. Correale, and F. Avallone, "Characterization of efficiency of energy deposition of a ns-DBD plasma actuator," *54th AIAA Aerospace Sciences Meeting*, no. January, pp. 1–16, 2016.
- [96] C. Lecuyer, *Makers of the Microchip: A documentary history of fairchild semiconductor*, 1st ed. MIT Press, 2010.
- [97] L. N. Dworsky, *Modern Transmission Line Theory and Applications*. Wiley, 1980.
- [98] T. Underwood, S. Roy, and B. Glaz, "Physics based lumped element circuit model for nanosecond pulsed dielectric barrier discharges," *Journal of Applied Physics*, vol. 113, no. 2013, 2013.
- [99] F. Sarvar, N. J. Poole, and P. A. Witting, "Pcb glass-fibre laminates: Thermal conductivity measurements and their effect on simulation," *Journal of Electronic Materials*, vol. 19, no. 12, pp. 1345–1350, 1990.
- [100] S. Ostrach, "An analysis of laminar free-convection flow and heat transfer about a flat plate parallel to the direction of the generating body force," *NACA-TN-2635*, 1952.
- [101] J. Dudley and L. Ukeiley, "Detached eddy simulation of a supersonic cavity flow

- with and without passive flow control," *20th AIAA Computational Fluid Dynamics Conference*, 2011.
- [102] C. Panigrahi, A. Vaidyanathan, and M. Nair, "Effects of subcavity in supersonic cavity flow," *Physics of Fluids*, vol. 31, no. 3, 2019.
- [103] J. Pereira and J. Sousa, "Influence of impingement edge geometry on cavity flow oscillations," *AIAA Journal*, vol. 32, no. 8, 1994.
- [104] T. Ukai, H. Zare-behtash, E. Erdem, K. Lo, and K. Kontis, "Effectiveness of jet location on mixing characteristics inside a cavity in supersonic flow," *Experimental Thermal and Fluid Science*, 2014.
- [105] O. W. Mcgregor and R. White, "Drag of rectangular cavities in supersonic and transonic flow including the effects of cavity resonance," *AIAA Journal*, vol. 8, no. 11, pp. 1959–1964, 1970.
- [106] K. Oswatitsch, "Pressure Recovery for Missiles with Reaction Propulsion at High Supersonic Speeds (The Efficiency of Shock Diffusers)". *Vieweg+Teubner Verlag*, 1980, pp. 290–323.
- [107] A. Ferri and L. M. Nucci, "The origin of aerodynamic instability of supersonic inlets at subcritical conditions," *NACA RM L50K30*, 1951.
- [108] C. L. Dailey, "Supersonic diffuser instability," Ph.D. dissertation, California Institute of Technology, 1954.
- [109] S. Hirt and B. H. Anderson, "Experimental investigation of the application of microramp flow control to an oblique shock interaction," *AIAA*, 2009.
- [110] H. Babinsky, Y. Li, and F. Pitt, "Microramp Control of Supersonic Oblique Shock-Wave/Boundary-Layer Interactions," *AIAA Journal*, 2009.
- [111] M. Vyas, S. Hirt, R. Chima, D. David, and T. Wayman, "Experimental investigation of micro vortex generators on a low boom supersonic inlet," *29th AIAA Applied Aerodynamics Conference*, 2011.
- [112] G. K. Suryanarayana and R. Dubey, "Performance enhancement of a ramjet air intake by passive bleed of boundary layer," *Journal of Spacecraft and Rockets*, 2018.
- [113] M. R. Soltani, J. S. Younsi, and M. Farahani, "Effects of Boundary-Layer Bleed Parameters on Supersonic Intake Performance," *Journal of Propulsion and Power*, 2015.
- [114] E. K. Damon and R. G. Tomlinson, "Observation of Ionization of Gases by a Ruby Laser," *Applied Optics*, vol. 2, p. 546, 1963.
- [115] G. Leuchs, "Multiphoton ionization of atoms," *Laser Physics*, vol. 182, pp. 174–194, 1983.

- [116] E. Panarella, "Theory of laser-induced gas ionization," *Foundations of Physics*, vol. 4, pp. 227–259, 1974.
- [117] Y. P. Raizer, "Heating of a Gas by a Powerful Light Pulse," *Soviet Physics JetP*, vol. 21, no. 5, 1965.
- [118] A. W. Ali, "On Laser Air Breakdown, Threshold Power and Laser Generated Channel Length," Naval Research Laboratory, Tech. Rep., 1983.
- [119] N. A. Generalov, V. P. Zimakov, and G. I. Kozlov, "Continuous Optical Discharge," *Soviet Physics JetP Letters*, 1970.
- [120] D. Sperber, H. A. Eckel, S. Steimer, and S. Fasoulas, "Objectives of Laser-Induced Energy Deposition for Active Flow Control," *Contributions to Plasma Physics*, vol. 52, no. 7, pp. 636–643, 2012.
- [121] A. Sasoh, Y. Sekiya, T. Sakai, J. Kim, and A. Matsuda, "Supersonic Drag Reduction with Repetitive Laser Pulses Through a Blunt Body," *AIAA Journal*, vol. 48, no. 12, pp. 2811–2817, 2010.
- [122] H. Yanjii, D. Wang, Q. Li, and J. Ye, "Interaction of single-pulse laser energy with bow shock in hypersonic flow," *Chinese Journal of Aeronautics*, vol. 27, no. 2, pp. 241–247, 2014.
- [123] T. Sakai, "Supersonic Drag Performance of Truncated Cones with Repetitive Energy Deposition," *International Journal of Aerospace Innovations*, vol. 1, pp. 31–43, 2009.
- [124] J. Kim, A. Matsuda, T. Sakai, and A. Sasoh, "Wave Drag Reduction with Acting Spike Induced by Laser-Pulse Energy Depositions," *AIAA Journal*, vol. 49, no. 9, pp. 2076–2078, 2011.
- [125] A. Sasoh, J. H. Kim, K. Yamashita, T. Sakai, and A. Matsuda, "Efficient supersonic drag reduction using repetitive laser pulses of up to 80 kHz," *AIP Conference Proceedings*, vol. 1402, no. 2011, pp. 424–429, 2011.
- [126] R. G. Adelgren, H. Yan, G. S. Elliott, D. D. Knight, T. J. Beutner, and A. A. Zheltovodov, "Control of Edney IV Interaction by Pulsed Laser Energy Deposition," *AIAA Journal*, vol. 43, no. 2, pp. 256–269, 2005.
- [127] T. Osuka, E. Erdem, N. Hasegawa, R. Majima, T. Tamba, S. Yokota, A. Sasoh, and K. Kontis, "Laser energy deposition effectiveness on shock-wave boundary-layer interactions over cylinder-flare combinations," *Physics of Fluids*, vol. 26, 2014.
- [128] E. Erdem, K. Kontis, T. Osuka, R. Majima, T. Tamba, and A. Sasoh, "Laser Energy Deposition for Shock Wave Boundary Layer Control at Supersonic Speeds," in *29th International Symposium on Shock Waves*, 2013, pp. 1411–1416.
- [129] T. Tamba, H. S. Pham, T. Shoda, A. Iwakawa, and A. Sasoh, "Frequency modula-

- tion in shock wave-boundary layer interaction by repetitive-pulse laser energy deposition," *Physics of Fluids*, 2015.
- [130] A. Iwakawa, T. Shoda, H. S. Pham, T. Tamba, and A. Sasoh, "Suppression of low-frequency shock oscillations over boundary layers by repetitive laser pulse energy deposition," *Aerospace*, 2016.
- [131] X. Veillard, R. Tahir, E. Timofeev, and M. S., "Limiting contractions for starting simple ramp-type scramjet intakes with overboard spillage," *Journal of Propulsion and Power*, 2008.
- [132] P. D. Welch, "The use of fast fourier transform for the estimation of power spectra: A method based on time averaging over short, modified periodograms." *IEEE Transactions on Audio Electroacoustics*, vol. 15, pp. 70–73, 1967.
- [133] R. W. Newsome, "Numerical simulatoin of near-critical and unsteady, subcritical inlet flow," *AIAA Journal*, 1984.
- [134] G. I. Taylor and J. W. Maccoll, "The air pressure on a cone moving a high speeds," *Proceedings of the Royal Society A*, 1933.
- [135] Y. Ogino, N. Ohnishi, S. Taguchi, and K. Sawada, "Baroclinic vortex influence on wave drag reduction induced by pulse energy deposition," *Physics of Fluids*, vol. 21, no. 2009, 2009.